



NASA CR-54846
214-220(Summary)

**STUDY OF PARAMETRIC PERFORMANCE
OF A TWO-STAGE REPETITIVELY
PULSED PLASMA ENGINE (REPPAC)**

N66-22904

FACILITY FORM 602

(ACCESSION NUMBER)	(THRU)
203	1
(PAGES)	(CODE)
CR-54846	28
(NASA CR OR TMX OR AD NUMBER)	(CATEGORY)

by

B. Gorowitz, P. Gloersen, and T. Karras

prepared for

NATIONAL AERONAUTICS AND SPACE ADMINISTRATION

contract NASw-1044

GPO PRICE \$ _____

CFSTI PRICE(S) \$ _____

Hard copy (HC) 6.00

Microfiche (MF) 1.25

ff 853 July 85

SPACE SCIENCES LABORATORY

GENERAL  ELECTRIC

MISSILE AND SPACE DIVISION

NOTICE

This report was prepared as an account of Government sponsored work. Neither the United States, nor the National Aeronautics and Space Administration (NASA), nor any person acting on behalf of NASA:

- A.) Makes any warranty or representation, expressed or implied, with respect to the accuracy, completeness, or usefulness of the information contained in this report, or that the use of any information, apparatus, method, or process disclosed in this report may not infringe privately owned rights; or
- B.) Assumes any liabilities with respect to the use of, or for damages resulting from the use of any information, apparatus, method or process disclosed in this report.

As used above, "person acting on behalf of NASA" includes any employee or contractor of NASA, or employee of such contractor, to the extent that such employee or contractor of NASA, or employee of such contractor prepares, disseminates, or provides access to, any information pursuant to his employment or contract with NASA, or his employment with such contractor.

Requests for copies of this report should be referred to

National Aeronautics and Space Administration
Office of Scientific and Technical Information
Attention: AFSS-A
Washington, D. C. 20546

CR No. 54846
GE 214-220 (SUMMARY)

SUMMARY REPORT

STUDY OF PARAMETRIC PERFORMANCE OF
A TWO-STAGE REPETITIVELY
PULSED PLASMA ENGINE (REPPAC)

by

B. Gorowitz, P. Gloersen, and T. Karras

Prepared for

NATIONAL AERONAUTICS AND SPACE ADMINISTRATION

March 31, 1966

CONTRACT NASw-1044

Project Manager
NASA Lewis Research Center
Cleveland, Ohio
Spacecraft Technology Division
Mr. Peter Ramins

GENERAL ELECTRIC COMPANY
SPACE SCIENCES LABORATORY
MISSILE AND SPACE DIVISION
P. O. Box 8555
PHILADELPHIA, PA. 19101

STUDY OF PARAMETRIC PERFORMANCE
OF A TWO-STAGE REPETITIVELY
PULSED PLASMA ENGINE (REPPAC)

by

B. Gorowitz, P. Gloersen, T. W. Karras

ABSTRACT

22904

Changes in the electrode geometry, propellant distribution, discharge triggering mode, voltage, and capacitance have resulted in an overall efficiency of 63%, at an I_{sp} of 5000 sec., for a repetitively pulsed coaxial plasma accelerator. Performance at a slightly lower level of 57%, 4800 sec. I_{sp} , calculated from thrust, mass flow and power input measurements, has been confirmed by several independent techniques including exhaust stream calorimetry, and probe measurements of neutral and ionized species distributions and energies. A ten hour run of the engine, which indicated no degradation of performance with time, demonstrated that the measured performance was equally valid for longer term operation of the engine.

(D)

TABLE OF CONTENTS

<u>Section</u>	<u>Page</u>
ABSTRACT	
I. INTRODUCTION	I-1
II. DISCUSSION OF THE MOST PERTINENT RESULTS	II-1
A. Description of the A-7D Pulsed Plasma Accelerator	II-1
B. Effects of Capacitance, Voltage, and Propellant Mass Flow on Engine Efficiency	II-9
C. Performance of the A-7D Accelerator with 144.5 μ fd Capacitance	II-9
C.1 Effects of Long Term Operation on Engine Performance	II-19
C.2 Possible Spurious Effects on Thrust and Mass Input	II-19
C.3 Calorimetric Determination of Exhaust Stream Energy	II-24
C.4 Corroboration of Engine Efficiency and Specific Impulse	II-25
D. Performance of the A-7D Accelerator with 218 μ fd Capacitance	II-26
E. Plasma Exhaust Characteristics	II-28
E.1 Measurements and Uncertainties	II-28
E.2 Data Reduction and Examples	II-30
REFERENCES	II-41
III. ACCELERATOR CHRONOLOGY	III-1
A. Mod A-4T Accelerator	III-1
A.1 Thrust Measurements	III-1
A.2 Propellant Mass Flow Measurements	III-1

<u>Section</u>	<u>Page</u>
A. 3 Electrode Erosion	III-4
A. 4 Overall Efficiency - $T^2/2 \dot{m} P$	III-5
A. 5 Energy Efficiency	III-5
A. 6 Faraday Cup Measurements	III-5
A. 7 Propellant Distribution Studies	III-11
a. Experimental	III-11
b. Results	III-12
c. Discussion	III-20
A-8 Emission Spectra from the Mod A-4T Gun Plasma Exhaust	III-21
B. Mod A-5 Accelerator	III-29
C. Performance of the Mod A-6 Accelerator - Use of Electrically Triggered Operation	III-29
D. Measurements with a Modified Injector Nozzle Geometry (Mod A-7 Gun)	III-33
E. The A-7D Accelerator - Operation in the Electrically- Triggered Mode with 45 μ fd Capacitance	III-37
E. 1 Performance Measurements	III-37
E. 2 Propellant Distribution Measurements	III-37
E. 3 Gridded Probe Measurements	III-41
E. 4 Current Measurements Outside of the A-7D Accelerator	III-47
F. The A-8D and A-9D Accelerators	III-55
F. 1 Overall Efficiency Measurements	III-55
F. 2 Calorimeter Measurements of Exhaust Stream Energy	III-59
F. 3 Gas Density Measurements on the A-9D Accelerator	III-60

<u>Section</u>	<u>Page</u>
G. The A-9DB Accelerator	III-65
H. A-8DB Results	III-67
I. Performance of the A-7D Accelerator as a Function of Capacitance	III-76
REFERENCES	III-81
IV. PROBLEM AREAS	IV-1
V. KEY COMPONENT TECHNOLOGY	V-1
A. Improved Propellant Feeds	V-1
B. The Capacitor Bank	V-2
C. Electrode and Insulator Materials	V-7
REFERENCES	V-10
APPENDIX A	A-1
Overall Efficiency Measurements	A-1
1. Thrust Measurements	A-1
a. Thrust Balance	A-1
2. Propellant Flow-Rate Measurement	A-3
a. Gaseous Propellant Flow	A-3
b. Eroded Mass Flow	A-5
3. Total Input Power	A-6
REFERENCES	A-7
APPENDIX B	
Gas Density Measurements	B-1
1. Probe Design	B-1
2. Probe Operation	B-1
3. Measurements	B-4
REFERENCES	B-7

<u>Section</u>	<u>Page</u>
APPENDIX C	C-1
Multigridded Particle Collector	C-1
APPENDIX D	D-1
Measurements of Magnetic Fields in the A-7D Accelerator	D-1
APPENDIX E	E-1
1. Introduction	E-1
2. Accelerator Operation Model	E-2
a. Current Build-Up	E-4
b. True Cathode Acceleration	E-4
c. Virtual Cathode Acceleration	E-4
d. Quasi-Stationary Discharge Acceleration	E-4
e. Corrected Circuit Equations	E-5
3. Theory of the Quasi-Stationary Discharge Acceleration	E-6
REFERENCES	E-16-17

LIST OF FIGURES

<u>Figure No.</u>		<u>Page</u>
		II-
II-1.	Drawing of Mod A-7D Accelerator	2
II-2.	(a) Mod A-7D Accelerator (b) Mod A-7D Center Electrode	3
II-3.	Circuit for Mod A-7D Accelerator	5
II-4.	Variable Capacitance Bank used with Mod A-7D Accelerator	6
II-5.	Capacitor Bank - 42" Overall Diameter	7
II-6.	One Module of the Capacitor Bank	8
II-7.	Thrust vs. Mass Flow for Various Efficiencies, Specific Impulses and Fixed Power Input	10
II-8.	Efficiency vs. Specific Impulse for Mod A-7D Accelerator, 42.5 μ fd, 2 KV	11
II-9.	Efficiency vs. Capacitance at a Specific Impulse of 5000 sec., A-7D Gun	12
II-10.	Efficiency vs. Specific Impulse for Various Mass Flows, 950 V, 144.5 μ fd, A-7D Gun	14
II-11.	Efficiency vs. Specific Impulse at Four Different Operating Voltages, 144.5 μ fd, A-7D Gun	15
II-12.	Efficiency vs. Voltage for Three Different Specific Impulses	16
II-13.	Propellant Mass Fraction vs. Valve Voltage for Mod A-7D Gun	17
II-14.	Fraction of Propellant Between the Accelerator Electrodes at Various Discharge Trigger Delay Times	18
II-15.	Outline of Plasma Accelerator Test Facility	21

<u>Figure No.</u>		<u>Page</u>
II-16.	Integrated Current with 7.5 cm Diameter Rogowski Loop	II-22
II-17.	Average Current Density vs. Radial Distance of Rogowski Loop from Center Line of A-7D Gun, 5 cm Downstream from Muzzle	23
II-18.	Overall Efficiency vs. Specific Impulse for Various Mass Flows	27
II-19.	Sample Gridded Probe Trace	29
II-20.	Ion Velocity Distribution on Axis, A-7D Gun, $\eta = 57\%$, $I_{sp} = 4800$ sec.	32
II-21.	Ion Velocity Distribution on Axis, A-7D Gun, $\eta = 57\%$, $I_{sp} = 4800$ sec.	33
II-22.	Total Velocity Distribution Function for all Ions Passing the Probe Position	34
II-23.	Total Ion Velocity Distribution on Axis, A-7D Gun, $\eta = 57\%$, $I_{sp} = 4800$ sec.	36
II-24.	Total Ion Velocity Distribution 45 cm off Gun Axis, A-7D Gun, $\eta = 57\%$, $I_{sp} = 4800$ sec.	37
II-25.	Fraction of Accelerated Propellant within a Beam Radius 2 m downstream from accelerator muzzle	38
II-26.	Average Ion Velocity at Various Radial Positions in a Plane Two Meters Downstream from the Accelerator Muzzle.	39

<u>Figure No.</u>		<u>Page</u>
III-1.	Mod A-4T Accelerator	III- 2
III-2.	Thrust vs. Voltage and Power - Mod A-4T Accelerator	3
III-3.	Center Electrode After Operation for 3000 Shots at 8 KV, Mod A-4T Accelerator	6
III-4.	Electrode Erosion vs. Initial Capacitor Voltage, Mod A-4T	7
III-5.	Overall Efficiency vs. I_{sp} , Mod A-4T, 45 μ fd Nitrogen	8
III-6.	Energy Efficiency vs. Voltage, Mod A-4T, Nitrogen	9
III-7-11.	Ion Velocity Distribution Curves from Faraday Cup Measurements	10
III-12.	Oscilloscope Trace of Fast Pressure Probe Signal	13
III-13.	Time Sequence of Gas Density Profile in Gun for N_2	14
III-14.	History of Gas Pressure Near Injector Ports	15
III-15.	Propellant Mass Utilized as a Function of Operating Voltage, A-4T Gun	17
III-16	Adjusted Overall Efficiency vs. Specific Impulse, A-4T Gun	18
III-17.	Quantity of Gas in Gun as a Function of Time, A-4T Gun	19
III-18.	Time Sequence of Gas Density Profile in Gun for He.	22
III-19.	Time Sequence of Gas Density Profile in Gun for Argon	23
III-20.	Time Profile of N II 3995 \AA Line in A-4T Gun Exhaust 10 cm Downstream from Muzzle, 3 KV, 45 μ fd, Nitrogen	25

<u>Figure No.</u>		<u>Page</u>
		III-
III-21.	Time Profile of A II 4267 Å Line in A-4T Gun Exhaust 10 cm Downstream from Muzzle, 3 KV, 45 μfd, Nitrogen	26
III-22.	Spectral Record of Luminous Exhaust Using Nitrogen, A-4T Gun, 3 KV, 45 μfd, Nitrogen, Observed 10 cm Downstream from Muzzle.	27
III-23.	Spectral Record of Mod A-4T Gun Exhaust, 10 cm Downstream from Muzzle, 3 KV, 45 μfd using Argon Propellant	28
III-24.	Drawing of Mod A-5 Gun	30
III-25.	Overall Efficiency vs. Specific Impulse -Mod A-5 Gun	31
III-26.	Drawing of Mod A-6 Gun	32
III-27.	Overall Efficiency vs. Specific Impulse-Mod A-6 Gun	34
III-28.	Overall Efficiency vs. Delay after Valve Actuation Mod A-6, 45 μfd	35
III-29.	Drawing of Mod A-4T and Mod A-7 Gun Nozzles	36
III-30.	Overall Efficiency vs. Specific Impulse - Mod A-7 Gun Gas-triggered Operation	38
III-31.	Two-Stage Mod A-7D Engine	39
III-32.	Performance of the A-7D Accelerator	40
III-33.	Propellant Fraction Curves A-7D, Xe, 4400 Valve Voltage	42
III-34.	Propellant Fraction Curves A-7D, N ₂ , 4400 Valve Voltage	43
III-35.	Isobars, A-7D Nitrogen, Valve: 4400 Volts	44
III-36.	Isobars, Xenon, Valve: 3900 Volts	45
III-37.	Gridded Probe for Measurement of Ion Energies	46
III-38.	Ion Velocity Distribution A-7D Gun, Various Stopping Potentials, Nitrogen 2 KV, 42.5 μfd .65 ms delay	48

<u>Figure No.</u>		<u>Page</u> III-
III-39.	Ion Velocity Distribution A-7D Gun, 0-100 V Stopping Potentials, Nitrogen 1.5 KV, 42.5 μ fd, .65 ms Delay	49
III-40.	Ion Velocity Distribution A-7D Gun, 100-225 V Stopping Potentials, Nitrogen 1.5 KV, 42.5 μ fd .65 ms Delay	50
III-41.	Ion Velocity Distribution A-7D Gun, Nitrogen 2 KV, 42.5 μ fd, Gas-triggered Operation	51
III-42.	Velocity Distribution of Ions in Exhaust of A-7D Gun at 2 KV, 42.5 μ fd On and Off Axis	52
III-43.	Rogowski Loop Signals of Currents External to the Mod A-7D Gun	53
III-44.	Average Current Density vs. Distance from Center Line of A-7D Gun	54
III-45.	Comparative Performance of A-7D, A-8D, and A-9 Accelerators with Xenon Propellant	56
III-46.	Mod A-8 with Straight Cylindrical Sleeve Mod A-8D with Diverging Sleeve	57
III-47.	Sketch of A-9D Center Electrode	58
III-48.	Isobars A-9D Gun, Xenon, 4400 Volts on Valve, Reading in Volts	62
III-49.	Propellant Fraction as a Function of Time, A-9D Gun, Xenon	63
III-50.	Isobars A-7D Gun, Xenon, Valve: 4400 Volts, 0.6 ms Delay	64
III-51.	Sketches of Valve Seats	66
III-52.	Isobars, A-8DB Gun, 4400 Volts Valve, Xenon, Reading in Volts	68
III-53.	Propellant Fraction Between Nozzles and Muzzle as a Function of Time -Axial Position: 0.5 cm, Mod A-8DB Xenon, 4400 Volts valve	71

<u>Figure No.</u>		<u>Page</u> <u>III-</u>
III-54.	Propellant Fraction Between Nozzles and Plane 5.5 cm Downstream from A-8DB Gun, Xenon, 4400 V valve	72
III-55.	Propellant Fraction Between Nozzles and Plane 10.5 cm Downstream from A-8DB Gun, Xenon, 4400 V Valve	73
III-56.	Isobars Beyond A-8DB Gun, Xenon, 4400 V Valve	74
III-57.	A-8DB Performance, Xenon Propellant	75
III-58.	Velocity Distribution of Ions in Exhaust of A-8DB Gun, Nitrogen, 2 KV, .65 ms. Delay	77
III-59.	A-7D Performance, 72 μ fd 1.55 KV, Xenon	78
III-60.	A-7D Performance, 96.5 μ fd, Xenon	79
III-61.	Gas Density Probe Trace Showing "Valve Bounce"	80
V-1	Piezoelectric Valve and Electrode Components	V-3
V-2	Piezoelectric Valve and Accelerator Electrode Assembly	V-4
V-3	Capacitor Life vs. Operating Voltage for Various Temperatures, Designs, and Winding Weight	V-6
V-4	Schematic Cross-Section of the Pre-Prototype Capacitor	V-8
A-1	Thrust Balance with Engine Housing	A-2
A-2	Thrust Record for A-7D Accelerator	A-4
A-3	Thrust Calibration Record	A-4
B-1	Gas Density Probe	B-2
B-2	Electrical Circuit for CK5702 Gas Density Probe	B-3
B-3	Sample Gas Density Probe Trace .5 ms/cm. .01 V/cm.	B-5

<u>Figure No.</u>		<u>Page</u>
C-1.	Gridded Probe for Measurement of Ion Energies	C-2
C-2.	Probe Head Support	3
C-3.	Gridded Probe in Shield	4
C-4.	Electrical Circuit for Gridded Probe	5
C-5.	Variation of Maximum Current Through 2nd and 3rd Grids, Not allowing a Potential Maximum Above that of 3rd Grid	6
D-1.	B_{θ} Probe Signals for Different Axial Positions Mod A-7D Accelerator 950 V, 144.5 μ fd, Xenon Sweep 2 μ sec/cm. Radial position, 4.5 cm from center line of Accelerator.	D- 2
D-2.	B_{θ} vs. Axial Position for Various Times	3
E-1.	Four-Stage Acceleration Process in the A-7D Accelerator	E- 3
E-2.	Schematic of Current Distribution	7
E-3.	Differential Current Loop	11

I. INTRODUCTION

This report is a description of experimentation and analysis carried out over a period of eighteen months and applied toward improvement of the performance of a repetitively pulsed coaxial plasma accelerator. The process of improving accelerator performance consisted primarily of changing the electrode geometry, electrical input characteristics, mode of discharge initiation and propellant distribution to affect an appropriate matching of these parameters. Early measurements of the performance of the pulsed plasma accelerator indicated that any increases in the efficiency of the engine were usually accompanied by undesirable increases in the specific impulse range. For example, prior to the series of parametric changes described here, the overall efficiency had been improved to a peak of 70% at a specific impulse of 9000 sec. The goal of ensuing efforts was to approach this efficiency in the specific impulse range of 2000 - 5000 sec. The accelerator which represented a culmination of these efforts was found, by thrust, mass flow and input power measurements, to operate with an overall efficiency of 63% at a specific impulse of 4860 seconds with xenon used as the propellant. At a stage in the accelerator development where a slightly lower level of performance (57% at 4960 sec.) had been measured, the engine was operated for a period of ten consecutive hours for the purpose of determining any possible degradations in performance. The test demonstrated that no such degradation occurred and that there were no apparent obstacles to operation for considerably longer duration.

In addition, a series of independent measurements were made to corroborate the performance as determined by thrust and mass flow measurements. Target calorimetry was used to determine the power in the exhaust stream. Two different particle probes were used to measure the injected propellant distribution and ionized particle energies and velocities, respectively. In addition to providing insight into the mode of operation of the accelerator, the results of these three measurements were used in the calculation of the specific impulse and efficiency of the device. The performance thus determined was in good agreement with that obtained from the thrust and mass flow measurements. With such agreement in hand, additional steps were taken to improve the engine performance. Such steps resulted in the efficiency and specific impulse levels mentioned above.

This report describes in detail the pertinent phases in the evolution toward the present level of accelerator performance and the experimental and analytical procedures used both for the purpose of determining this performance and for the purpose of obtaining further insight into the nature of the acceleration process in an efficient pulsed coaxial plasma gun. It also discusses straightforward solutions to some of the key problem areas,

both of a technical and practical nature, which remain to be executed prior to the progression of this device from the laboratory stage of development to the hardware stage and potential space flight application.

II. DISCUSSION OF THE MOST PERTINENT RESULTS

In this section, we shall discuss the accelerator-capacitance combinations with which the highest levels of performance were achieved.

A. DESCRIPTION OF THE A-7D PULSED PLASMA ACCELERATOR

The design and principles of operation of the pulsed plasma accelerator have been described elsewhere^{1,2} in some detail. They will be reviewed here only briefly in order to provide a more complete description of the entire engine system. As a result of the series of parametric changes leading to its present configuration, the accelerator has been designated the "A-7D". It is this designation which will be used throughout this discussion.

The A-7D accelerator consists of a pair of cylindrically symmetric concentric copper electrodes separated by a Pyrex insulator at the breech. It is equipped with a propellant injection system inside the inner electrode and a set of discharge trigger wires in the interelectrode region. The outer electrode is a segment of a diverging cone; the inner electrode is of a convergent design. Figures II-1 and II-2 illustrate the design of this accelerator in more detail.

One of the most important features of this accelerator is the propellant injection and discharge initiation sequence. It was found that when the propellant loading of this accelerator was sufficiently high to cause the onset of the electrical discharge without auxiliary electrical triggering, the overall efficiency was poor. The main reason for this poor performance was the fact that more than one-half of the propellant was still in the propellant inlet nozzles at the time of discharge when operating in this mode. In this particular accelerator configuration, it was found to be more advantageous to load the interelectrode region with an amount of propellant insufficient to self-trigger the discharge at any time after the opening of the gas inlet valve and to incorporate a set of discharge trigger electrodes to initiate the discharge at an appropriate time after the opening of the valve. In this way, the inlet nozzles could be almost entirely empty before the discharge started. In practice, with fixed mass flow and input power, the delay time was varied until maximum thrust was observed, thereby signifying maximum efficiency. A typical delay time between actuation of the gas valve and the initiation of the discharge was 750 microseconds for xenon, the most commonly used propellant. This time delay generally agreed with that found by neutral density measurements (described below) to be necessary for a maximum fraction of injected propellant to be between the electrodes of the accelerator.

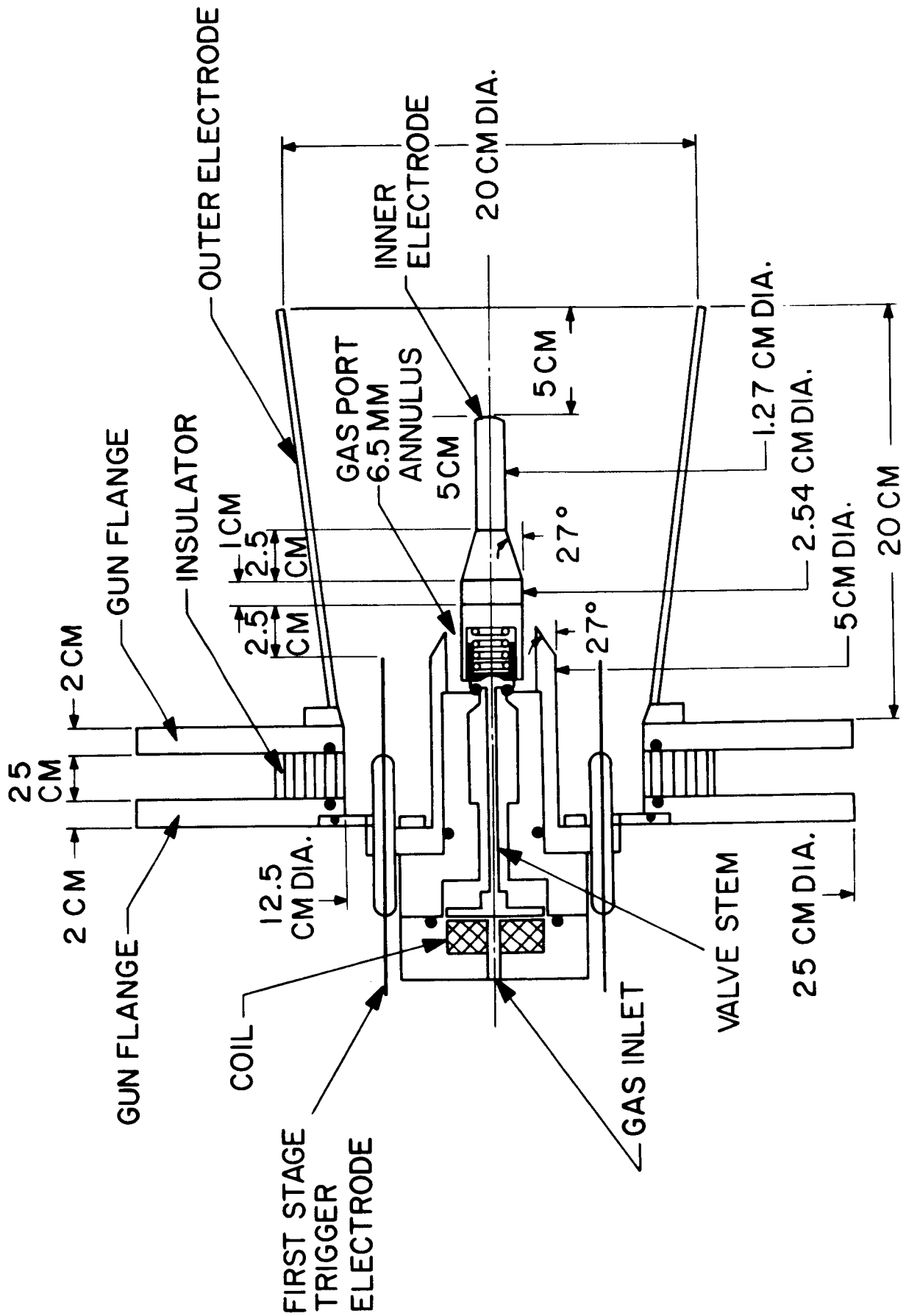


Figure II-1. Drawing of Mod A-7D Accelerator

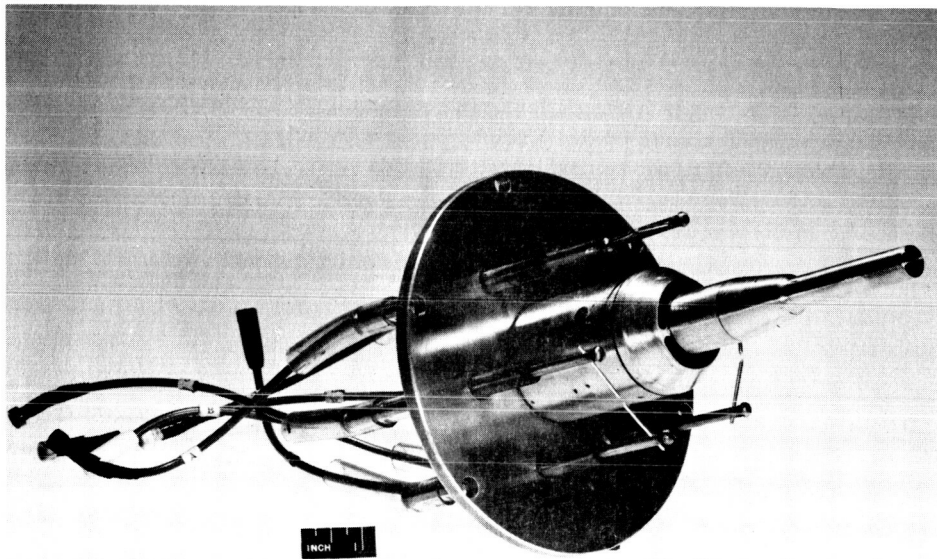
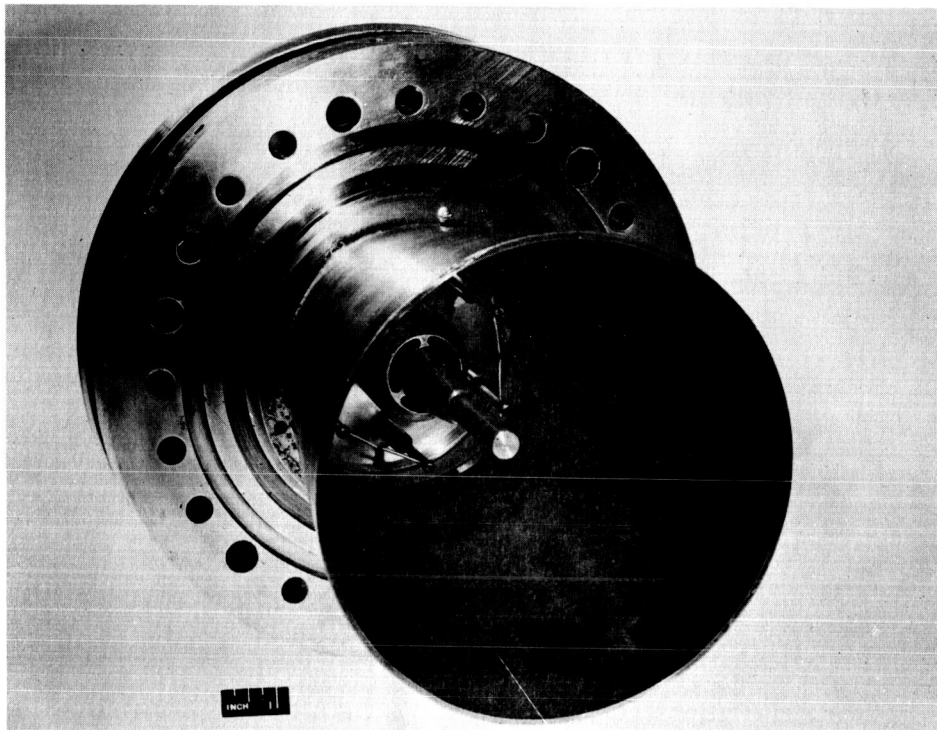
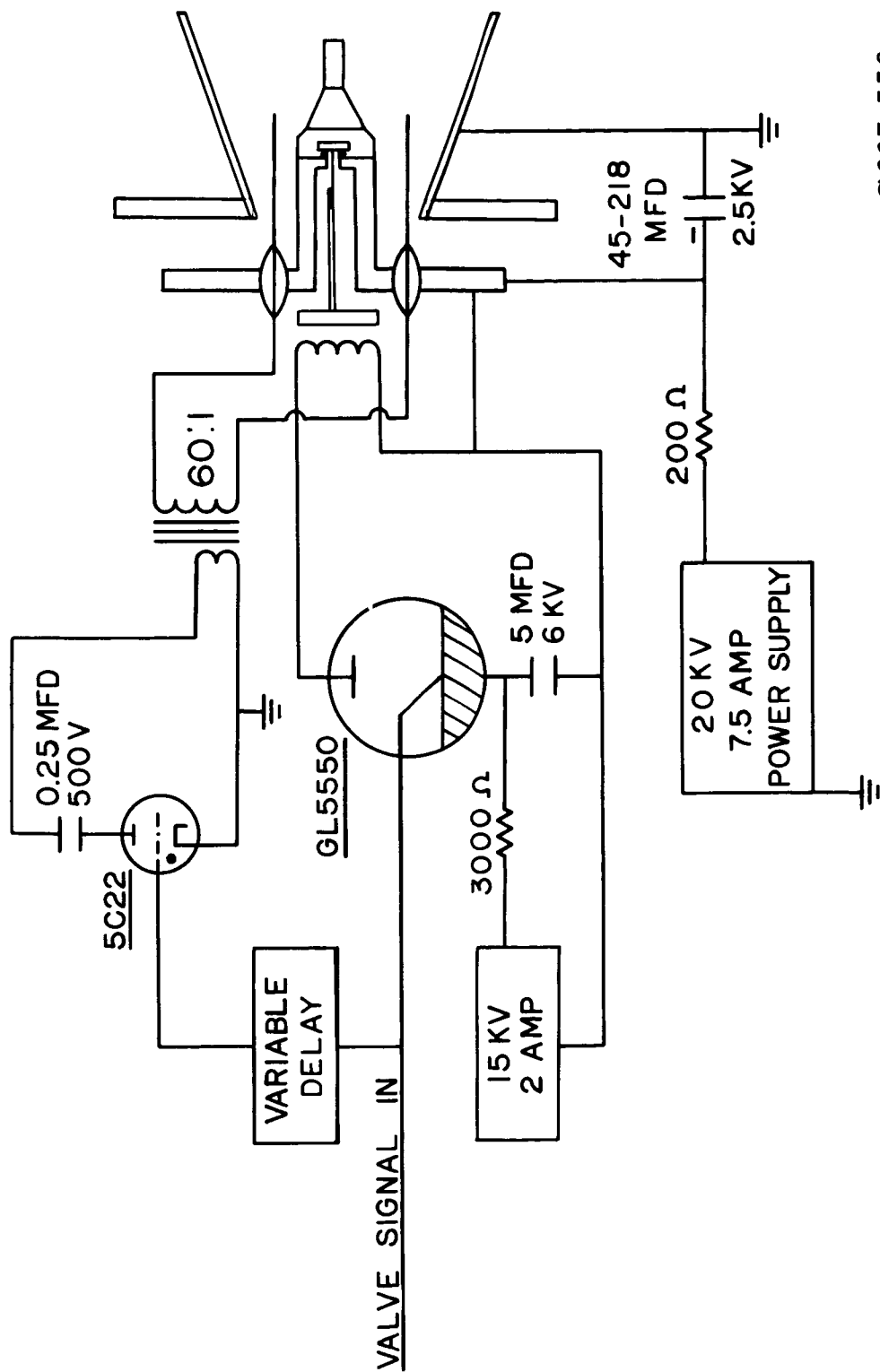


Figure II-2. (a) Mod. A-7D Accelerator
(b) Mod. A-7D Center Electrode

The valve used to admit the gas to the accelerator was a modified version of one described elsewhere³. Briefly, it consists of a moving disc sealed against a Teflon "O" ring seat. The disc is moved by the magnetic field from a nearby coil which is energized by a capacitor discharge. The electrical circuit for the valve and for the accelerator is shown in Figure II-3. The power consumed by this valve system was not incorporated in the performance numbers quoted for the accelerator since it was not of an efficient design. More efficient valving schemes have been devised and, to some extent, tested (see section V) but these were not included in the accelerator for the experimental measurements discussed here. The trigger electrodes used to initiate breakdown were brought into the vicinity of the discharge region through insulating vacuum seal lead-throughs located in the inner electrode flange. These are shown in Figure II-2. The trigger wires were made out of tungsten and exhibited negligible erosion after over 500,000 discharges. The trigger circuit (see Figure II-3) consumes a negligible amount of power.

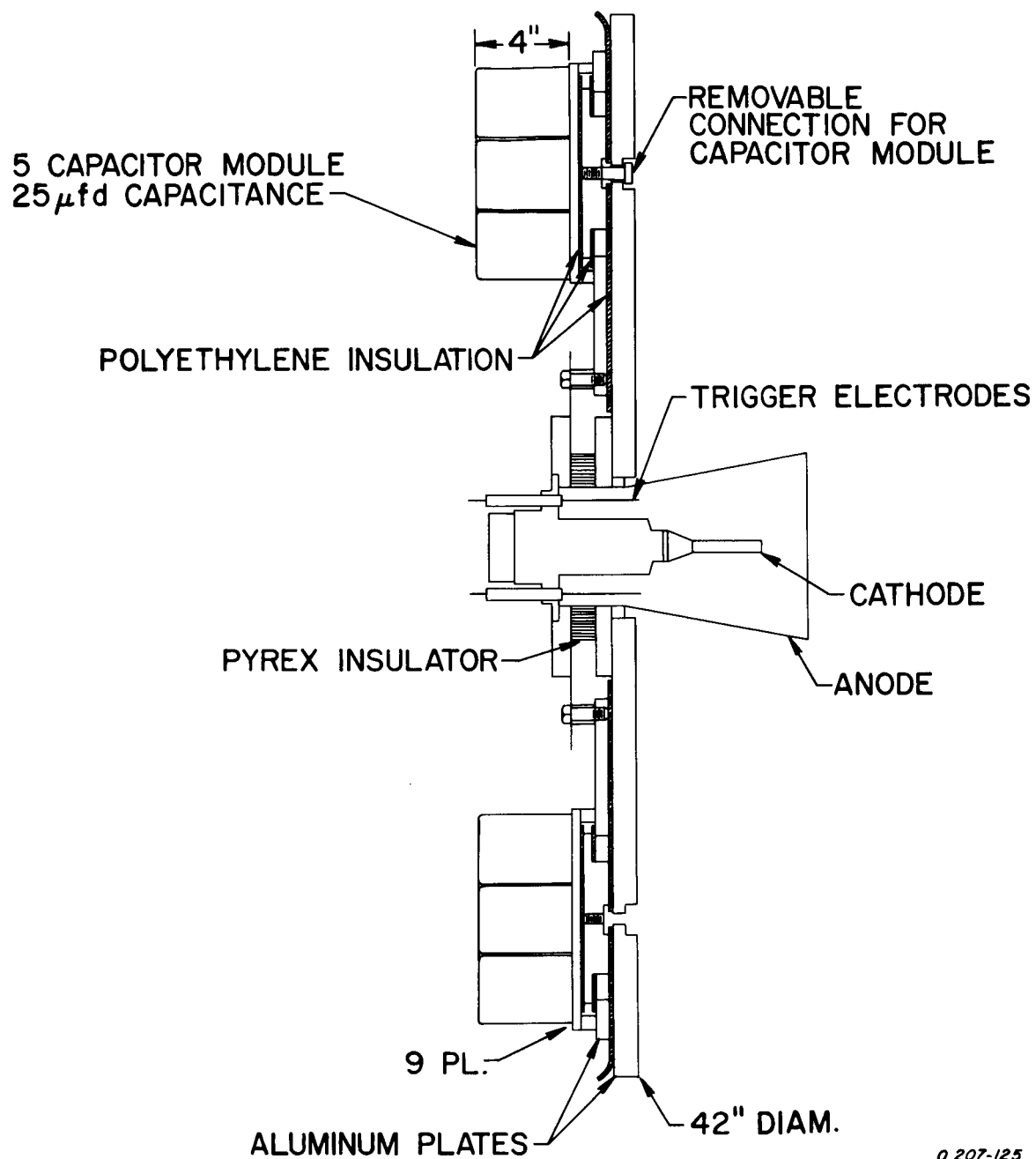
Of almost equal importance in the successful operation of the accelerator is the special design of the gas inlet ports. In addition to having a high conductance so that the propellant will be nearly completely injected in a reasonable amount of time, they were designed to direct the bulk of the gas along the inner electrode so that a relatively large amount of propellant could be injected without self-triggering the electric discharge. This manner of injection had the additional benefit of placing most of the propellant in a region where the discharge current density and hence the electromagnetic force was the highest.

The capacitor bank used for these studies was designed primarily to provide a flexible research tool. The capacitors used are dry mylar dielectric, Dearborn "Hi-Jul" units, rated at 2.5 KV, 5 microfarads with a "Q" of 14 @ 100 KC. They are arranged in 5-capacitor modules, nine of which are assembled on two large parallel discs which feed the electrical energy radially inwards to the accelerator electrode flanges. The stray inductance in this bank is two nanohenries and the capacity can be varied up to an actual measured capacity of 218 microfarads. This is accomplished by inserting or by removing the electrical connections between the modules and the plates without disturbing the position of the modules and hence the load distribution on the thrust balance. A drawing of the capacitor bank and accelerator arrangement is shown in Figure II-4. Photographs of the capacitor bank and of an individual module are shown in Figures II-5 and II-6.



207-330

Figure II-3. Circuit for Mod A-7D Accelerator



O 207-125

Figure II-4. Variable Capacitance Bank used with Mod A-7D Accelerator

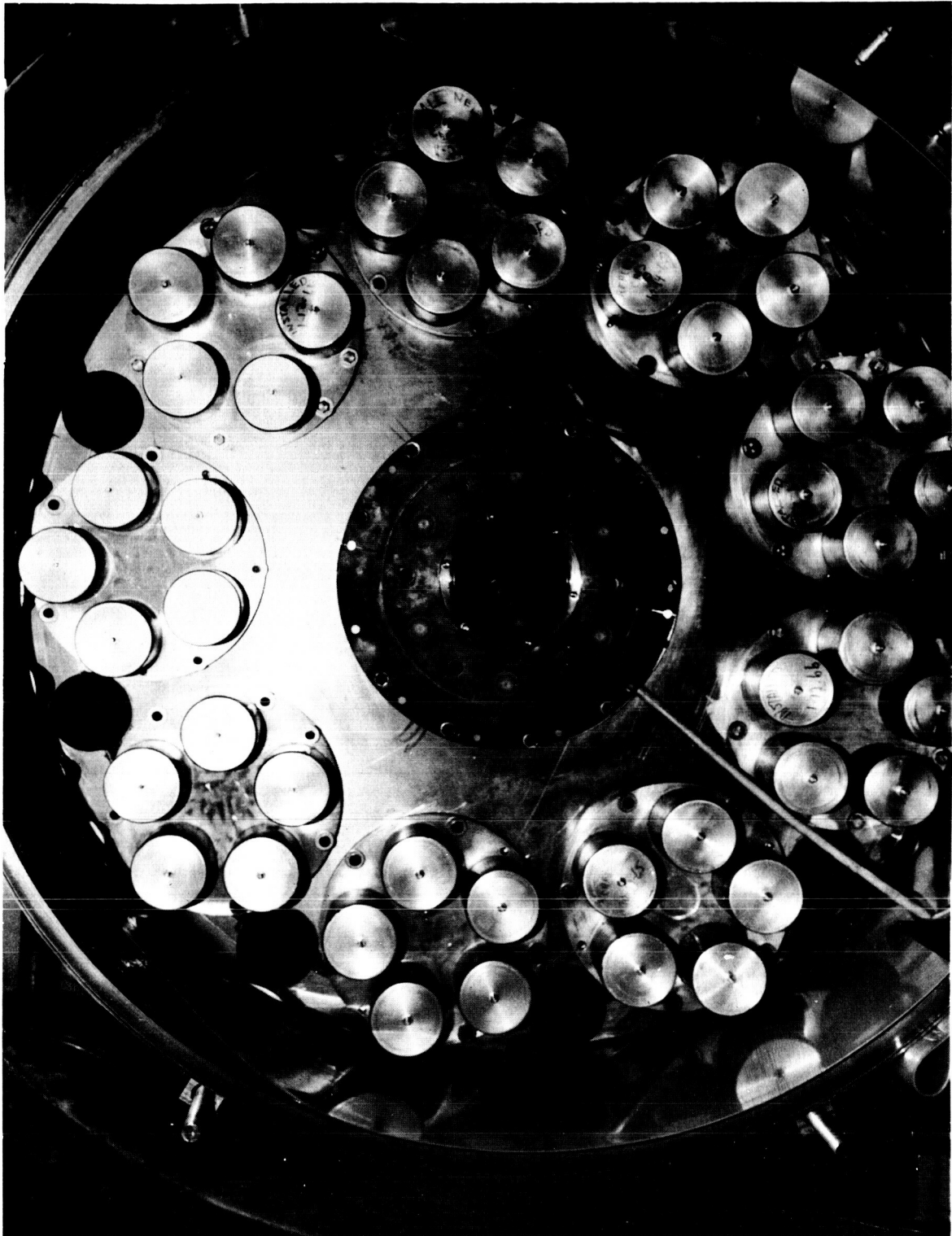


Figure II-5. Capacitor Bank - 42" Overall Diameter

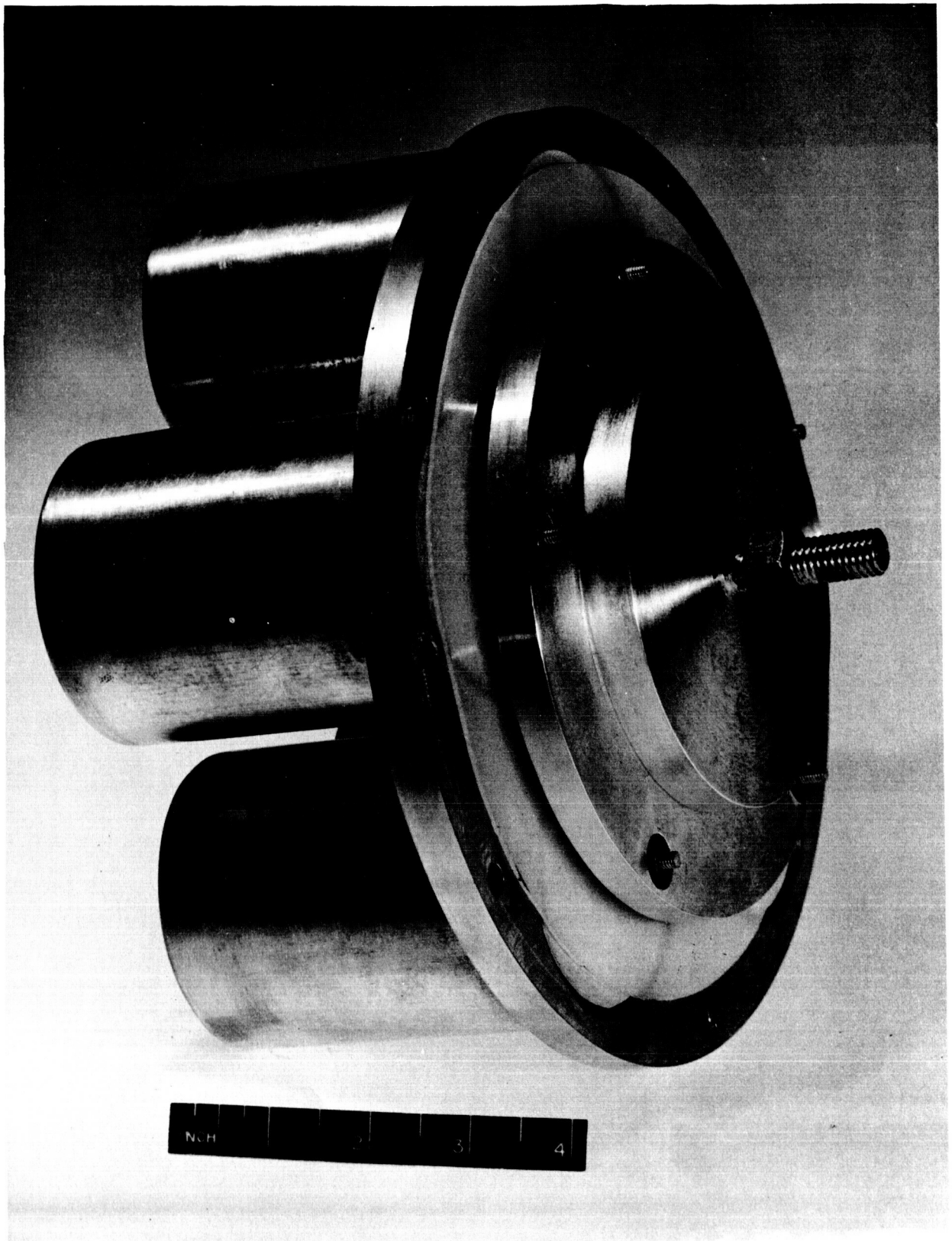


Figure II-6. One Module of the Capacitor Bank

B. EFFECTS OF CAPACITANCE, VOLTAGE, AND PROPELLANT MASS FLOW ON ENGINE EFFICIENCY

Ideally, for a particular engine voltage, capacitance, and firing rate, it should be possible to decrease the specific impulse, T/\dot{m} g, without decreasing the overall efficiency, $T^2/2\dot{m}P$, by increasing the propellant mass flow rate, \dot{m} (along with an appropriate increase in T). This is graphically illustrated in Figure II-7 which plots thrust vs. mass flow for various efficiencies and specific impulses and a fixed power input level representing what were typical operating conditions of 2 KV, 45 μ fd and 10 cps firing rate. The peak performance point obtained under these conditions, 70% at 9000 seconds, with an engine designated the "A-7D" is also indicated in Figure II-7. It may be seen that for 70% efficiency at 5000 sec., an almost four-fold increase in propellant flow is required above that associated with 9000 sec. In actual practice, it was found that the Paschen breakdown conditions were such that the necessary mass flow could not be injected into the A-7D accelerator without producing premature gas-triggering of the discharge. Furthermore, over the range of increased propellant flows which could be reliably injected, lower efficiencies resulted albeit at lower specific impulse. This is illustrated in Figure II-8 in which efficiency vs. specific impulse is plotted for various mass flows at a particular operating condition. The techniques used for the measurement of thrust, total mass flow and input power are described in Appendix A. The power input for all performance data presented in this report is defined as $P = 1/2 CV_0^2 (1-1/Q) \nu$, where Q is characteristic of the particular capacitor used. For the dry mylar dielectric capacitors used in these studies the Q was 14 at a frequency of 100 KC, so that about 93% of the power in the capacitor is available for transfer to the accelerator. Higher Q capacitors presently available would undoubtedly raise the power transfer. The engine firing rate, ν , was with few exceptions which are noted, 10 cps for the thrust runs which were used for the determination of engine performance.

Operation at the same capacitance and voltages lower than 2 KV permitted the use of increased amounts of propellant; but the lower currents, lower driving fields, and reduced discharge periods resulted in decreased coupling between the plasma and the fields. This was evidenced by a decrease in overall efficiency. The most direct means of increasing the amplitude and duration of the current waveform at voltages less than 2 KV was to increase the capacitance. The effect of capacitance on efficiency for a specific impulse of 5000 sec is summarized in Figure II-9.

C. PERFORMANCE OF THE A-7D ACCELERATOR WITH 144.5 μ fd CAPACITANCE

In the course of the successive increases in capacitance, denoted in

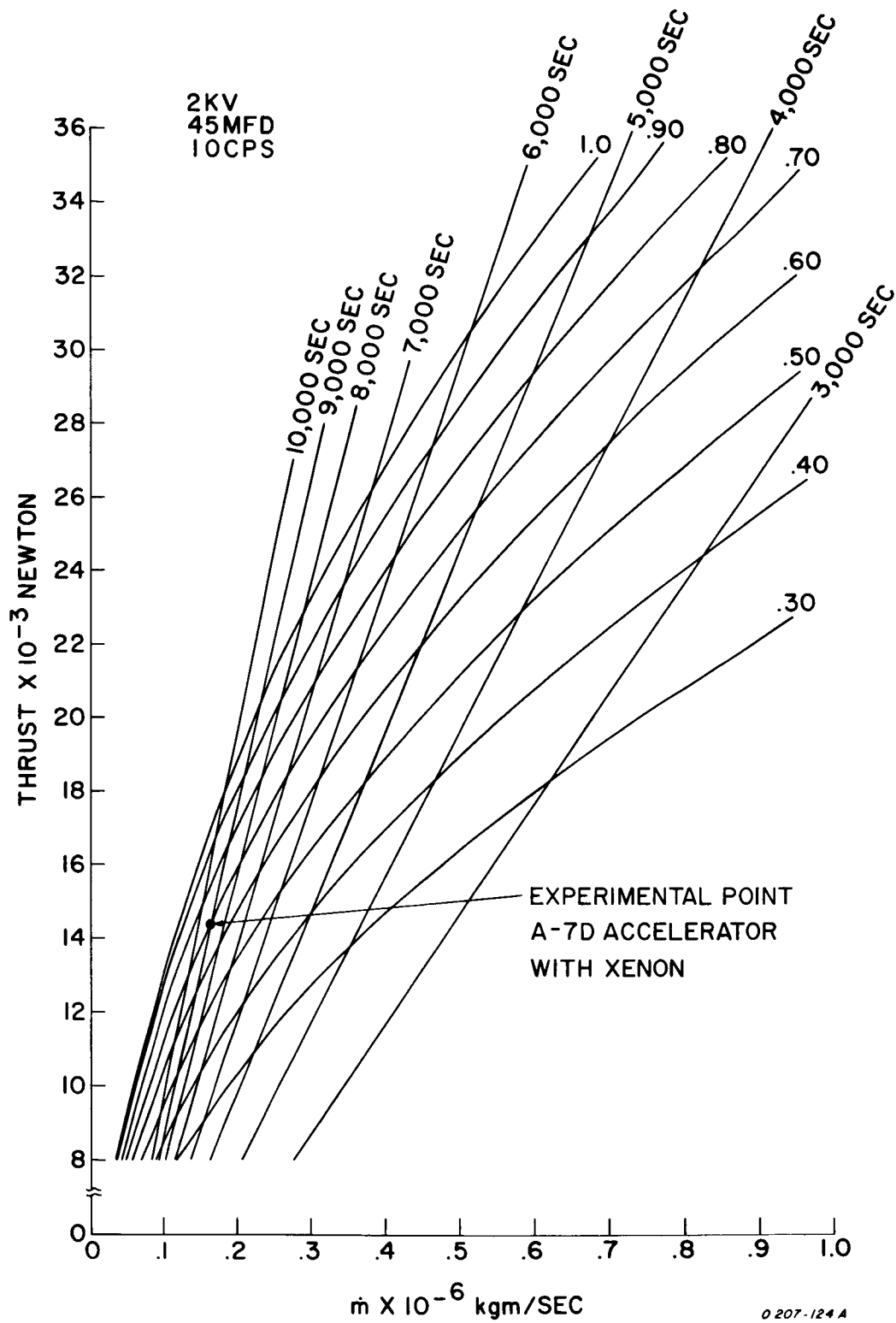


Figure II-7. Thrust vs. Mass Flow for Various Efficiencies and Specific Impulses and Fixed Power Input

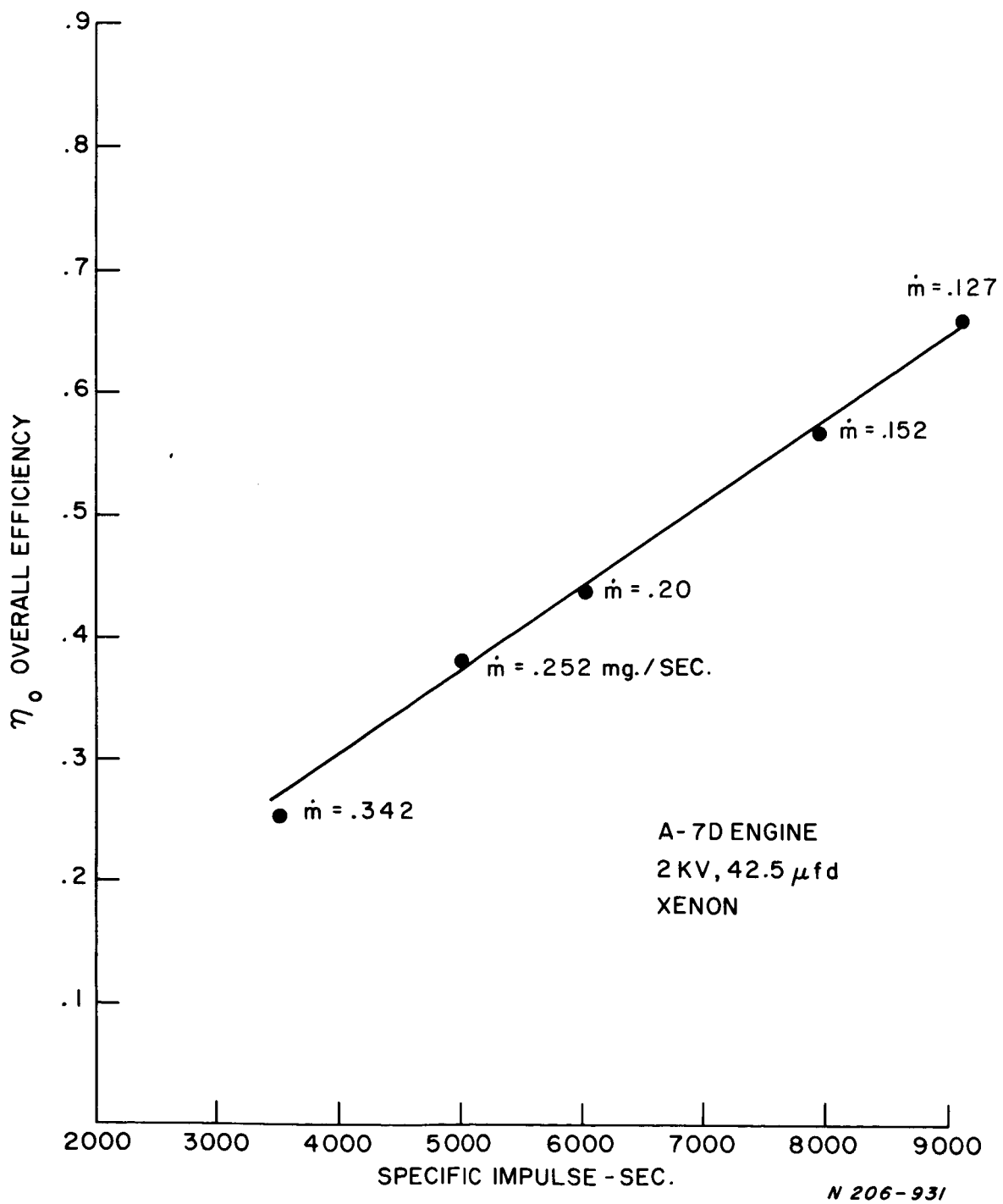
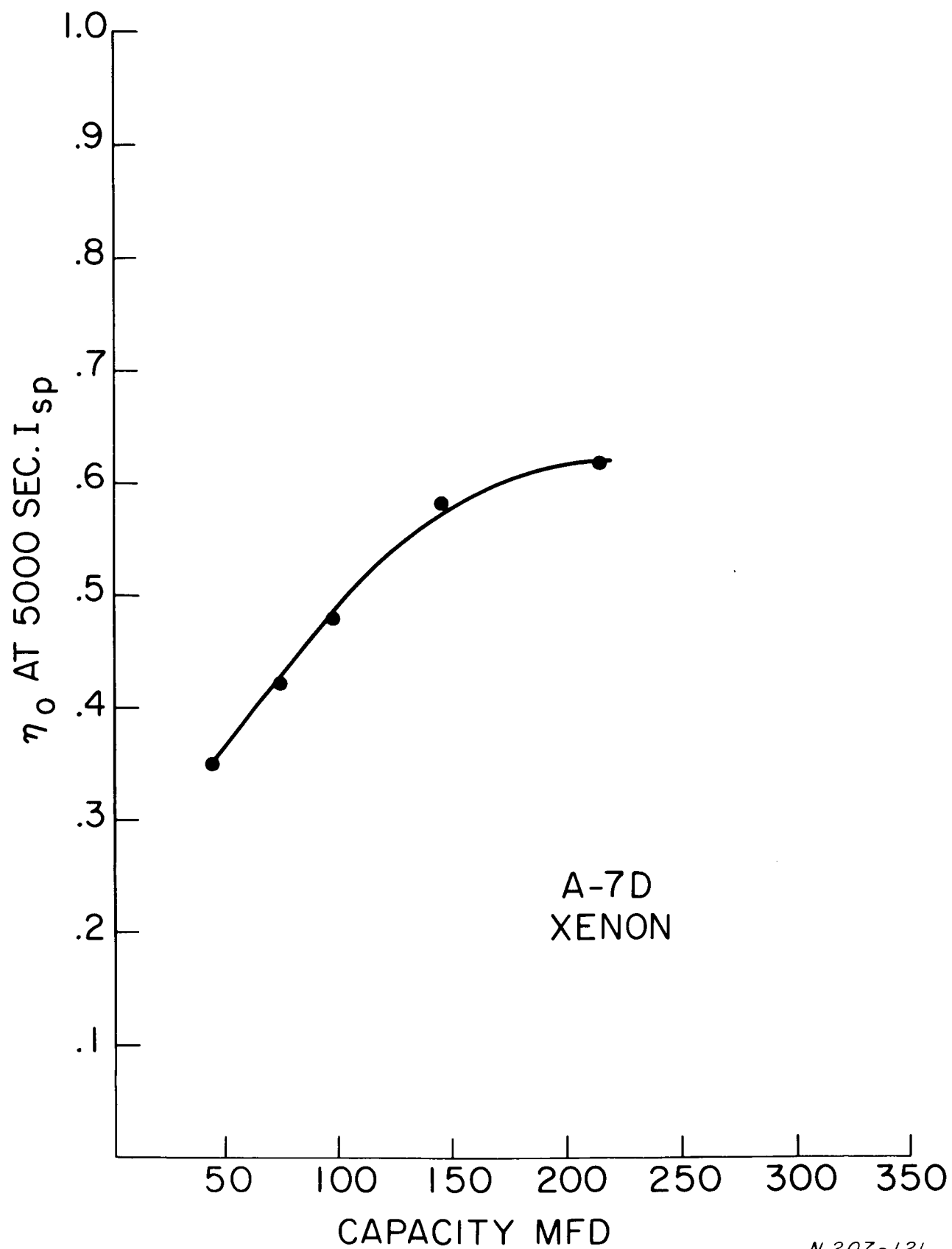


Figure II-8. Efficiency vs. Specific Impulse for Mod A-7D Accelerator, 42.5 μ fd, 2 KV



N 207-121

Figure II-9. Efficiency vs. Capacitance at a Specific Impulse of 5000 sec., A-7D Gun. Obtained from Lines Drawn Through Best Performance Points Representing Various Voltages and Mass Flows

Figure II-9, the A-7D, 144.5 μ fd accelerator-capacitance combination was deemed to be of sufficiently high overall efficiency to warrant a more extensive investigation of its performance than had been afforded the lower capacitance engines.

In Figure II-10, overall efficiency vs. specific impulse is plotted for operating conditions of 950 V, 144.5 μ fd, 10 cps firing rate, and several different mass flows. In the curve shown, the slanted fluctuation bars result partially from fluctuations in either the thrust or mass flow, or both, altering the overall efficiency and the specific impulse at the same time. The remaining contribution to the spread in indicated performance is due to the cumulative inherent accuracies of the thrust, mass flow and power measurements. For purposes of clarity of presentation, fluctuation bars have been omitted throughout with the exception of this illustrative curve.

It is instructive to note the change in overall efficiency at a fixed capacitance with various capacitor voltages. In Figure II-11 overall efficiency vs. specific impulse is shown for four different operating voltages and a capacitance of 144.5 μ fd. From these trends, one can obtain approximate values for the overall efficiency at several values of the specific impulse as a function of voltage, as shown in Figure II-12. It can be seen that an optimum operating voltage is indicated for a given specific impulse, and that for these conditions one voltage is indicated to be optimum at all specific impulses.

The propellant distribution and the fraction of injected propellant made available to the discharge by the A-7D valve and injector nozzle geometry were measured with a fast ion gauge probe described in Appendix C. Although it might at first be assumed that the distribution and propellant fraction would be unchanged under the present accelerator operating conditions, this was not the case. The use of increased propellant flows with lower voltages and higher capacitance, for the purpose of decreasing the specific impulse, required greater valve openings and hence higher valve voltages. The relationship of propellant mass fraction to valve voltage is shown in Figure II-13. For a valve voltage of 5.3 KV which was used to inject a xenon propellant flow of 0.296 mg/sec for the 144.5 μ fd capacitance engine (performance shown in Figure II-10), the available mass fraction was over 90%. This is also shown in Figure II-14 where the available propellant mass fraction is plotted vs. the interval between actuation of the propellant valve and triggering of the discharge. Invariably, the triggering time at which the highest efficiency was observed (i.e. the highest thrust for a given mass flow) corresponded to the time for maximum available propellant fraction. For the lower valve voltages associated

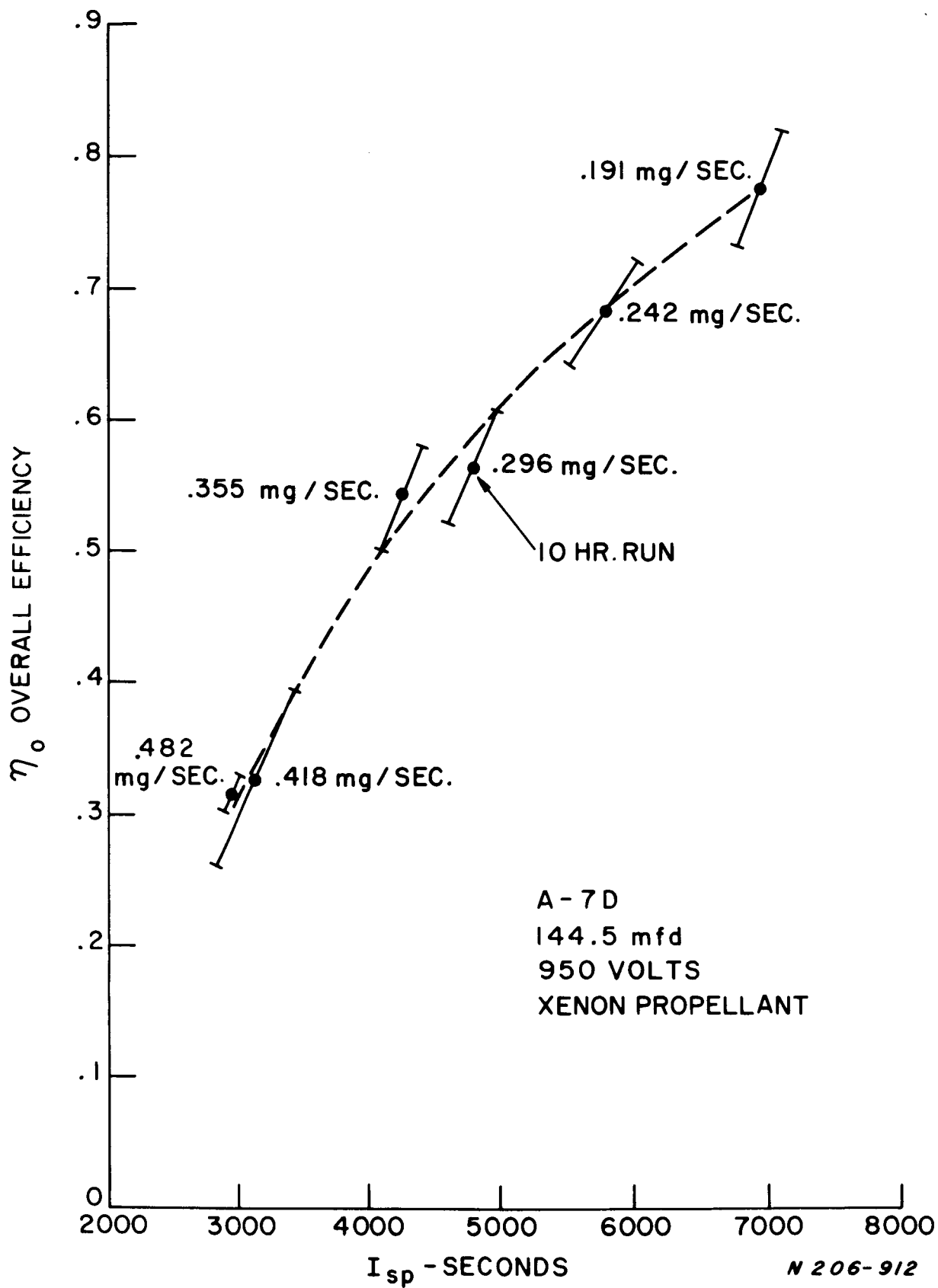


Figure II-10. Efficiency vs. Specific Impulse for Various Mass Flows,
950 V, 144.5 μ fd, A-7D Gun

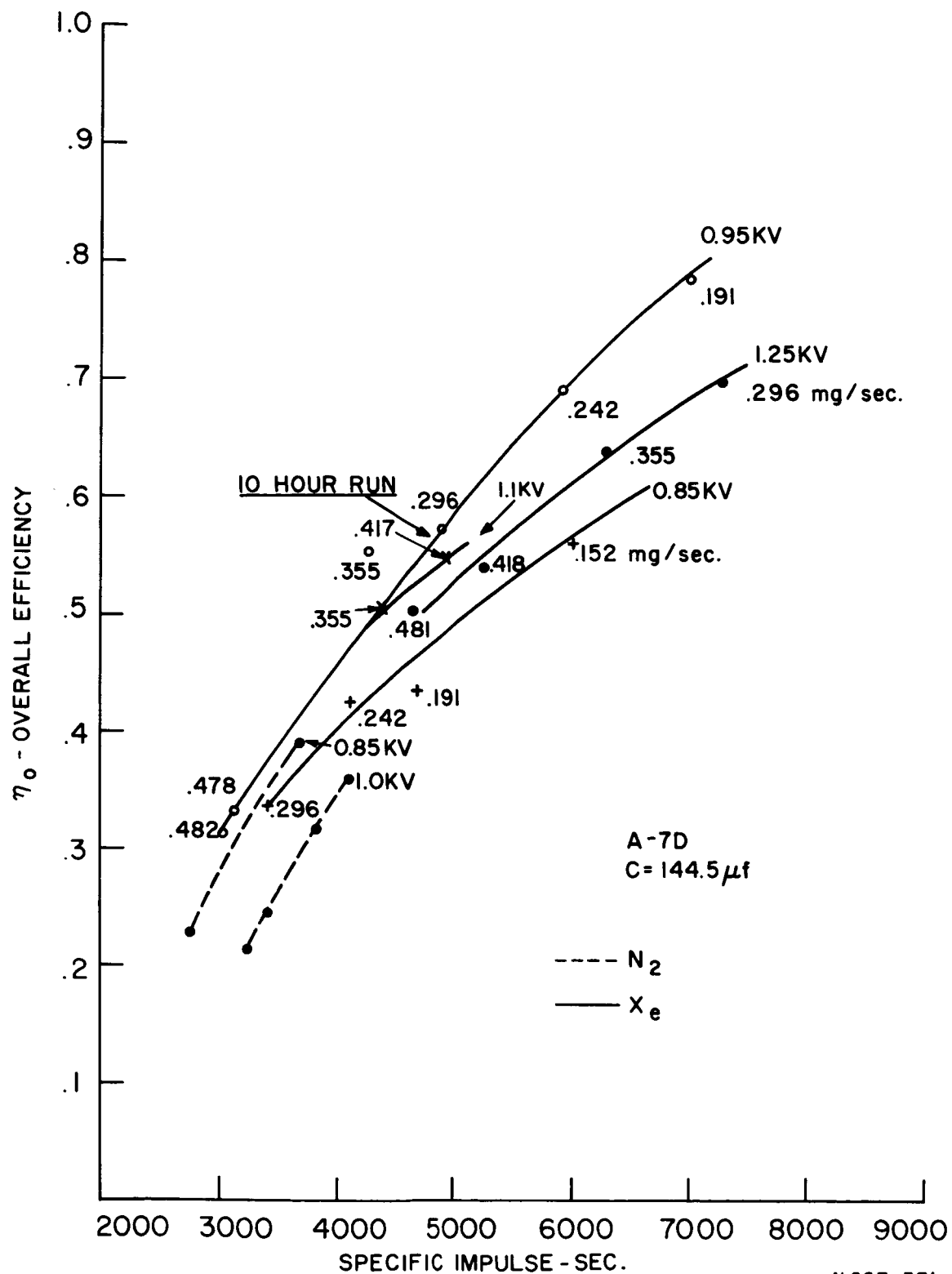


Figure II-11. Efficiency vs. Specific Impulse at Four Different Operating Voltages, 144.5 μf , A-7D Gun

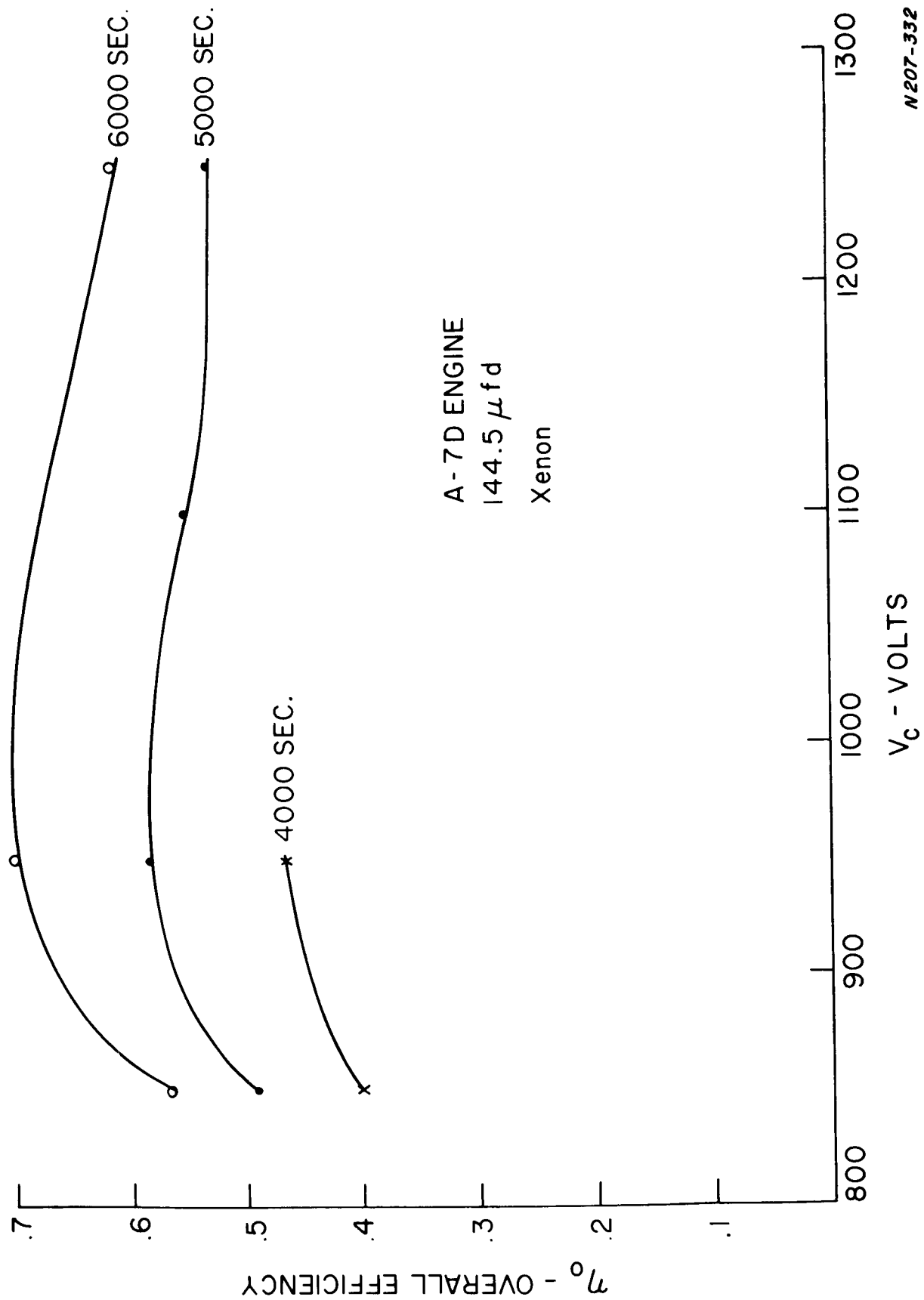
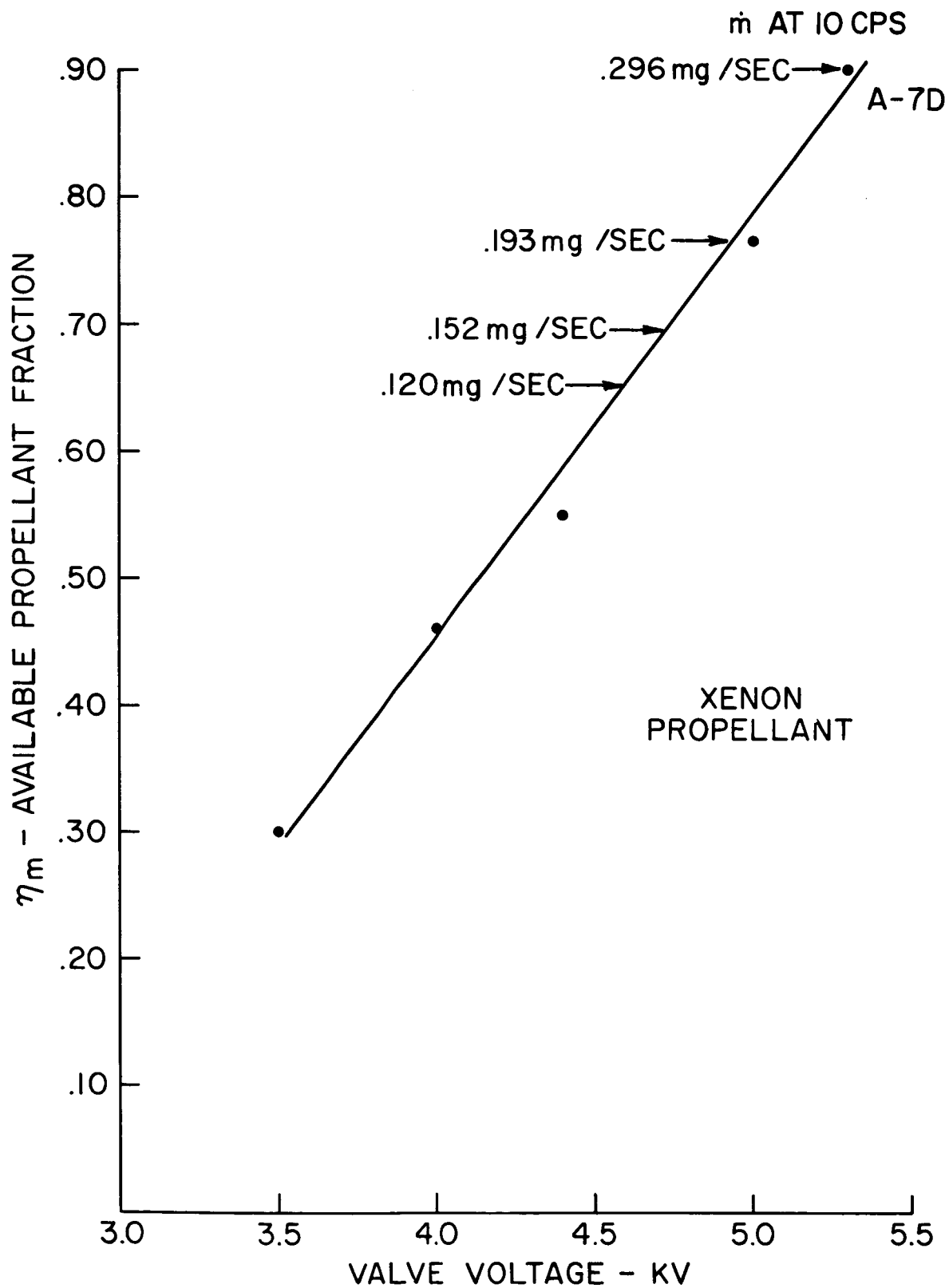


Figure II-12. Efficiency vs. Voltage for Three Different Specific Impulses



N 207-126

Figure II-13. Propellant Mass Fraction vs Value Voltage for Mod A-7D Gun

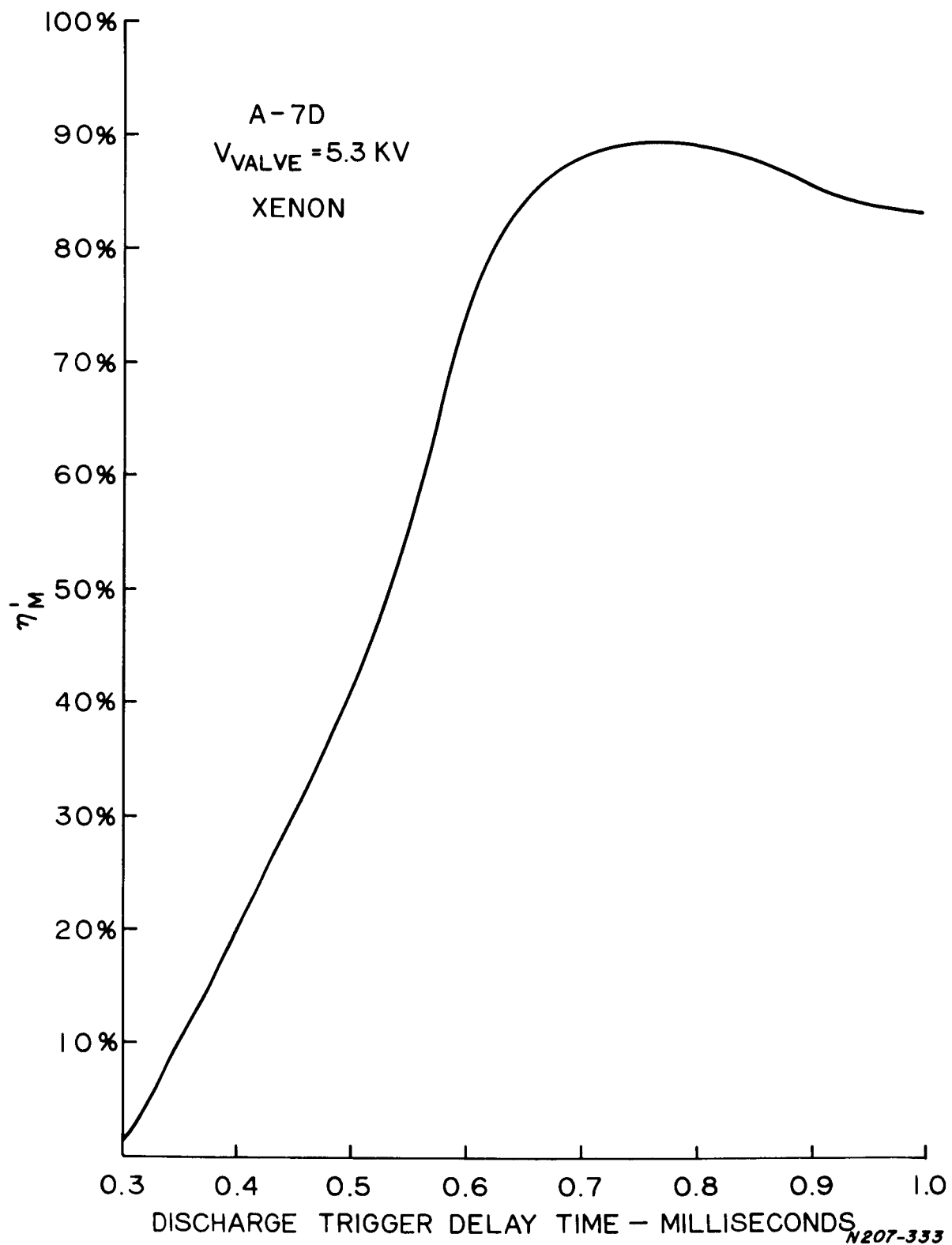


Figure II-14. Fraction of Propellant Between the Accelerator Electrodes at Various Discharge Trigger Delay Times

with operation at 45 μ fd, this fraction had ranged from 50% to 80%. The increased mass fractions accounted, in part, for the improved performance of the A-7D engine. The higher pressures in the injector ports, resulting from the increased valve opening, may also have decreased the radial components of flow in the cold gas stream so that more propellant was placed in the vicinity of the center electrode where the current density and driving fields are most intense. This also could serve to increase the efficiency of the engine.

C.1. Effects of Long Term Operation on Engine Performance

In order to determine any possible degradations in engine performance, and to obtain, at a fixed operating point, an accurate value for erosion rates within the accelerator, the A-7D engine was run for 10 consecutive hours at a pulsing rate of 5 times per second. The energy storage capacitance was 144.5 microfarads, charged to 950 Volts. At the above firing rate, the average power input level was 325 watts. The xenon propellant flow rate was 1.5×10^{-7} kg/sec. Thrust, propellant mass flow, input voltage, and repetition rate were monitored continuously, and calibrations of the thrust balance were made every hour. The eroded masses of the center electrode and trigger electrodes were obtained by weighing these components on a balance with a sensitivity of 0.1 mg. The overall efficiency of the engine determined from these measurements was 57%. The I_{sp} was 4930 seconds. The contribution of eroded mass to the input propellant mass was 1.15×10^{-9} kg/sec, less than 1% of the total mass flow. It was noted that the thrust varied by only $\pm 5\%$ over the entire course of the run, indicating essentially no degradation of performance in the ten hours of operation.

C.2. Possible Spurious Effects on Thrust and Mass Input

Since the determinations of overall efficiency and specific impulse may be affected by unaccounted for contributions to either the indicated engine thrust or the measured propellant input, including eroded materials, it was important to identify any possible spurious effects and to measure their magnitude.

Current to the vacuum tank walls and thrust balance structure (which would then appear as current through the thrust balance legs) was investigated to establish if any contribution to the thrust could result from this interaction. The flow of current through the thrust balance legs was reduced to a vanishingly small value by inserting a 5000 ohm resistor in series between the capacitor bank and the thrust balance which was connected to ground. (The current through the legs was 100 amps maximum without the resistor). With the

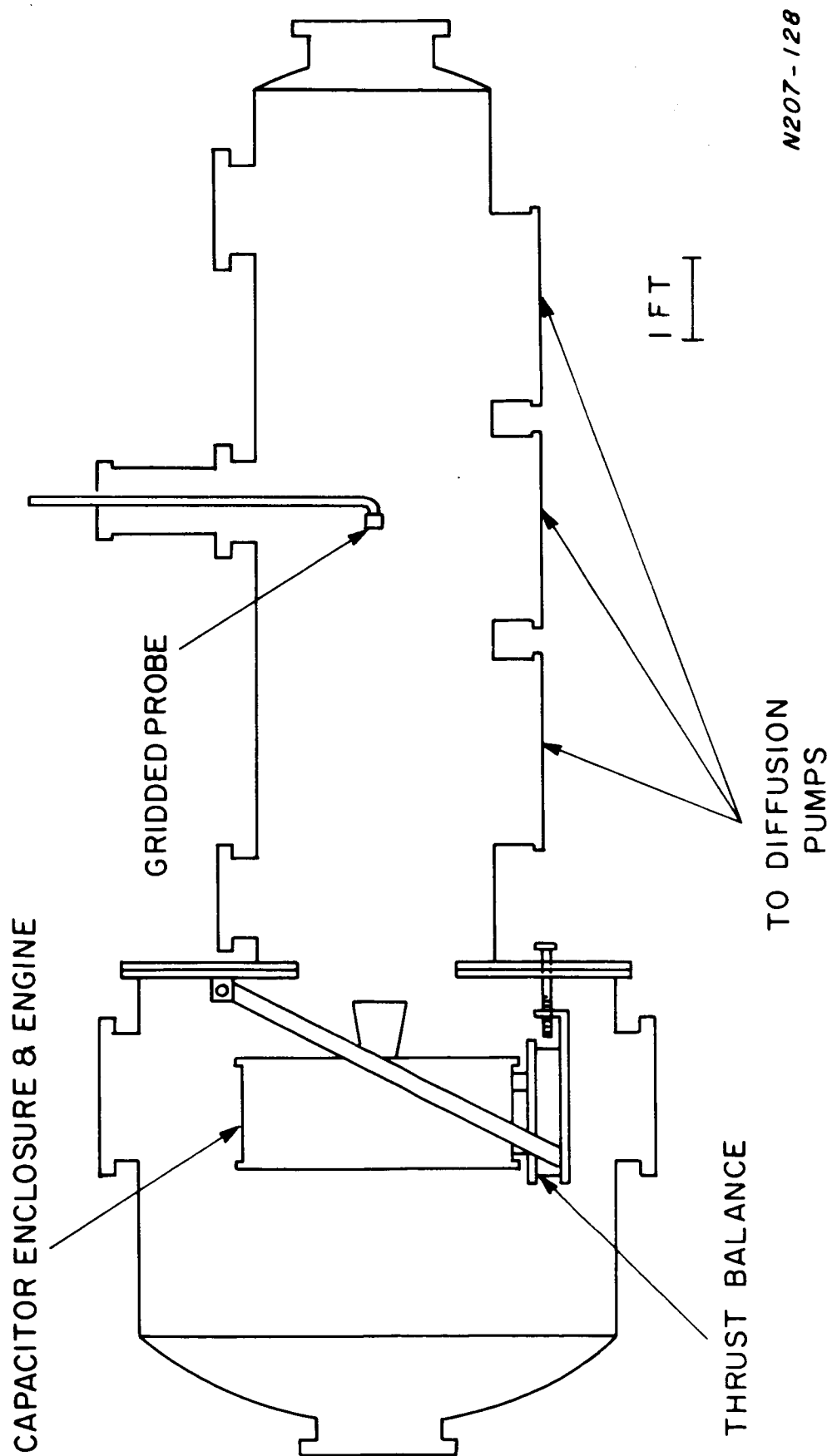
engine operated at typical propellant flow rates, power input, and triggering conditions, the performance was unchanged from the values measured previously without the current limiting resistor.

Since the engine fires through a 22" diameter hole into the test facility main pumping tank, (the experimental arrangement is drawn in Figure II-15) there was some question as to whether the accelerator currents to the edge of the hole and the associated fields might produce a back force on the engine, thereby enhancing the measured thrust. A magnetic field probe was placed at the edge of the hole to measure the field at that point. The field measured, with the engine operated repetitively, was 7.4 gauss. If this field is assumed, as an upper limit, to be constant over the entire area of the 3 sq. meter plate around the hole, and the pulse width of the field is assumed to be $10 \mu \text{ sec}$, the thrust calculated for a 10 sec^{-1} repetition rate is 6.9×10^{-5} newtons. The typical engine thrust at the 650 watt power level was of the order of 1.5×10^{-2} newtons. The contribution of the fields at the plate are therefore negligible.

Using a Rogowski loop, the peak current at the muzzle of the accelerator was found to be 6000 amperes, or 15% of the total accelerator current. In terms of reactive force on the thrust stand, if all of this current were to extend to the surrounding walls (which it does not), the contribution could be about 2.25% of the total force. These measurements indicated also that 700 amps, or less than 2.0% of the peak total current, is returned to the outside of the capacitor housing to which the gun is attached.

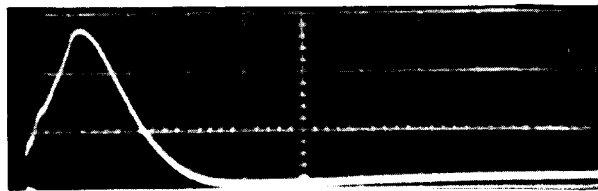
A 7.5 cm diameter Rogowski loop was used to map the current density distribution across the exhaust at a location 5 cm downstream from the accelerator. This measurement was performed under the best conditions of operation for capacitances of $45 \mu \text{fd}$ and $144.5 \mu \text{fd}$. The results for the $45 \mu \text{fd}$ capacitance have been reported previously¹. Investigations of the integrated current waveforms for $144.5 \mu \text{fd}$ shown in Figure II-16 indicate that the current density and distribution is not significantly different for the two capacitances. A plot of average current density vs. radial position of the loop is shown in Figure II-17. The negligible currents measured at a radius as little as 5 cm from the edge of the outer electrode are additional evidence of negligible interaction between the thrust balance and the vacuum chamber.

In order to minimize possible thermal effects on the thrust balance, the engine was thermally isolated from the balance with the exception of a single ground lead. The thrust balance had been fabricated from super invar, a low thermal expansion material, to further minimize such effects. At the power levels used, shifts in the thrust balance zero point after engine operation were negligible.



N207-128

Figure II-15. Outline of Plasma Accelerator Test Facility



$r = 0 \text{ cm}$
2.4 K amps/cm



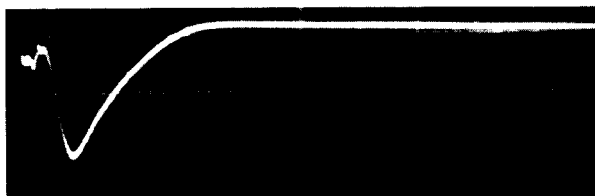
$r = 2.54 \text{ cm}$
1.2 K amps/cm



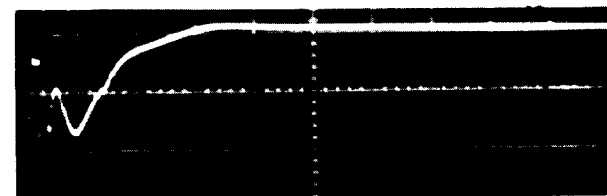
$r = 5.08 \text{ cm}$
1.2 K amps/cm



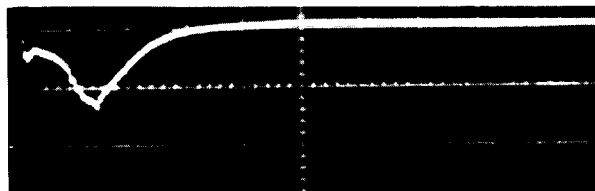
$r = 6.35 \text{ cm}$
1.2 K amps/cm



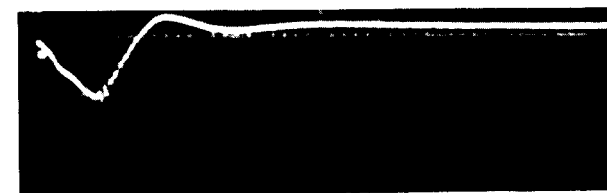
$r = 7.62 \text{ cm}$
1.2 K amps/cm



$r = 10.16 \text{ cm}$
0.6 K amps/cm

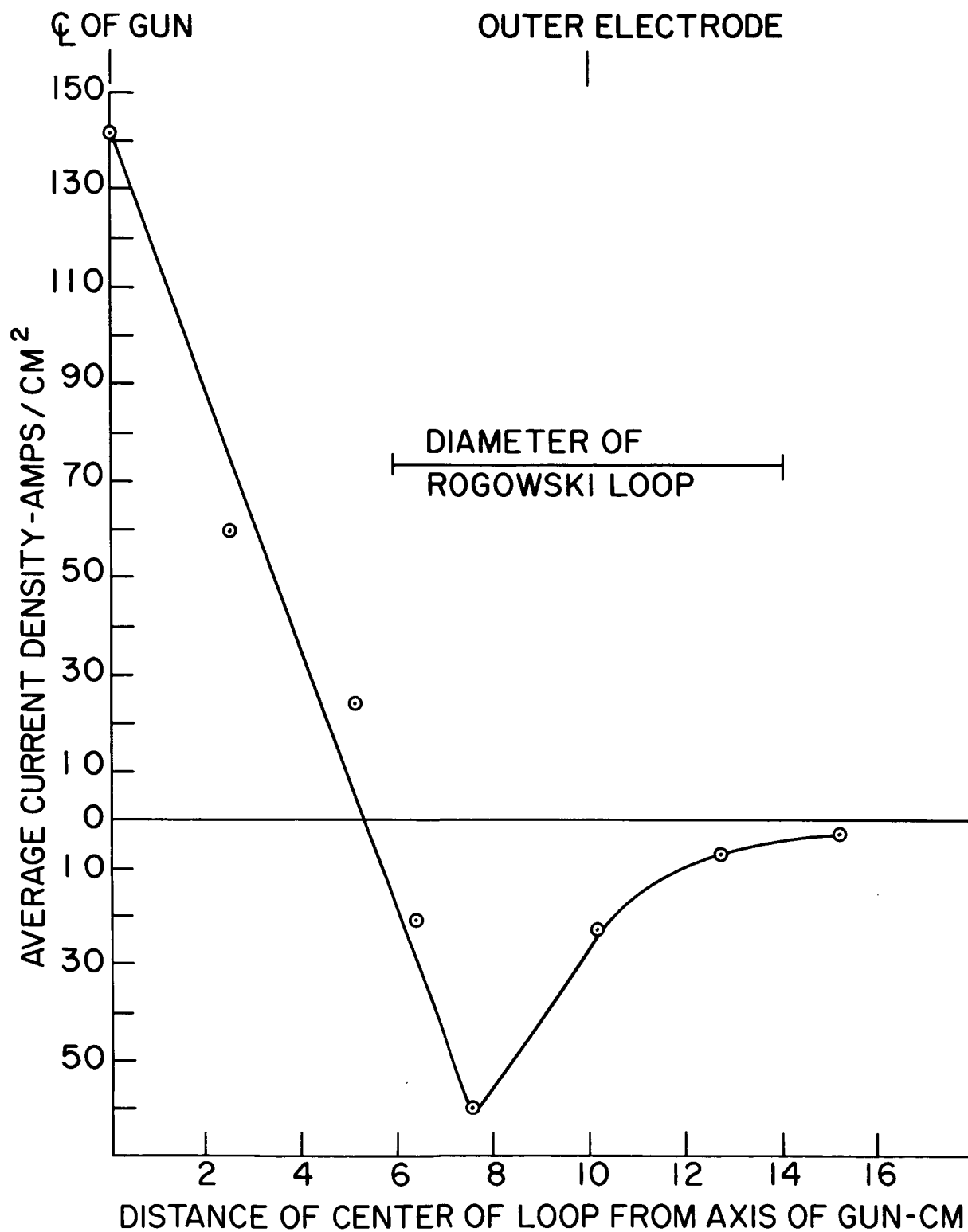


$r = 12.70 \text{ cm}$
0.24 K amps/cm



$r = 15.24 \text{ cm}$
0.12 K amps/cm

Figure II-16. Integrated Current with 7.5 cm Diameter Rogowski Loop
5 cm Downstream from Muzzle at Radial Locations Specified
Sweep 5 usec/cm. A-7D Accelerator, 950V, 144.5 ufd, Xenon



N 206-913

Figure II-17. Average Current Density vs. Radial Distance of Rogowski Loop from Center Line of A-7D Gun, 5 cm Downstream from Muzzle

Propellant addition from the background gas in the test chamber may influence the thrust and be unaccounted for in the calculation of overall efficiency $T^2/2mP$ if it is not identified. The fact that thrust did not vary significantly as the temperature of the electrodes increased over the course of engine runs extending up to 10 hours is an indication that the degassing of the electrodes of gas adsorbed prior to the operation of the gun (or even of gas originally entrained in the electrode material) plays a small role in mass addition.

Test chamber environmental pressure may influence the thrust either because of recirculation of mass or changes in the distribution of the currents and fields outside of the accelerator. The engine was operated and its performance measured at repetition rates from 2 to 10 shots per second into environmental pressures ranging from 10^{-6} to 10^{-4} Torr. In all cases, it was found that the thrust produced was directly proportional to the repetition rate, indicating that the environmental pressure, which was also determined by the firing rate, had no effect on the overall engine performance.

C. 3. Calorimetric Determination of Exhaust Stream Energy

In order to determine the energy in the exhaust stream of the A-7D accelerator, a water-cooled copper calorimeter 25 cm in diameter and 45 cm long was installed in the vacuum chamber with its front edge 10 cm downstream from the accelerator. The base of the calorimeter was an inverted cone designed to provide enhanced trapping of the intercepted plasma.

Electrically insulated thermocouples were inserted in the inlet and outlet water lines of the calorimeter. With the reference junction at 0°C , the thermocouple outputs were measured on a strip chart recorder which had been calibrated against an auxiliary potentiometer-standard cell arrangement.

The temperature rise of the water was continuously monitored during the course of engine runs, which were of up to 45 minute duration. Temperature changes of the water for a flow of 600 cc/min, engine firing rates of 4 and 5 times per second, and an accelerator voltage of 950 V with 144.5 μfd capacitance, were in the range of $4-5^{\circ}$. For the operating conditions associated with an overall efficiency of 57% at a specific impulse of 4800 sec, the exhaust stream energy, calculated on the basis of the temperature rise of the calorimeter coolant, was 72% of the input energy $(1/2 C V_o^2 (1-1/Q))$.

Among the possible effects which might increase the calorimeter readings are those of extended accelerator currents and fields which might

heat the calorimeter resistively, the effects of radiation losses from the plasma and, more significantly, radiation from the electrodes. Measurements of currents external to the accelerator described above indicate that their effect is negligible. The energy in ionization of the propellant under the optimum conditions of operation has been calculated to be less than 1% of the input energy; radiation from this source to the calorimeter is therefore also negligible. Under most of the conditions of exhaust stream calorimetry, the effect of electrode radiation to the calorimeter has been calculated and experimentally found to be negligible. By means of a movable carriage, it was possible to place the calorimeter in close proximity to the electrodes after several minutes of engine operation. No temperature rise was observed in the calorimeter after this operation, indicating the insignificant effect of radiation for the relatively low power levels used in these tests.

The possible effects that would tend to decrease the calorimeter reading are the reflection of particles out of the calorimeter, sputtering due to the high energy ions incident on the copper surface and incomplete interception of the exhaust stream. The results of gridded probe measurements of the ion distribution indicated that the angle of interception was slightly larger than the angle of divergence of the beam, so that this latter consideration did not apply in the operation described here.

C.4. Corroboration of Engine Efficiency and Specific Impulse

The overall efficiency can be broken into several factors which to a first approximation are independent of each other:

$$\eta_o = \eta_E \eta_m \left(\frac{\bar{v}^2}{v^2} \right) \overline{\cos^2 \alpha} \quad (1)$$

where η_E is the efficiency of conversion from electrical energy to exhaust kinetic energy, η_m is the mass utilization factor, \bar{v} is the average particle velocity in the exhaust, and $\overline{\cos^2 \alpha}$ is obtained from the average divergence of the particles in the exhaust. Measurements were made in order to determine these various factors separately, so that the parts could be combined to provide another determination of η_o for comparison with that obtained directly from thrust, mass flow, and input power measurements. Also, these measurements were used to obtain an independent determination of I_{sp} .

The factors $\frac{\bar{v}^2}{v^2}$ and $\overline{\cos^2 \alpha}$, were determined by the use of a multigridded probe. The operating principles and the data obtained with this probe are described in detail in section E. The values reported there

are:

$$\frac{2}{v} \frac{1}{v^2} = 0.85 \text{ and } \overline{\cos^2 \alpha} = 0.97 \quad (2)$$

The beam edge was found to be at a half-angle of about 14° .

In order to estimate the η_m factor, a fast pressure probe was used to map the neutral propellant density distribution in the interelectrode volume of the accelerator into which the electrical energy was deposited. This measurement indicated that the fraction of the injected propellant available to the discharge in each pulse, and hence an upper limit to the factor η_m was approximately 0.90.

Finally, combining all of these results with η_E which, as mentioned above, was indicated to be a minimum of 0.72, it was found that η_o so determined agreed within 10% with η_o calculated from $T^2/2 \dot{m} P^o$ (57% at 4800 sec I_{sp}). This degree of agreement is considered well within the $\pm 20\%$ estimated cumulative accuracies of the various measurements involved in the η_o determinations.

For the same conditions, the average ion velocity for the entire beam was found to be 5.3×10^4 m/sec. If one takes into account the fact that the maximum fraction of injected propellant available to the discharge was 0.9

a value of 4.75×10^4 m/sec is obtained for the average velocity of the entire exhaust. This corresponds to an I_{sp} of 4750 seconds, which compares very favorably with the 4,800 second figure obtained from considerations of thrust and gross mass flow in the same accelerator. In the light of the cumulative accuracies of measurement, this agreement may be at least partially fortuitous.

D. PERFORMANCE OF THE A-7D ACCELERATOR WITH 218 μ fd

CAPACITANCE

Having obtained satisfactory confirmation of performance for the A-7D, 144.5 μ fd accelerator-capacitance combination, the way was cleared for further steps aimed at improving the overall efficiency. The capacitance of the energy storage bank was thus increased to 218 μ fd.

The performance of the accelerator with this capacitance, a voltage of 900 V, and several different mass flows is summarized in Figure II-18. It is pointed out that this most recently measured performance has not yet been substantiated by the various independent measurements to which the 144.5 μ fd engine was subjected. However, it appears not unreasonable to believe that these results are as valid as those demonstrated for the lower capacitance engine described above.

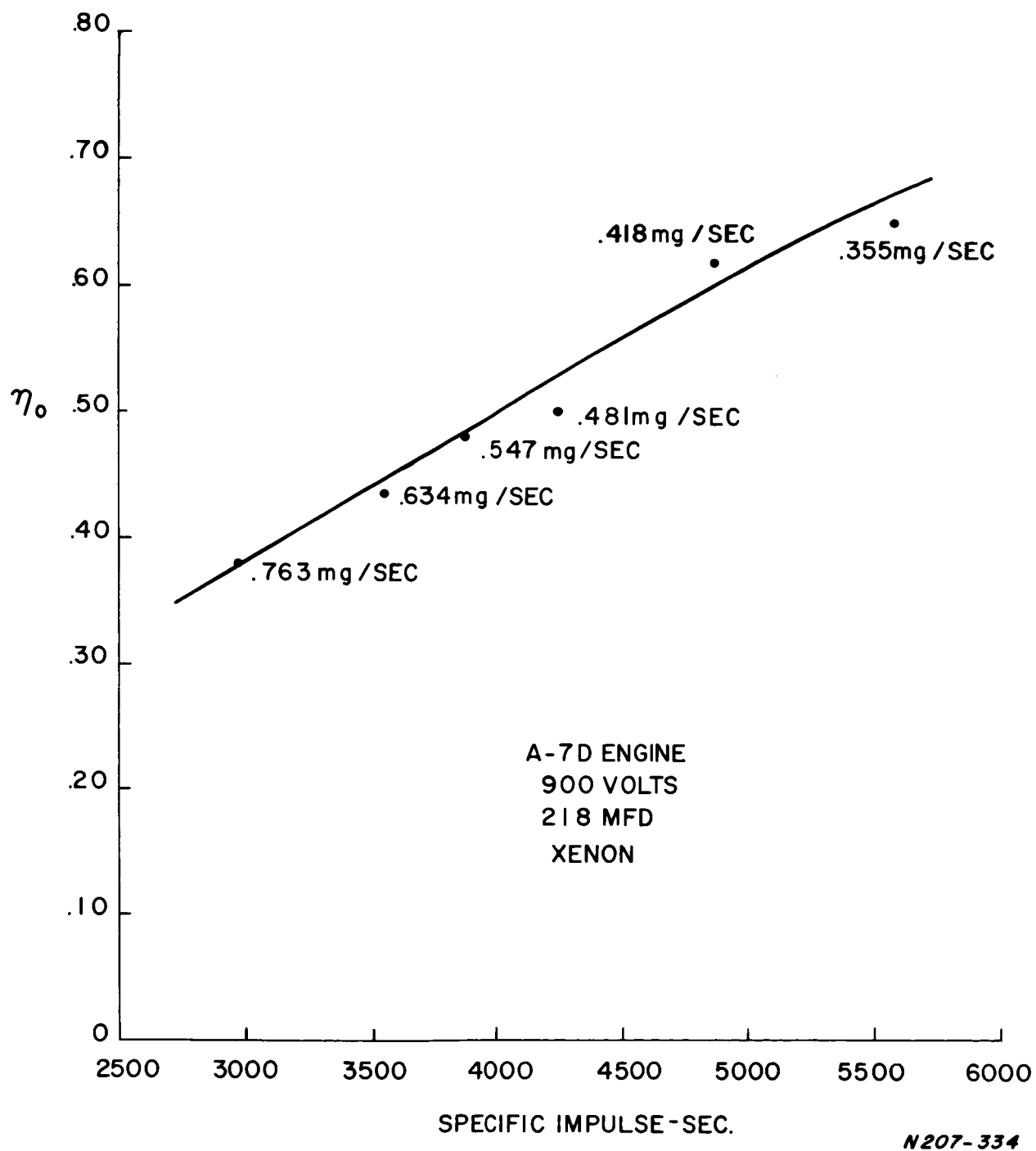


Figure II-18. Overall Efficiency vs Specific Impulse for Various Mass Flows

E. PLASMA EXHAUST CHARACTERISTICS

The plasma exhaust from the A-7D plasma accelerator has been investigated by the use of a multigridded particle collector⁴ described in Appendix C. The specific exhaust characteristics sought were: an identification of multiply ionized species, a determination of the velocity distribution of the incident ions, an absolute measure of the number of ions, and a measure of these characteristics at different positions so that a distribution could be obtained for the entire exhaust of a coaxial plasma accelerator. All this was accomplished by applying different stopping potentials to the grids of the probe to determine particle energy and observing the time-of-flight of the ions that got through to determine particle velocity. Although some measurements were made with the A-7D accelerator operating at lower capacitances, the most extensive examination of the accelerator exhaust was made with a capacitance of 144.5 μ fd at 950 V, a xenon propellant flow of 0.296 mg/sec., and an optimum trigger delay time of 0.75 ms - a combination of conditions which had demonstrated an overall efficiency of 57% at a specific impulse of 4800 sec.

E.1 Measurements and Uncertainties

The probe was placed on the beam axis at a point two meters downstream from the gun muzzle plane. Charges collected on the cup go to ground through the resistor indicated in Figure D-4. The voltage drop across the resistor was then monitored on an oscilloscope and the trace recorded photographically. Measurements were made from the photographs. A sample is shown in Figure II-18.

Due to the intense electromagnetic pulse accompanying the triggering of the discharge, pick-up problems were unusually severe. If ground leads were injudiciously placed, a large fraction of the observed signal could result from this effect. As a control test, the probe was turned by 180° to see if the signal disappeared. In addition, it should be noted that a reduction in the signal obtained by increasing the stopping potential on the positive grid also must represent real ions. Consequently, differences between two traces obtained with different stopping potentials gave meaningful data even when pick-up was present. Nonetheless, data were generally obtained when the pick-up was reduced to a negligible value.

The main uncertainty in processing the data from the pulsed coaxial gun lies in the shot-to-shot fluctuations in the signal. Significant variations in the amplitude (up to $\pm 20\%$) and waveform of the signal occurred under some conditions. Under others, variations were less than 5%. To compensate for this, a large number of photographs were obtained under the same conditions and a photograph was chosen as typical. Data reduction took place from a series of such typical photographs taken with different stopping potentials.

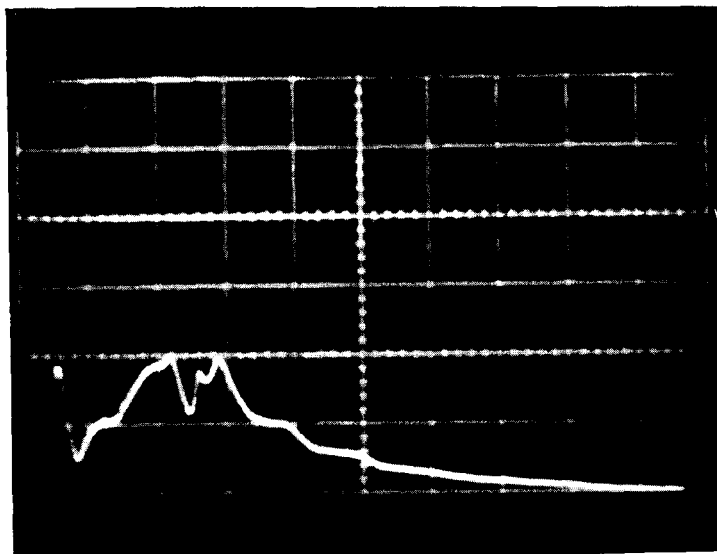


Figure II-19. Sample Gridded Probe Trace
0 - stopping potential
950 volts gun voltage, 144.5 μ fd, Xenon
5300 volts valve voltage
20 μ sec/cm .02 v/cm

Another point of confusion might result from the negative dip that can be seen at high sensitivity and high stopping potentials at the time one would ordinarily see the arrival of ions, were the high positive potential not applied. This dip has been interpreted as consisting of electrons emitted from the downstream side of the negative grid as a result of either bombardment by ions stagnated by the positive grid or photoelectric emission by photons produced during this stagnation, or both. Tentative substantiation of this has been obtained by reducing the amount of propellant, and thus the density of stagnating ions. The dip is reduced and almost disappears. To avoid confusion, the zero level must always be taken as the long time asymptote and any negative dips ignored.

E. 2. Data Reduction and Examples

When the difference is taken between signals obtained with different stopping potentials, this difference represents ions with an energy in the range set by the voltage interval (or some integral multiple of those voltages if the ions are multiply ionized). Since the energy of these ions is well defined, their time-of-flight and velocity should be also and their velocity distribution can be expressed as

$$f(v) \equiv \frac{dn}{dv} = \frac{dn}{dt} \cdot \frac{dt}{dv} = -\frac{I}{ze} \cdot \frac{t^2}{d} \quad (3)$$

where I is the ion current, z is the number of charges per ion, $v = d/t$ is the velocity of the particles arriving at the probe at a time t , and d is the distance to the probe from the accelerator muzzle.

This equation may be applied to a group of ions with a well-defined energy,

$$\frac{1}{2} m v^2 = ze (V_o + \delta V) \quad (4)$$

By arbitrarily assuming $z = 1$ and plotting $f_1(v)$ vs. v on a graph, the singly ionized particles will be represented by one peak, the doubly ionized by another etc., since

$$v(z, m) = \frac{d}{t} = \sqrt{2zeV_o/m} ; z = 1, 2, \text{ etc.}, \quad (5)$$

assuming, also, that all particles have the same mass. (Different mass particles will appear in their own peaks.) However, the ordinates of the peaks corresponding to multiply charged ions will be too high by a factor z . Since the real value of z for each peak is then known, a new and correct graph of $f(v)$ vs. v may be drawn for this group of ions. It should be emphasized at this point that the time-of-flight used is that be-

tween the accelerator muzzle and the probe. Since the ions do not leave the gun at the instant of gun triggering, which is time zero for the oscilloscope, some average time lapse may be determined from the correction that must usually be applied to bring $\frac{1}{2} m v^2$ from the time-of-flight into agreement with the $z e V$ characteristic of the voltage interval. For the $\eta_o = 57\%$, $I_{sp} = 4800$ sec. operating point of the A-7D accelerator, when one considers the bulk of the ions, this time lapse is nine microseconds, or two microseconds less than the duration of the current waveform (11 microseconds). The time lapse was only one or two microseconds after triggering for any fast ions ($v \approx 10^5$ meters/second). This last effect has been interpreted as being ions created and accelerated near the gun muzzle during the first few microseconds of discharge.

Velocity distribution plots may be obtained for all energy groups of the ions intercepted by the probe while in a given position (see Figures II-20 and II-21 for the distribution plots obtained for the 57%; 4800 sec. operating point). The sum of all these amplitudes gives a total velocity distribution for all the ions in that part of the exhaust (Figure II-22).

Some dn/dv vs. v peaks are observed for particles of different mass, as was pointed out for Equation (5). It is interesting to observe the carbon, oxygen, and hydrogen peaks in Figure II-20. These must result from pump oil broken up and accelerated in the plume of the discharge. The low energies involved tend to substantiate this since the acceleration must then have taken place in regions of low current. Despite the seemingly large numbers of particles involved (about 10%), their atomic weight is so low that their impulse contribution is negligible. It is also important to note that no copper electrode species were observed. This tends to confirm observations, made visually and by weighing, that little electrode erosion was occurring.

The average velocity for all ions at this position can be obtained by graphical integration and use of the following expression

$$\bar{v} = \frac{\int v f(v) dv}{\int f(v) dv} \quad (6)$$

The average velocity computed for the data in Figure II-22 is 5.2×10^4 m/sec.

With the limited data on hand, we have found that identical detailed results are not always obtained when the same operating conditions are used at a different time. This is illustrated in Figure II-23, where it can be seen that the most striking difference from Figure II-22 is the near absence of the carbon ion peak. The high energy tail and the relative

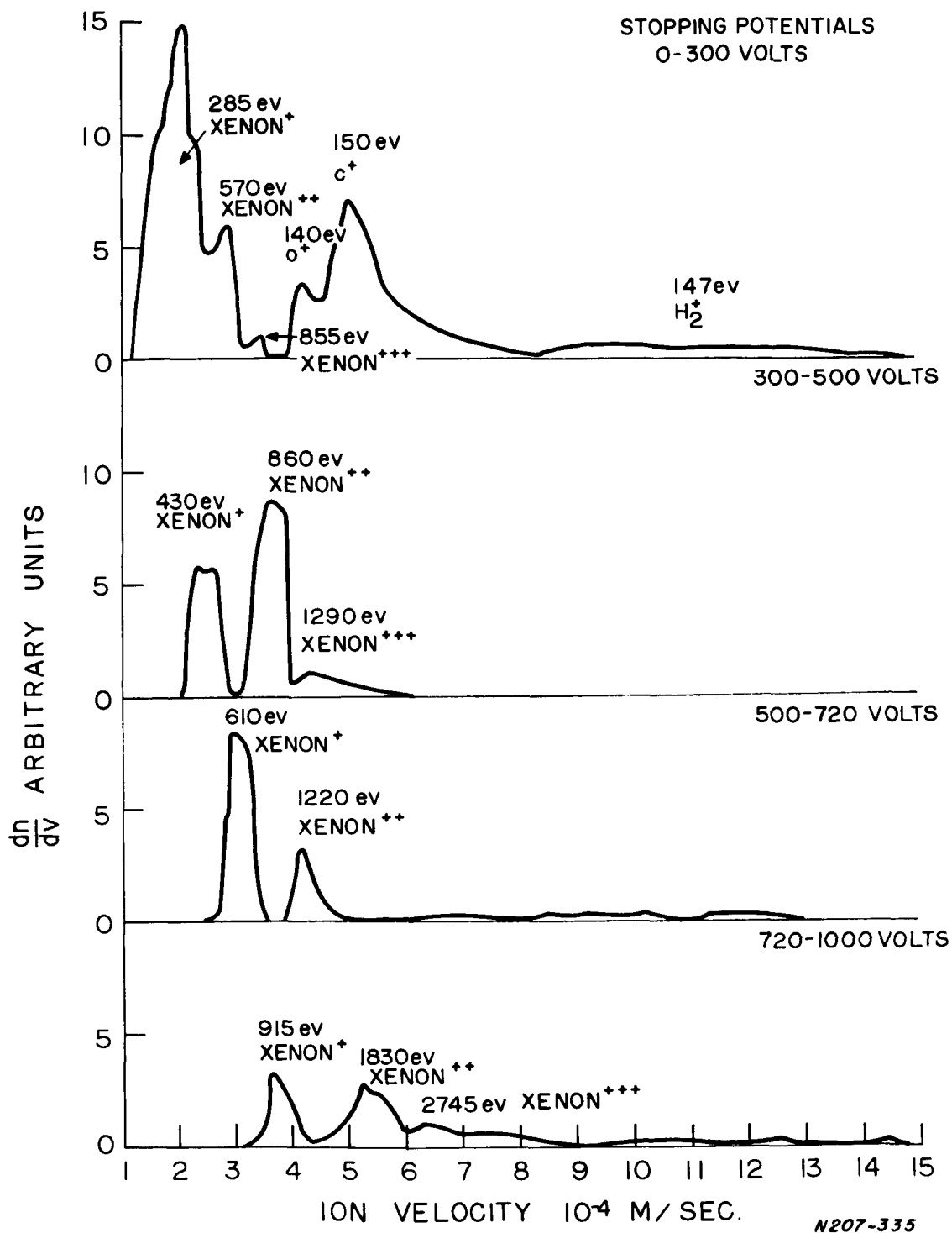


Figure II-20. Ion Velocity Distribution on Axis, A-7D Gun, $\eta = 57\%$,
 $I_{sp} = 4800$ sec, 950 V, 144.5 μ fd, .296 mg/sec. Xenon
 0 - 1000 V Stopping Potential.

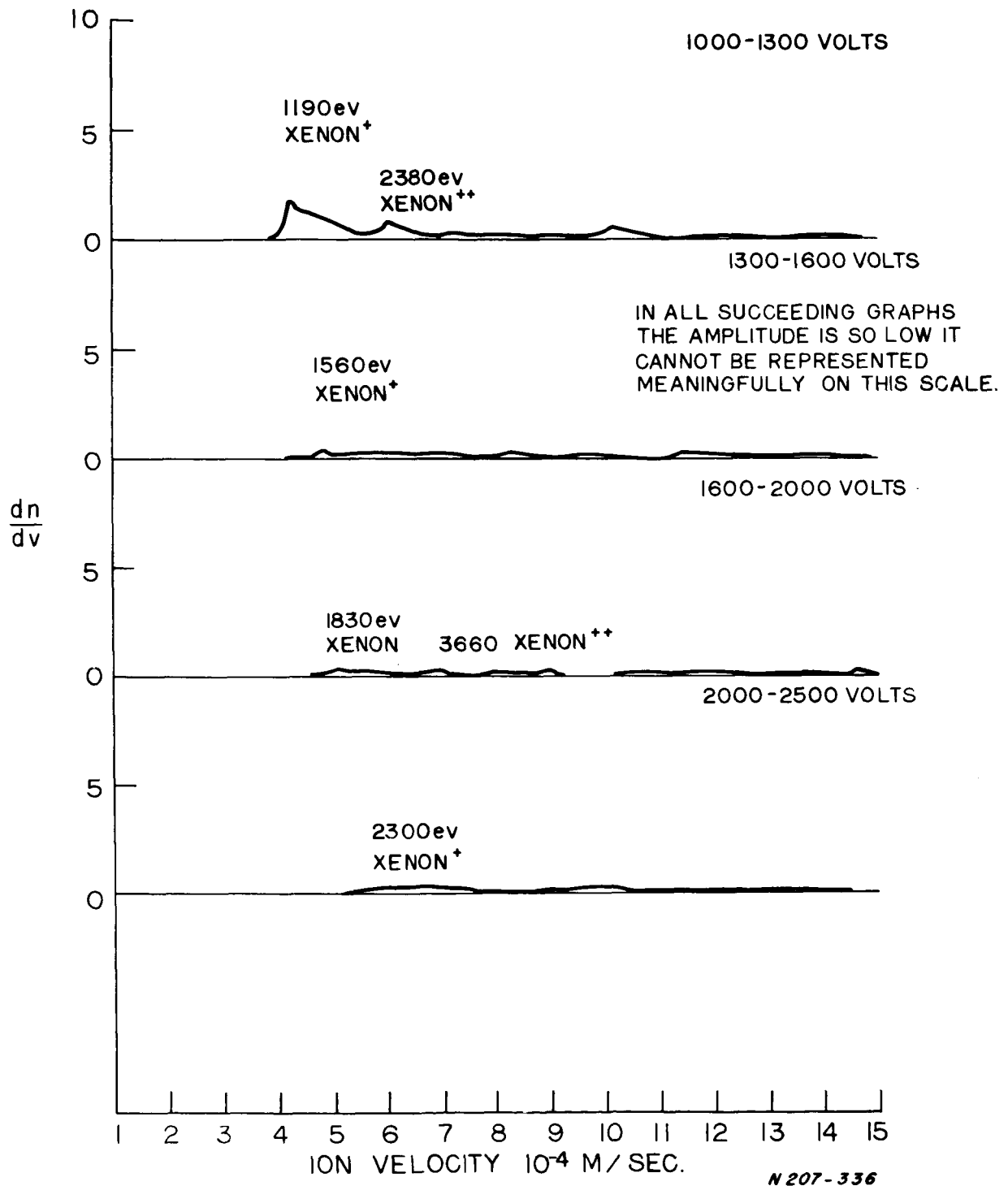


Figure II-21. Ion Velocity Distribution on Axis, A-7D Gun, $\eta = 57\%$,
 $I_{sp} = 4800$ sec., 950V, 144.5 μ fd, .296 mg./sec Xenon
 1000 - 2500 V Stopping Potential
 II-33

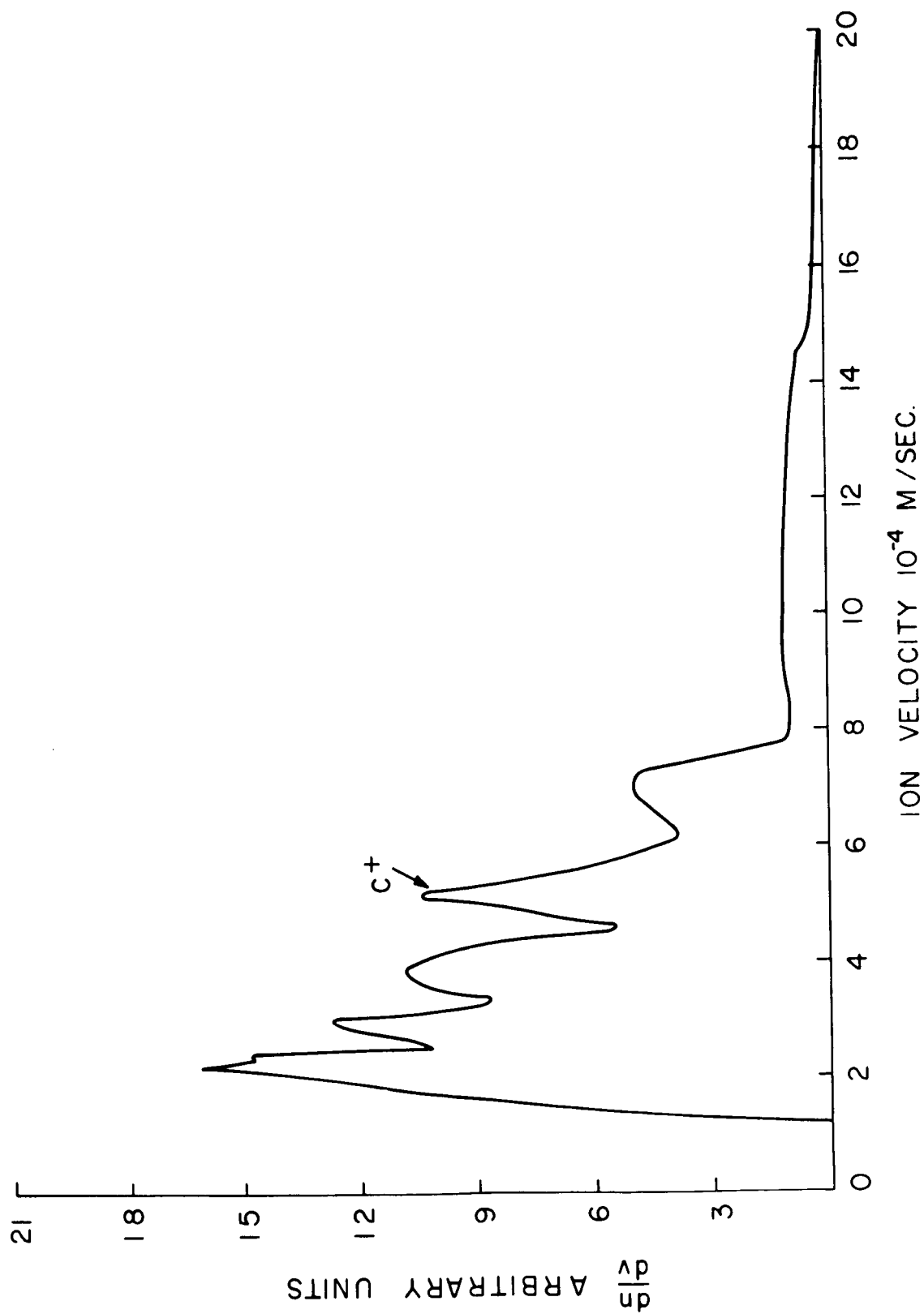


Figure II-22. Total Velocity Distribution Function for all Ions Passing the Probe Position, Mod A-7D,
 $\eta = 57\%$, $I_{sp} = 4800$ sec., 950V, 144.5 μ fd, .296 mg/sec Xenon

heights of the various xenon peaks are also different. In spite of these differences, the average velocity obtained from the distribution function of Figure II-23 is 5.55×10^4 m/sec, within 7% of the other value, and well within the estimated experimental error of $\pm 20\%$.

Essentially the same results were obtained when the probe was moved 43 cm off-axis in the plane 2 m downstream from the muzzle (see Figure II-24). Data were obtained also at a number of intermediate radial points to permit determination of a radial distribution function, and also a true average velocity in the beam.

The expression

$$\frac{\int_0^R \rho r dr}{\int_0^\infty \rho r dr} \quad (7)$$

where ρ is the total number of ions per cm^2 intercepted by the probe at a position r , was integrated for various values of R , the radial distance from the accelerator axis. This computation tells what ratio of the beam ions are inside of the radius R . The result is plotted in Figure II-25. Using this information and knowledge of \bar{v} across the beam (see Figure II-26), the average velocity of all ions in the exhaust was obtained from

$$\bar{v} = \frac{\int_0^\infty \bar{v}(r) \rho r dr}{\int_0^\infty \rho r dr} \quad (8)$$

This was found to be 5.3×10^4 m/sec when the gun was operating under conditions giving the above mentioned 57% overall efficiency and 4800 second I_{sp} . However, it is important to note that since about ten percent of the injected propellant was not acted upon by the discharge, the average velocity of all the exhaust is about 4.75×10^4 m/sec.

As was shown above, two other figures of merit for the accelerator obtained from these measurements may be utilized. One of these, the quantity $\overline{v^2} / \bar{v}^2$, is obtained from squaring the result obtained from Equation (6) and dividing it by the quantity

$$\overline{v^2} = \frac{\int v^2 f(v) dv}{\int f(v) dv}, \quad (9)$$

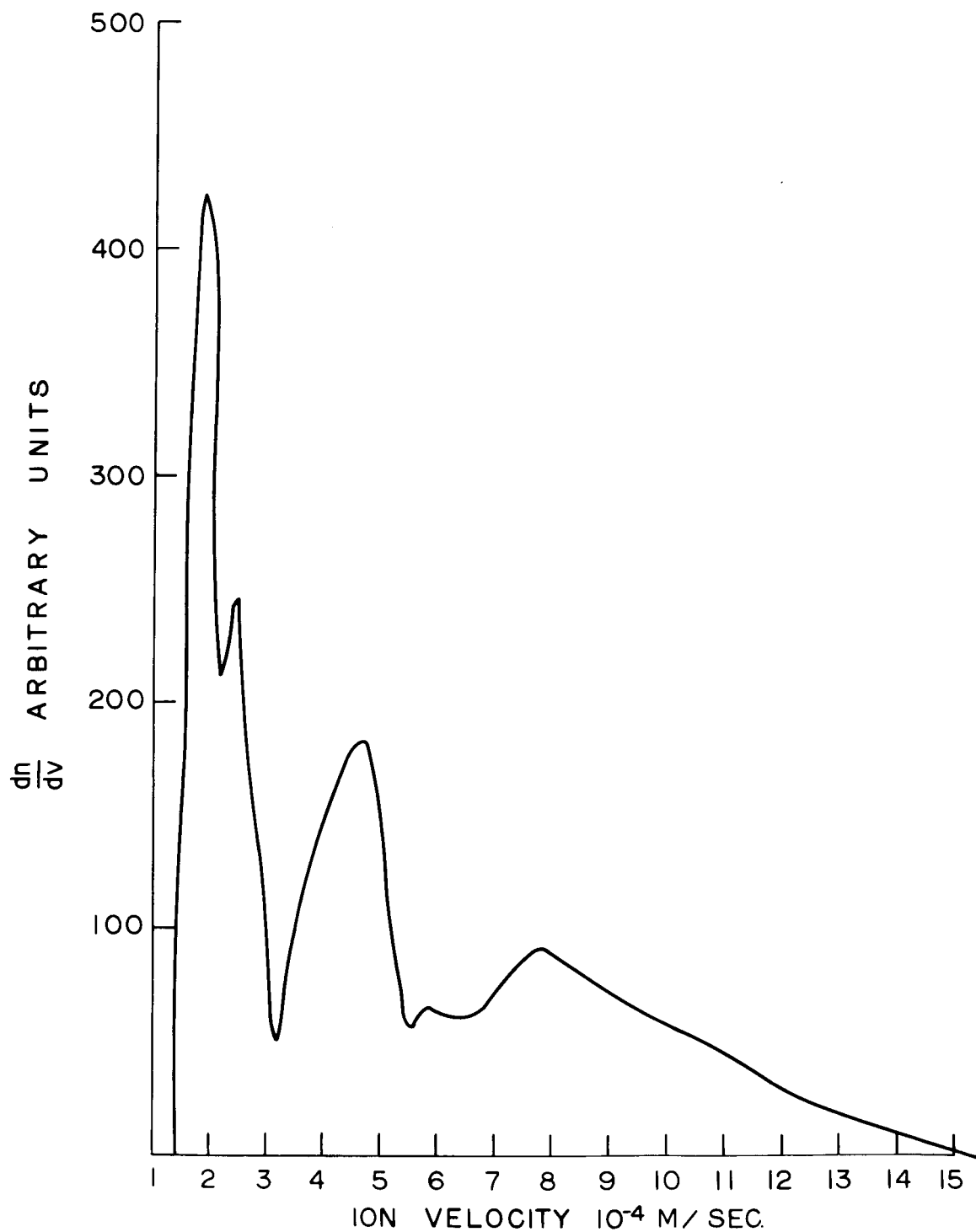
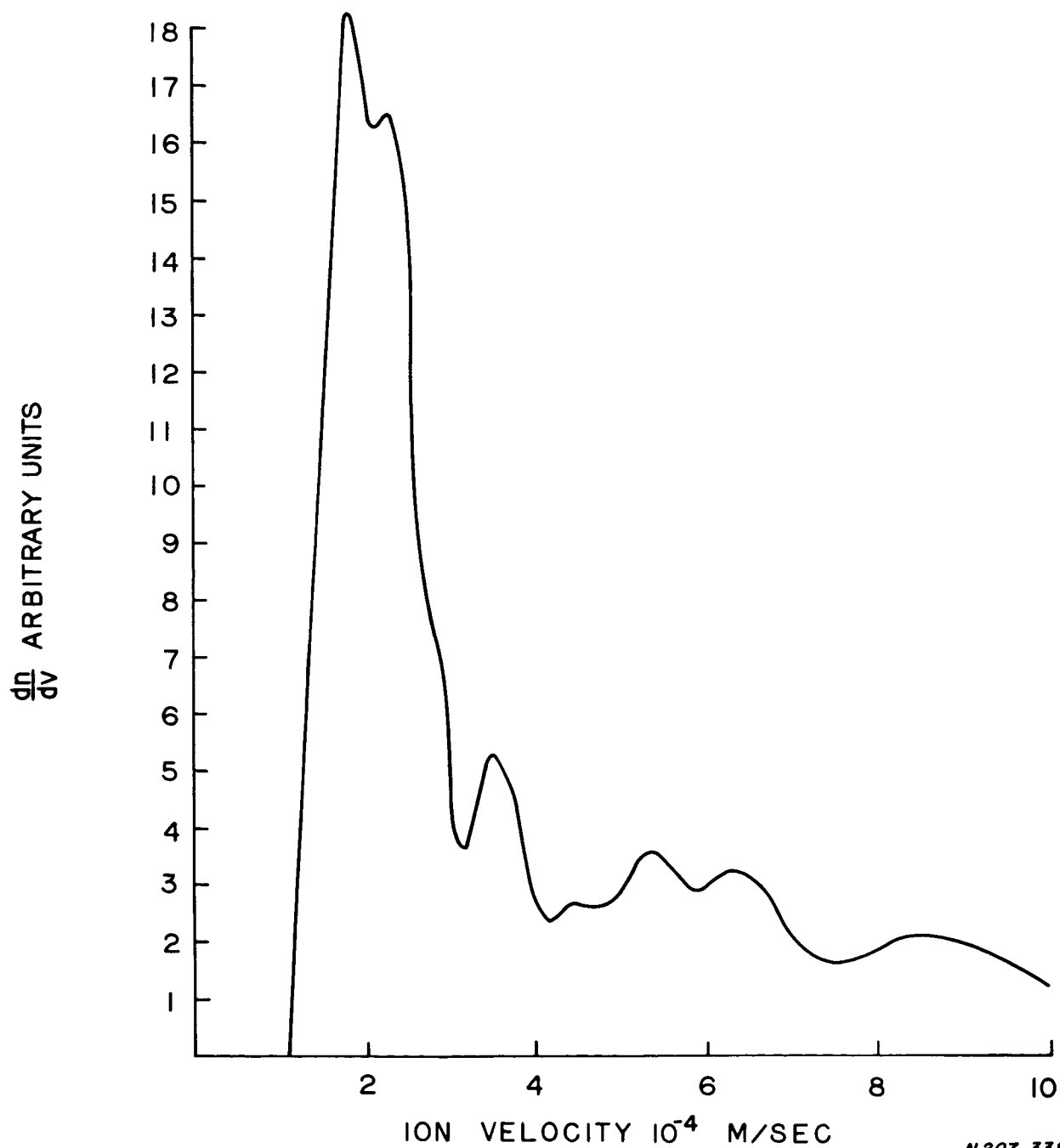
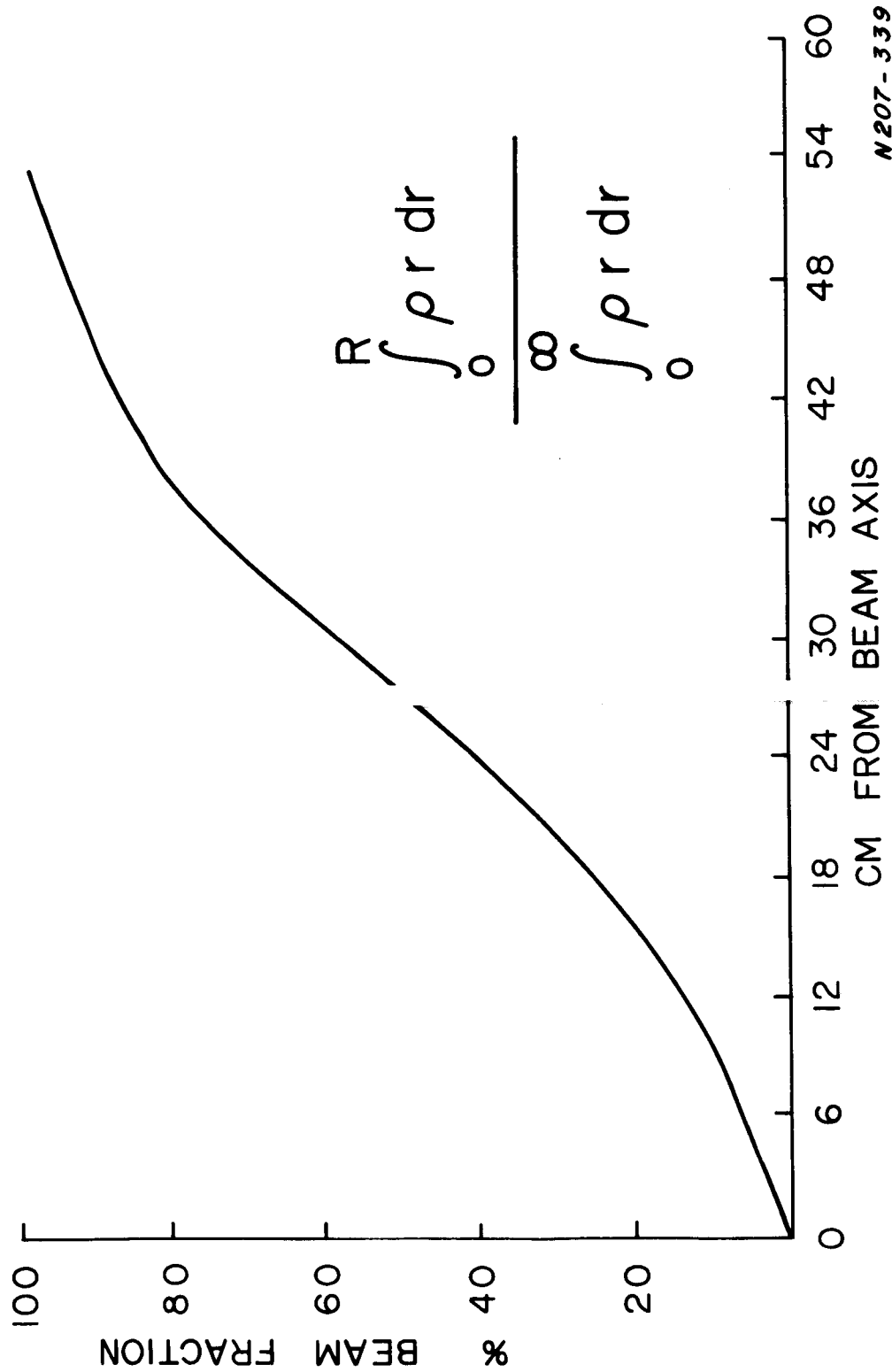


Figure II-23. Total Ion Velocity Distribution on Axis, A-7D Gun, $\eta = 57\%$,
 $I_{sp} = 4800$ sec., 950V, 144.5 μ fd, .296 mg/sec Xenon



N207-338

Figure II-24. Total Ion Velocity Distribution 45 cm. off Gun Axis, A-7D Gun
 $\eta = 57\%$, $I_{sp} = 4860$ sec., 950V, 144.5 μ fd, .296 mg/sec. Xenon



N207-339

Figure II-25. Fraction of Accelerated Propellant with in a Beam Radius, 2m Downstream from Accelerator Muzzle. Mod A-7D, $\eta = 57\%$, $I_{sp} = 481$ sec., 950V, 144.5 μ fd, .296 mg/sec Xenon

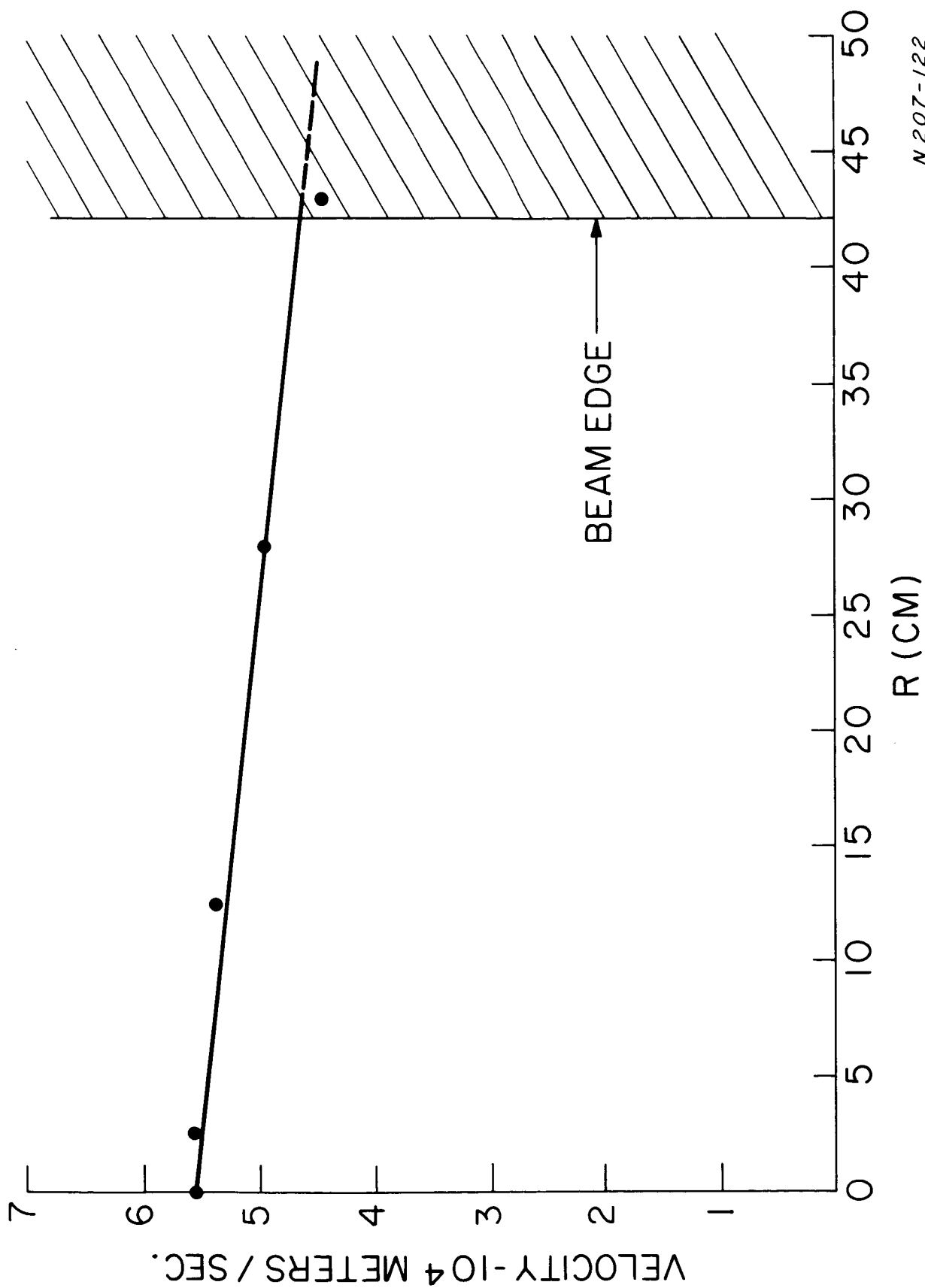


Figure II-26. Average Ion Velocity at Various Radial Positions in a Plane Two Meters Downstream From the Accelerator Muzzle. Mod A-7D, $\eta = 57\%$, $I_{sp} = 4800$ sec., 950V, 144.5 μ fd, .296 mg./sec Xenon

N 207-122

Again, the integration was done graphically. The results for the A-7D accelerator at the 57%, 4800 second operating point was $\frac{\overline{v}^2}{\overline{v}^2} = 0.85$. The other quantity, $\cos^2 \alpha$, where α is the half-angle of the divergence of the beam ions, was found by approximating the curve in Figure II-25 by a straight line. In this case, the angular distribution function is a constant and it can readily be calculated that $\overline{\cos^2 \alpha} = 0.97$ since the beam edge, which was rather well-defined, was found to occur at around 14° .

REFERENCES

- II-1. "Performance Study of a Repetitively Pulsed Two-Stage Plasma Propulsion Engine," B. Gorowitz, P. Gloersen, A. Ruess, and J. Kenney, Summary Report - NASA Contract No. NAS3-3570, (1964), CR-54064.
- II-2. "A 20 KW Solar Powered Pulsed Plasma Engine System Concept" B. Gorowitz, P. Gloersen and T. Karras, AIAA Third Aerospace Sciences Meeting, New York, 1/24-26, 1966, AIAA Paper No. 66-114.
- II-3. "A Magnetically Driven, Fast-Acting Valve for Gas Injection into High Vacua", B. Gorowitz, P. Gloersen and K. Moses. Rev. Sci. Inst. 31, 146, 1960.
- II-4. The gridded probe used for these measurements is similar to that used by H. S. Bridge, et al, J. Geophys. Res, 65, 3053, (1960), but was independently designed.

III. ACCELERATOR CHRONOLOGY

The following information is presented in order to review the evolution of the accelerator from its status at the outset of the period covered by this report to its present status (as described in section I). In addition, it demonstrates several of the trends in performance which may be appropriate for further improvement of accelerator efficiency.

A. MOD A-4T ACCELERATOR

Details of the A-4T accelerator are shown in Figure III-1. In addition to the straight cylindrical outer electrode shown here, a diverging outer electrode was tested. The A-4T was operated in the propellant-triggered mode.

A.1. Thrust Measurements

Curves of thrust vs power for the two types of outer electrodes are shown in Figure III-2. The points on the curves represent thrusts produced using the lowest quantity of injected propellant which could be used to self-trigger breakdown between the electrodes at the various applied potentials. As might be expected, these quantities decreased as the potential between the electrodes was increased.

A.2. Propellant Mass Flow Measurements

Calibrated flow meters were used to measure the flow of cold gas into the gun while it was fired at a 10 cps repetition rate. Typical flows are listed in Figure III-2.

The contribution of eroded mass to the effective propellant flow is discussed in the next section. The role of gas adsorbed in the electrodes or present in the composition of the electrode or insulator materials has not been quantitatively determined through experiment. However, the relative stability of thrust with time and its direct proportionality to pulse repetition rate suggest that these effects of extraneous gas were negligible, at least at the mass flows and background pressure at which this engine was operated. Further study of the possible mechanisms and magnitudes of gas adsorption by the electrodes was carried out to substantiate this indication.

Operation of the Mod A-4T gun was carried out in the voltage range from 2-8 KV with a thermocouple affixed to the exterior of the outer electrode. At 3 KV, a temperature rise of 203° was measured after four minutes of firing at 10 shots per second. At 8 KV, only 30 sec. were required for a temperature rise of 215° at the same repetition rate. As might be expected,

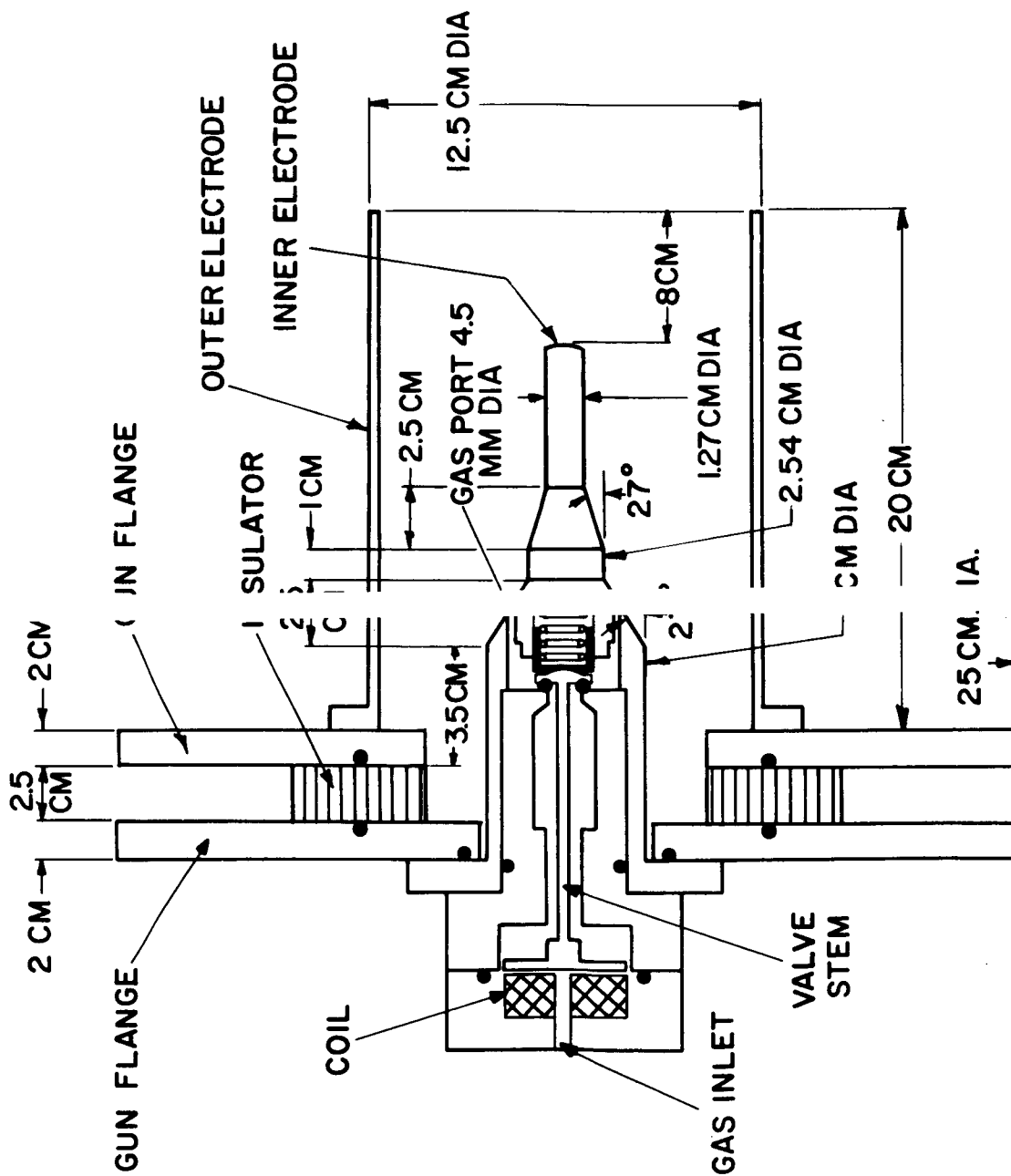


Figure III-1. Mod A-4 Accelerator.

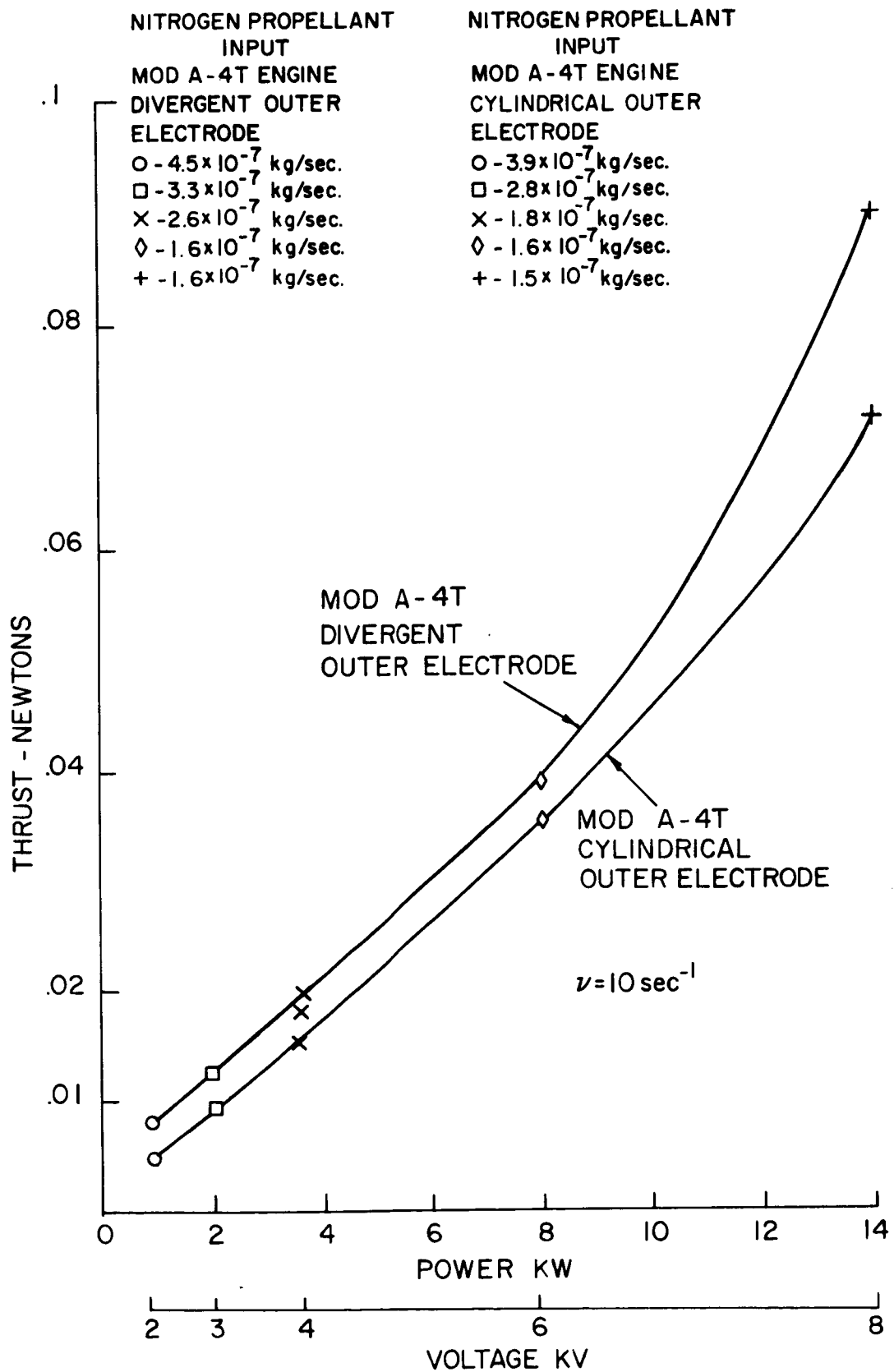


Figure III-2. Thrust vs. Voltage and Power - Mod A-4T Accelerator

the temperature rise for all of the various gun voltages was in line with the relative energy inputs and calorimetrically measured efficiencies. The maximum temperature measured was 450°C after one minute of firing at 8 KV. The temperature of the inner electrode was considerably higher, since during thrust runs at 6 KV and 8 KV melting of the tip of the electrode occurred.

The fact that thrust did not vary as the temperature of the electrodes increased (in the temperature range observed) is an indication that degassing of the electrodes plays a small role in mass addition. Data from Dushman¹ indicates that for commercial copper heated to 1000°C in vacuum, about .8 cc of gas, STP is evolved per Kg. of metal. This is equivalent to 1 mg of N_2 . "Interior" gas evolved, primarily during volatilization of the metal, amounts to about 4.5 cc or 6 mg of gas per Kg. of metal. Thus even if all of the surface and interior gas were evolved (which it is most certainly not), for the present electrode weight of about 3 Kg. a maximum of 21 mg might be added as propellant. At a firing rate of 10 shots per second and an average propellant flow rate of .02 mg per shot, assuming no propellant evolved from the electrodes between shots, a maximum of 100 seconds would be required to introduce an amount of gas equal to that measured with the flowmeters. The guns are operated in the vacuum for durations several orders of magnitude greater than this, without changes in the average observed thrust.

An additional consideration is the possible use by the gun of gas exhausted into the vacuum chamber, pumped back into the gun and adsorbed on the electrodes. For this to be true, the gas injection valve would have to be sufficiently fast that a small enough amount of gas flowed into the gun after the discharge had occurred so that the pressure in the gun was lower than that in the chamber. Gas profile measurements indicate that this in itself is probably not true. However, assuming that the gun acts as a pump, a calculation of the pumping speed of the 5" diameter gun muzzle yields a value of about $1000 \ell/\text{second}$ at 10^{-5} mm . The flow of injected gas is equivalent to about $80,000 \ell/\text{second}$ at the same pressure. Thus, even if the gun were an ideal pump, it could accumulate only about 1% of the total injected mass flow. The efficiency $\eta = T^2/2\dot{m}P$ would therefore be influenced by 1%.

A. 3. Electrode Erosion

Operating of the accelerators for several hundred thousand shots at voltages from 2 to 8 KV resulted in the following observations:

a. Electrode erosion as observed visually was concentrated at the tip of the inner electrode and was negligible elsewhere.

b. At 6 and 8 KV (8 and 14 KW), after approximately 3000 consecutive shots at a repetition rate of 10 cps, the front surface at the tip of the center electrode was melted and contained a crater at its center, as shown in Figure III-3.

c. Weighing of the forward section of the center electrode on which virtually all of the erosion was observed disclosed an average range of losses of from 5×10^{-9} Kg per shot at 2 KV to 25×10^{-9} Kg per shot at 8 KV. The values for erosion vs. operating voltage are plotted in Figure III-4.

The substitution of a center electrode which was 15 cm longer than the outer electrode resulted in a sharp decrease in the observed rate of erosion to less than 10^{-9} Kg per shot at 6 KV.

A.4. Overall Efficiency - $T^2/2 \dot{m} P$

Overall efficiency as defined by $T^2/2 \dot{m} P$ was calculated from the values of thrust given in Figure III-2 and those of propellant mass flow (Figure III-2) and eroded mass (Figure III-4). A graph plotting overall efficiency vs. $I_{sp} \equiv T/\dot{m} g$ is given in Figure III-5.

A.5. Energy Efficiency

Energy in the engine exhaust stream had been measured calorimetrically previously with the engine operated on a single shot basis and with a radiatively-cooled rather than a liquid-cooled collector. The results are plotted in Figure III-6. The fact that the curves in Figures 5 and 6 cross at the higher voltages points up either the inadequacies of these particular calorimeter measurements, or the presence of unaccounted for mass addition. As stated above, the latter possibility seems unlikely as a major contributor, in our opinion. The former possibility has been discussed in section I. The aforementioned problems are intensified by the increased radiative losses from the calorimeter used in these tests and the fact that only a 15° half-angle was subtended by this calorimeter.

A.6. Faraday Cup Measurements

The cup was biased by a set of batteries in parallel with a large capacitor which in turn was connected to ground through a resistor. The voltage across the resistor was then fed to an oscilloscope. From the current vs. time information obtained in this way the ion velocity distribution could be obtained (see section II). Figures III-7 through 11 show the distributions that were calculated from the data obtained. These represent preliminary measurements, and mass flows were not recorded.

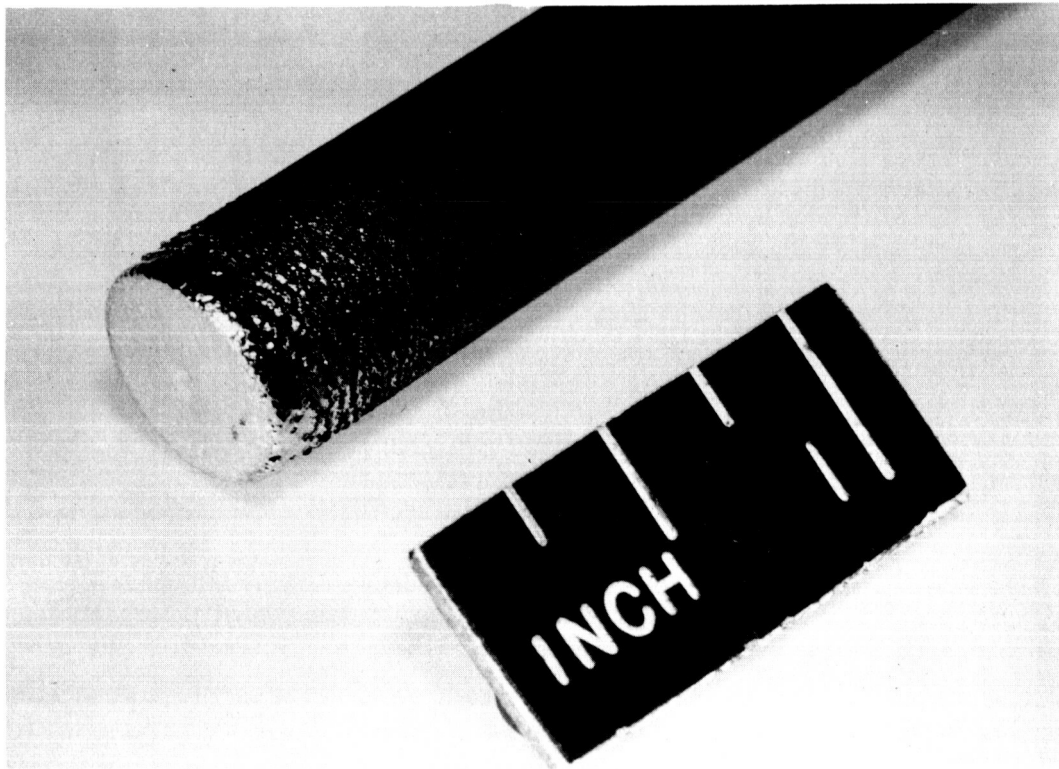
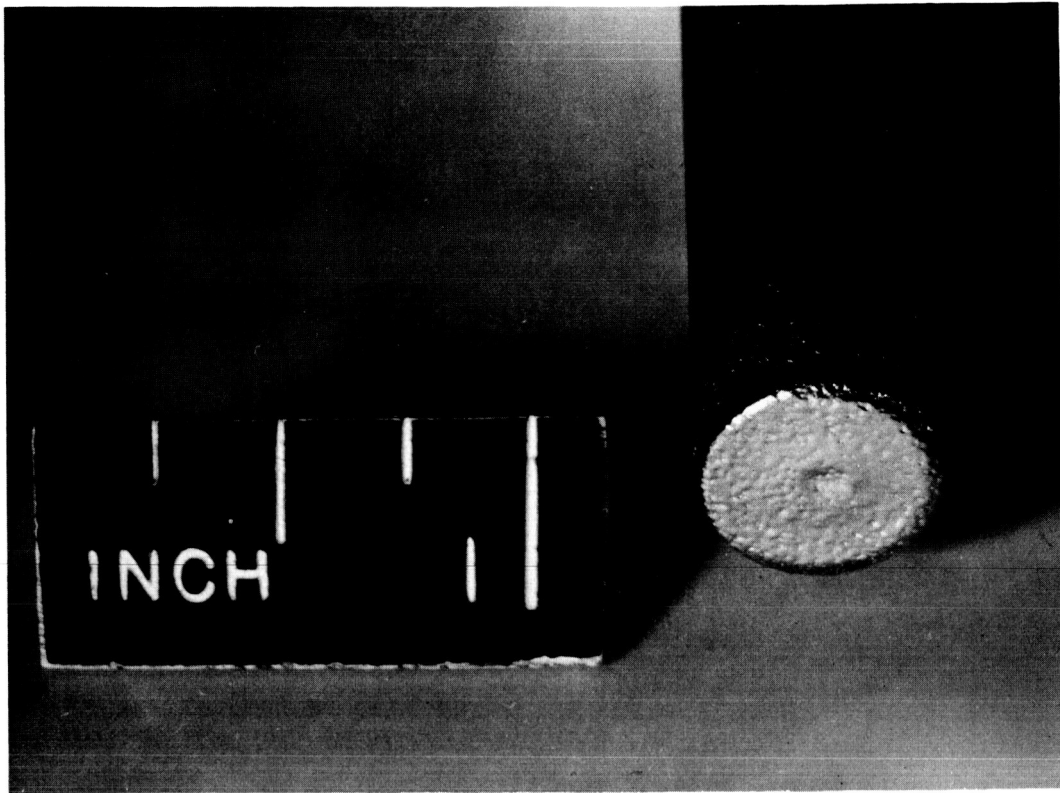


Figure III-3. Center Electrode After Operation for 3000 Shots at 8 KV, Mod A-4T Accelerator.

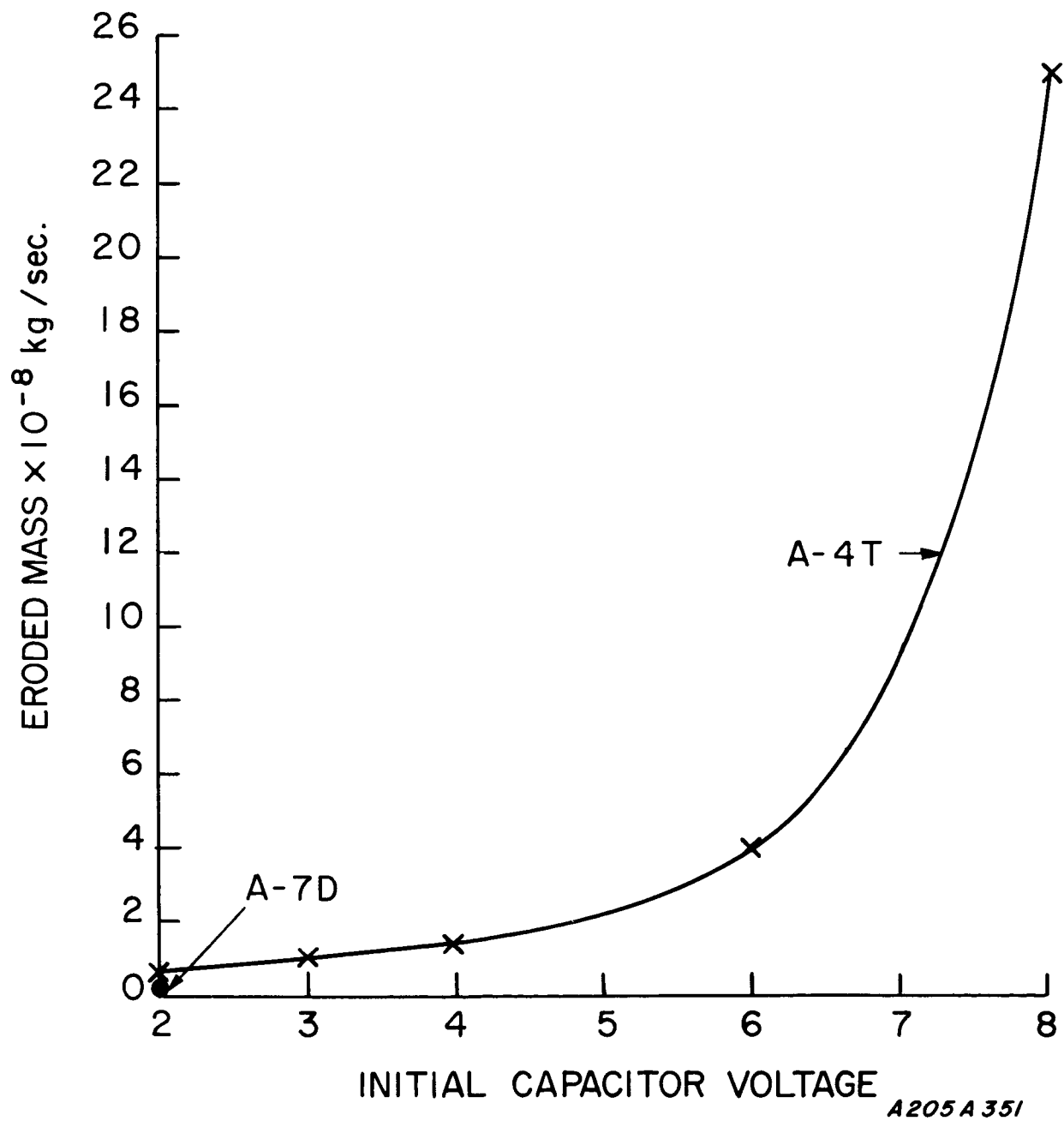


Figure III-4. Electrode Erosion vs. Initial Capacitor Voltage, Mod A-4T, 45 μ fd, Nitrogen propellant, 10 cps.

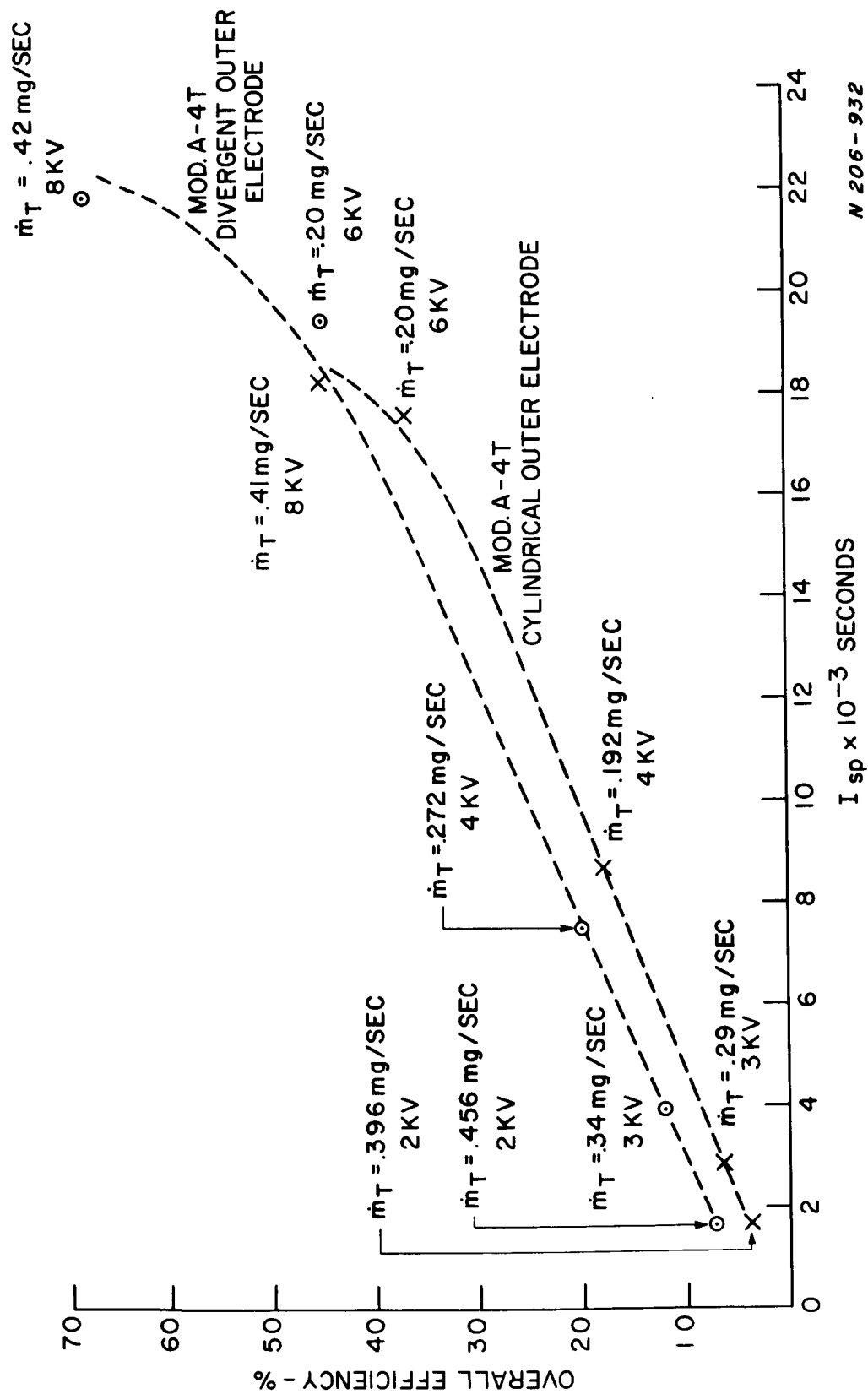


Figure III -5. Overall Efficiency vs. I_{sp} , Mod A-4T, 45 μ fd, Nitrogen.

N 206-932

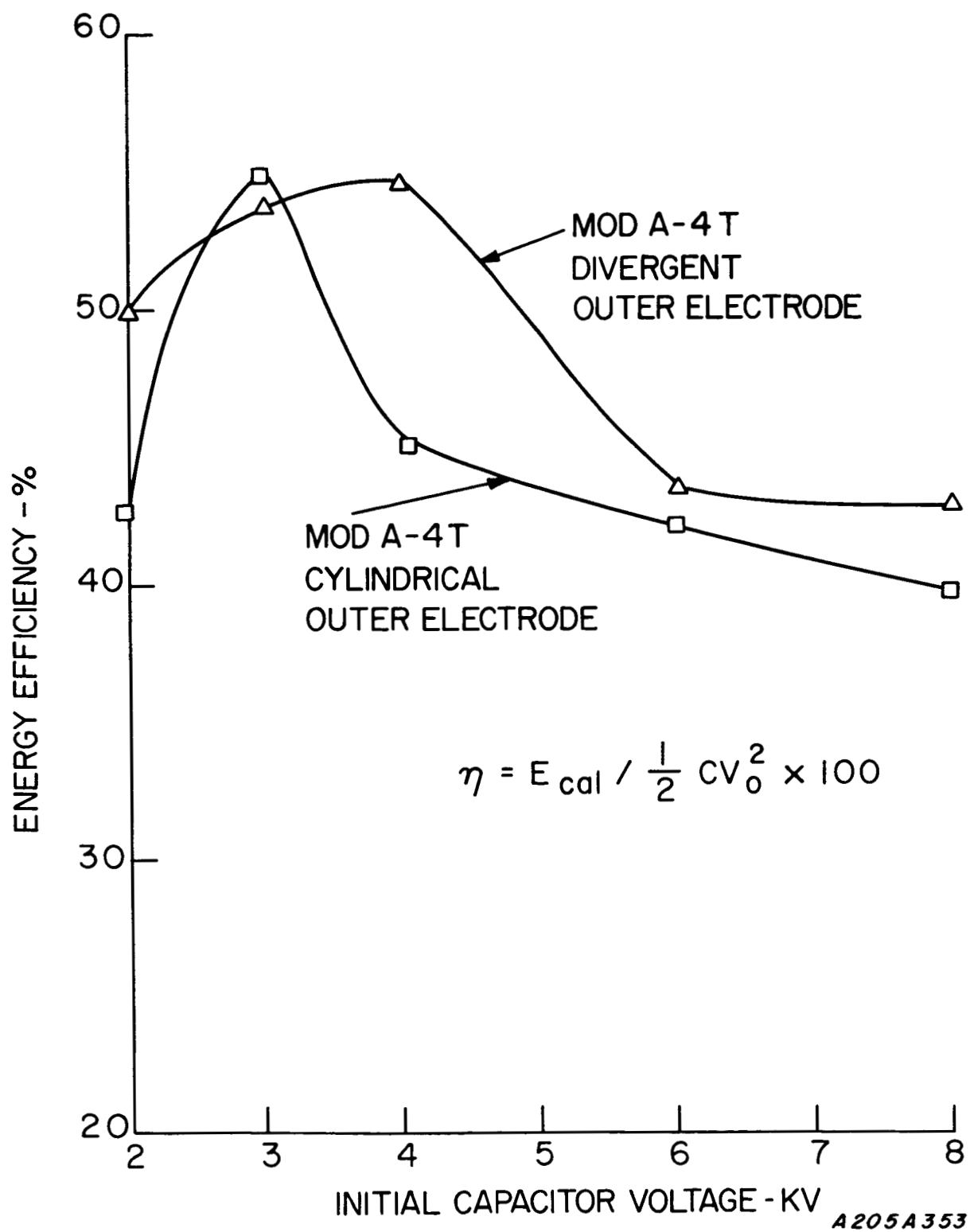


Figure III -6. Energy Efficiency vs. Voltage, Mod A-4T, Nitrogen.

ION VELOCITY DISTRIBUTION CURVES FROM FARADAY CUP MEASUREMENTS

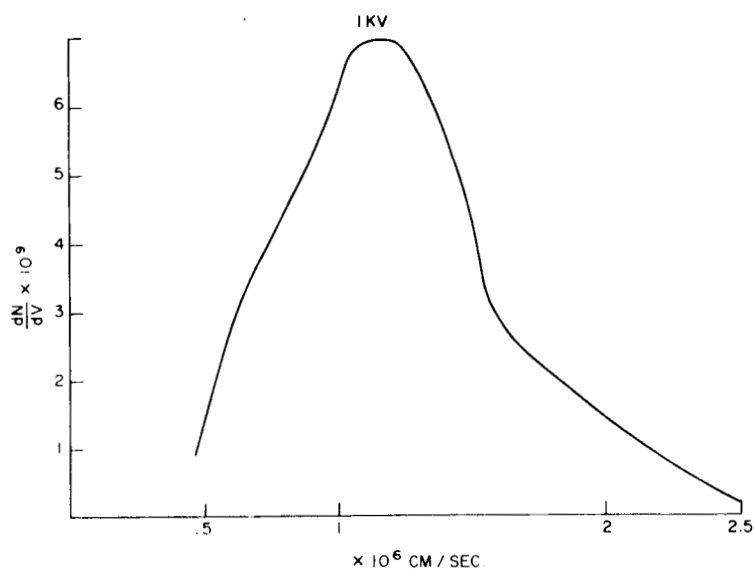


Figure III-7
2KV
CURRENT SHEET MOVES
AT $7.3 \times 10^6 \text{ CM/SEC.}$

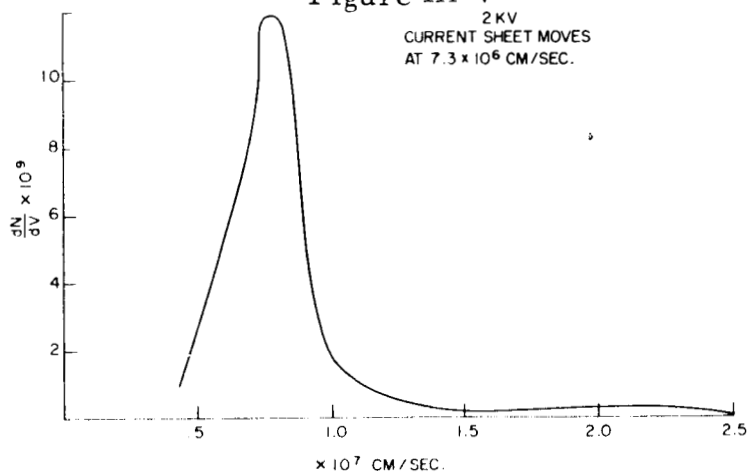


Figure III-8

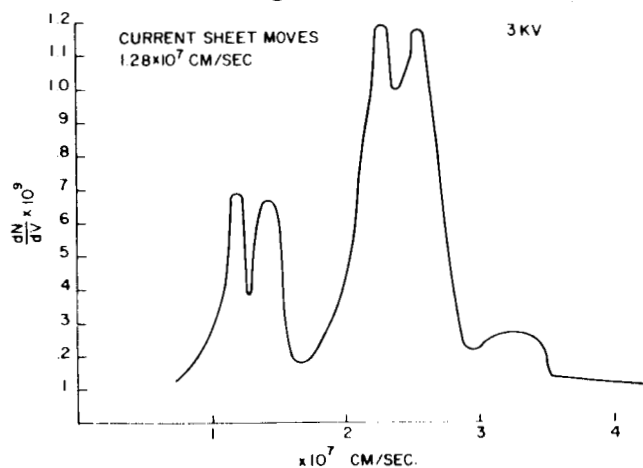


Figure III-9

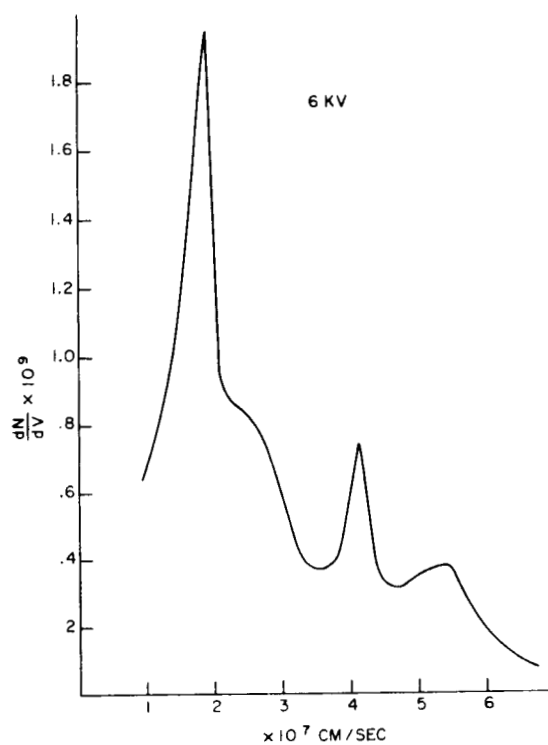


Figure III-10

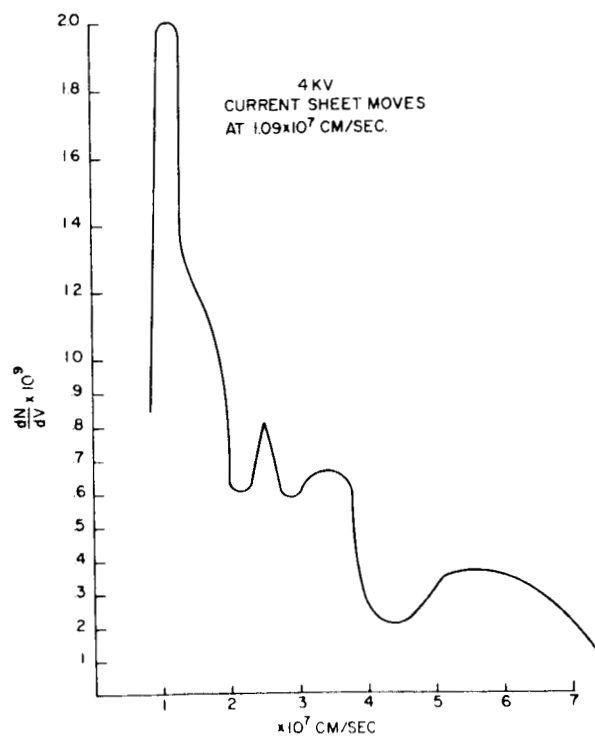


Figure III-11

The extremely high \bar{v} inferred by the low velocity peaks in Figures III-8, 9, and 11, are comparable with the velocities of the current sheet at the time of peak current obtained with magnetic probes^{III-2} at 2, 3, and 4 KV. The higher velocity maxima observed for 3, 4, and 6 KV have no such correspondence, however. Simultaneously obtained luminosity time-of-flight data tended to infer a time of arrival that was an average of all peaks.

Maximum plasma densities of the order $10^{17} / \text{m}^3$ were calculated from the Faraday cup currents and the velocity data for a probe location 2.75 meters downstream from the gun muzzle. This corresponds to a Debye length of several centimeters at an estimated upper limit electron temperature of 10 eV. The grid wire spacing of .025 cm in the probe was close enough so that the electric fields could be felt throughout the plasma as it entered the probe.

A more elaborate multigridded probe was later constructed; however, this preliminary study was very useful as a guide to the more detailed future work.

A.7. Propellant Distribution Studies

a. Experimental

A fast ionization gauge was used to measure gas distributions in the Mod A-4T gun. This probe was similar to that used by Marshall^{III-3}.

The ionization gauge tube was mounted on a stainless steel tube which could be moved axially through a sliding vacuum seal. The tube was at a radial position 3-1/2 cm from the gun axis so that it could be moved without obstruction over the entire gun length. Measurements were obtained from a position 20 cm beyond the muzzle to a position 6 cm behind the gas supply nozzles.

In early experiments conducted several years ago, it was observed that gauge life was severely limited if the gauge tube was exposed to the atmosphere for more than a minute or so. A similar effect was observed here. Thus, in order to minimize this problem, no modifications were made in the gauge tube other than to remove its glass envelope. Immediately after the tube was opened, it was placed on the probe carriage and the facility was evacuated.

The tube life was also shortened if the gauge was in front of the gun while it was being fired. In the facility in which these tests were made, this difficulty was unavoidable, since there was no way to change the radial position of the probe. Several shots were required in order to determine the minimum valve voltage corresponding to self-triggering of the discharge

at a given gun voltage. Deterioration of the gauge resulted, contributing to uncertainty in calibration to absolute pressures. Other uncertainties arose from the calibration procedure itself.

Calibration was performed in the following manner. The vacuum chamber was closed off from the vacuum pump and rapidly raised to a given pressure. This pressure was immediately read by the ionization gauge and, after a few seconds, by a calibrated thermocouple gauge. Uncertainties arose from the fact the ionization gauge tended to saturate after a second or two, for high pressures, and would drift. Additional uncertainties came from the usual problems one encounters with pressure gauges (i. e., differences in sensitivity to a given gas etc). Because of these uncertainties, the calibration was not included in any computation. However, the response was found to be linear at pressures up to 1 mm Hg, well above the maximum pressures observed at the nozzles.

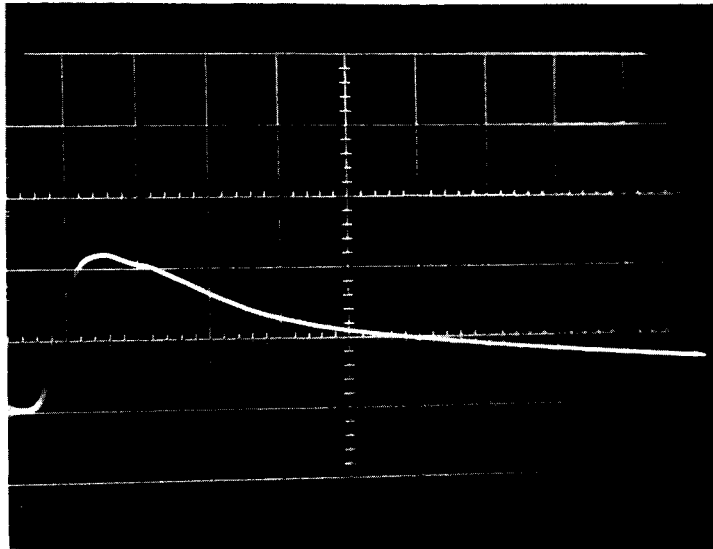
b. Results

The pressure data were obtained as oscilloscope traces whose amplitude was proportional to pressure (see Appendix B) as a function of time for a fixed position (Figure III-12). When data were obtained for a series of positions, the axial gas density distribution could be plotted at various times. This was done for a series of valve voltages and plenum pressures.

Figure III-13 shows how the gas density distribution varied as a function of time. It should be noted that about 600 microseconds after the valve capacitor was fired, a secondary peak in the pressure distribution appeared downstream from the primary peak (opposite the feed nozzles). One secondary peak was roughly opposite the end of the center electrode and may in some way have resulted from a reflection at that boundary. Clearly, neither gas peak propagated and no peak appeared at a position between the two maxima. One is forced to conclude that the gas was not filling the barrel in any simple or uniform manner.

Gas-triggering generally occurred at about 500 microseconds, before any secondary density peaks had developed or much of the gas had moved beyond the region of the gas entry nozzles. In fact, very little gas ever penetrated to the region in which the discharge begins and in which the inductance per unit length is small. This observation tends to verify the view that the force on the plasma in an efficient accelerator (such as the A-4T) will primarily be applied in a region of high inductance per unit length.^{E-1} Evidently the breech region serves only to get the discharge started, and the less gas wasted there the better.

However, examination of a time trace reveals that a great deal of gas was being wasted elsewhere. Figure III-14 shows the pressure as a function



Nozzle:	Mod. A-4T
Propellant:	Nitrogen
Valve Voltage:	4KV
Plenum Pressure:	15 psig
Time Scale:	.5 millisec./cm
Sensitivity:	.1 V/cm
Probe Position:	17 cm from front face of center electrode flange

Figure III -12. Oscilloscope Trace of Fast Pressure Probe Signal

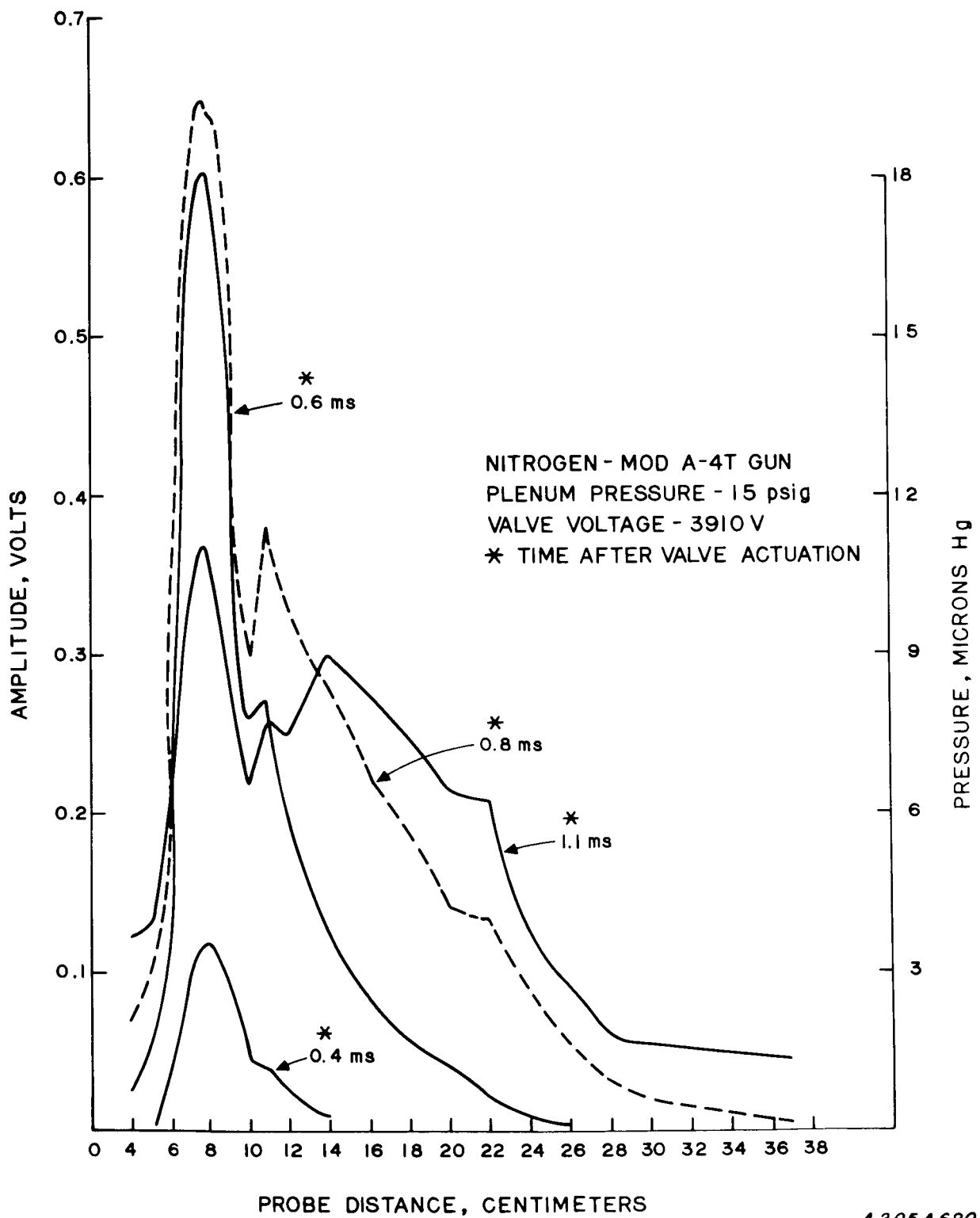
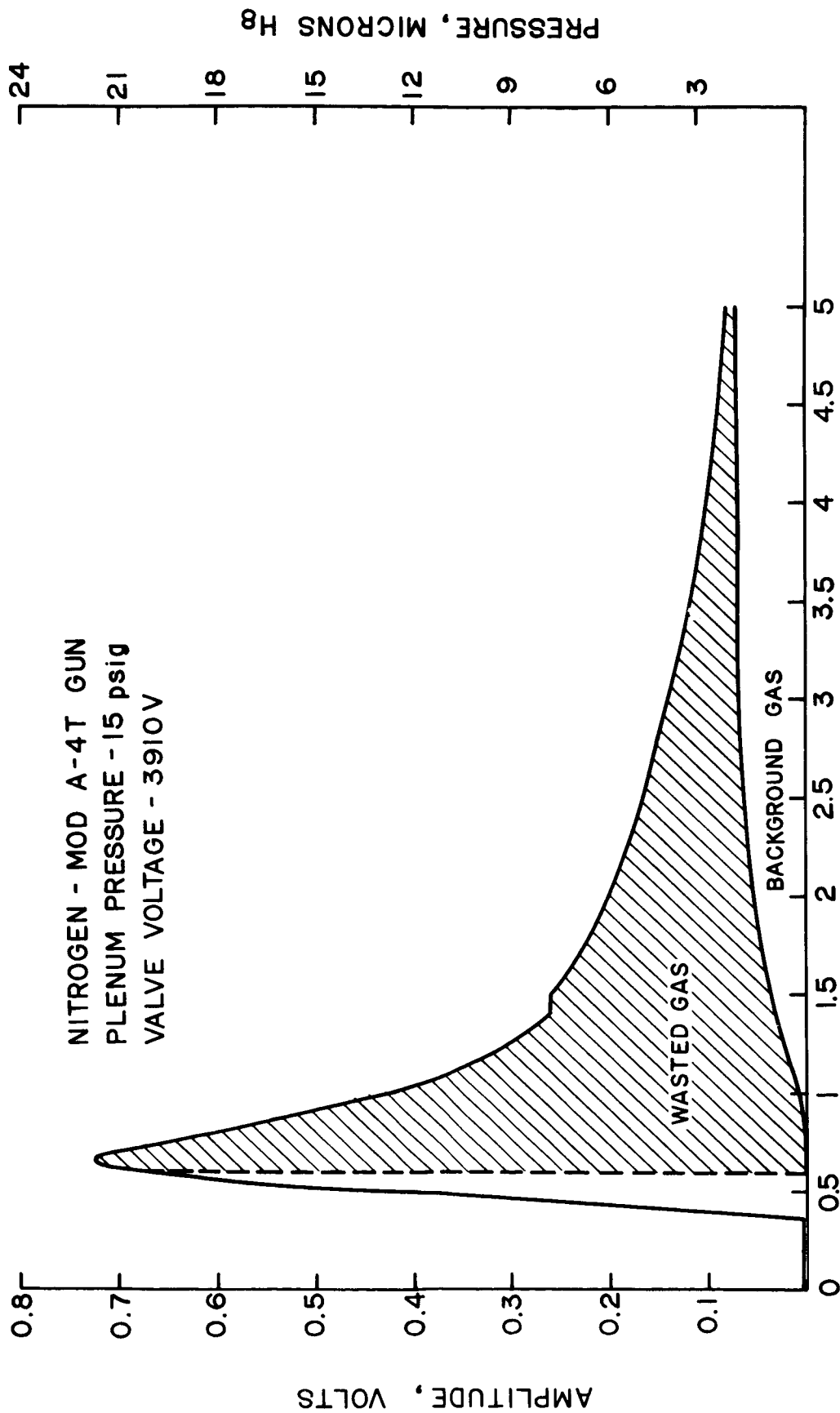


Figure III-13. Time Sequence of Gas Density Profile in Gun for N_2 .



TIME, MILLISECONDS AFTER VALVE ACTUATION

Figure III-14. History of Gas Pressure Near Injector Ports.

A205A691

of time at a position about 5 cm from the nozzles. This radial position is most nearly opposite the nozzles and should be intercepting a constant fraction of the gas that leaves these feed tubes. The computational procedure, based on this assumption, that leads to a determination of the fraction of the injected gas that has passed the feed nozzles as a function of time is given in Appendix B as

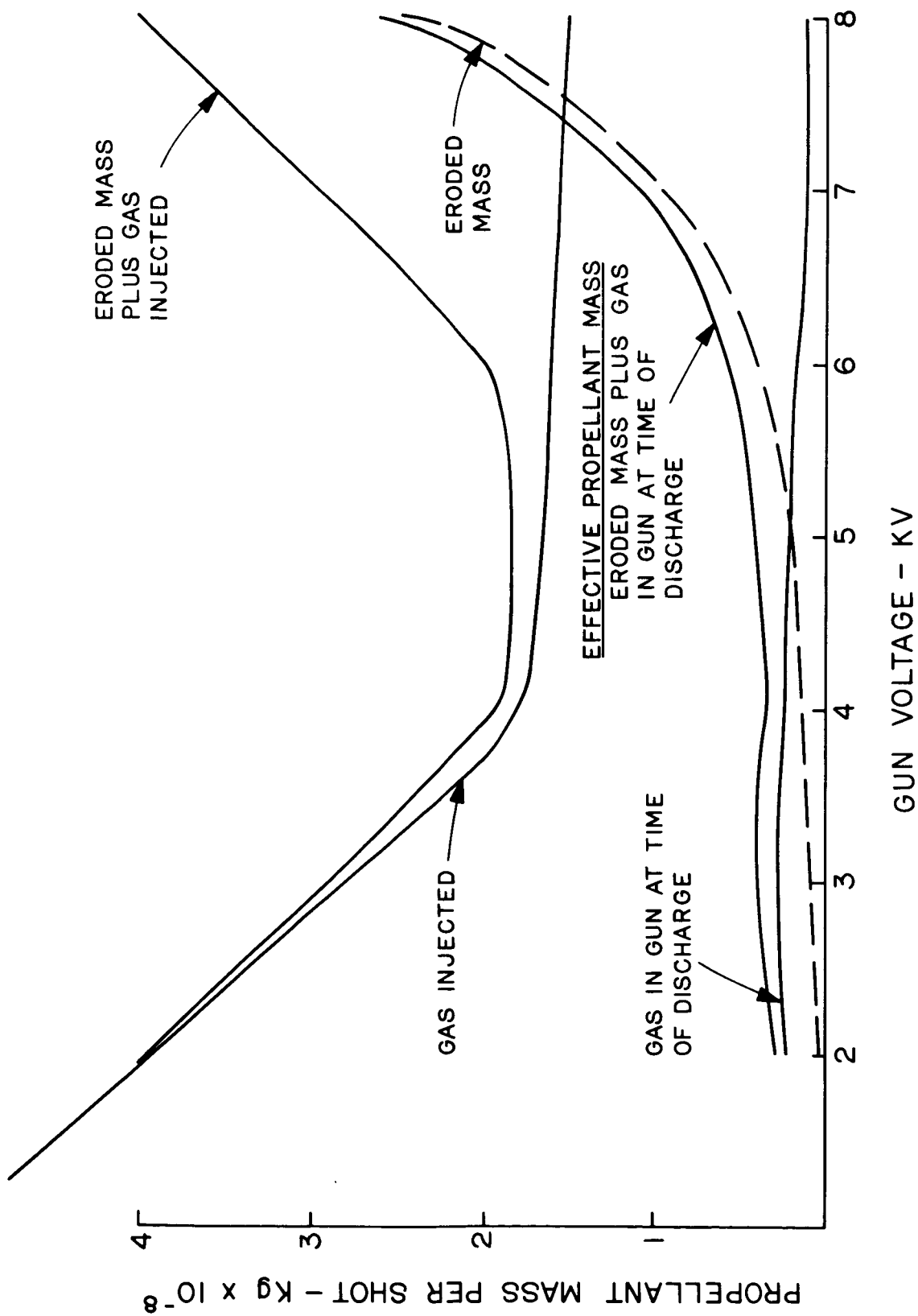
$$\frac{M(T)}{M(\infty)} \sim \frac{\int_0^T p \, dt}{\int_0^\infty p \, dt} \quad (1)$$

One correction must be made however. Due to inadequate pumping speed, the small vacuum chamber used for these studies begins to fill up with a uniform background and the curve in Figure (III-14) becomes asymptotic for large times to something other than zero. A probe downstream can determine the magnitude of this stationary gas and it is indicated by the low solid curve in Figure III-14) that begins to rise at one millisecond.

If T is taken as 600 microseconds, the equation will give the gas fraction out of the nozzles at the time of gun discharge. The figure 600 microseconds was chosen rather than 500 microseconds because the gas that had just left the nozzles at 500 microseconds required 100 microseconds more to reach the gas density probe in its off-axis position. Thus the gun firing at 500 microseconds used the gas fraction seen by the probe at 600 microseconds.

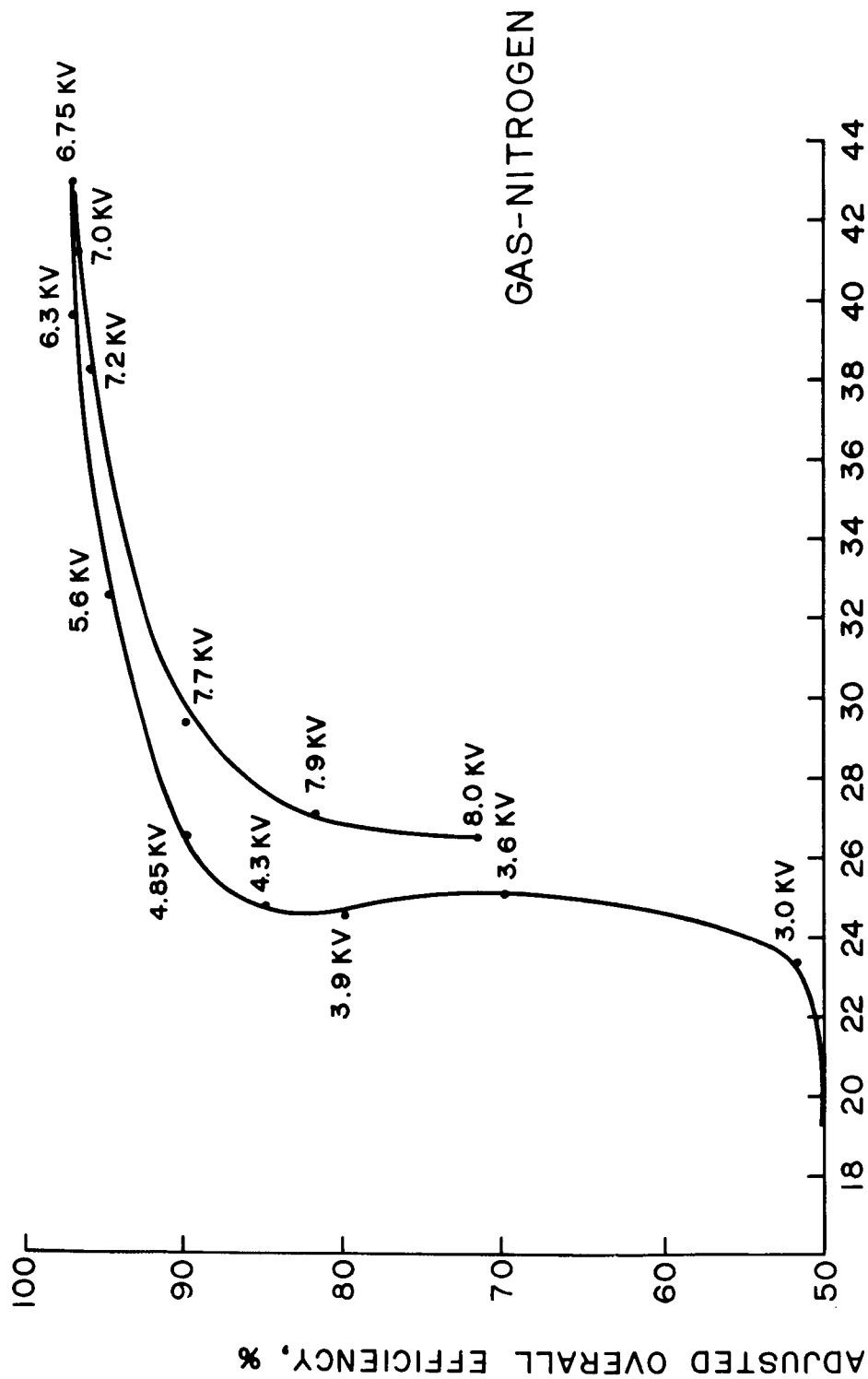
This gas fraction in the gun at the time of gun firing was at most the order of ten to fifteen percent of the amount injected. Clearly, most of the gas admitted by the valve into this nozzle geometry was not made available to the discharge and led to low overall efficiency ($T^2/2 \dot{m} P$) for the gun.

If one considers only the gas present in the interelectrode region and any eroded electrode mass as the propellant mass to be used in determining efficiencies and I_{sp} 's, a plot of adjusted overall efficiency vs. adjusted I_{sp} may be obtained. Figure (III-15) shows the amount of propellant and eroded material involved at each gun operating voltage. Figure(III-16) shows the resulting efficiency and I_{sp} . It is clear that much higher efficiencies than had previously been observed ^{sp} are to be expected if the gun could be fired when a greater percentage of the gas is in the interelectrode region. Figure (III-17) shows a plot of the amount of gas in the gun as a function of time. A maximum occurs at one millisecond - clearly the optimum time for gun triggering for this nozzle geometry.



A205A692

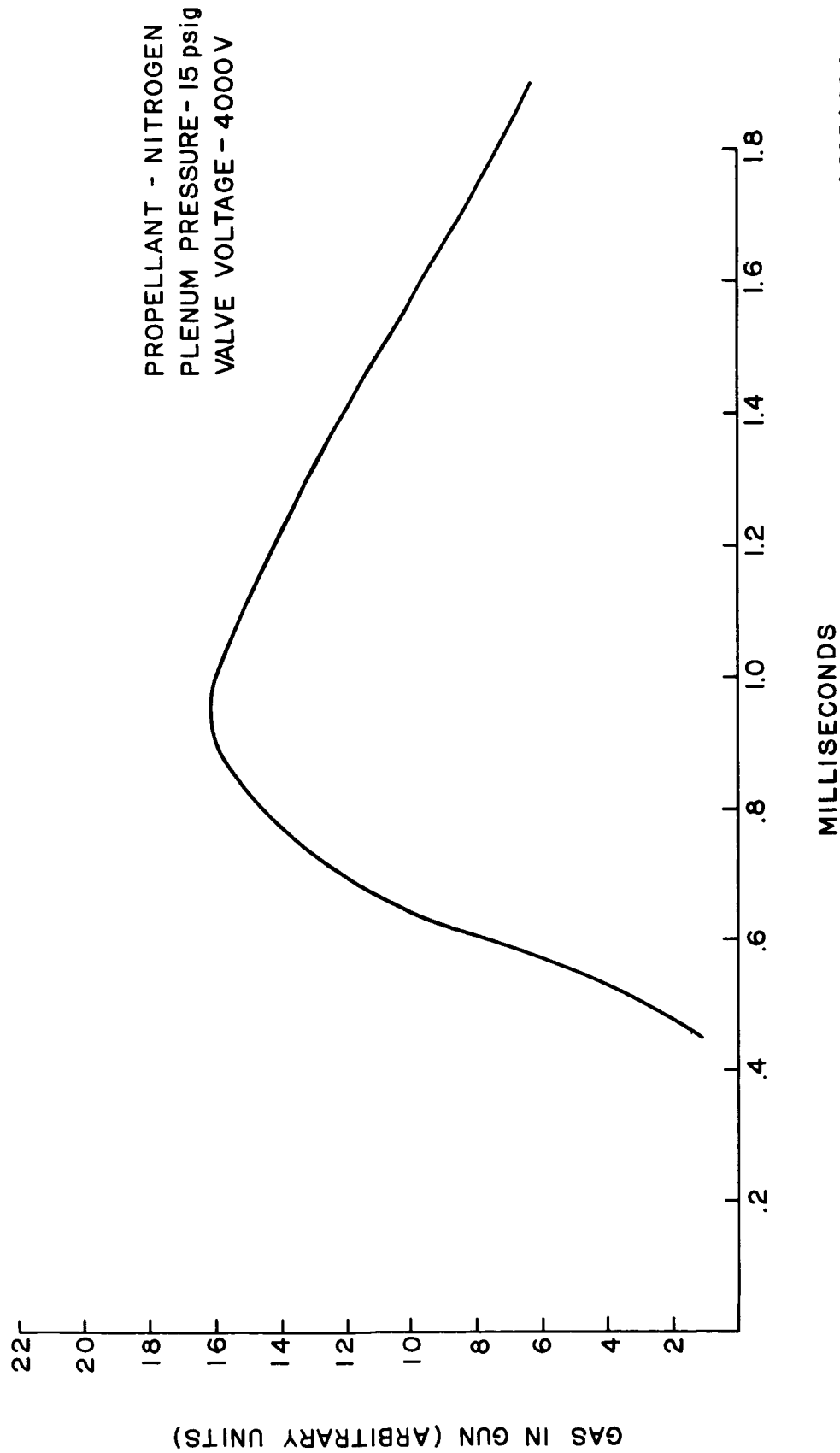
Figure III-15. Propellant Mass Utilized as a Function of Operating Voltage, A-4T Gun.



ADJUSTED $I_{sp} \times 10^{-3}$

A 205 A 693

Figure III-16. Adjusted Overall Efficiency vs. Specific Impulse, A-4T Gun.



A 2054694

Figure III-17. Quantity of Gas in Gun as a Function of Time, A-4T Gun.

c. Discussion

It was obvious that two goals were to be pursued; first, to find a means of insuring that most of the gas admitted by the valve was between the gun electrodes at the time of discharge and, second, to discover a way to reduce the I_{sp} of the exhaust. The first problem was best attacked through determination of what limited the gas flow.

In order to predict whether the pressure decay observed inside the gun was limited by the conductance of the electrodes or the conductance of the 4.5 mm feed tubes a crude computation was performed.

An expression for the emptying time of a cylindrical tube has been computed to be III-2

$$\Delta_t = \frac{2.303 V}{F_t} \left[\log \frac{P_1}{P_2} - \log \left(\frac{P_1 + k/b}{P_2 + k/b} \right) \right] \quad (2)$$

where V is the tube (and any associated reservoir) volume, P_1 is the initial pressure, P_2 is the final pressure, a is the tube radius, ℓ the tube length, T the gas absolute temperature and M is molecular weight,

$$k = \frac{F_t}{V}, \quad b = .0736 \quad \frac{a F_t}{c V} \quad \text{and} \quad F_t = 30.28 \quad \frac{a^3}{\ell} \quad \sqrt{\frac{T}{M}}.$$

Reference to Figure III-1 shows that the feed tubes are 4.5 mm in diameter, 4 cm long, and the empty space behind them has a volume of 7.6×10^{-3} liters. The outer gun electrode is 20 cm long and 12.5 cm in diameter. The effects of the inner electrode can be ignored since it is quite thin in the regions of interest.

If we observe that 2.0×10^{-5} gms of propellant are injected for each shot at 3-4 KV, then the initial pressure within the feed tubes may be computed to be about 1.6 mm.

Inserting this information into the above equations, one can now determine that the time required for the propellant gas to leave the feed tubes, so that the pressure is down to 10% of its original value, is on the order of 2.5×10^{-3} seconds. This time is very close to the characteristic decay time of the gas density observed with the pressure probe.

The emptying time of the gun itself can, in a similar way, be computed as approximately 0.2×10^{-3} seconds. This computation takes into consideration the dimensions noted earlier and the fact that only a 10-15 cm length of the barrel is involved.

Clearly, the slow decay of gas from the gun was limited by the conductance of the feed tubes and not of the gun. Since it was desirable to have the gun barrel be the limiting conductance, the feed system had to be modified to increase its conductance.

Such modifications would have the effect of reducing the time over which gas is emerging and would put a larger fraction of the gas in the gun at one time. If the discharge time of the gun could then be controlled so that it occurred when the propellant mass in the gun was a maximum, as with trigger electrodes, much better utilization of the gas should take place. Experiments conducted in line with this reasoning will be discussed below.

Not only was there hope for higher overall efficiency, but it was thought possible that a more useable I_{sp} could be realized. This last possibility could come as a result of the fact the total impulse could be distributed over more particles.

Little help was expected at this time from variations in other obvious parameters such as plenum pressure and valve voltage. Significant changes in these parameters would alter the amount of injected propellant so that it no longer matched the gun capacitance and voltage.

Change in the species of propellant also promised little effect upon the feed nozzle conductance. There is a slight tendency for light molecules such as helium to get out faster (compare Figures III-18 and III-19) as indicated by Equation (2), but this is not a dominant effect. However, there is reason to believe heavier ions could lead to a lower I_{sp} and thus more than compensate for their lower conductance. This point will also be discussed later.

A-8. Emission Spectra From the Mod A-4T Gun Plasma Exhaust

III-4

Some previously developed spectrometric techniques were applied to study the exhaust plume of the Mod A-4T gun operated at 3 KV, with the primary motive being to determine the extent to which impurities exist in the plasma. Briefly, the technique consists of using a scanning monochromator (JACO 500 mm Ebert) in conjunction with a gated photomultiplier detector and a variable time delay for the gate. Two modes of operation are possible, and both were used to study the plasma exhausts resulting from the acceleration of both nitrogen and argon propellants: The first mode is to

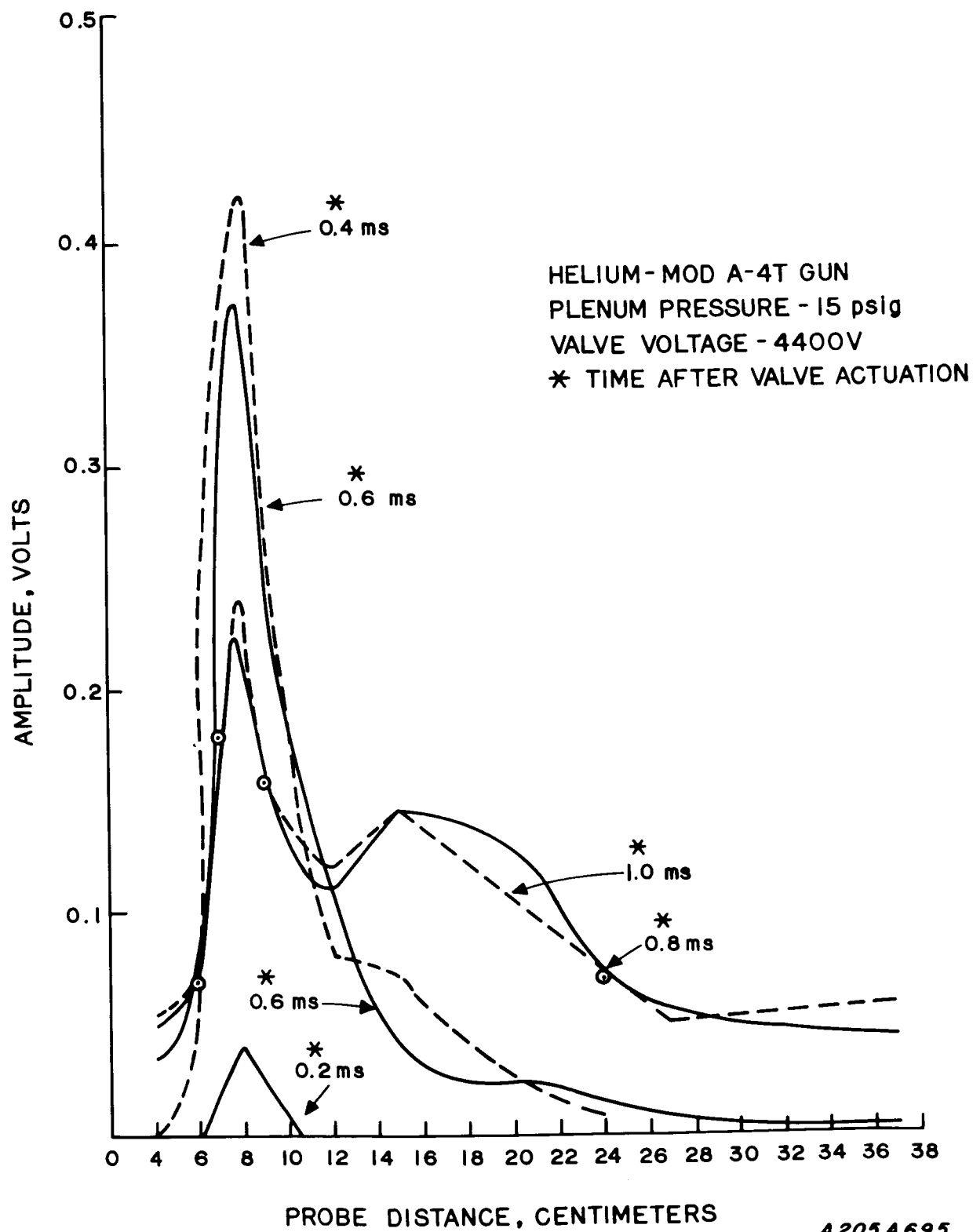


Figure III-18. Time Sequence of Gas Density Profile in Gun for He.

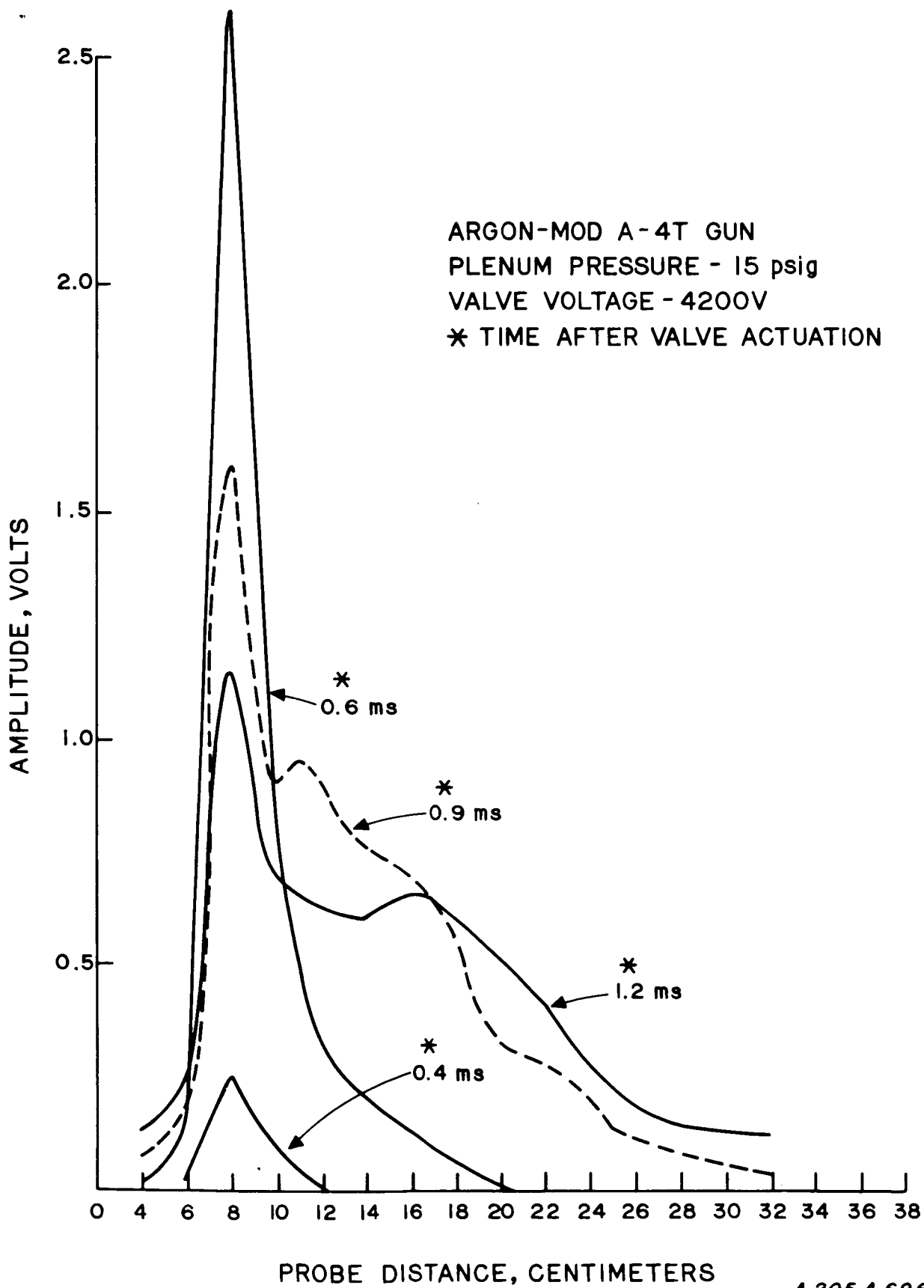
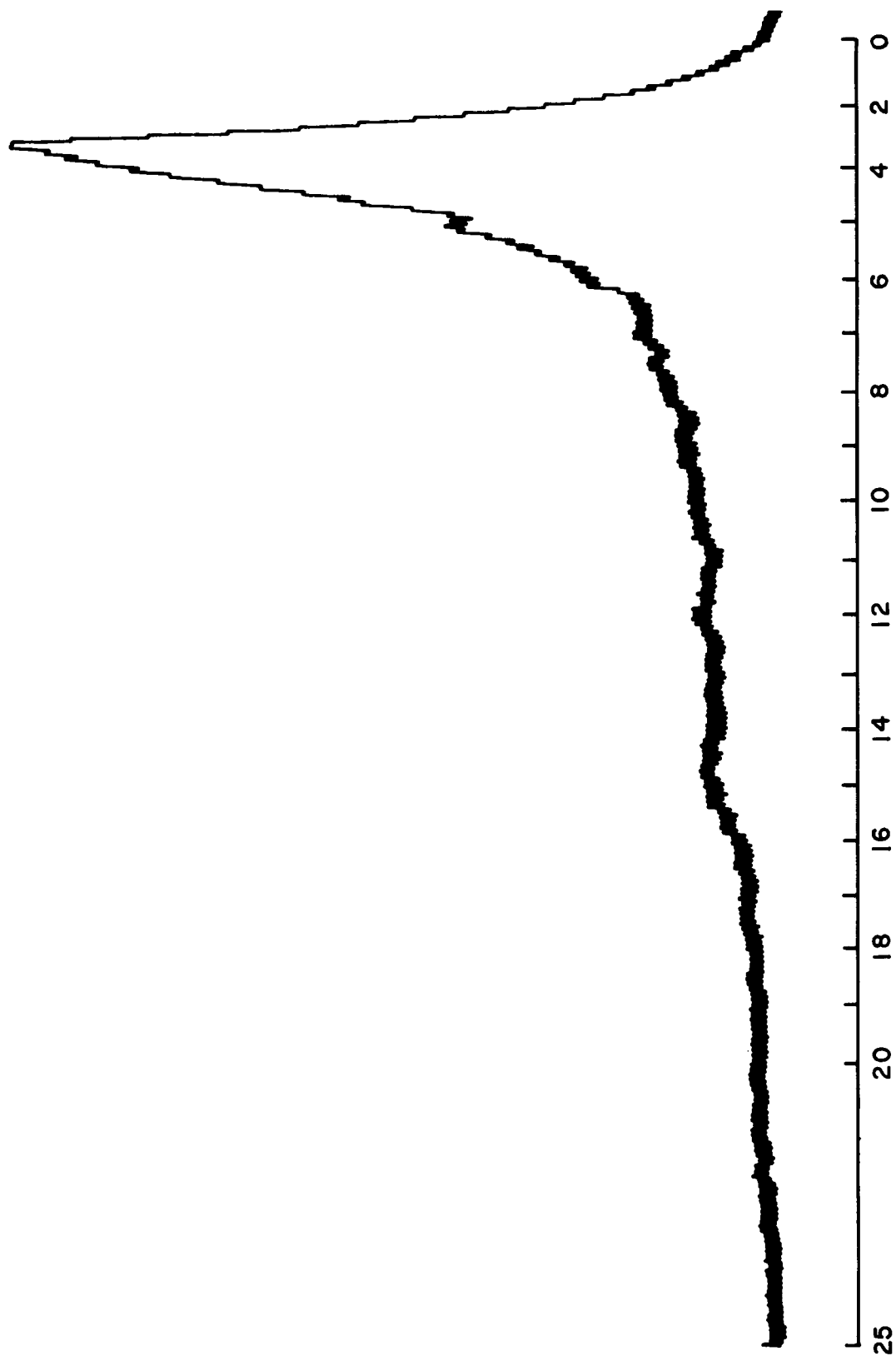


Figure III-19. Time Sequence of Gas Density Profile in Gun for Argon.

fix on a strong spectral line and use a clock motor to drive the variable time delay for the photomultiplier gate. The results of such operation are shown in Figures III -20 and III-21. The second mode of operation consists of choosing an appropriate, fixed time delay (after gun discharge breakdown) and using a clock motor to drive the scanning monochromator. The results of this mode of operation are shown in Figures III-22 and III-23, where the fixed time delay chosen corresponded to the time near which the intensity peaks shown in Figures III -20 and III-21 occur.

The results from this study are as follows: Despite a deliberate search for lines belonging to Cu I and II; Si I, II, III; O I, II, III, and other impurities previously observed^{III-5}, no such lines were observed at a point 10 cm downstream from the muzzle when either nitrogen or argon were used as propellants. All but a few lines were positively identified as belonging to the propellant atoms and their various ions. Referring to Figure III-15, it is evident that Cu is present in significant amounts under this operating condition. Consequently there appears to be a need for the use of another diagnostic technique (e. g., absorption spectroscopy) for more thorough identification of species. In addition, it was discovered that emission spectra were observable only within 10 cm of the muzzle of the accelerator. While well-developed spectra, including time contours of the gaseous propellant emission lines were obtained at this position, it was later realized that the accelerator discharge extended this far, and, in fact, the position and time contour of the light corresponded (as shown in Figure III-20, for example), roughly to that of the extended current plume. (The temporal shape of the luminous pulses differed somewhat for the two propellants, that of nitrogen being narrower than that for argon.) Since we were unable to obtain emission spectra outside of this region, this was further reason to abandon this particular technique as a useful diagnostic tool.



MICROSECONDS

Figure III-20. Time Profile of N II 3995 Å Line in A-4T Gun Exhaust, 10 cm. Downstream from Muzzle, 3KV, 45 μ fd, Nitrogen.

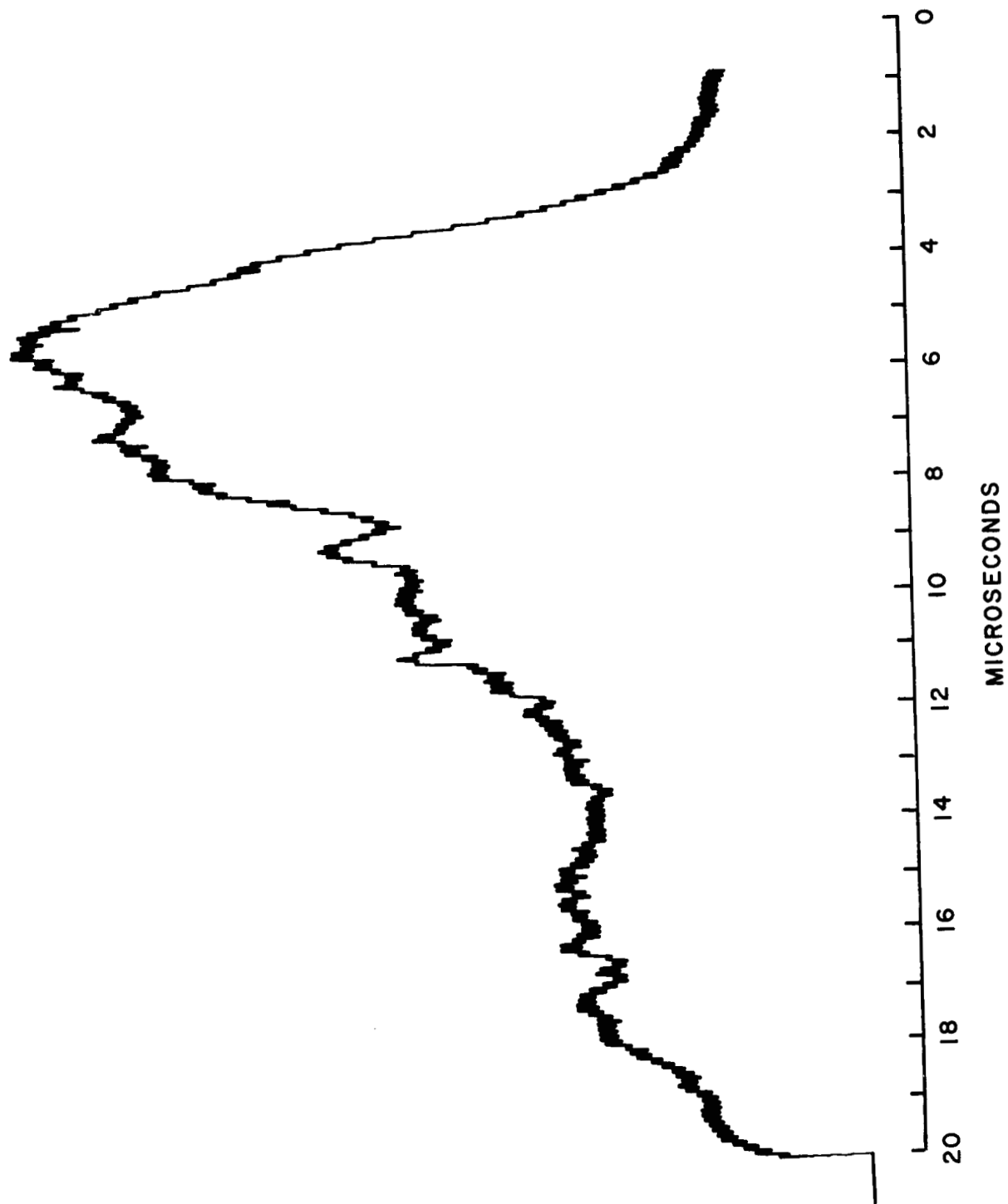


Figure III-21. Time Profile of A II 4267 Å Line in A-4T Gun Exhaust, 10 cm Downstream from Muzzle
3KV, 45 μ fd, Nitrogen.

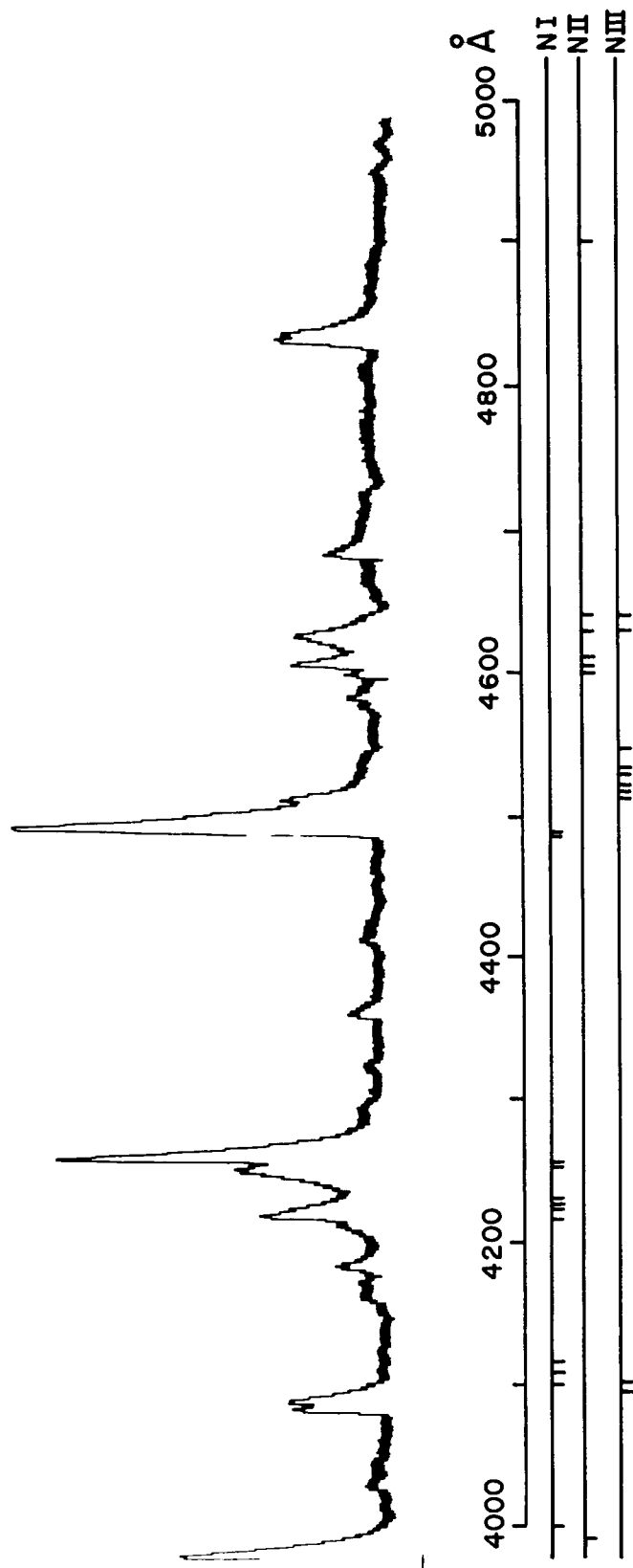


Figure III-22. Spectral Record of Luminous Exhaust Using Nitrogen, A-4T Gun, 3 KV, 45 μ fl, Nitrogen Observed 10 cm Downstream from Muzzle.

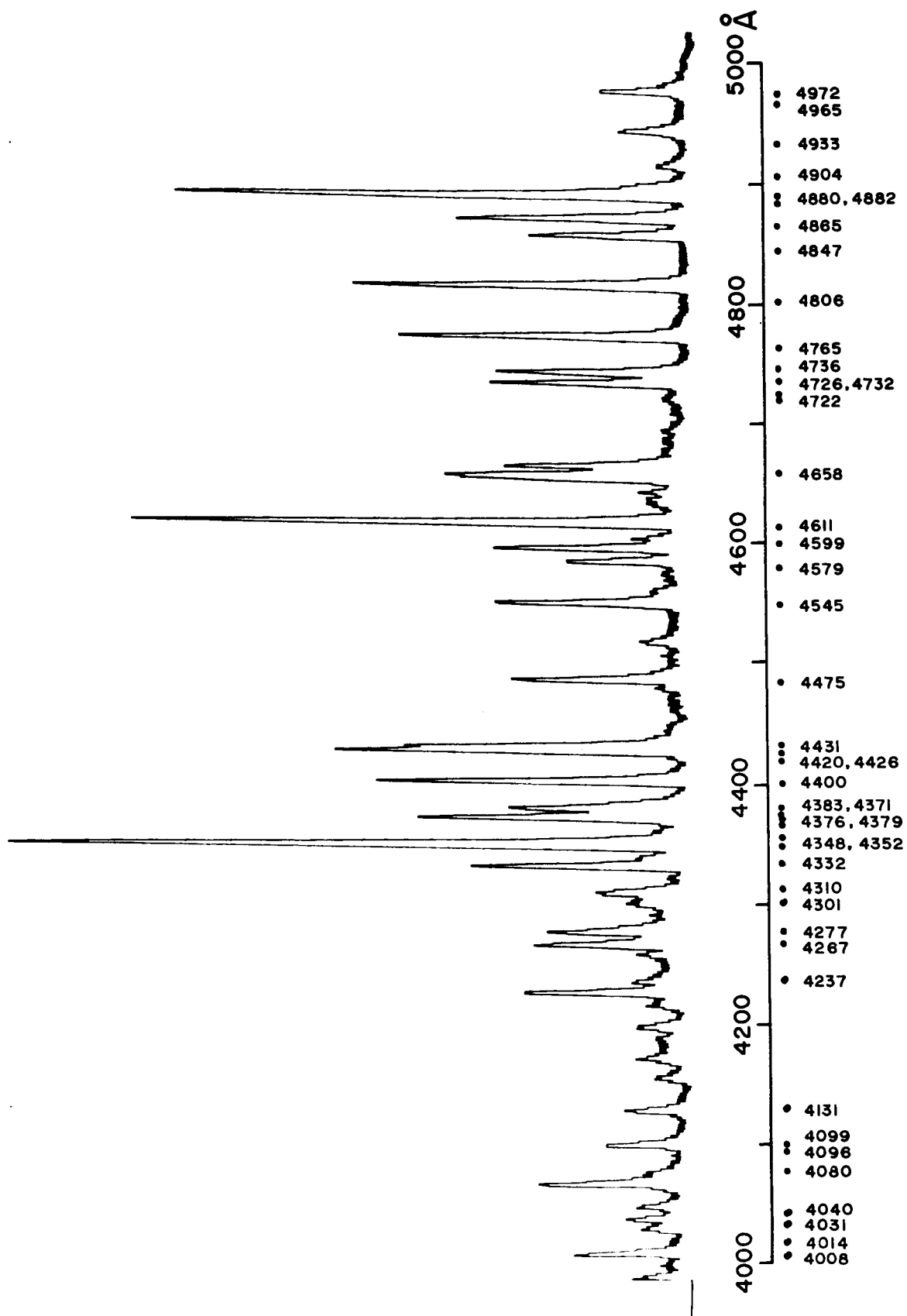


Figure III-23. Spectral Record of Mod A-4T Gun Exhaust, 10 cm. Downstream from Muzzle, Argon Propellant, 3KV, 45 μ fd. All Lines Observed are Attributed to A II.

B. MOD A-5 ACCELERATOR

Some additional changes in the Mod A-4T gun electrode geometry were made in order to study their effect on engine efficiency. The inner electrode was modified by increasing its breech diameter to 10 cm from the original diameter of 5 cm., leaving unchanged the gas injection ports and 1 cm. diameter center electrode extension. This change also required some appropriate gun flange modifications. The purpose of the new electrode shape designated Mod A-5, was to provide a more pronounced change in \dot{L} in the gun and a lower initial inductance. A drawing of the electrode with a comparison to the A-4T electrode is shown in Figure (III-24).

Rogowski loop measurements of the current at the flange of the gun indicated the expected increase in rate of current rise, with approximately the same peak currents and subsequent current shape as had been observed previously with the Mod A-4T gun.

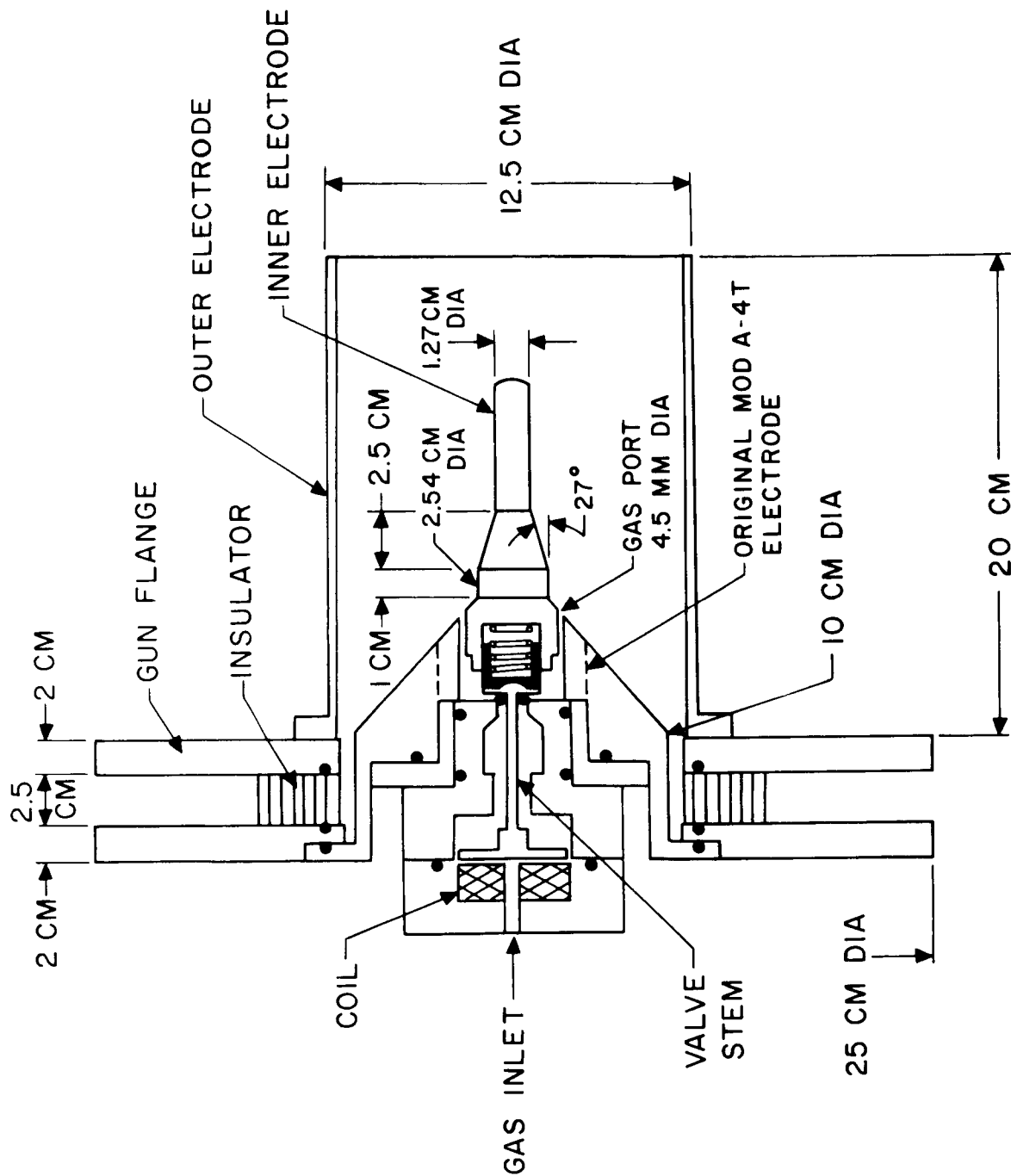
Calorimeter measurements with nitrogen and xenon as the propellants indicated energies of the gun exhaust which were not significantly different from each other but were about 10% higher than the values obtained with the Mod A-4T configuration. The peak calorimetrically measured efficiency was 63% at 3 KV and 45 μ fd.

Thrust and propellant mass flow measurements were made with the engine operated at repetition rates of 10 cps. Overall efficiency, as defined by $T^2/2\dot{m}P$, is plotted vs. I_{sp} ($T/\dot{m}g$) in Figure (III-25). The \dot{m} used in these calculations includes the measured electrode erosion, but is not adjusted for the unutilized mass entering the gun after discharge.

It should be noted that the performance of the engine with xenon is a significant improvement over that observed with nitrogen for both this electrode configuration and the original A-4T configuration. Further studies with this gun were temporarily halted to make way for the installation of the electrically triggered, Mod A-6 Accelerator.

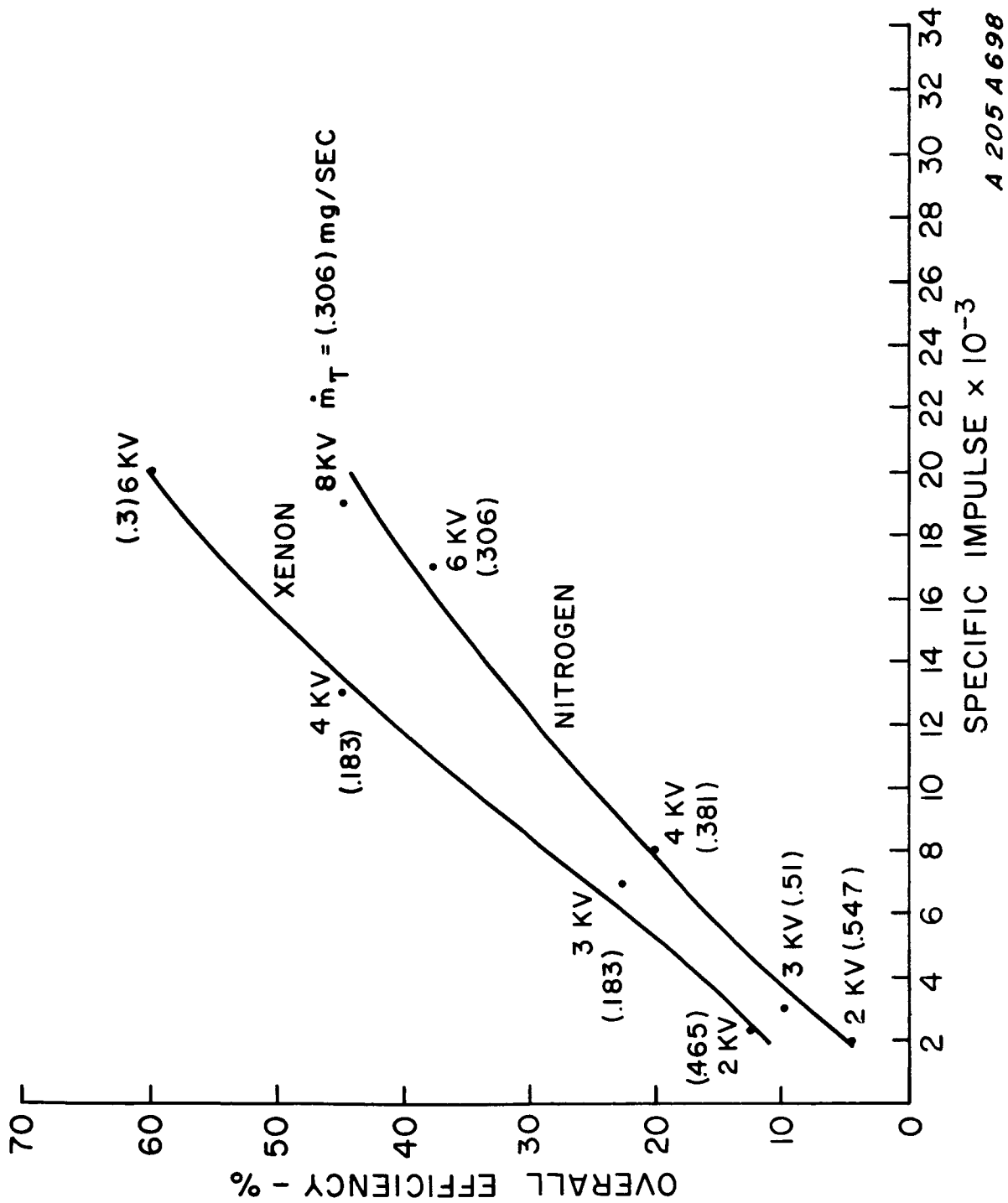
C. PERFORMANCE OF THE MOD A-6 ACCELERATOR - USE OF ELECTRICALLY TRIGGERED OPERATION.

To effect better control of propellant distribution and time of triggering, a first stage consisting of three pairs of trigger electrodes was installed in the Mod A-4T gun. The gun designated as the A-6 is shown in Figure (III-26). Each pair of trigger electrodes was connected across the secondary of a pulse transformer capable of delivering spikes of about 18 KV. The input to the pulse transformer could be variably delayed after actuation of the fast-acting valve.



A 205 A 697

Figure III-24. Drawing of Mod. A-5 Gun.



A 205 A 698

Figure III-25. Overall Efficiency vs. Specific Impulse - Mod A-5 Gun.

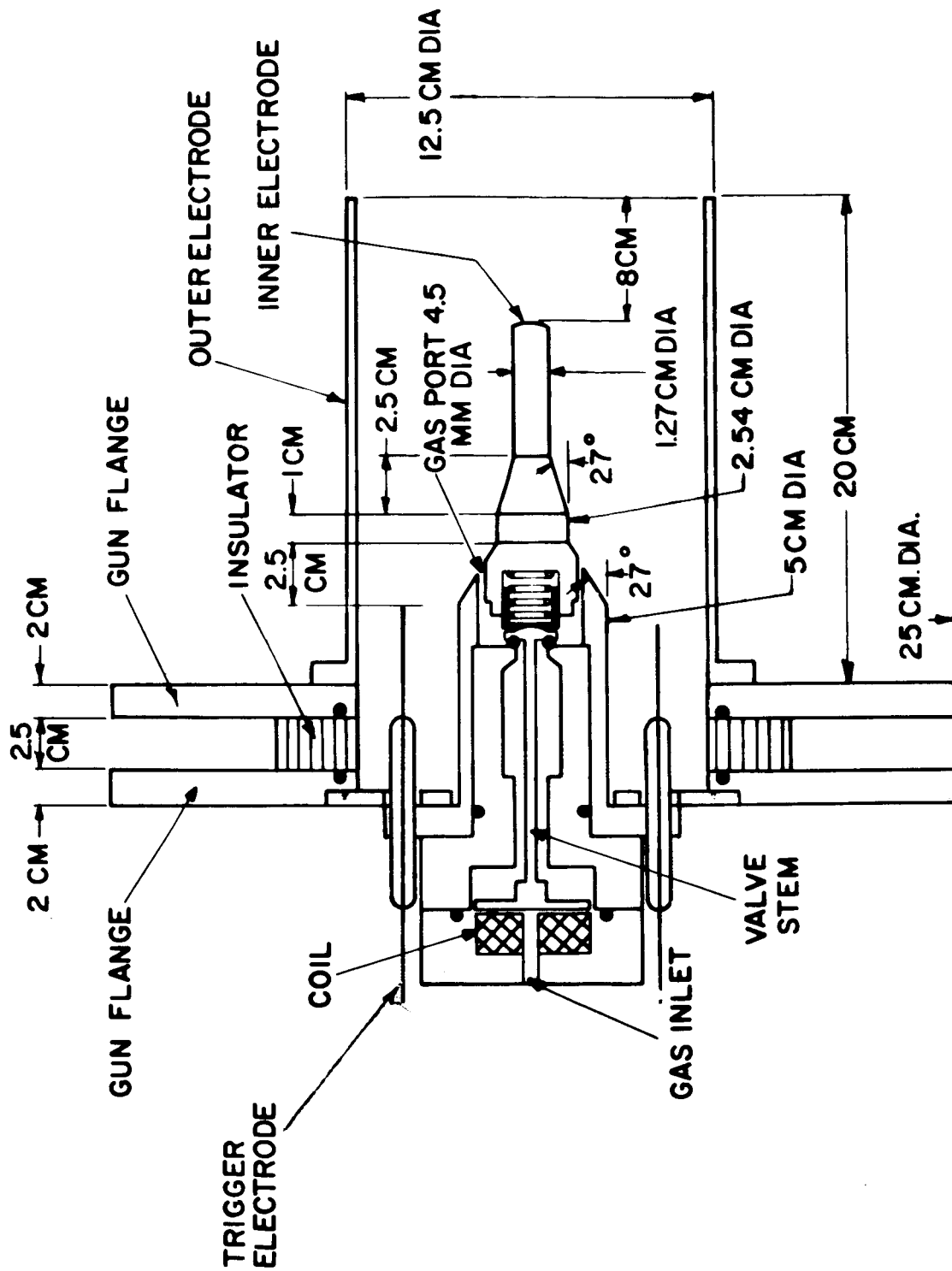


Figure III-26. Drawing of Mod A-6 Gun.

Although self-triggering of the discharge took place at times from 500 - 600 μ sec after valve actuation, depending on gun voltage, the trigger electrodes could be used to cause earlier breakdown at times down to 350 μ sec. Operation in this mode, however, was undesirable, since even more gas was wasted after the discharge. More efficient operation at lower specific impulse requires more mass accelerated per joule of energy input, not less, as in this mode. A different mode of operation is to admit less total gas into the gun so that self-triggering does not occur. In this mode of operation, it was found that the gun could be triggered reliably in a range of delay times from 500 μ sec to 3 milliseconds after valve actuation. This procedure could be carried out at the typical repetition rate of 10 shots per second. Figure (III-27) shows a plot of overall efficiency vs. specific impulse for the range of voltages from 1 to 3 KV, at 45 μ fd. The efficiencies presented are those obtained at delay times found to be the optimum for each voltage and quantity of gas injected. A plot of efficiency vs. delay time is shown in Figure (III-28). It is interesting to note that the 1 millisecond delay time found to be optimum is the same as that determined by the gas density probe studies to provide a maximum amount of gas in the gun. The quantity of gas used in the two-stage, triggered runs was the minimum amount which could be used consistent with reliable operation of the gun. This amount was found to be as little as 10% of that used for self-triggered operation, and accounted for the bulk of the increase in efficiency and specific impulse, since the thrusts measured did not vary greatly from the values measured earlier. A most important area of operation was not examined during these runs. This is the mode of operation where a quantity of gas just short of the self-triggering quantity is used. This would have provided greater loading of the gun than had been achieved earlier, with resulting higher efficiencies at lower specific impulse. A second area that was not examined involves the use of heavier propellant (xenon) with triggered operation to help achieve the same goal.

Eventual coating of the insulators around the trigger electrodes and consequent unreliable operation of the first stage necessitated redesign of the electrodes. At this point, it was decided to incorporate a number of design improvements which had suggested themselves.

D. MEASUREMENTS WITH A MODIFIED INJECTOR NOZZLE GEOMETRY (MOD A-7 GUN).

In line with the necessity for increasing the mass utilization of the gun by increasing the emptying time of the injector nozzles, a new nozzle geometry was adopted. The annular geometry of the Mod A-7 gun, shown in Figure (III-29), had approximately four times the conductance of the Mod A-4T nozzles, also shown in Figure (III-29). Overall efficiency vs. specific impulse using nitrogen propellant in the gas-triggered mode is plotted

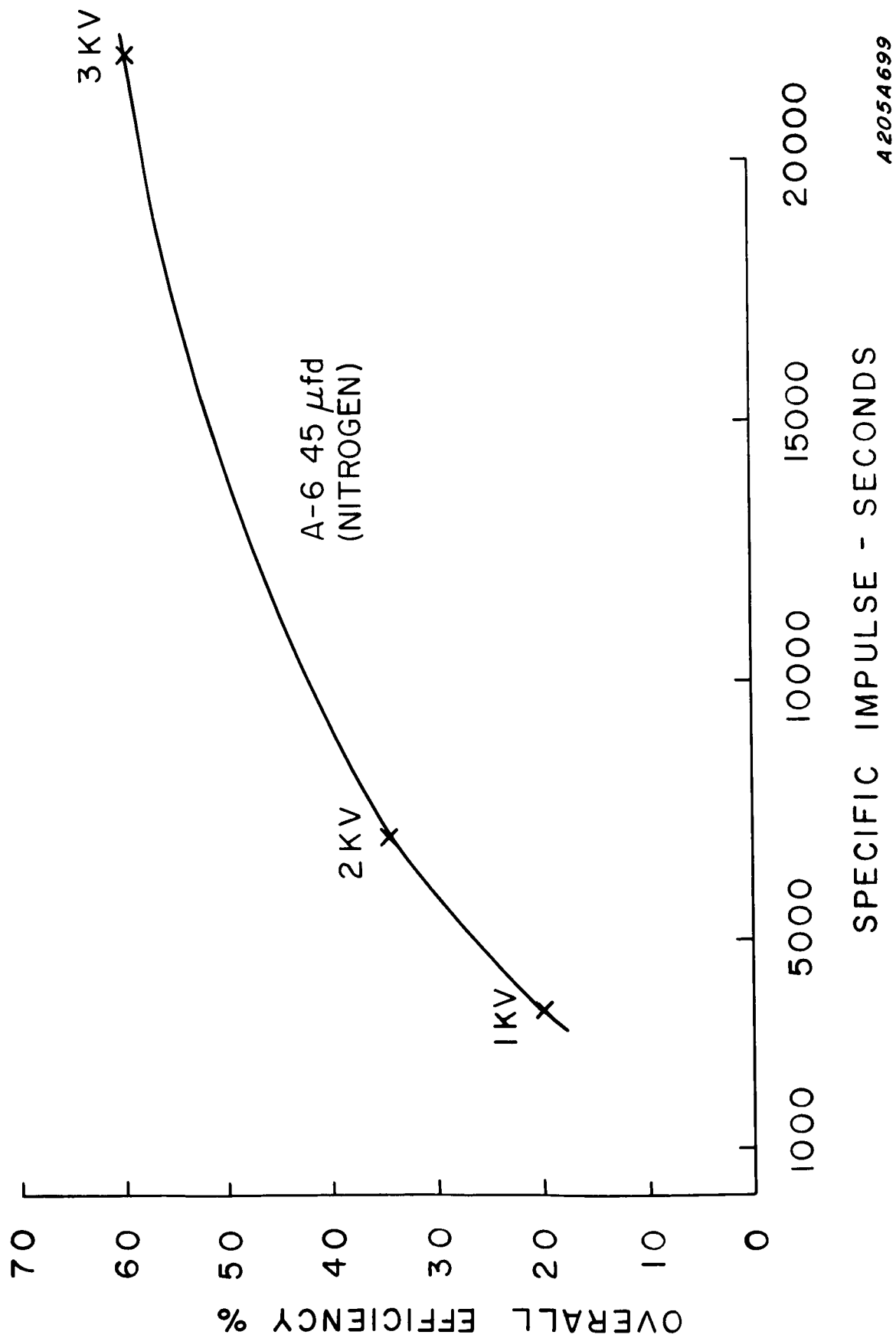


Figure III-27. Overall Efficiency vs. Specific Impulse - Mod A-6 Gun.

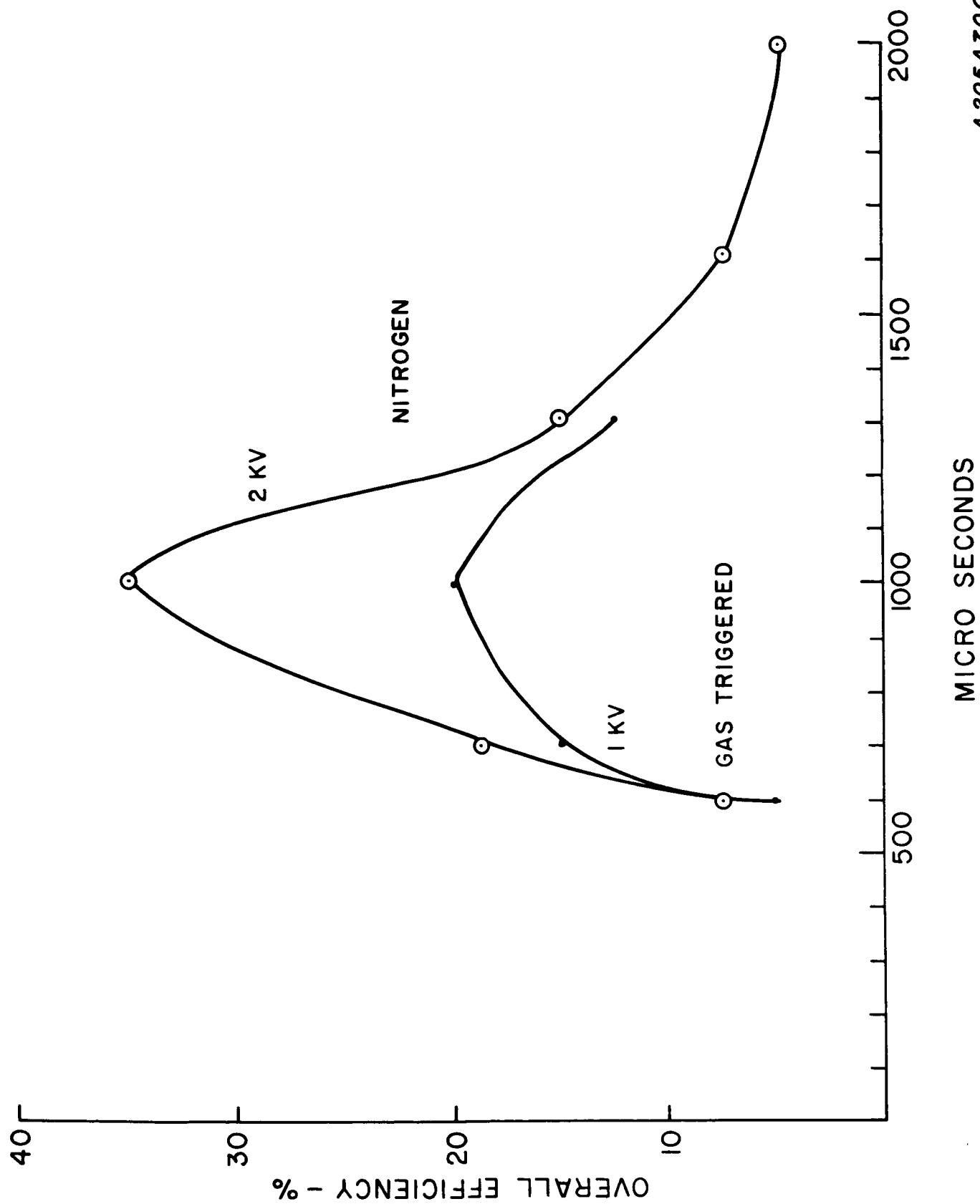
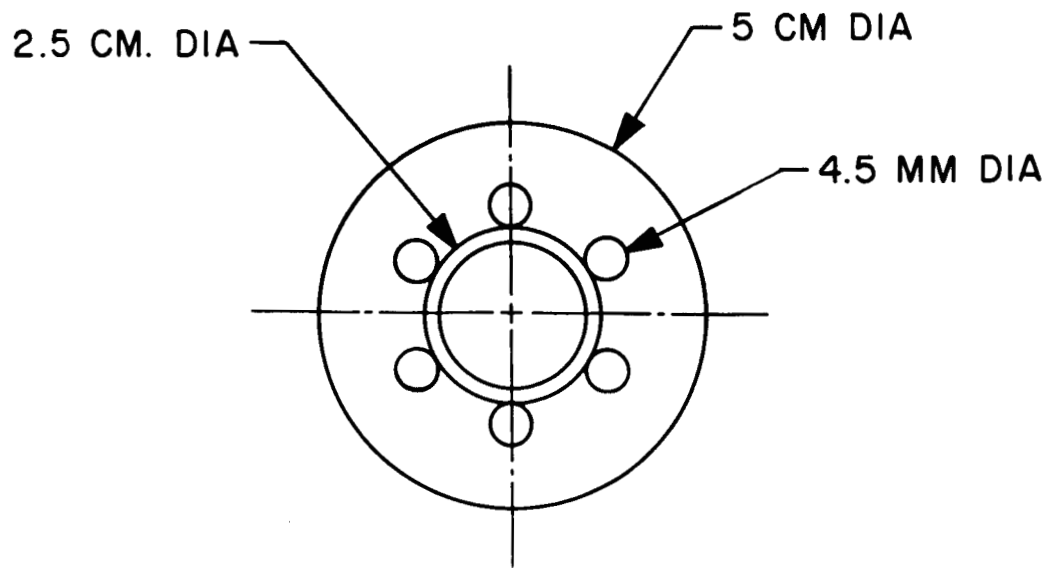
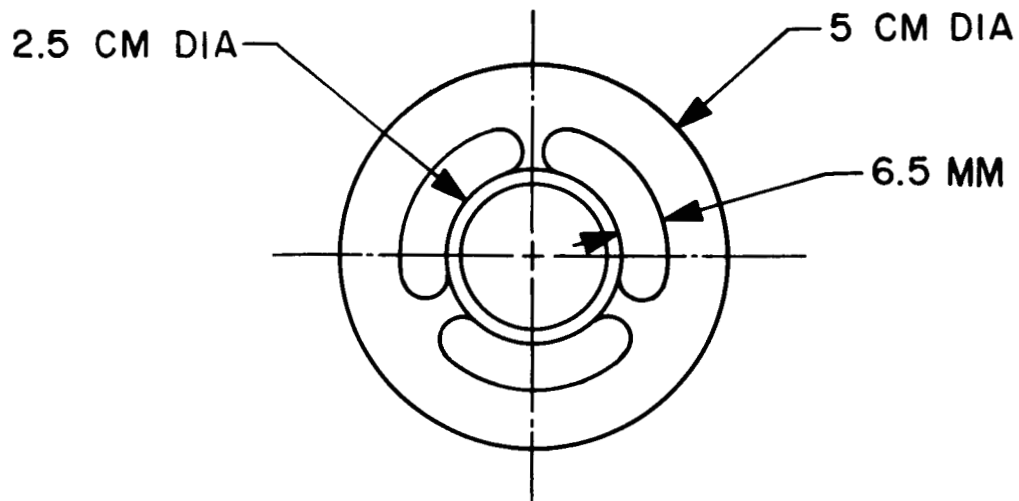


Figure I II-28. Overall Efficiency vs. Delay After Valve Actuation, Mod A-6, 45 μ fd.



CIRCULAR PORT GEOMETRY -MOD-A-4T



ANNULAR PORT GEOMETRY -MOD-A-7D
A205A701

Figure III-29. Drawing of Mod A-4T and Mod A-7 Gun Nozzles.

in Figure (III-30). It is to be noted that these efficiencies are appreciably greater than those of the Mod A-4T gun at a given gun voltage. In addition, encouraging overall efficiencies are shown in the important specific impulse range of 2000 - 8000 seconds. Further improvement was expected from triggered operation.

E. THE A-7D ACCELERATOR - OPERATION IN THE ELECTRICALLY-TRIGGERED MODE WITH 45 μ fd CAPACITANCE.

E.1 Performance Measurements

Simultaneous thrust balance and propellant input flow measurements were made on a Mod A-7D engine with the electrode configuration shown in Figure (III-31). The engine was operated using xenon and nitrogen propellant, at a pulse repetition rate of 10 c.p.s., and with a bank capacitance of 45 μ fd at voltages ranging from 900 V to 2000 V.

The first-stage trigger electrodes were fired at various delay times ranging from 0.55 to 1.0 milliseconds after actuation of the fast-acting valve to provide longer delay times than those previously obtained with the gas-triggering mode (0.45 - 0.50 milliseconds). The propellant mass injected ranged from 20 - 60% of that required for gas-triggering.

The results of this mode of operation are shown in Figure (III-32). Overall efficiency is plotted vs. specific impulse, where $\eta_o = T^2 / 2 \dot{m} P_{in}$ and $I_{sp} = T / \dot{m} g$.

The propellant mass \dot{m} used in the various runs is shown in Figure (III-32) for the individual performance points. The contribution of erosion to \dot{m} was negligible since weighing of the electrode after 250,000 shots indicated an erosion rate of less than 0.25 gms per shot, about 2% of the typical injected propellant mass.

E.2. Propellant Distribution Measurements

Two types of measurements were performed, both on the A-7D electrode configuration while in its position on the thrust stand. One set of measurements

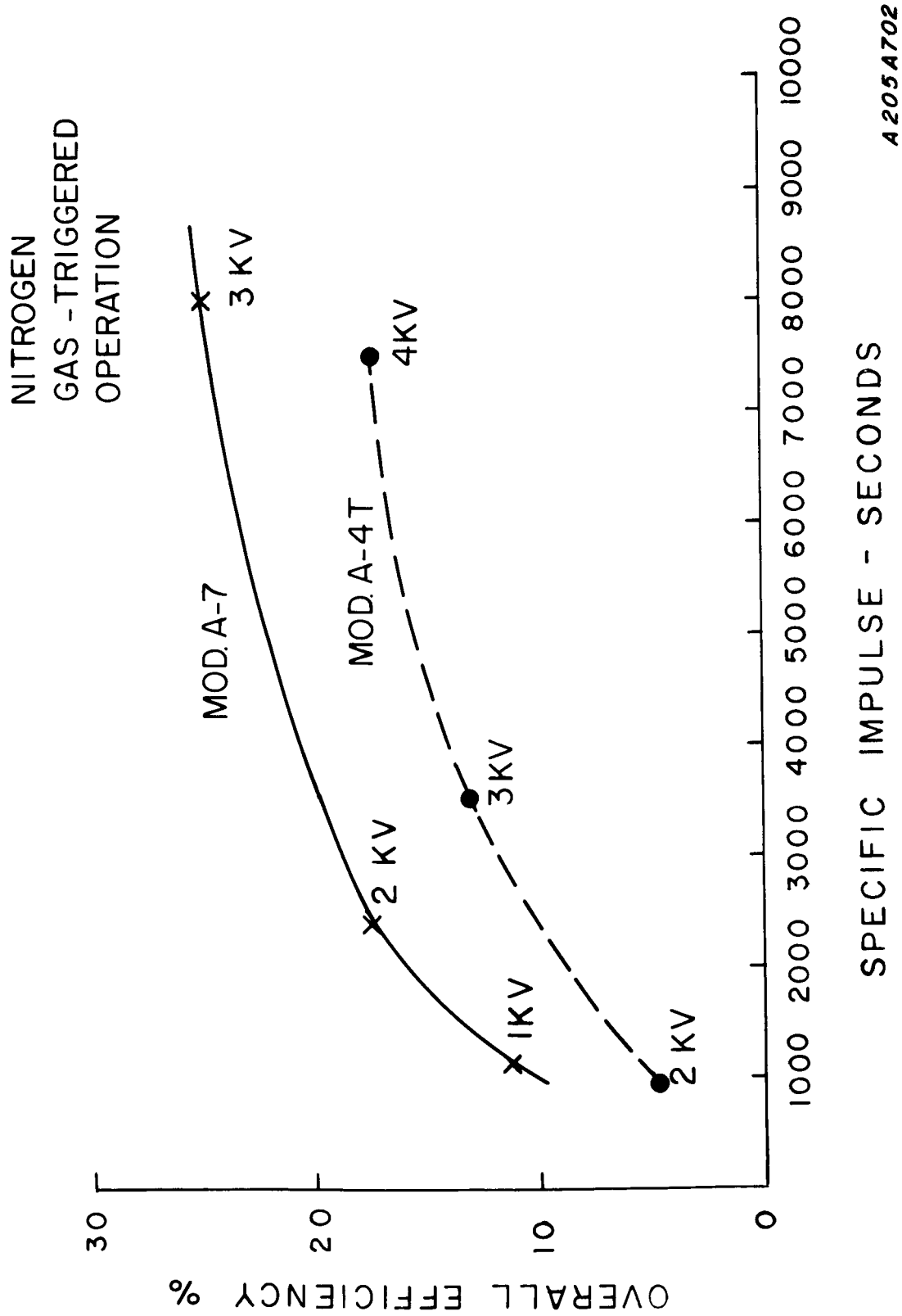


Figure III-30. Overall Efficiency vs. Specific Impulse - Mod A-7 Gun. Gas-Triggered Operation.

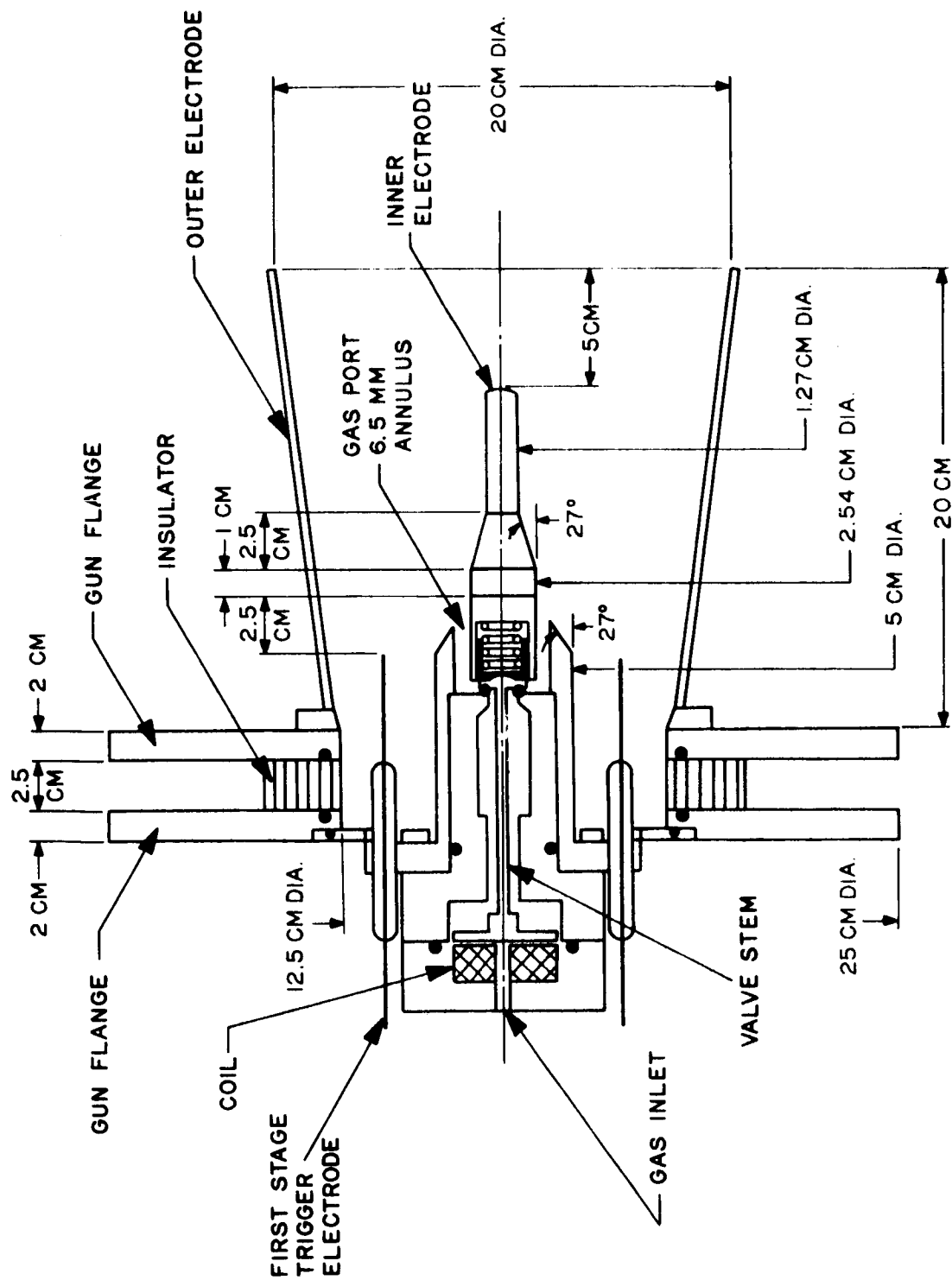


Figure III-31. Two-Stage Mod A-7D Engine

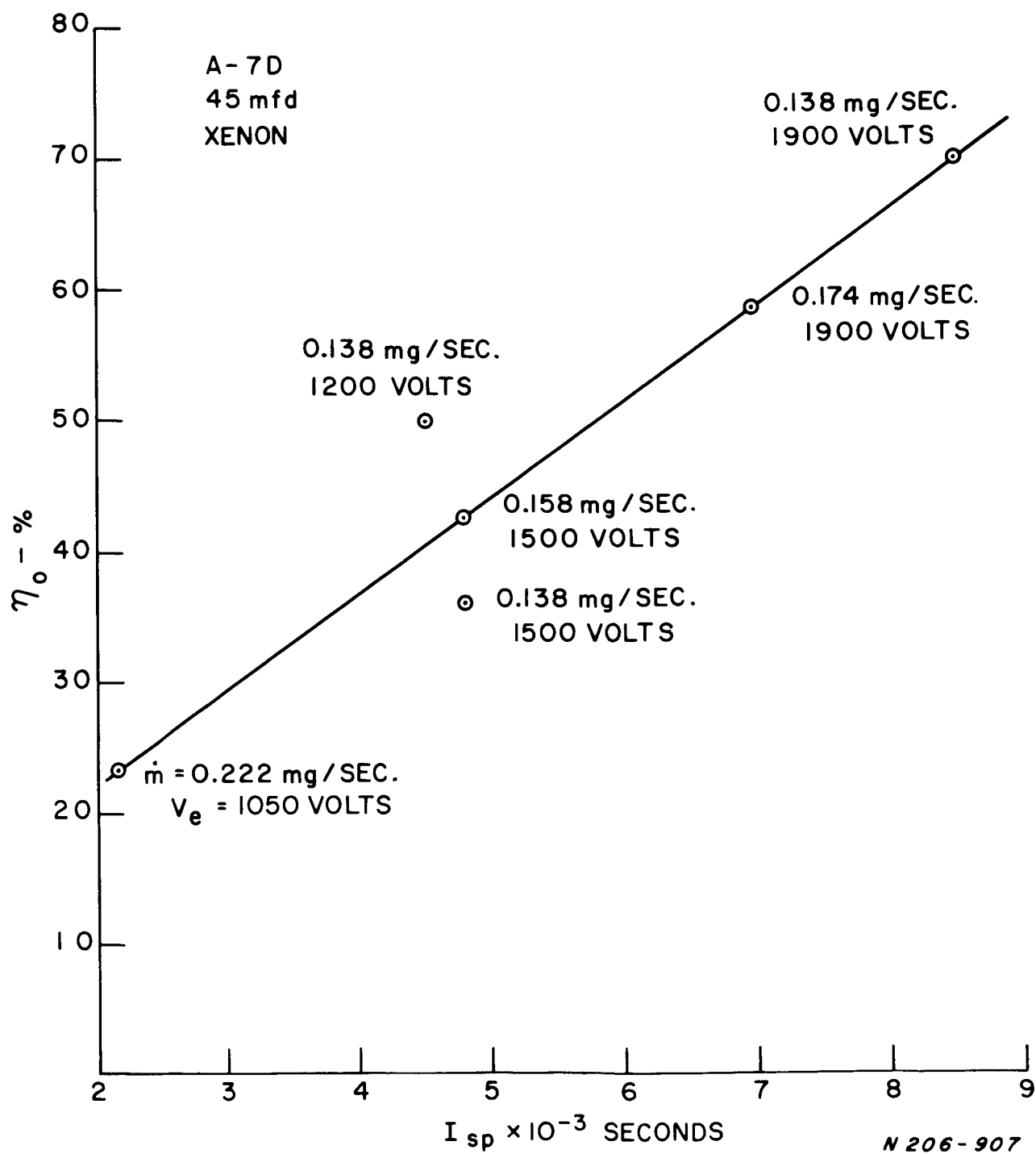


Figure III-32. Performance of the A-7D Accelerator.

was of the pressure immediately in front of the feed nozzles as a function of time. The gauge position was intended to intercept the overwhelming bulk of the propellant leaving the part of the nozzle in front of it. In only this way could the probe trace be representative of all the gas entering the gun. Unfortunately, a small wobble in the rack and pinion assembly which held the probe made return to this critical position very difficult without opening the vacuum tank. Thus, once this position was set, all measurements were taken without moving the probe. Measurements were performed for xenon and nitrogen over a wide variety of valve capacitor voltages. Integration of the resulting pressure vs. time curves allowed determination of the propellant fraction that had left the feed nozzles as a function of time (using the procedure in Appendix B). Figure II-10 shows a curve of how the maximum xenon propellant fraction that had entered the gun increased with valve capacitor voltage. The details of this dependence were not investigated at this time because the valve voltage required was fixed at a relatively low value by the gun capacitance and gun voltage then in use. Using the valve voltages then considered typical, the propellant fraction that had left the feed nozzles as a function of time since valve actuation is shown on Figures (III-33 and III-34) for xenon and nitrogen for 4400 volts on the valve capacitor. The propellant fraction that had left the gun muzzle at any given time could be determined from the data obtained from a propellant density survey. This procedure is described in Appendix B and its result is shown on Figures (III-33 and III-34). Finally, the fraction of the injected gas within the active regions of the gun can be determined from the difference between the solid curves in the above figures. This difference is also shown there. In Figures III-33 and III-34, the propellant fraction within the accelerator does not include additional gas between the muzzle and a plane 5 cm away from the muzzle which measurements of extended currents indicated to be available to the discharge. However, this gas has been included in the values shown in Figure II-10.

The second type of measurement, the detailed propellant density survey was also obtained for several valve capacitor voltages. Axial symmetry was assumed and pressure vs. time traces were obtained at five radial positions and up to 15 axial positions for each radial position.

Isobars (lines of constant pressure) were drawn directly from this data, Figure (III-35) shows the pressure distribution in this manner for delay times of 0.5, 0.6, 0.8, and 1 millisecond in nitrogen expelled with 4400 volts on the valve capacitor. Figure (III-36) shows isobars in xenon expelled with 3900 volts on the valve capacitor. Similar distributions were observed for nitrogen at 3900 volts and xenon at 4400 volts.

E3. Gridded Probe Measurements

Gridded probe measurements have been made with a multi-gridded electrostatic probe (see section II and Figure III-37). This probe was a

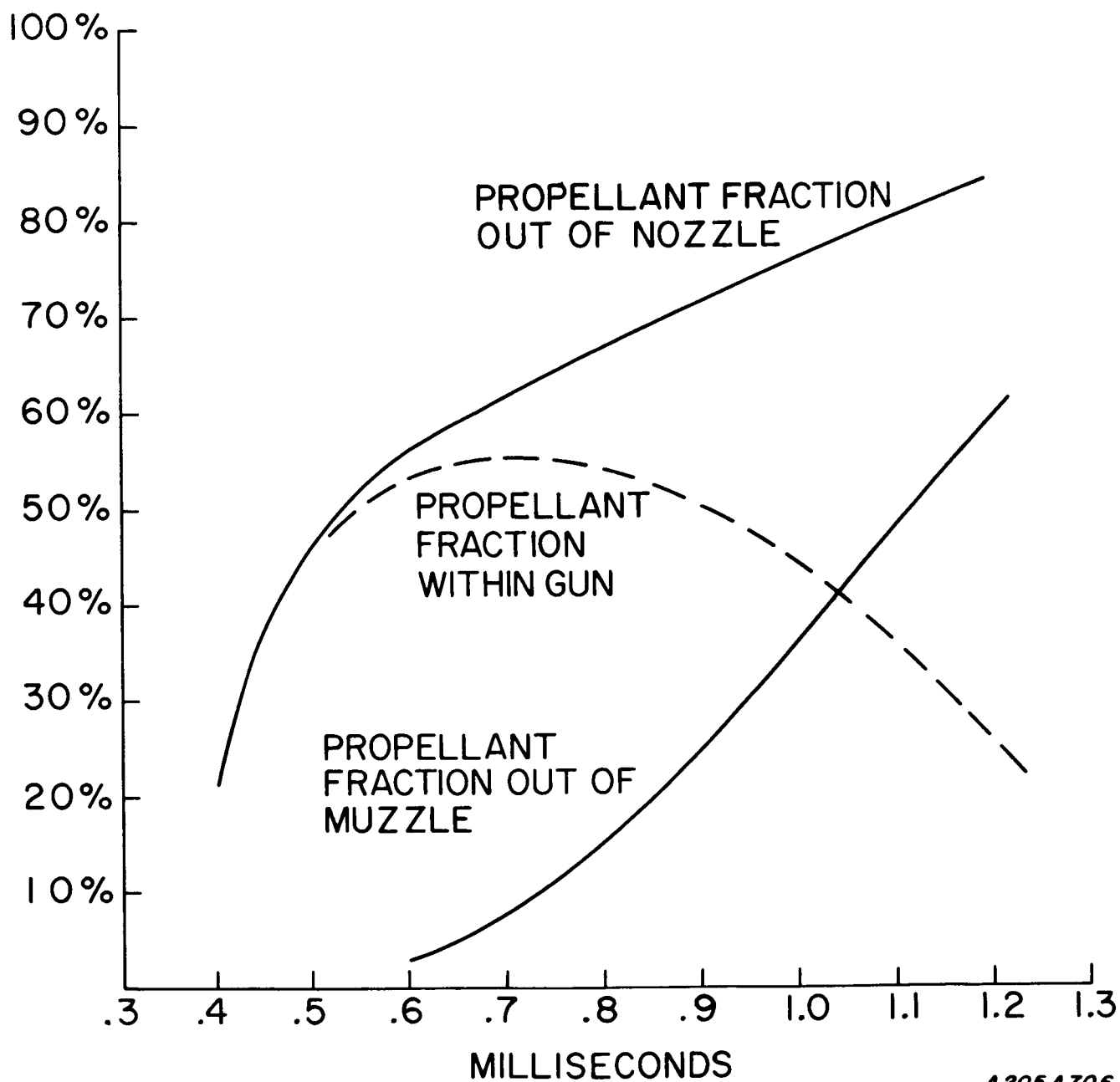
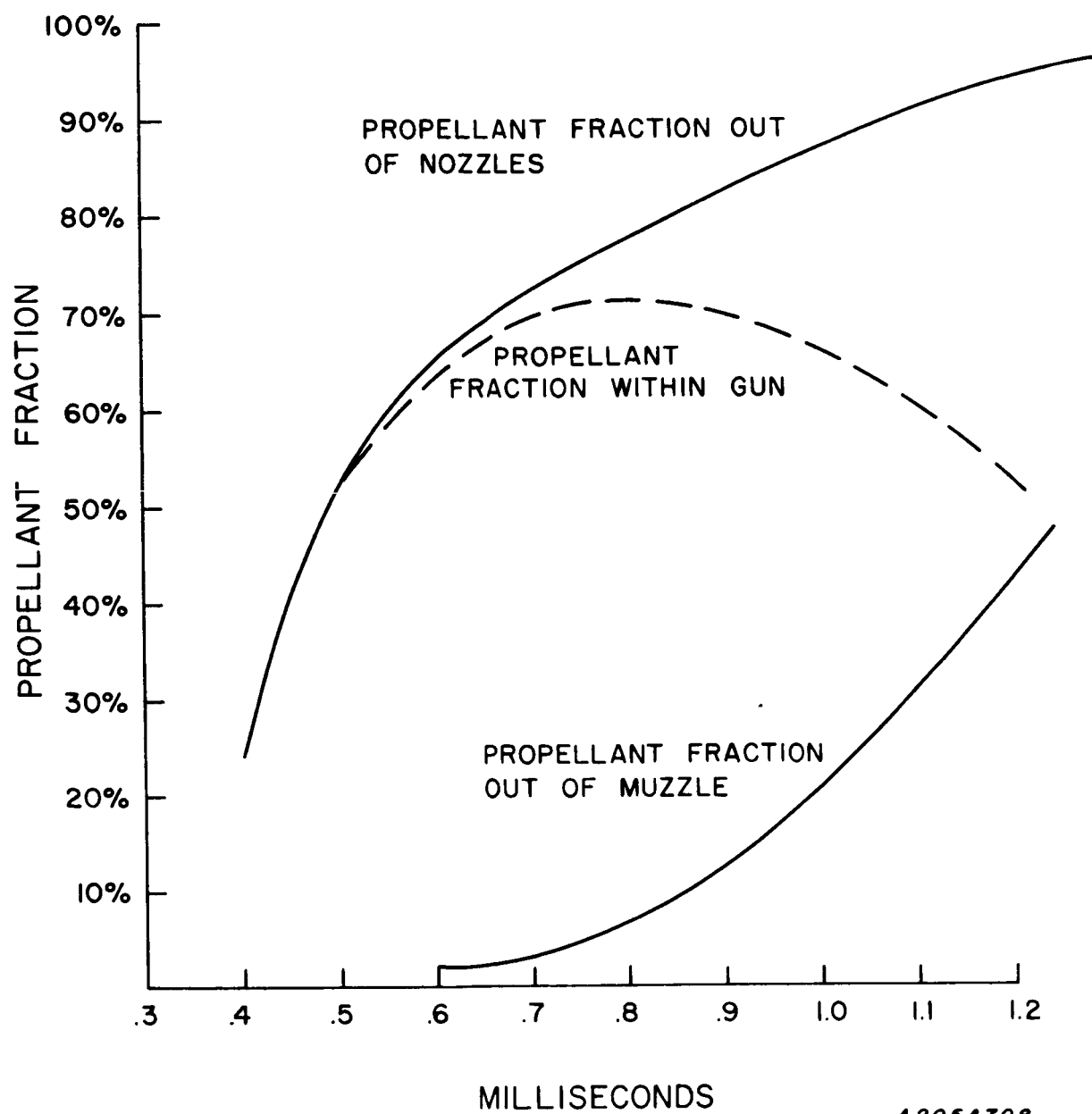


Figure III-33. Propellant Fraction Curves A-7D, Xe, 4400 Valve Voltage.



A205A708

Figure III-34. Propellant Fraction Curves A-7D, N_2 , 4400 Valve Voltage.

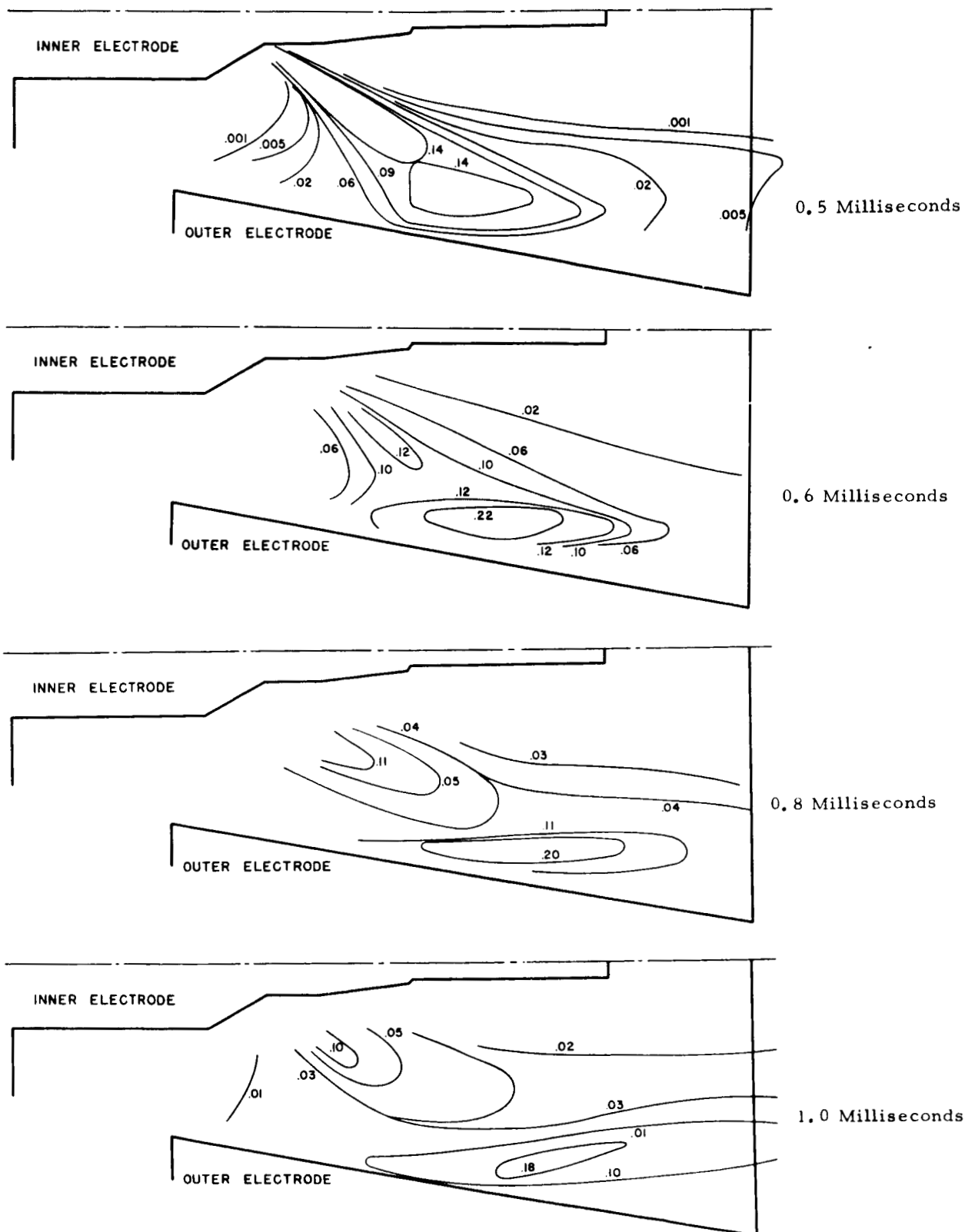
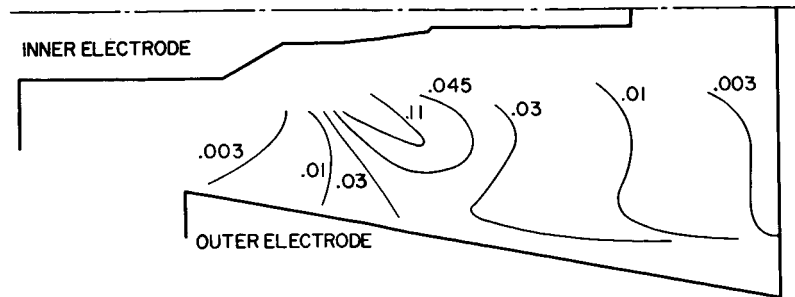
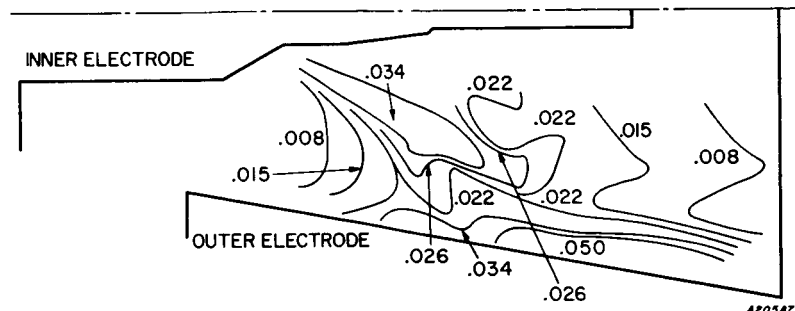


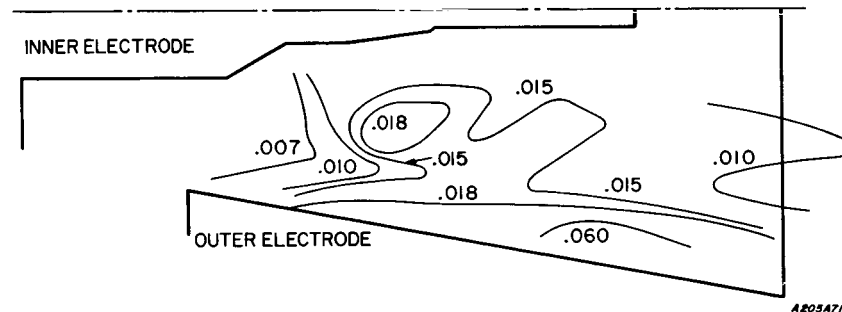
Figure III-35. Isobars, A-7D Nitrogen, Valve: 4400 Volts



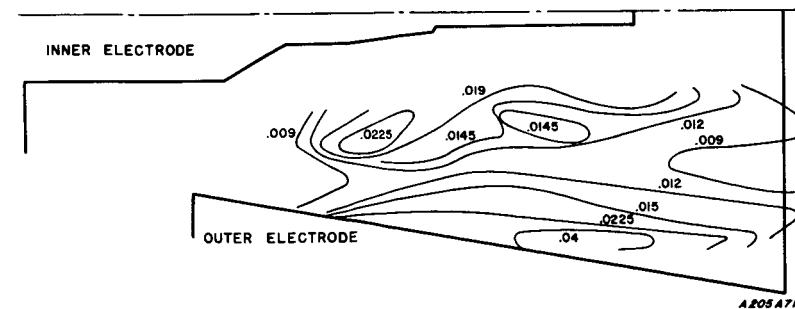
0.5 ms.



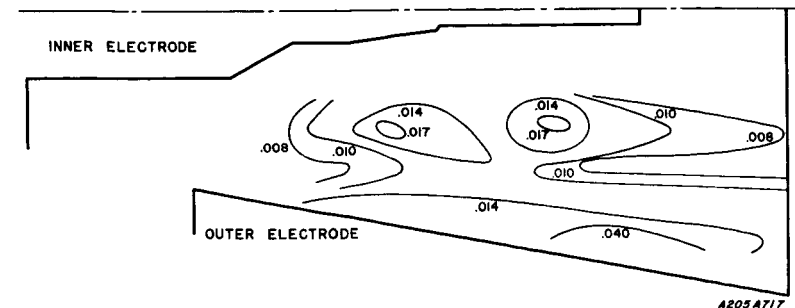
0.6 ms.



0.8 ms.



1.0 ms.



1.2 ms.

Figure III-36. Isobars, Xenon, Valve: 3900 Volts.

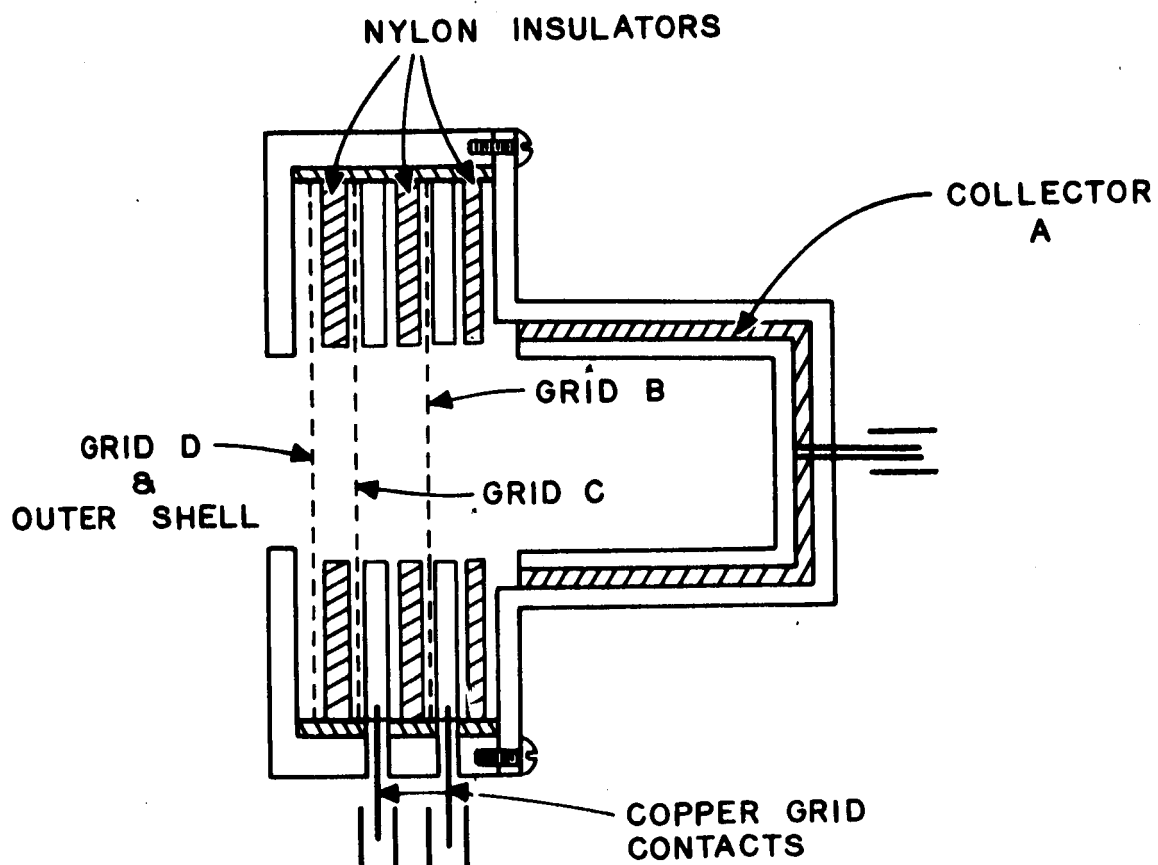


Figure III-37. Gridded Probe for Measurement of Ion Energies

forerunner of that shown in Figure II-19. It contained one less grid and did not employ the inverted cone to improve charge collection characteristics. The initial data were obtained with nitrogen. The analysis for the interpretation of these data was also given in section II .

Initial experiments were directed toward determination of the plasma potential by variation of the voltage reflecting the electrons or that reflecting the ions. Both of these studies indicated a plasma potential of approximately -5.0 volts. One might qualitatively expect this since the center gun electrode is generally negative and the outer electrode at ground, causing space potential to be somewhere in between, but nearer to ground, the potential of the vacuum tank walls.

A sample of the information obtained with nitrogen is shown in Figures (III-38-42). Each figure represents the velocity distribution in various energy ranges of the bulk of the ions collected by the probe under a given set of operating conditions. Note that doubly and triply ionized nitrogen species ($z = 2$, $z = 3$) represent a substantial fraction of the exhaust.

Thrust and mass flow measurements obtained under the same conditions give an overall efficiency and I_{sp} . If the \bar{v} is corrected for the amount of gas actually within the gun at the time of firing ($\sim 70\%$), an average ion velocity can be established and is listed on Figures (III-38-41). A rough determination of the average ion velocity from an integration of gridded probe data is also listed on each caption. The degree of agreement tended to corroborate the thrust and mass flow measurements.

Similar confirmation has been seen on several other runs, including when the probe is placed in an off-axis position (see Figure III-42).

E. 4. Current Measurements Outside of the A-7D Accelerator.

A Rogowski loop current probe (described in section II) was used to examine currents outside of the A-7D accelerator when a capacitance of $45 \mu\text{fd}$ was used. The integrated current waveforms obtained with the loop are shown in Figure (III-43). The average current density distribution across the muzzle at a point 5 cm downstream from the accelerator is plotted in Figure (III-44). The magnitude and shape of the distribution are not significantly different from that obtained with a capacitance of $144.5 \mu\text{fd}$.

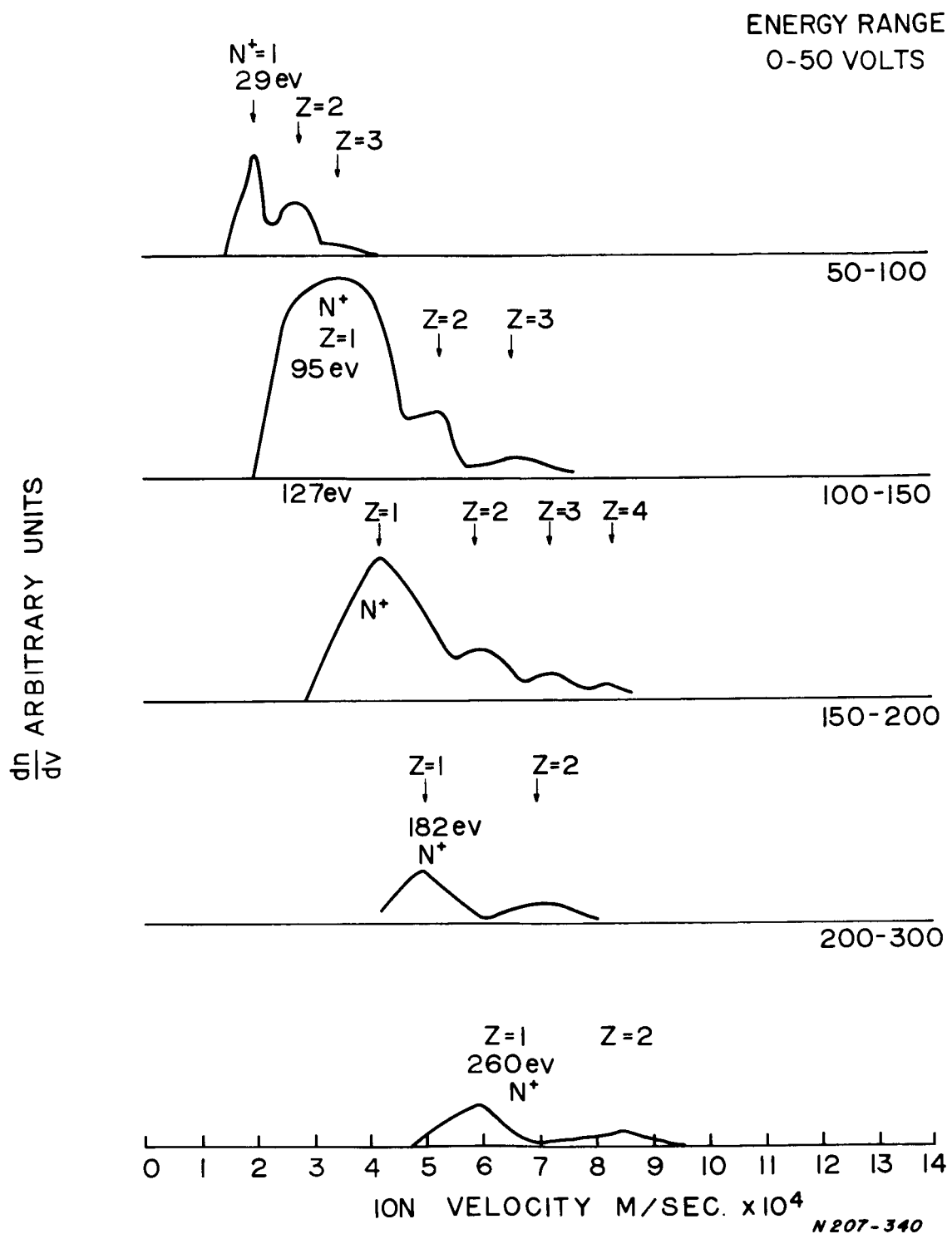


Figure III-38. Ion Velocity Distribution A-7D Gun, Various Stopping Potentials, Nitrogen 2 KV, 425 μ fd, .65 ms delay, 33 μ gm/Shot.
 Thrust based $\bar{v} = 4.3 \times 10^4$ m/sec
 Gridded probe based $\bar{v} = 4.5 \times 10^4$ m/sec

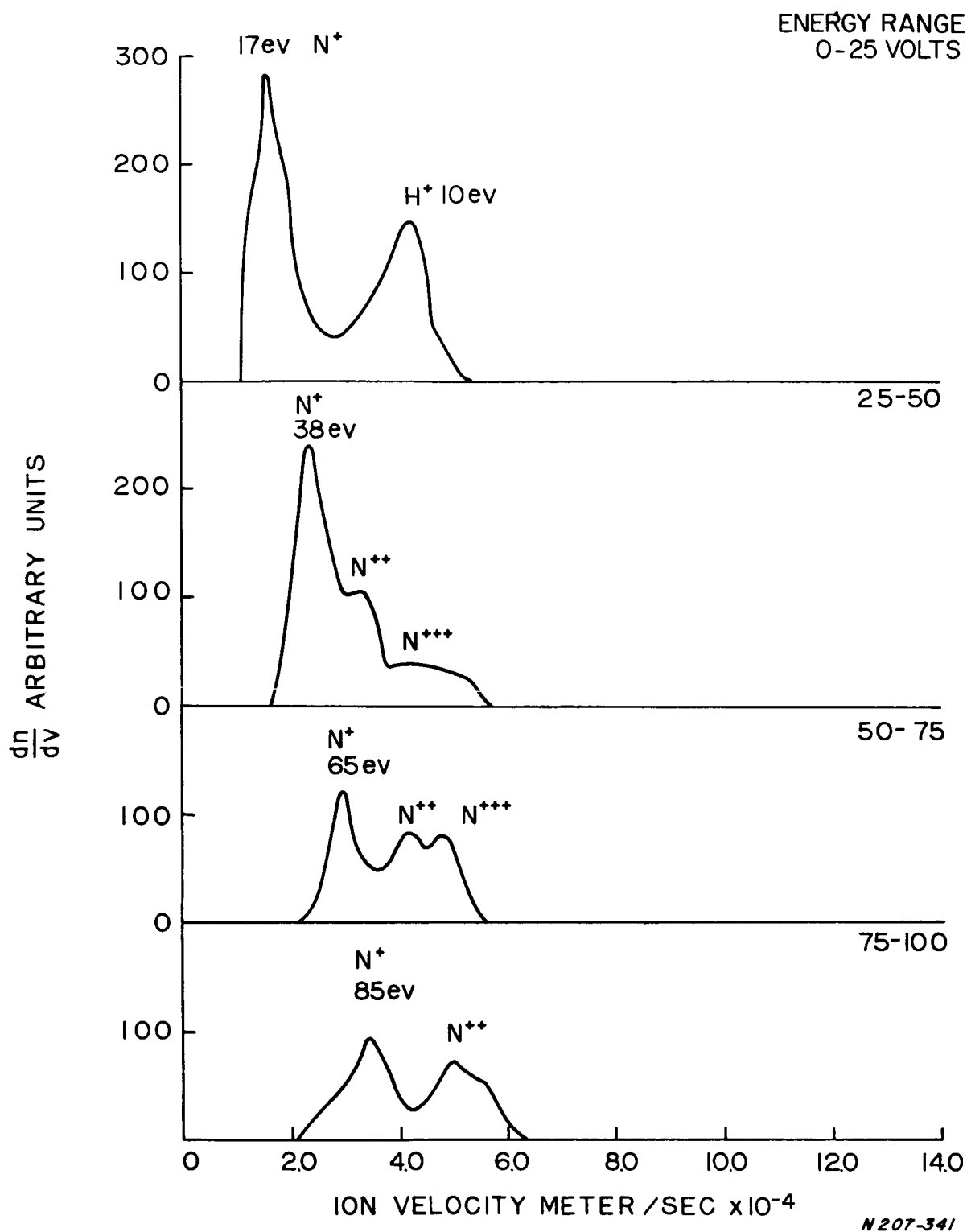


Figure III-39. Ion Velocity Distribution A-7D Gun, 0-100V Stopping Potentials, Nitrogen 1.5 KV, 42.5 μ fd, .65 ms delay, 33 μ gm/Shot
 Thrust based $\bar{v} = 3.2 \times 10^4$ m/sec
 Gridded probe based $\bar{v} = 3.65 \times 10^4$ m/sec

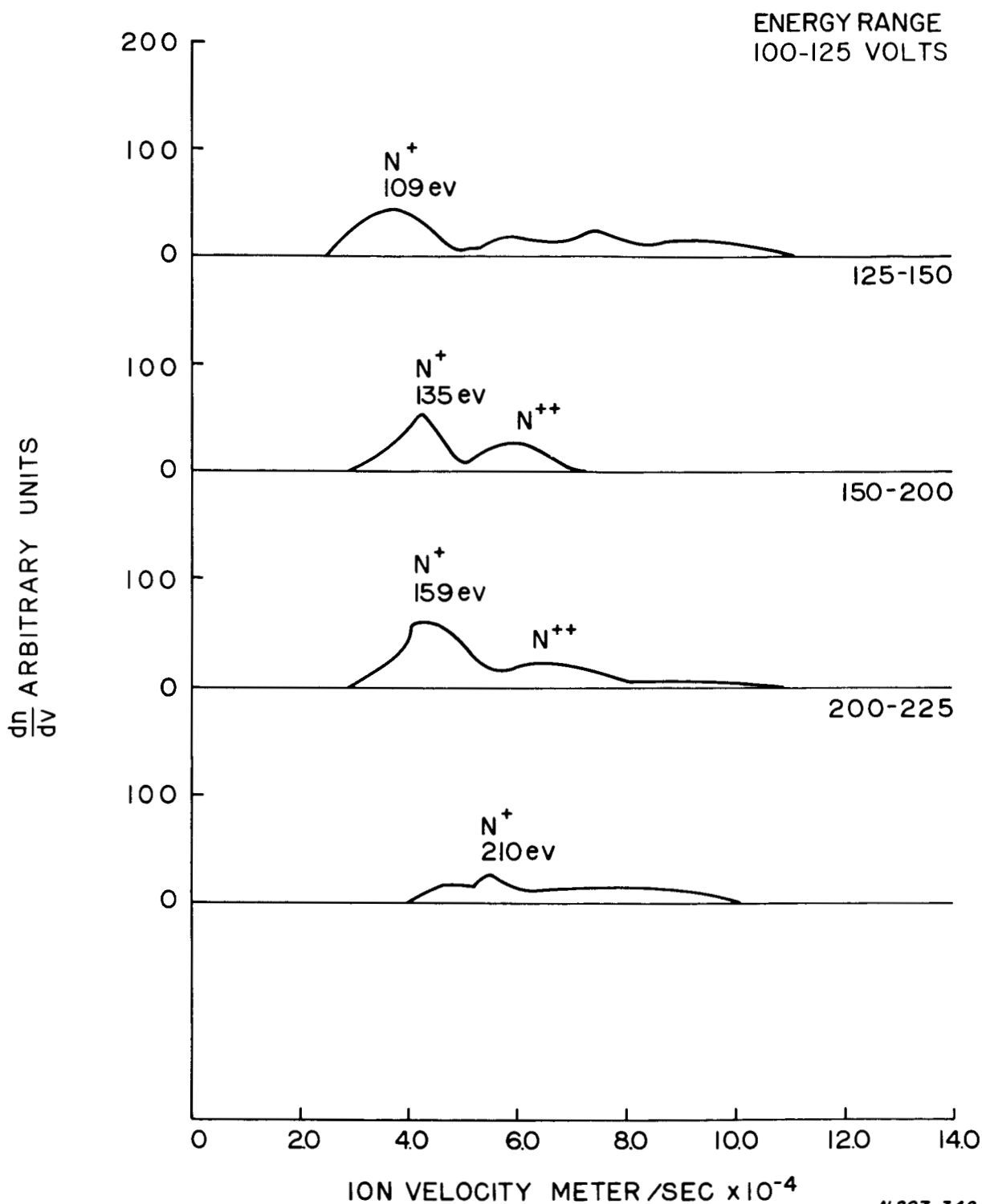


Figure III-40. Ion Velocity Distribution A-7D Gun, 100-225 V **Stopping Potentials**, Nitrogen, 1.5 KV, 42.5 μ fd, .65 ms delay, 33 μ gm/shot.
 Thrust based $\bar{v} = 3.2 \times 10^4$ m/sec
 Gridded probe based $\bar{v} = 3.65 \times 10^4$ m/sec

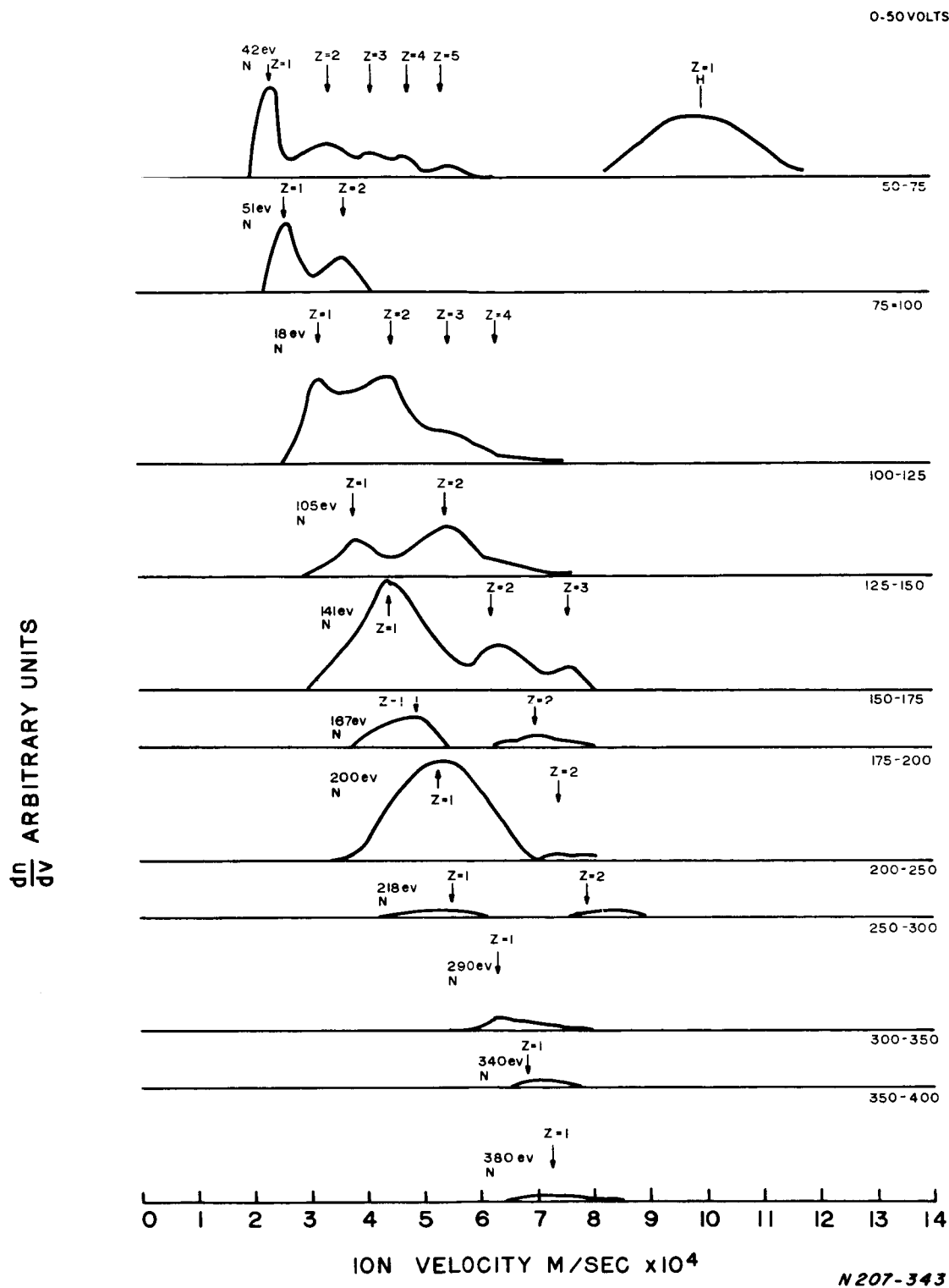


Figure III-41. Ion Velocity Distribution A-7D Gun, Nitrogen 2 KV, 42.5 μ fd.
 Gas-Triggered Operation 60 μ gm/shot
 Thrust based $\bar{v} = 4.7 \times 10^4$ m/sec
 Gridded probe based $\bar{v} = 4.7 \times 10^4$ m/sec

A7D GUN AT 2KV, 50-100 VOLTS, .65 ms DELAY 30 μ gm / SHOT, N₂

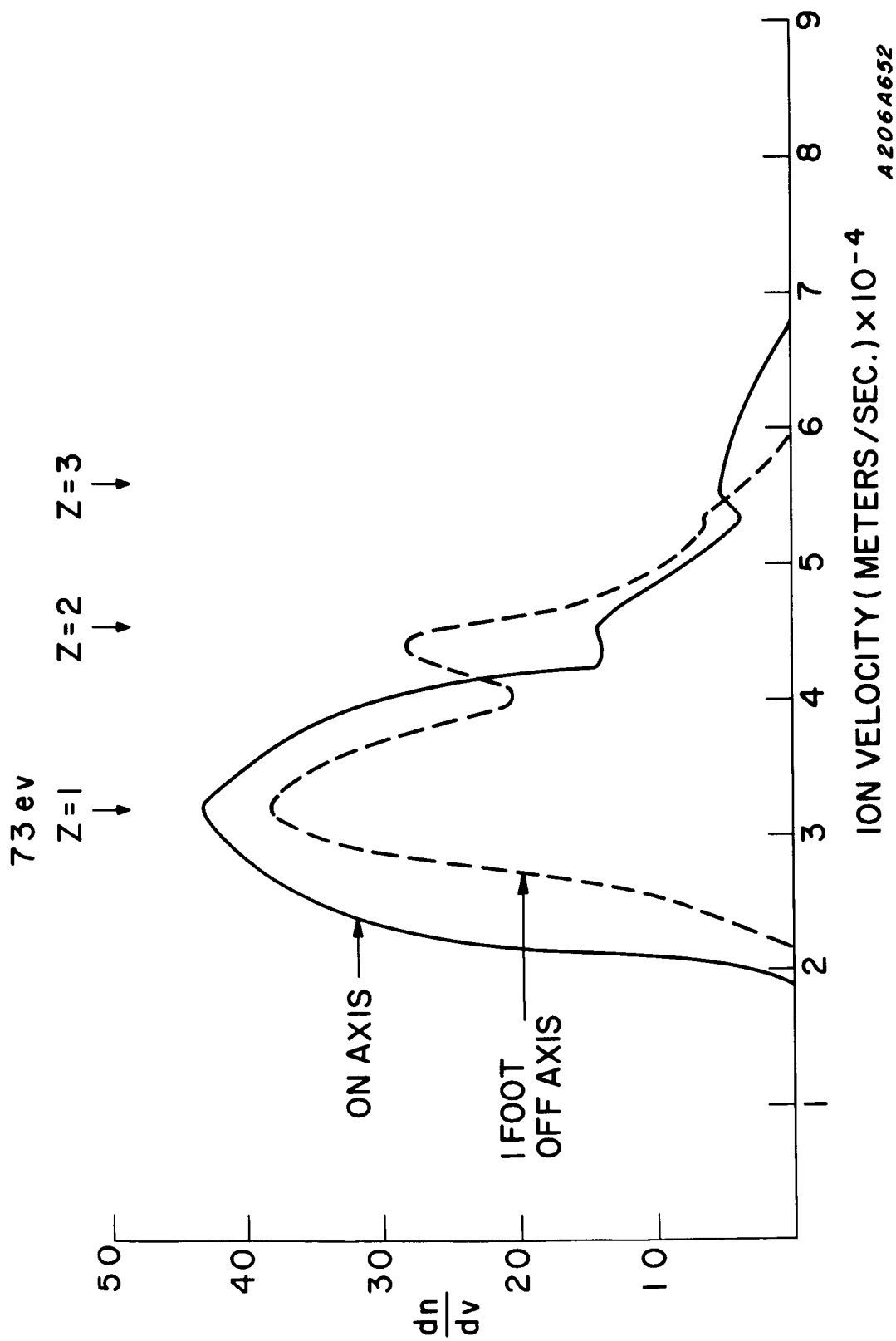
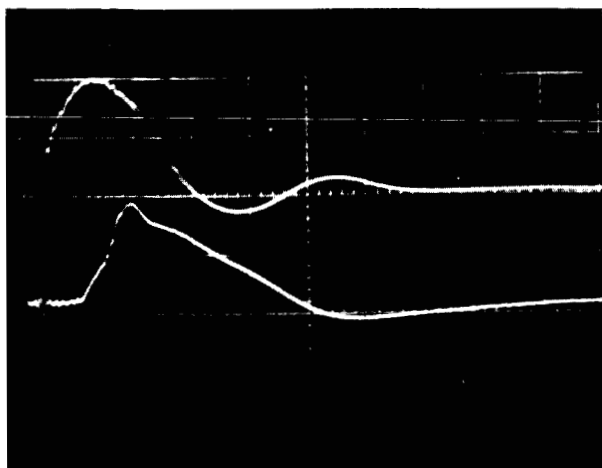


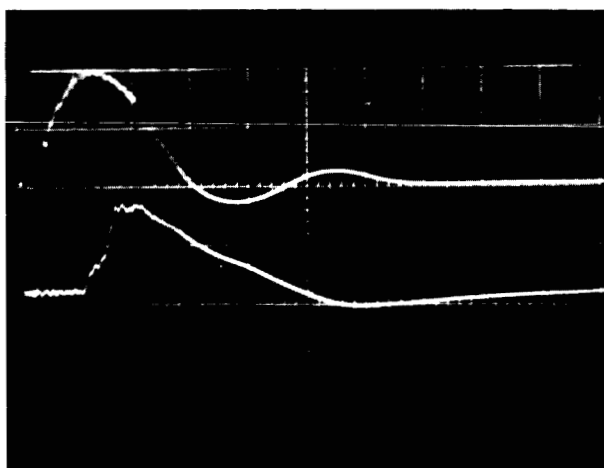
Figure III-42. Velocity distribution of Ions in Exhaust of A-7D Gun at 2 KV, 42.5 μ fd, On and Off Axis

$z = 5 \text{ cm}$ $r = 0 \text{ cm.}$



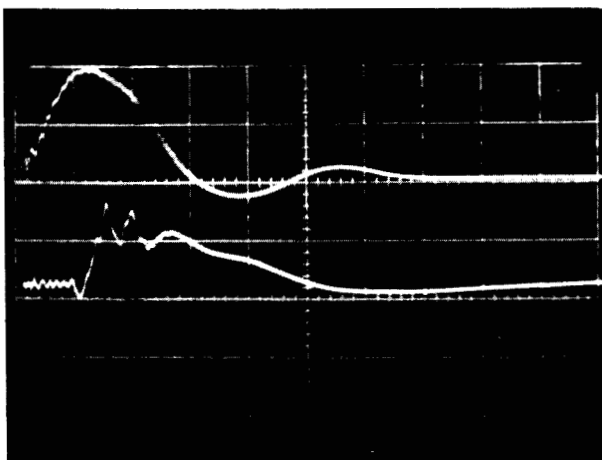
Upper trace - Ampl.: 22.4 K amps/cm.
Sweep: 2 usec/cm.
Lower trace - Ampl.: 3 K amps/cm.
Sweep: 2 usec/cm.

$z = 5 \text{ cm}$ $r = 2.5 \text{ cm.}$



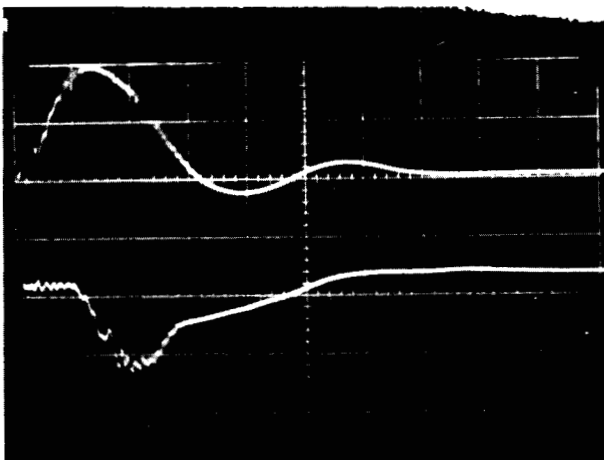
Upper trace - Ampl.: 22.4 K amps/cm.
Sweep: 2 usec/cm.
Lower trace - Ampl.: 3 K amps/cm.
Sweep: 2 usec/cm.

$z = 5 \text{ cm}$ $r = 5 \text{ cm}$



Upper trace - Ampl.: 22.4 K amps/cm.
Sweep: 2 usec/cm.
Lower trace - Ampl.: 1.2 K amps/cm.
Sweep: 2 usec/cm.

$z = 5 \text{ cm}$ $r = 7.5 \text{ cm.}$

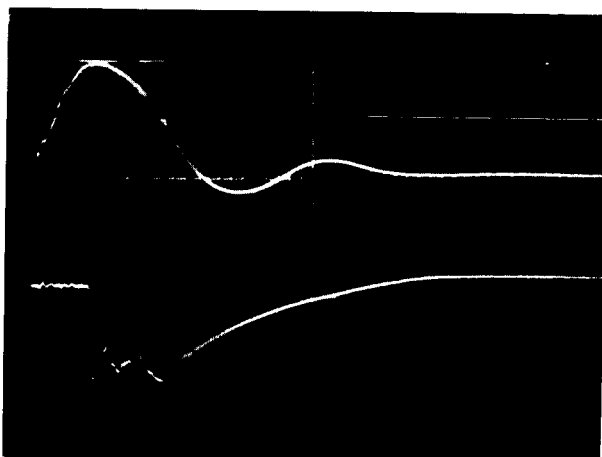


Upper trace - Ampl.: 22.4 K amps/cm.
Sweep: 2 usec/cm.
Lower trace - Ampl.: 1.2 K amps/cm.
Sweep: 2 usec/cm.

Upper trace - Integrated discharge current with Rogowski loop between gun flanges.
Lower trace - Integrated current with 7.5 cm diameter Rogowski loop at muzzle
at locations specified.

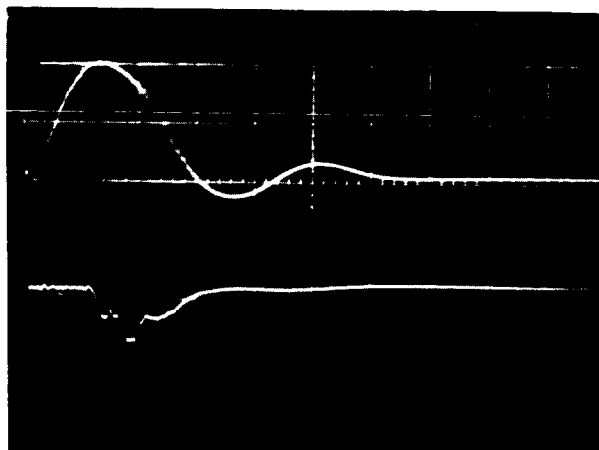
Figure III-43. Rogowski Loop Signals of Currents External to the MOD A-7D Gun, 1.9 KV, 45 μ fd, Xenon Propellant

$z = 5 \text{ cm}$ $r = 10 \text{ cm.}$



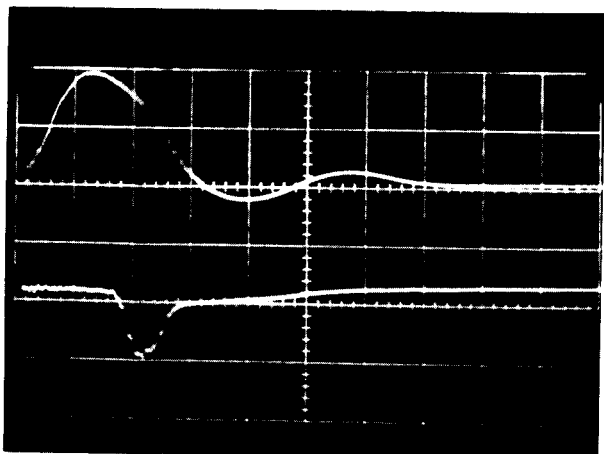
Upper trace - Ampl. : 22.4 K amps/cm.
Sweep: 2 usec/cm.
Lower trace - Ampl. : 1.2 K amps/cm.
Sweep: 2 usec/cm.

$z = 5 \text{ cm}$ $r = 12.5 \text{ cm.}$



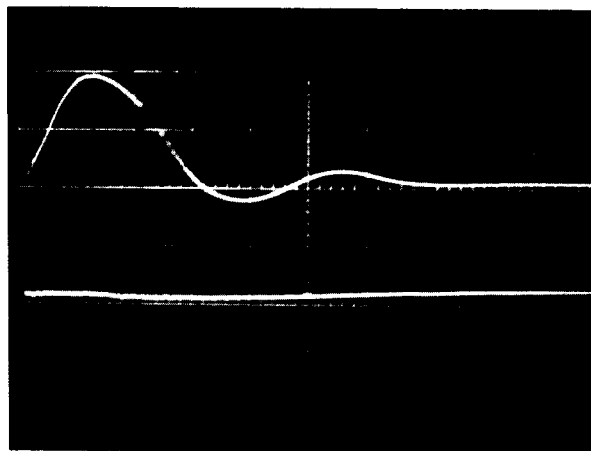
Upper trace - Ampl. : 22.4 K amps/cm.
Sweep: 2 usec/cm.
Lower trace - Ampl. : 1.2 K amps/cm.
Sweep: 2 usec/cm.

$z = 5 \text{ cm.}$ $r = 13.75 \text{ cm.}$



Upper trace - Ampl. : 22.4 K amps/cm.
Sweep: 2 usec/cm.
Lower trace - Ampl. : .6 K amps/cm.
Sweep: 2 usec/cm.

$z = 5 \text{ cm}$ $r = 17.5 \text{ cm.}$



Upper trace - Ampl. : 22.4 K amps/cm.
Sweep: 2 usec/cm.
Lower trace - Ampl. : .6 K amps/cm.
Sweep: 2 usec/cm.

Upper trace - Integrated current with Rogowski loop between gun flanges.
Lower trace - Integrated current with 7.5 cm diameter Rogowski loop at muzzle at locations specified.

Figure III-43. (Cont'd). Rogowski Loop Signals of Currents External to the MOD A-7D Gun, 1.9 KV, 45 μ fd, Xenon Propellant

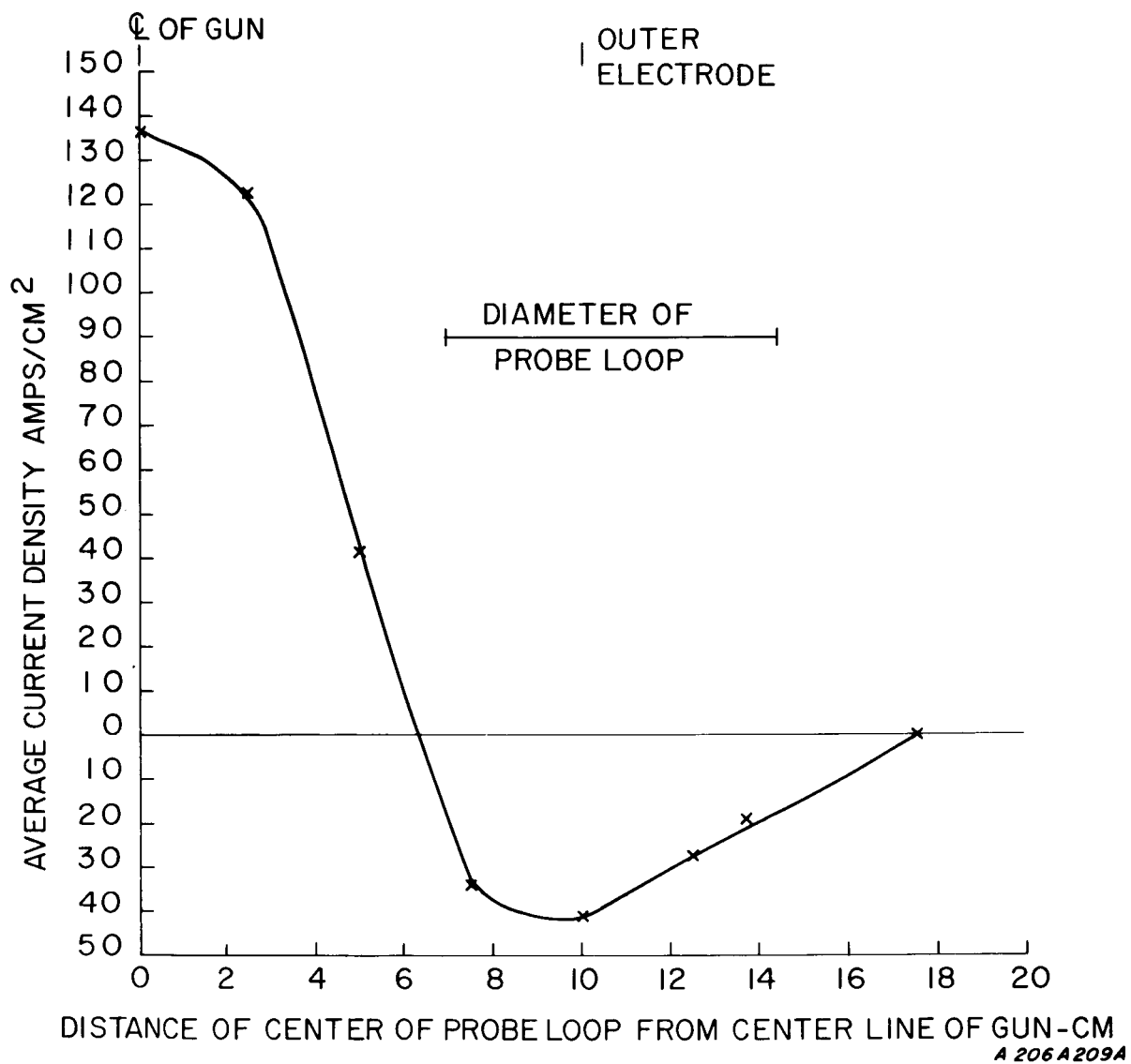


Figure III-44. Average Current Density vs. Distance from Center Line of A-7D Gun.

F. THE A-8D and A-9D ACCELERATORS

F.1. Overall Efficiency Measurements

The A-8D and A-9D accelerators were similar in basic external geometry to the A-7D electrode structure. However, they differed in the design of the propellant injector ports of the center electrode where successive changes were made in order to improve the fraction of the injected propellant which was in the accelerator at the time of discharge. The A-8D center electrode is very similar to that of the A-7D except that the radius transition in the inner electrode where the injector ports are located is steeper, and the slots have been made shorter and wider so that the conductance of its nozzles was approximately twice that of the A-7D nozzles. In spite of the increased amount of propellant available to the discharge, the overall efficiency of the A-8D accelerator was little different from that of the A-7D. The comparative performance of these accelerators (and that of several other accelerators) for 45 μ fd nominal capacitance, is shown in Figure (III-45). The A-8D accelerator was found to be operable at considerably lower propellant input flows than previous accelerators, an indication that a larger fraction of the injected gas was more radially directed and consequently more available toward the breech end of the accelerator in the region of the trigger electrodes.

In order to redirect additional gas toward the muzzle, a straight cylindrical sleeve was placed around the ports and forward of them. This arrangement is shown in Figure (III-46). The sleeve apparently directed the propellant flow too well, since it either prevented triggering of the gun at delay times after .7 ms., or necessitated excessive propellant input which caused frequent gas triggering of the discharge. The few experimental points which were obtained were in general similar to those for the A-8D without such a sleeve, but no trends could be conclusively established. A second sleeve of divergent design (See Figure III-46) was adapted to provide some compromise in the direction of the gas. As a result, the accelerator was operable over a wider range of conditions. The overall efficiency - specific impulse relationship was in this case also relatively insensitive to the change. It appeared that if the propellant distribution was to be the variable used to improve accelerator efficiency, a much more radical change in port design was required. Such a change was incorporated in the "wide open" Mod A-9D geometry.

In the Mod A-9D design, shown in Figure (III-47), there were virtually no confining walls to impede the flow of propellant from the valve seat to the interelectrode space. As was expected, measurements of the time to self-triggering of the gun after actuation of the valve indicated

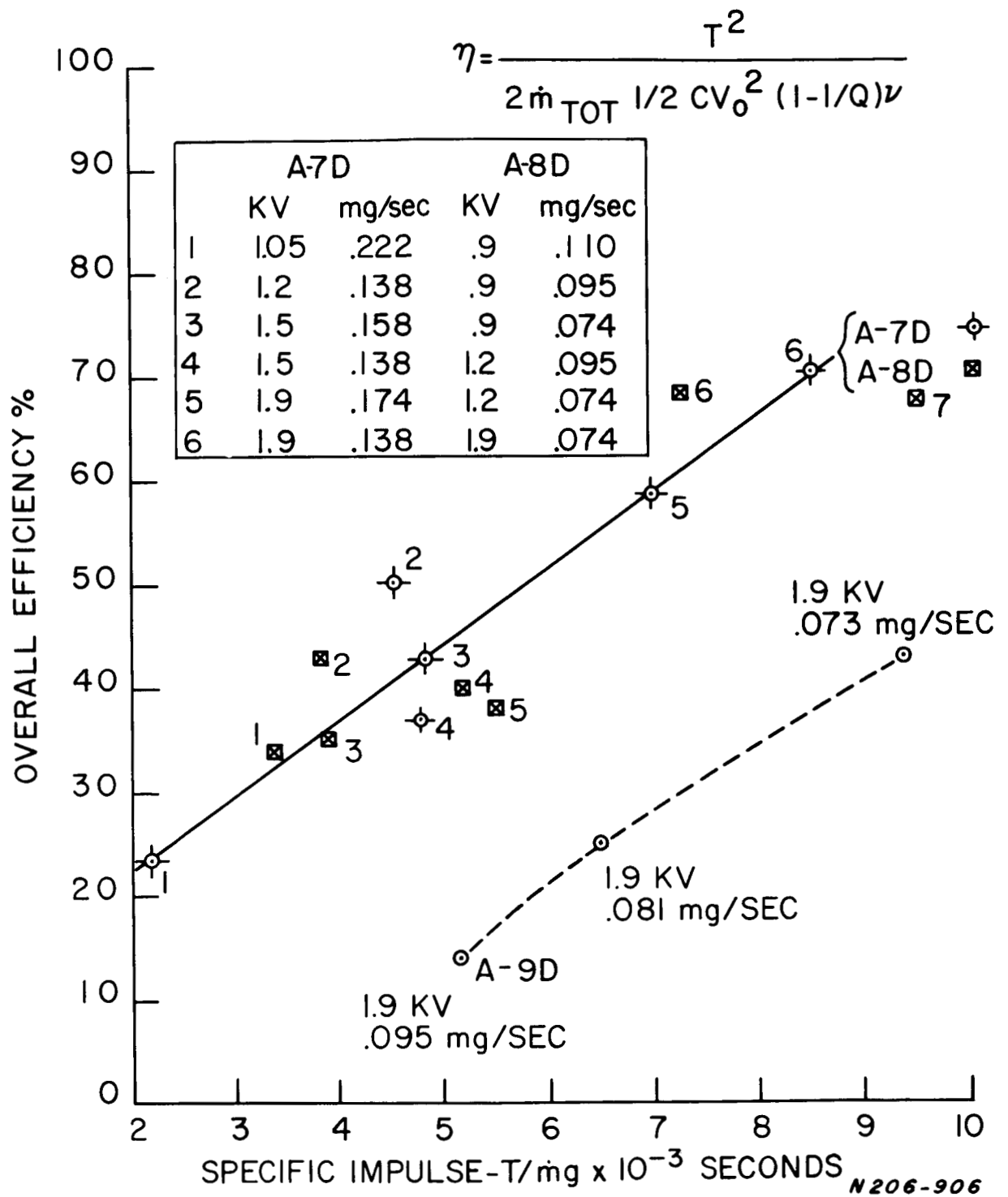
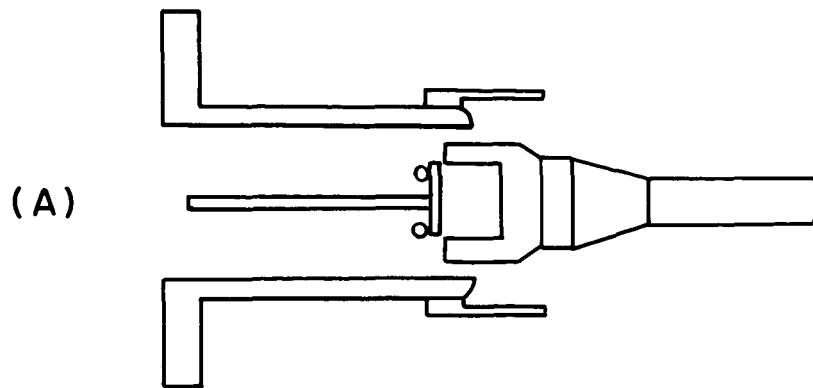
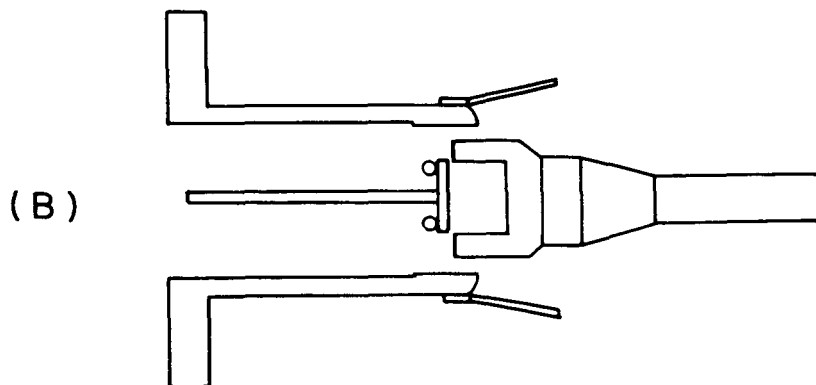


Figure III-45. Comparative Performance of A-7D, A-8D, and A-9 Accelerators with Xenon Propellant.



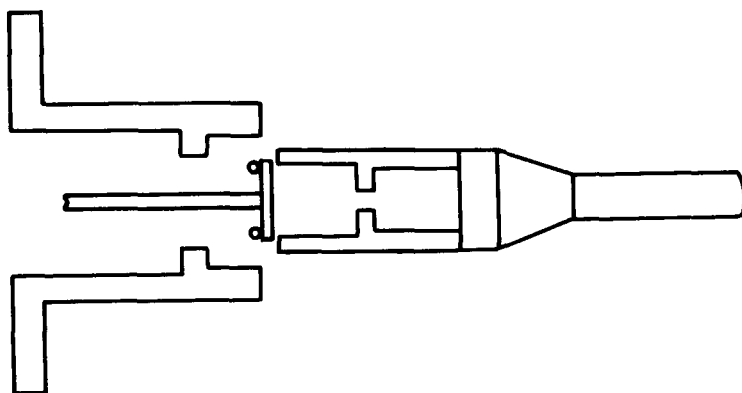
(a) Mod A-8D with Straight Cylindrical Sleeve



(b) Mod A-8D with Diverging Sleeve

N 206-908

Figure III-46.



N 206-909

Figure III-47. Sketch of A-9D Center Electrode.

earlier departure from the nozzle of sufficient quantities of propellant to initiate the discharge. Self-triggering times for the A-9D nozzle were found to be about 220 microseconds compared to 350 microseconds for the A-8D and 500 for the A-7D nozzles. The amounts of propellant which could be injected either for gas-triggering or for electrical triggering of the gun were much smaller than could be used previously; so small, in fact, that considerable difficulty was encountered in using the capillary flowmeter type of mass flow measurement.

Thrusts recorded on this engine were about 30% lower than were obtained with the A-7D gun. Thus, with propellant flows of the order of 8×10^{-8} Kg/sec peak overall efficiencies were about 43% at 9000 seconds (See Figure III-45). Similar thrust levels were measured with still lower flows which could not be accurately measured. This would indicate higher efficiencies but also higher specific impulse.

F. 2. Calorimeter Measurements of Exhaust Stream Energy

Several different calorimeter configurations were used in determining the energy per pulse in the Mod A-8D engine exhaust stream. The original calorimeter used in previous measurements was deemed unsuitable here since its diameter was too close to that of the outer electrode to effectively intercept the entire exhaust cross section. In initial tests, however, it recorded energy efficiencies of 60-62% (where

$$\eta = \frac{E_{cal}}{1/2 C V_o^2 (1 - \frac{1}{Q})} \text{) at}$$

2 KV engine voltage.

A second conical calorimeter, 37.5 cm in diameter and 15 cm deep was installed, but failed to render reliable readings due to the relatively long time (14 min.) for the establishment of thermal equilibrium throughout its mass. There was not only difficulty in determining the temperature which the unit had attained, but there were undoubted radiation losses which could not be accurately taken into account. The prime source of the long equilibrating time was the thinness (1/64") of the copper sheet from which the calorimeter was fabricated.

A third calorimeter was fabricated in which doubling the sheet metal thickness resulted in a drop in the equilibrating time to two minutes. Energy efficiencies obtained with this calorimeter at 2 KV were in the 60-65% range. Visual inspection of the calorimeter indicated an area of heating concentrated at the apex of the cone about 2 cm in diameter surrounded by a ring of less intense heating followed by an area of greater heating 22 cm in outside diameter. The relatively intense heating at the apex thermocouple resulted in temperatures more than three times that of the equilibrium temperature.

This suggested that a redistribution of weight in the calorimeter would cause the apex to attain a temperature closer to that of the rest of the calorimeter.

It is interesting to note here that energy efficiencies were not only lower in self-triggered operation than in two-stage operation, but that the ratio of heating of the calorimeter apex area to the edge areas was greatest with two-stage operation, indicative of significantly less spreading of the exhaust stream with this mode of triggering.

A fourth calorimeter employing a redistribution of mass was conical, 37.5 cm in diameter and 15 cm deep with an inverted cone of about 1400 gm mass at the apex, surrounded by a cylinder 12 cm diameter, and 10 cm long to provide a reentrant design and more efficient trapping of the exhaust stream. The total mass of the calorimeter was 2933 gm. Typical calorimeter runs at 2 KV were of 20 second engine firing duration at 5 shots per second. The redistribution problem was less pronounced with this configuration, although there is no doubt that heat losses due to radiation could not be fully taken into account. Peak efficiencies of from 68-75% were measured at 2 KV with a 0.6 millisecond delay between valve activation and triggering of the discharge. Self-triggered operation yielded efficiencies of 44-48% at this voltage. A summary of energy efficiencies at the voltages examined is shown below:

<u>Voltage</u>	<u>Energy Efficiency</u>
1 KV	28 - 29%
1.2 KV	37 - 39%
1.5 KV	35 - 42%
2.0 KV	68 - 75%

F. 3. Gas Density Measurements on the A-9D Accelerator

Since the A-9D nozzle configuration appeared to be the ultimate in high conductance for the propellant feeds thus far designed, it was feasible to study the distribution of propellant which it injected.

Detailed measurements of the time dependent propellant profile in the A-9D gun were made with the accelerator mounted in a large vacuum chamber (6' x 3') pumped by a 2000 l/s diffusion pump. The measurement was made by a suitably modified CK5702 vacuum tube mounted on the end of a 1/2" stainless steel tube inserted from a port opposite the gun muzzle. The assembly through which the stainless steel tube was inserted allowed both radial and axial mapping of the interelectrode region of the gun.

The techniques of these measurements are described in Appendix B.

The pressure profiles are recorded as pictures of isobars at five different times (see Figure III-48). The propellant fraction within the gun is shown in Figure (III-49).

The most striking result is, of course, the fact that over 93% of the propellant was present between the feed nozzles and the muzzle at one time (0.6 ms). (This should be compared to the maximum propellant fraction of 53% within the A-7D gun at the same valve voltage as shown on Figure (III-33). If the interaction region is extended beyond the muzzle, as current distribution studies indicate, even this may be increased.

Less desirable from the performance standpoint, the bulk of the propellant is near the outer electrode at optimum discharge time. This is most clearly shown by a contrast of Figure(III-48) with Figure (III-50) which show the isobars in the A-7D gun under comparable conditions. Because of the lower conductance, propellant is still streaming from the nozzles in the A-7D, keeping a good fraction of it in a reasonable position for coupling with the E-M fields.

An equally important cause of the change in propellant distribution is the angle the propellant stream makes with the gun axis. In the A-7D, some degree of pipe flow remains and the stream makes an angle of $30-35^{\circ}$ with the axis. Pipe flow is largely lost in the A-9D and the propellant stream diverges until it makes an angle of about 50° with the gun axis. In some respects, this angle is so large that the flow pattern resembles that of radial injection. The worst consequence of this flow pattern is the fact that the high density gas front moved almost directly to the outer electrode (see Figure III-48). This allowed gas-triggering with far less propellant than pure axial injection because the high local gas density had not had a chance to spread as it would have over the longer path of a more axial stream. Thus the gas densities required for gas-triggering were produced near the outer electrode with a smaller total injected mass in the A-9D than in any previous axial injection configuration. Measurements of the propellant flow indicate that this total mass was too small for efficient gun operation at specific impulses of interest.

Clearly, despite the great improvement in potential mass utilization through increased nozzle conductance, poorer overall efficiency was realized with the A-9D, (See Figure III-45).

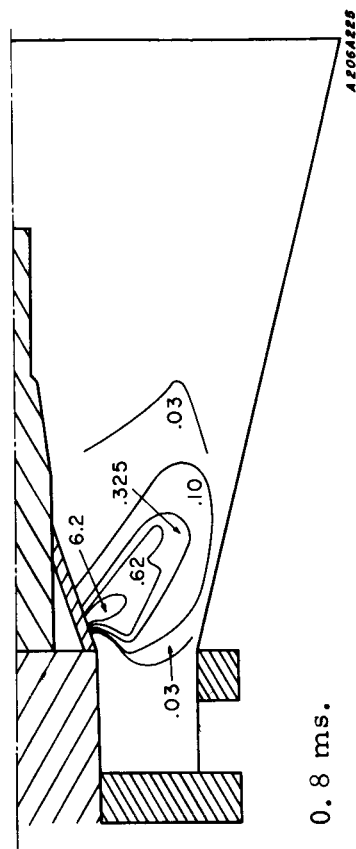
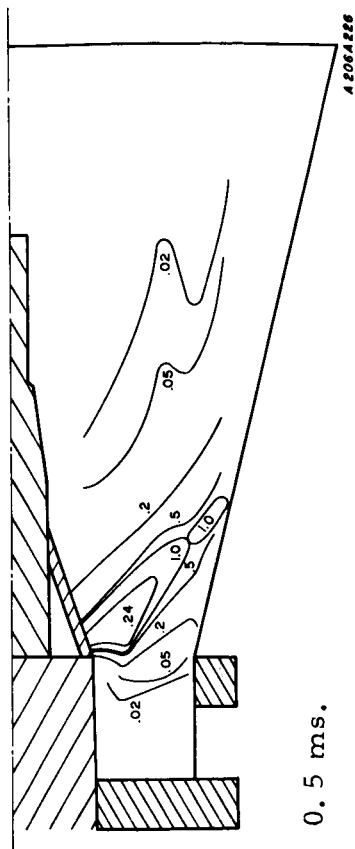
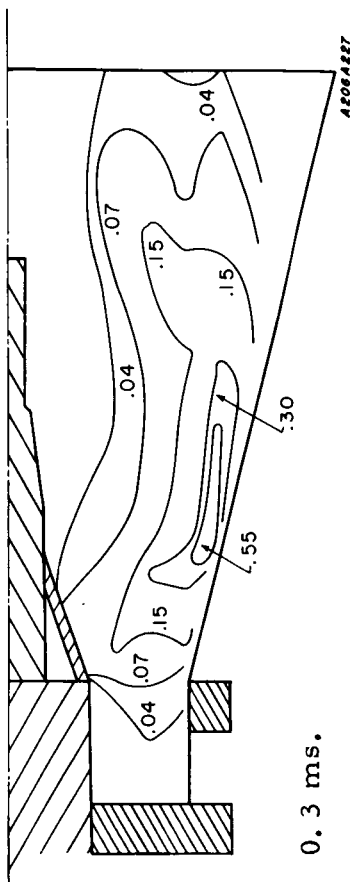
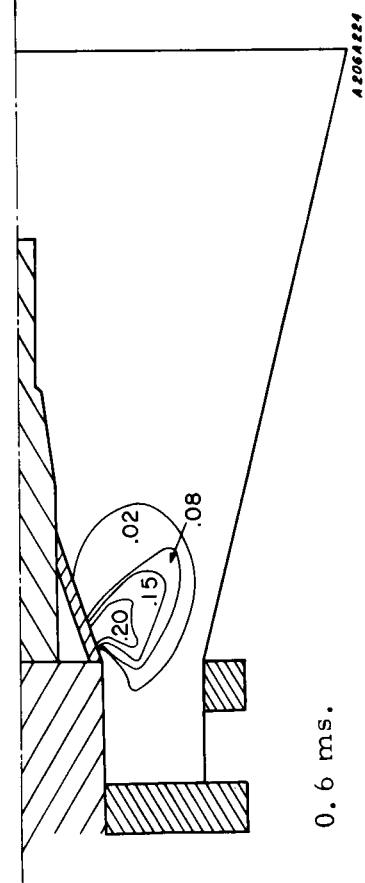
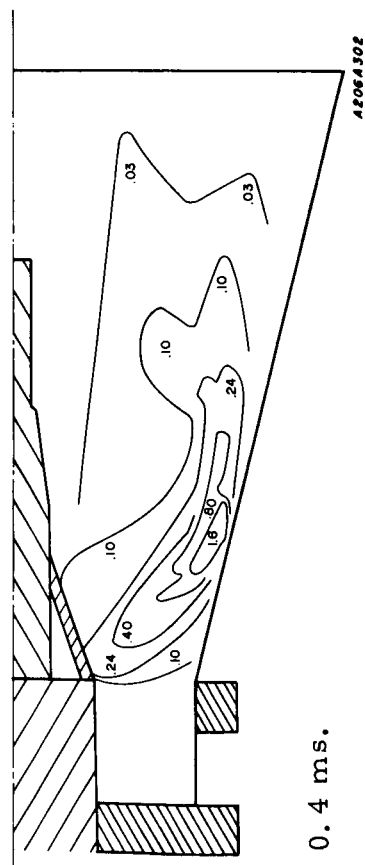
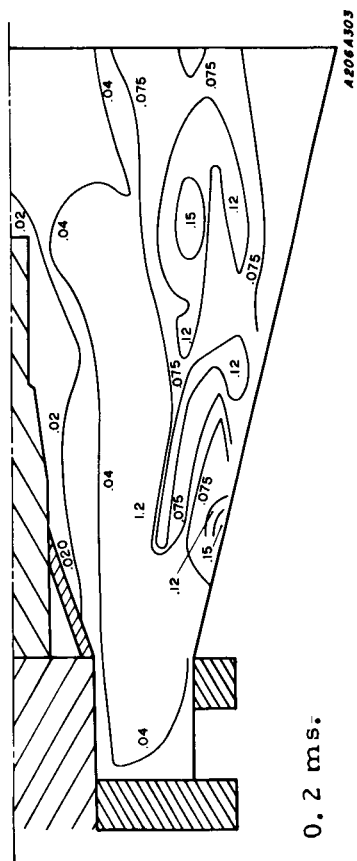
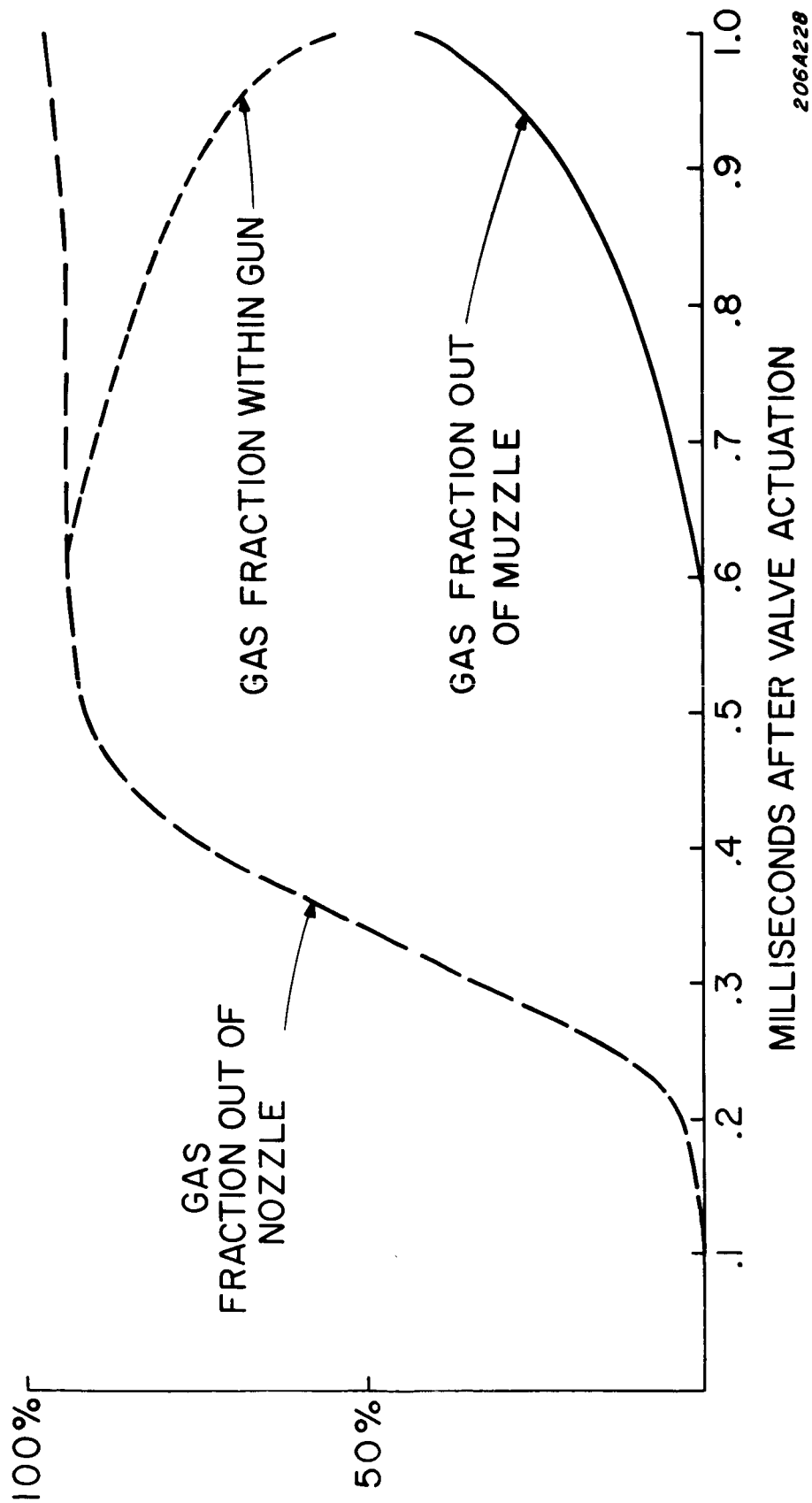
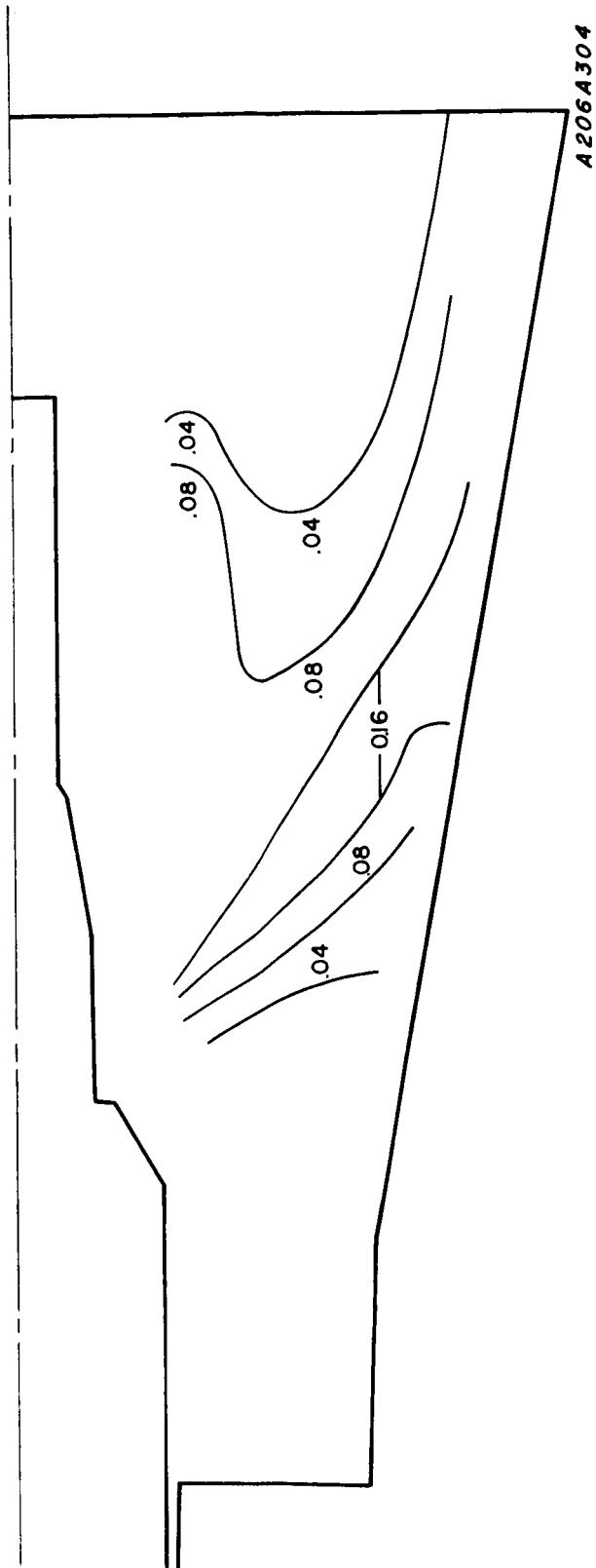


Figure III-48. Isobars A-9D Gun, Xenon, 4400 Volts on Valve, Reading in Volts.



206A228

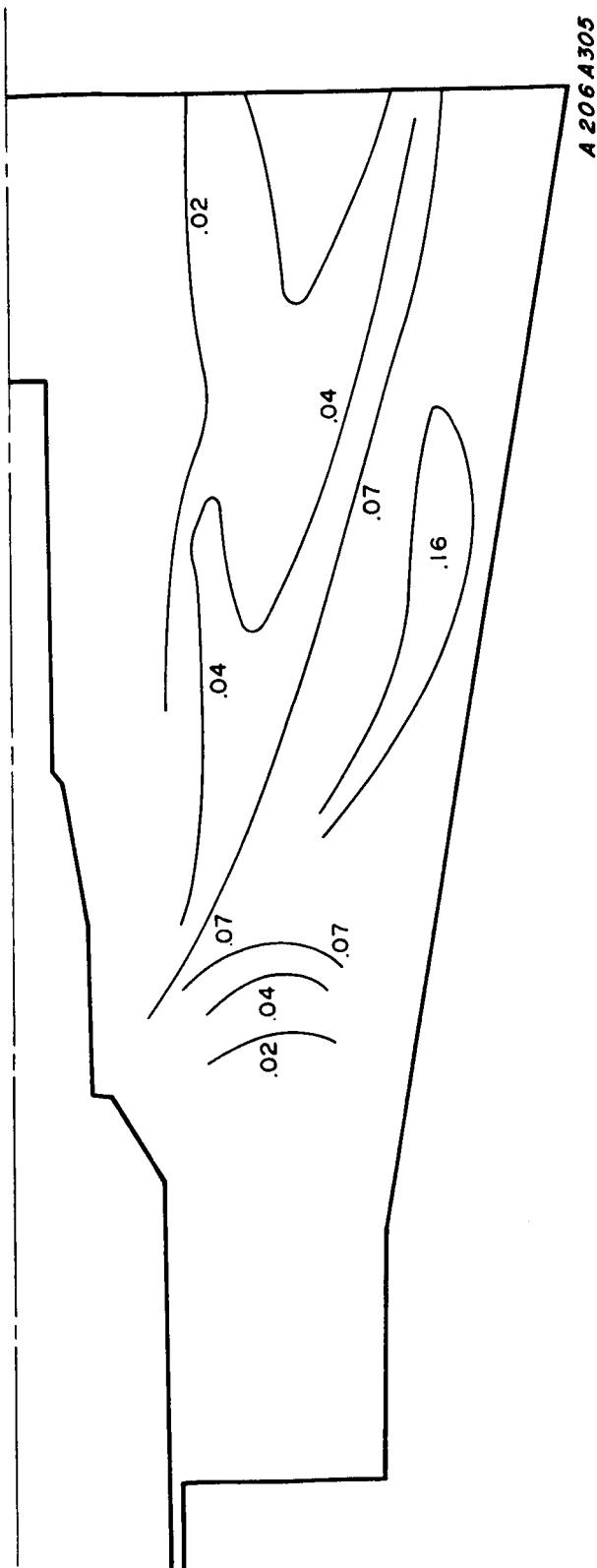
Figure III-49. Propellant Fraction as a Function of Time, A9-D Gun, Xenon



0.6 ms.

A206A304

III-64



0.7 ms.

A206A305

Figure III-50. Isobars A7-D Gun, Xenon, Valve: 4440 Volts, .6 ms Delay

G. THE A-9DB ACCELERATOR

Since the use of a sleeve for directing the propellant properly while maintaining high feed nozzle conductance was not successful, a second technique for propellant placement was conceived, involving a directive valve seat. Instead of sealing the Teflon O-ring with a flat plate that allows the gas to escape only radially, a valve seat that tends to direct the stream axially was used. The motivation for this goal has been discussed previously. In addition, the positioning of the propellant in a region of low field strength also seemed undesirable. The drop in efficiency observed from performance measurements on the A-9D gun tended to verify this and fit in with the view that a more axial flow must be given to the propellant. Redesign of the fast-acting valve seat provided a means for controlling the propellant distribution in the gun without changing the shape of the center electrode. The new valve seat, drawn in Figure (III-51); consists of a Teflon O-ring mated with a stainless steel ball which is of appropriate diameter with relation to the I. D. of the "O" ring to control the axially of the propellant flow, i. e., the most pronounced axial flow is obtained when the ball diameter is closest to the "O" ring I. D. This should be contrasted with the old valve seat shown in Figure (III-51). Propellant distribution measurements using the CK5702 ion gauge probe were made for such valve seats installed in the A-8 and A-9 nozzle geometry. (The series of guns using the ball seat valve are henceforth designated with a "B" suffix, i. e., A-9DB and A-8DB.)

An initial crude study was performed on the A-9DB configuration until it became clear that the more efficient A-8DB would be used rather than the A-9DB for the more extensive performance measurements to follow.

A water-cooled calorimeter was used to determine the energy in the exhaust stream of the A-9DB engine for various voltages and propellant mass inputs. The highest energy efficiency consistently obtained from measurements on the A-9DB engine was 65% at 2 KV and a mass flow of .07 mg/sec of xenon. This efficiency, however, was found to occur under comparatively low mass flow conditions which implied undesirably high I_{sp} 's. This was confirmed by subsequent thrust and mass flow measurements at the same conditions which led to the above performance, which resulted in an overall efficiency ($T^2/2mP$) of 61% at an I_{sp} of 12,000 sec. Under self-triggered operation with a larger mass flow^{sp}, an efficiency of 35% at an I_{sp} of 5400 sec. was measured. Thus, the requirement for injecting more mass prior to the controlled triggering of the discharge had not been entirely solved by use of the ball valve seat in the "wide-open" A-9D configuration. The A-8DB, with additional nozzles ahead of the valve seat to provide augmented directivity of the flow, offered the possibility of increasing the performance.

A206A635

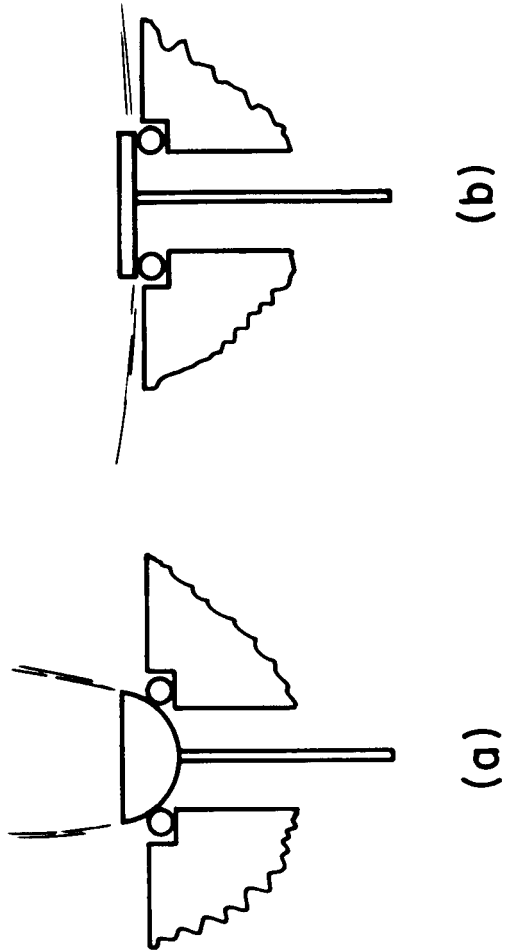


Figure III-51. Sketches of Valve Seats

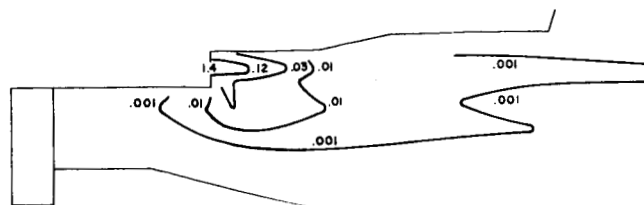
H. A-8DB RESULTS

An A-8DB gun which had been consistently giving calorimetrically obtained efficiencies of over 72% was separated from its outer electrode and installed in the gas density measuring facility with an identical outer electrode. Since the entire center electrode assembly was moved, the propellant injection apparatus was the same as that just used to fire the gun for the performance measurements. After the gas density measurements were over, the center electrode assembly was replaced in its original position and efficiency measurements were made again. Once more, energy efficiencies of over 72% were obtained, indicating that the propellant injection system had been operating in an optimum manner during the gas density measurements.

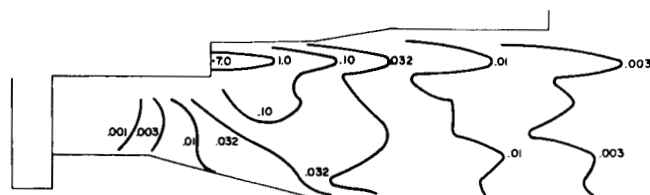
Isobaric charts showing lines of constant pressure within the gun at succeeding times are shown in Figure(III -52). In contrast to the almost radial high density stream coming from the A-9D gun, here the stream enters purely axially. It runs parallel to the center electrode and near the nozzle it is so narrow that radial movement of the probe by only 1/2 cm results in a drop in pressure of more than an order of magnitude. Thus, hopes that the new **valve design** would provide more axial flow were completely satisfied. In addition, there is a strong indication that an enlarged sphere with the same O-ring will yield a stream that makes a slight angle with the gun axis. The flat disc used previously corresponds to a sphere of infinite radius and so the angle that its stream makes with the axis should be considered as the limit one could obtain.

The ability to direct the high density stream purely axially does not imply that gas can be kept away from the outer electrode to an equal degree. As can be seen in Figure (III-52), the high density stream develops a low density wing that moves to the outer electrode. This wing, like the main stream in the A-9D gun, makes an angle of about 50° with the gun axis. There is no physical structure to direct the gas in this direction other than the inner electrode wall and so the low density wing must be interpreted as the natural sideways expansion of the high density stream.

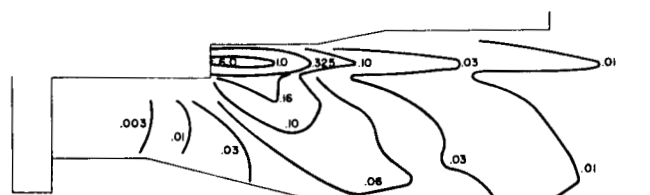
A completely axial stream injected from the present nozzle position will give the largest fraction of propellant that can be obtained near the center electrode, and so, despite this large amount of propellant expansion toward the outer electrode, the A-8DB represents the optimum gun for propellant loading in that location. No alteration in the stream position can be expected to change this situation. A nozzle with a much higher length over diameter ratio might conceivably increase the center electrode loading but the decreased nozzle conductance would more than compensate.



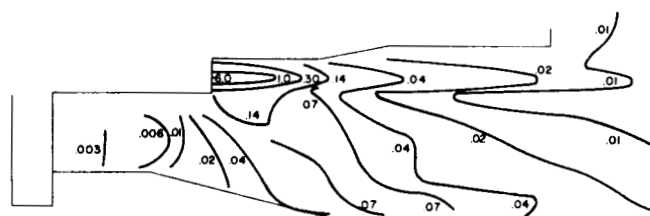
. 3 ms.



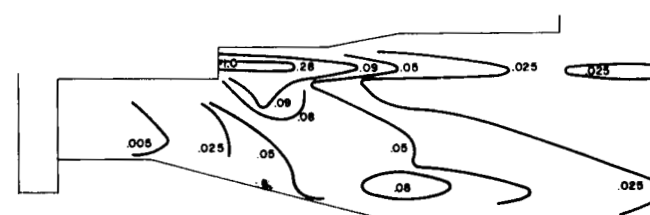
. 5 ms.



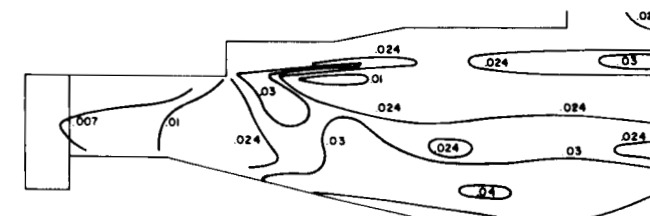
. 6 ms.



. 7 ms.



. 8 ms.



1. 0 ms.

Figure III-52. Isobars, A-8DB Gun, 4400 Volts Valve, Xenon, Readings in Volts

It was noted that the outer electrode becomes quite hot during extended operation with the A-8DB, while the center electrode remains cool. Previous guns had left the outer electrode cold. Since the relative decrease of gas near the outer electrode is a prime characteristic of the A-8DB, it is possible that a slight increase in the pressure near the outer electrode would result in both electrodes running cool. Any electrode heating results in engine inefficiency and so improved performance could result from its elimination.

In addition to the gross observation of the axial high density stream and its expansion into the interelectrode region, more detailed comments are possible. First, the gun is now more completely filled than in previous valve configurations. Examination of Figure (III-48) shows that the region around the central electrode of the A-9D gun was almost completely devoid of propellant. In fact, a pressure drop of two orders of magnitude was observed. This is not the case for either the A-8DB or the A-9DB guns. The pressure drop between any point on the anode and a point opposite it on the cathode is rarely more than a factor of four (except at the feed nozzles). It is not certain that this is necessarily desirable.

As has been implied earlier, more propellant can be injected into the interelectrode region prior to gas-triggering when the gas-triggering time is longer. It has been noted that gas-triggering seems to occur when an isobar of a certain density hits the outer electrode. For xenon propellant and a CK4702 tube ion gauge, this isobar has been represented by .03 volts. Table 1 shows the gas-triggering time and the approximate time of arrival of the .03 isobar at the outer electrode.

TABLE 1

Gun	Gas-Triggering Time - msec	Approximate time of .03 isobar arrival-msec
A-9D	.220	.250
A-7D	.500	.475
A-8DB	.550	.525
A-9DB	.500	.500

Clearly, gas-triggering has been delayed considerably in the A-8DB and the A-9DB gun configurations, and all evidence points to the more axial propellant flow as the cause. This effect was anticipated as was the greater flow required to induce gas-triggering.

To further understand the detailed effects of this mode of propellant injection, it is necessary to know what fraction of the propellant can be acted upon as a function of time after valve actuation. This has been computed in the same way as it was for the A-7D and the A-9D. Figure (III-53) shows the fraction of the propellant that is present between the feed nozzles and the muzzle as a function of time. Since gun currents extend beyond the muzzle, similar computations were made for the fraction of propellant between the feed nozzle and two planes 5.5 cm and 10.5 cm beyond the muzzle. The latter plane represents the farthest extension of measurable currents and the former the farthest extension of significant thrust density ($J \times B$). Figures (III-54 and III-55) show the result of these last two computations.

Within the uncertainties of the measurement, the maximum propellant fraction within the gun occurs near 0.8 milliseconds for all three cases. The only difference lies in the value of this maximum fraction. Even this peak value does not vary much, however, and is over 90% in any case.

The type of propellant density distribution that exists in this region beyond the gun muzzle is indicated by the isobars shown on Figure (III-56). The form of a flat density front is approached at distances 15 cm beyond the muzzle, while closer in the stream type of profile still dominates. The progress of the gas away from the gun can be traced very clearly here.

Thus gas density measurements have shown that the propellant injected by the new ball valve emerges in a well-defined axial stream that fills the rest of the gun through sideways expansion. This leads to more gentle pressure gradients within the gun than had heretofore been observed. Since the main gas stream no longer intercepts the outer electrode, the arrival of the isobar that gas-triggers the discharge is delayed and the gas-triggering time is extended to .55 milliseconds. In addition, the total amount of propellant that must be injected so that the gun will gas-trigger is also much increased, once more due to the new direction of the propellant stream.

The performance of the A-8DB gun was somewhat lower than that of the A-7D configuration (see Figure III-57). There are several possible reasons for the lack of improvement in overall efficiency at a given I_{sp} .

- (1). Redirection of the propellant stream may be necessary.
- (2). A mechanical problem occurring occasionally in the use of the spherical seat may be responsible for an undesirable alteration of the propellant input. At times, the amount of propellant required to gas-trigger the gun would drop to very low values. This was interpreted as being a

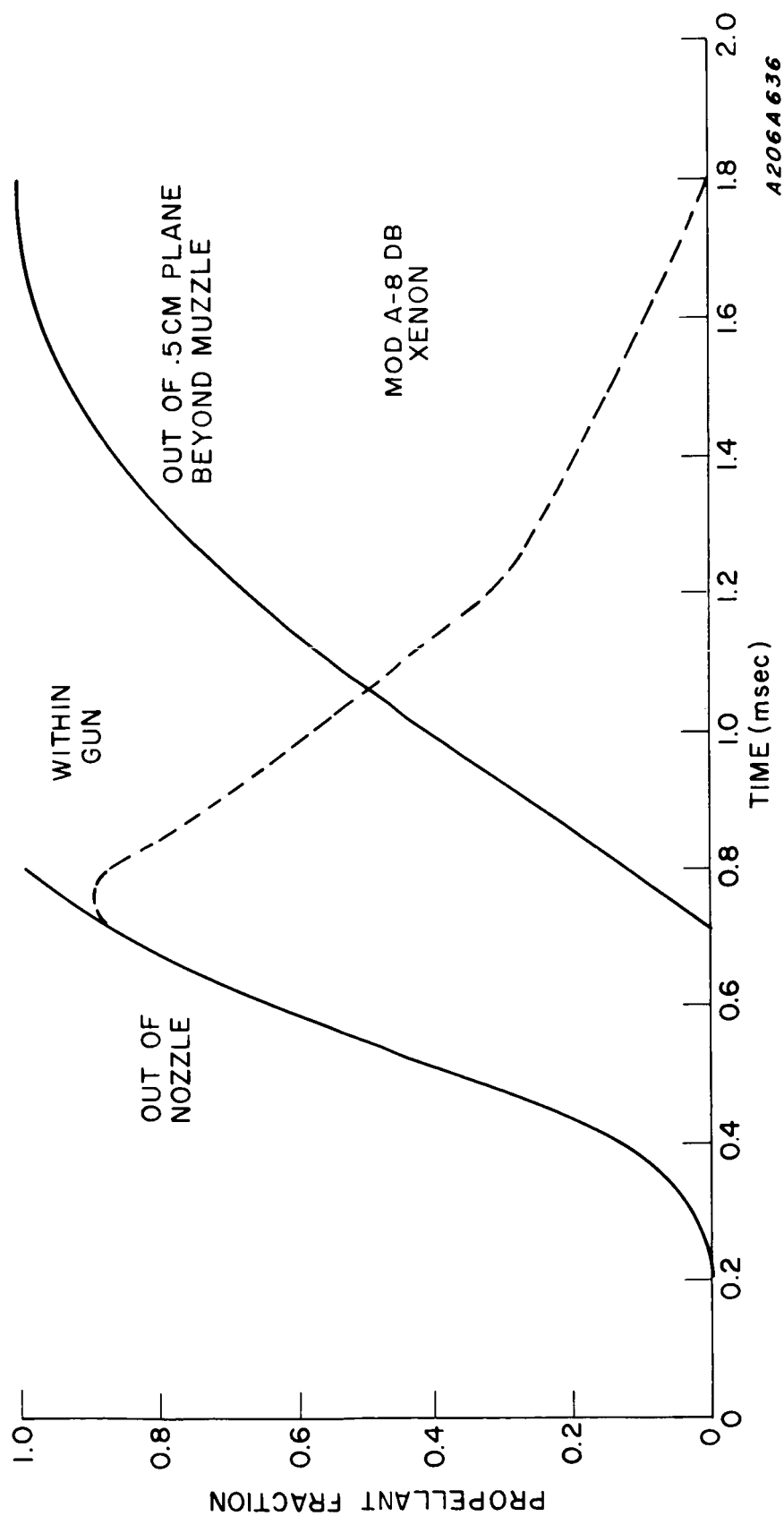


Figure III-53. Propellant Fraction Between Nozzles and Muzzle as a Function of Time - Axial Position = .5 cm, Mod A-8DB, Xenon, 4400V, Valve

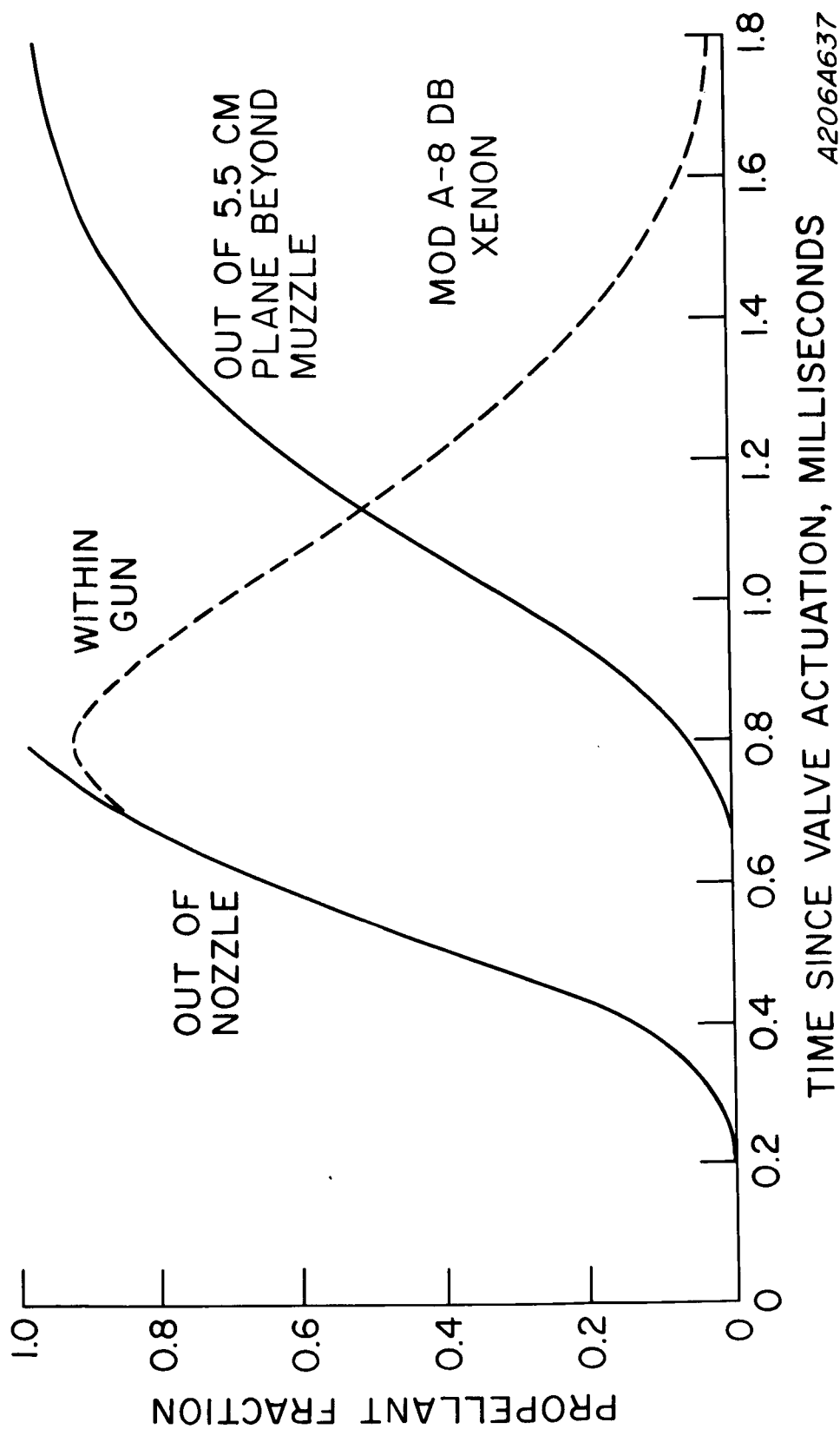


Figure III-54. Propellant Fraction Between Nozzles and Plane 5.5 cm. Downstream from A-8DB Gun, Xenon, 4400V. Valve.

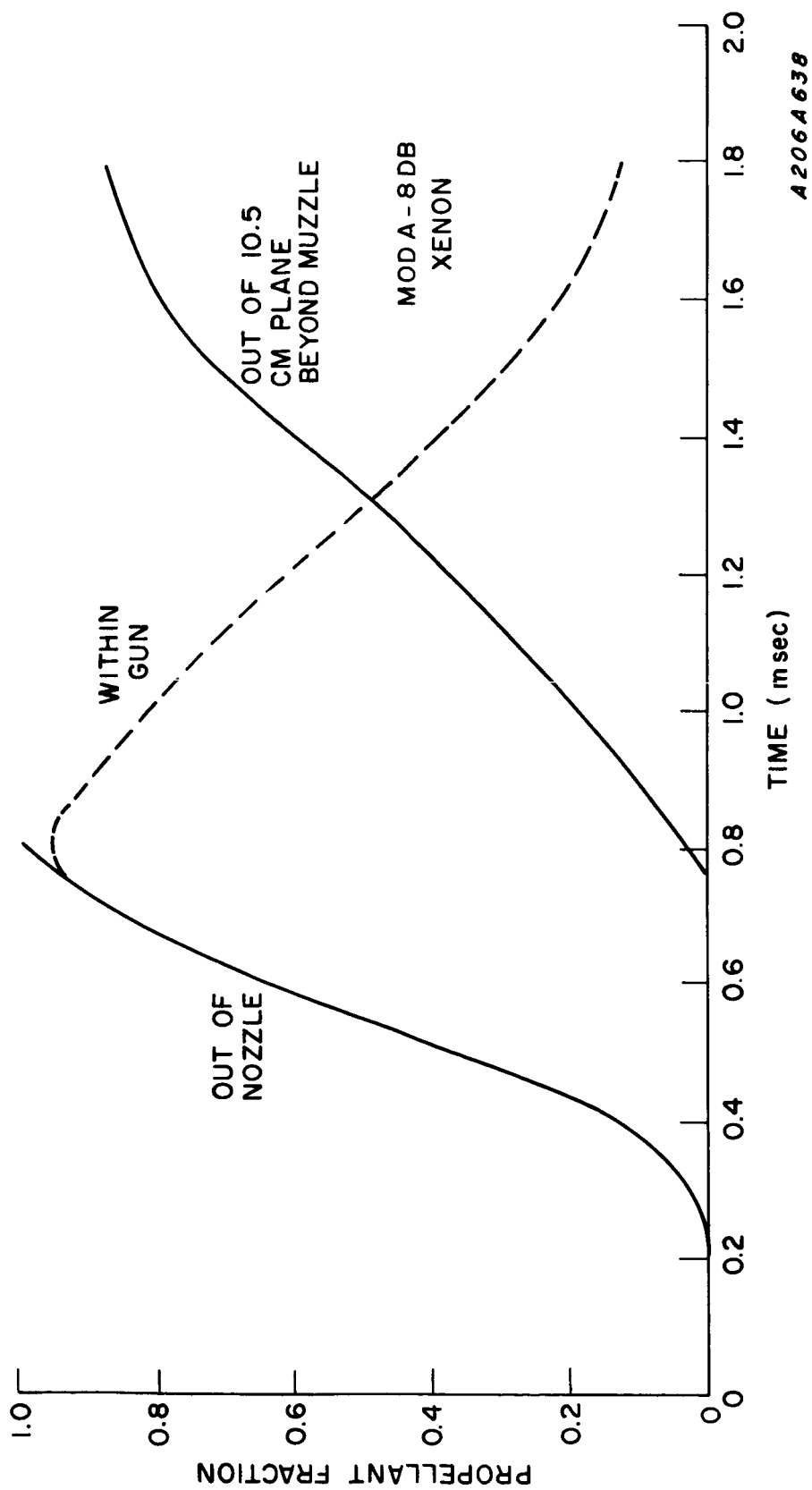


Figure III-55. Propellant Fraction Between Nozzles and Plane 10.5 cm. Downstream from A-8DB Gun, Xenon, 4400 V Valve

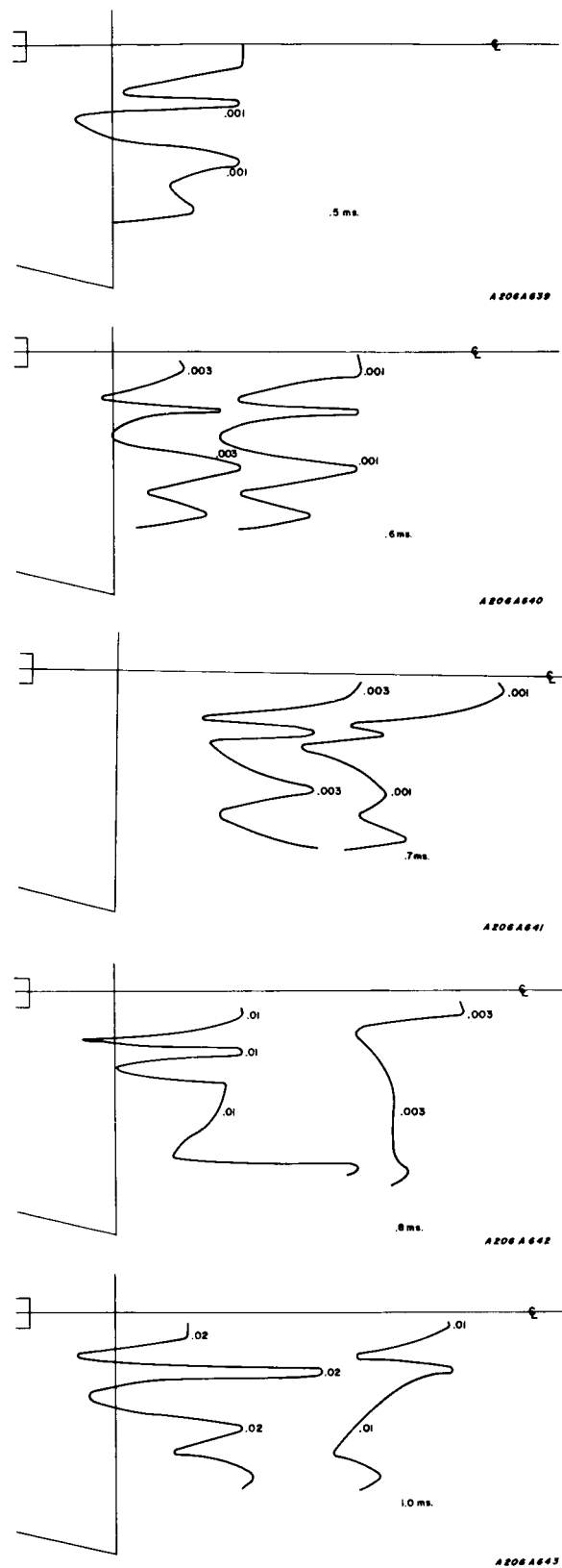


Figure III-56. Isobars Beyond A-8DB Gun, Xenon, 4400V on Valve

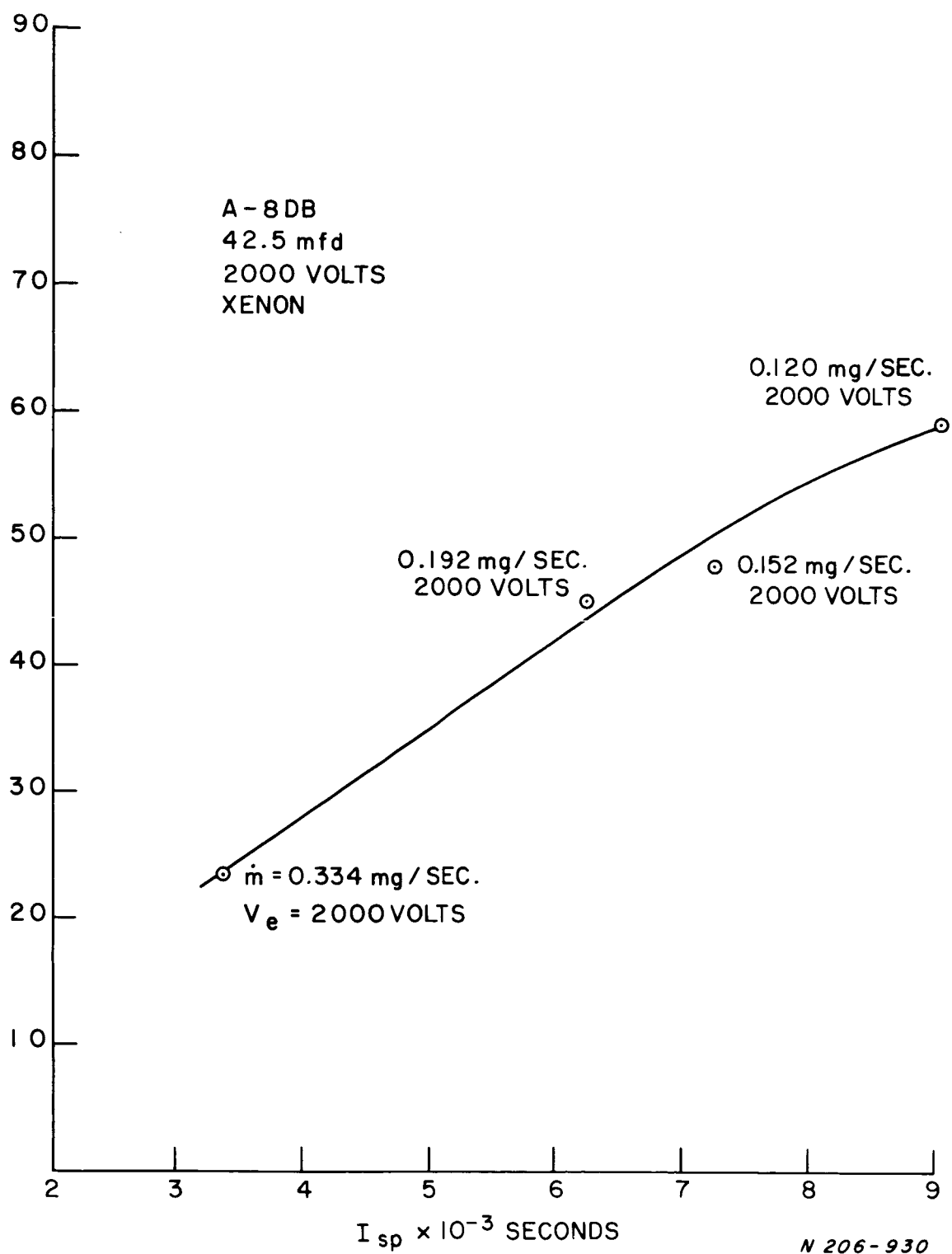


Figure III-57. A-8DB Performance, Xenon Propellant

result of uneven opening of the valve which would lead not only to the lower mass flows for gas-triggering but a non-uniform distribution of the propellant which was injected. This irregularity was not disclosed by the gas density probe measurements, probably because these measurements are made on a single shot basis and the total number of shots expended represents less than a minute of repetitive operation. In addition, despite this fact, seemingly reliable data were obtained at times, as indicated in Figure (III-57). Improved design of the valve opening mechanism could thus lead to improved performance.

Electrostatic gridded probe measurements have also been performed upon this gun while using nitrogen as propellant. Figure (III-58) shows the type of distribution of ions that result.

I. PERFORMANCE OF THE A-7D ACCELERATOR AS A FUNCTION OF CAPACITANCE

Since after all the foregoing changes in the gas injection system there was no distinct improvement over the performance of the A-7D accelerator, it was decided to return to this configuration to examine capacity and voltage trends in accordance with the rationale discussed in section II. Overall efficiency vs. specific impulse for capacitances of 72 and 96.5 μfd are plotted in Figures (III-59 and III-60). The results for capacitance of 144.5 and 218 μfd have been presented in section II. A plot summarizing the trend to increased efficiency with increased capacitance, at a given specific impulse, is shown in Figure (II-9). It should be pointed out that although the slope of the curve indicated in Figure (II-9) has decreased sharply, there appears to be some opportunity for further increase in efficiency via an increase in capacitance with the same electrode geometry and propellant distribution.

It is also of interest to note that at the high valve voltages required to produce the gas flow needed, a small amount of valve "bounce" has been observed. The pressure trace in Figure (III-61) demonstrates this clearly. Since almost all of the gas exiting during the second bounce ($\sim 10\%$ at 5300 volts on the valve) is lost, further improvement in performance might be expected if the "bounce" could be eliminated.

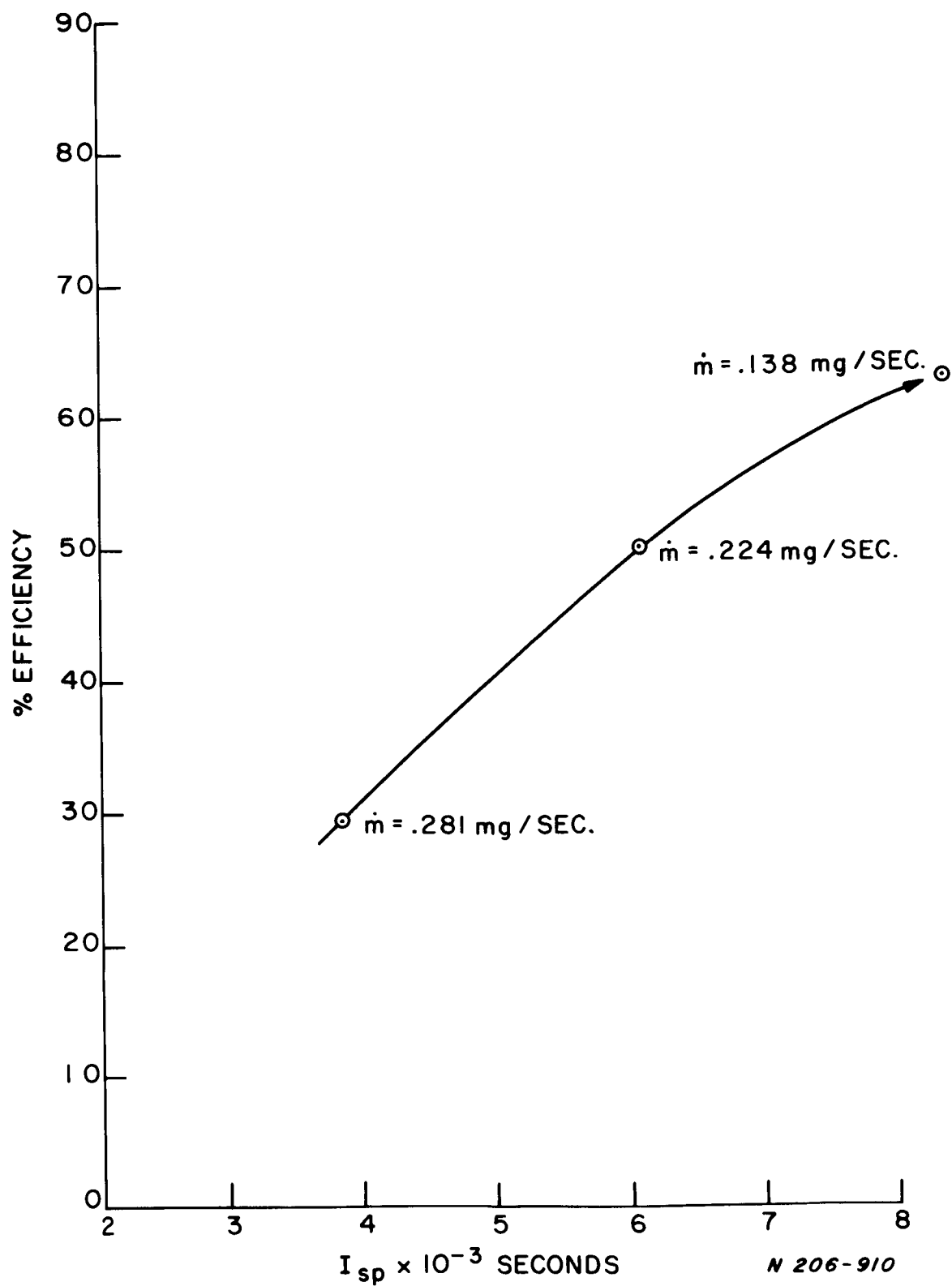


Figure III-59. A-7D Performance, 72 μ fd, 1.55 KV, Xenon

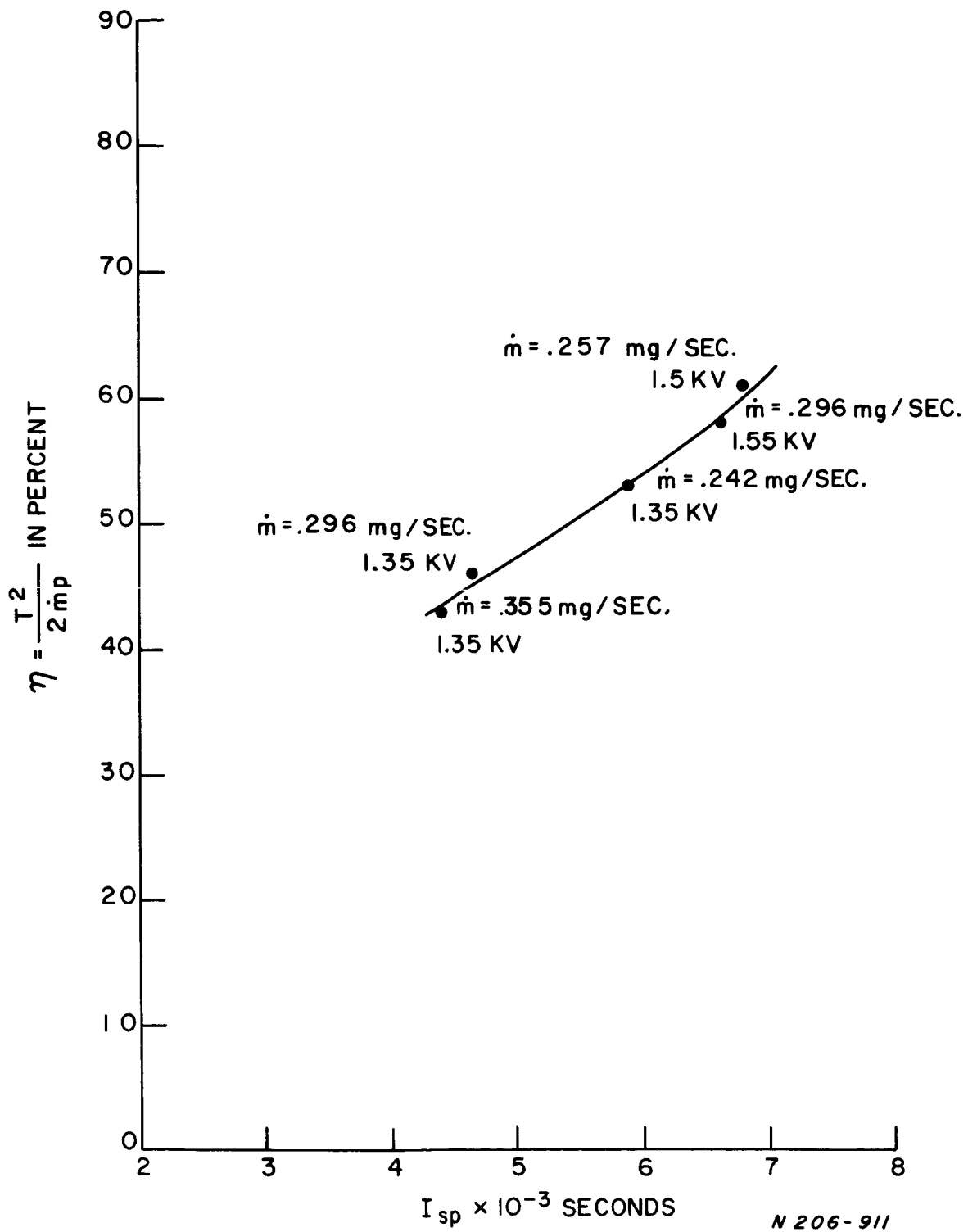


Figure III-60. A-7D Performance 96.5 μ fd, Xenon

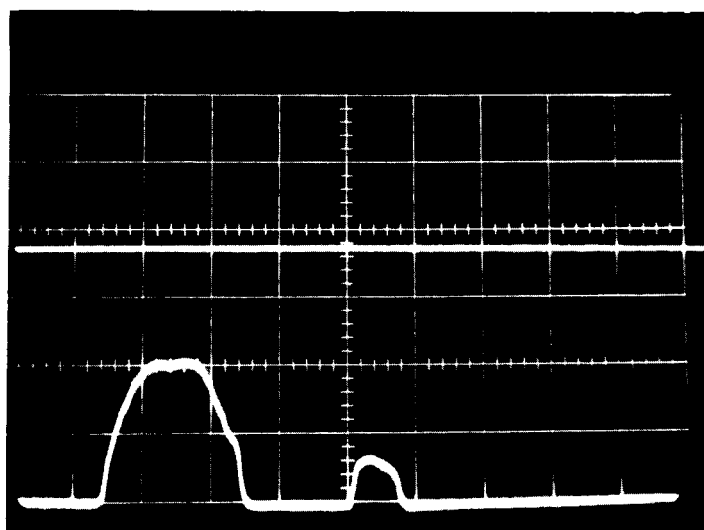


Figure III-61. Gas Density Probe Trace Showing "Valve Bounce"
.2 ms/cm 5 V/cm

REFERENCES

- III-1. B. Gorowitz, P. Gloersen, A. Ruess and J. Kenney, "Performance of a Repetitively Pulsed Two-Stage Plasma Propulsion Engine", Final Report, Contract NAS3-3570, October, 1964, CR-54064
- III-2. Dushman, Vacuum Technique, Wiley & Sons, 1949.
- III-3. Marshall, J., "Hydromagnetic Plasma Gun", Proceeding of the Fourth Lockheed Symposium in MHD Plasma Acceleration, S.W. Kash, Editor, Stanford University Press, 1960.
- III-4. B. Gorowitz, P. Gloersen, and J. H. Rowe, "Performance Study of a Repetitively Pulsed Two-Stage Plasma Propulsion Engine", Final Report, Contract No. NAS3-2502, November 20, 1963.
- III-5. P. Gloersen, B. Gorowitz, and W. Palm, "Experimental Performance of a Pulsed Gas Entry Coaxial Plasma Accelerator", Paper No. 1535-60 - ARS 15th. Annual Meeting, Washington, D.C. December 1960.

IV. PROBLEM AREAS

Some of the more important problem areas which were disclosed in the course of these studies and which are associated with the investigation and understanding of accelerator operation are discussed below.

One of the most interesting phenomena which was observed was the distinct difference between experimental results obtained, in general, by single shot operation of the accelerator (i. e. , tens of seconds between shots) and those obtained under repetitive operation. The first indication of this was the fact that the accelerator terminal voltage and current waveforms were considerably different when comparing the first shot with, e. g. the fifth and subsequent shots of the accelerator when firing in a rapid sequence (i. e. , at a repetition rate of 1 sec.^{-1} or higher). This was illustrated in Reference II-1. In the course of exhaust stream calorimetry, it was found that the thermal energy initially increased for succeeding shots up to the point of a steady state level of operation which was reached after a few seconds. This discovery has forced us to insure that whenever detailed plasma diagnostic measurements are made, operating conditions consistent with steady state characteristics of the accelerator are obtained. It would be desirable to make gridded probe and B_θ probe measurements during high repetition frequency operation of the accelerator since it is under these conditions that the overall efficiency data are obtained. While this is not such a difficult specification for obtaining B_θ probe data, the present design of the gridded probe does not permit such operation because the gas does not leave the probe volume rapidly enough. We are reasonably confident, however, that operation at a frequency of 1 sec.^{-1} does reasonably approximate the higher frequency operation insofar as the characteristics of the plasma exhaust pulses are concerned. The possibility remains that in higher frequency operation the components are heated to a greater extent and the erosion rates are higher, leading to possible differences in the exhaust characteristics. Periodic gridded probe sampling of the exhaust during the course of high repetition rate extended runs can provide indications of any possible changes in the mode of operation. In addition to being aware of the problems involved in making detailed diagnostic measurements under the unrealistic conditions of single shot operation, one must also be aware of the potential pitfalls of making single shot measurements of mass flow and impulse.

The correlation of experimental results to theory is a problem area which requires further attention. Various attempts were made at fitting the experimental data to either moving current sheet or slug model mechanisms of operation, with the result that it became readily apparent that such models are inappropriate. Clearly, the assumptions of these models, that in the gun circuit equation the plasma loading term may be described simply as the

product of one-half the total electromagnetic force and the velocity of the moving current sheet is inapplicable. Elimination of this one assumption has gone far towards a better understanding of processes actually taking place in the accelerator discharge (e. g., that the electromagnetic thrust is applied throughout the interelectrode volume of the accelerator at any instant of time during the discharge rather than simply in the moving current sheet). Details of this new concept have been worked out to some extent for the case of the pulsed plasma accelerator. (See Appendix E) Further work would be desirable for this case. In conjunction with such an undertaking, it would also be desirable to obtain a much more detailed mapping than has been thus far obtained for the magnetic field in the inter-electrode volume, both in position and time for a variety of operating conditions.

Design of the gridded probe used in the studies reported here required a high degree of sophistication. For one thing, plasma densities are relatively high in the exhaust at reasonable distances from the accelerator muzzle. The resulting rather small Debye length dictates that very fine mesh screening be used for the probe grids. We found that we were just able to meet such requirements for the finest mesh screens commercially available. It was also discovered as a result of early experience that too few grids in the collector will give rise to undesirable coupling with the plasma accelerator and/or the potential of the plasma pulses as they approach the probe. It was found that no fewer than 4 grids were required to avoid such interactions and also to suppress secondaries from the final collecting element in the probe. While these multi-gridded probes worked with practically no problems when studying pulsed plasma accelerators with a nitrogen propellant in the specific impulse range of 5,000 seconds, operation in the same specific impulse range when using xenon as a propellant is considerably more difficult because of the very high stopping potentials required (several kilovolts). We have had success operating in this regime as well, but probes have a rather short lifetime and require frequent repair.

In our experience, it has been desirable to alter the capacitance and voltage with other parameters held fixed to obtain improved performance. For this reason, it is highly desirable to provide a flexible capacitor bank in which the capacitance may be varied over a wide range without effecting the total weight of the package in order that the thrust balance need not be altered, necessitating long operational shut downs. The cost of capacitors is of practical importance when making a large number of changes of this nature. As described in section IV-C, we have to a large extent provided such flexibility using capacitors with reasonable expense, lifetime, and dissipation factor. We had offered some thought to extending this sort of flexibility in terms of constructing an energy source capable of providing

the current in various waveform shapes for similar reasons. However, in retrospect, while this would be desirable from the standpoint of elegant technical approach, practicality demands and present experience supports the propriety of being satisfied with a variable capacitance energy storage unit. If the interelectrode volume of the accelerator were uniformly filled with propellant along its axis and if the electrodes were coaxial straight cylinders, a square wave input waveform for the current might be appropriate. However, changes in the electrode geometry of the accelerator appear to have circumvented such a requirement.

Erosion rate studies for several operating conditions have been made for our A-4T accelerator. In the case of the A-7D accelerator, however, statistical data are available only at the 5,000 second, 320 watt operating point. It would be desirable to extend these studies to other specific impulses and higher power operation. Furthermore, it would be desirable to study erosion rates as a function of various electrode materials. It is a remaining problem, therefore, to make a more detailed study of erosion rates incorporating, among other things, a comprehensive spectroscopic survey of the species in the exhaust stream.

Another long range requirement for practical application of these devices to space propulsion missions is a more systematic study of key components in the gun, particularly in the areas of energy storage, capacitance, and power conversion techniques, not to mention the ultimate requirement of a light weight and reliable energy source. Some informal studies have been made to this end already but a much more formal undertaking of this sort would be highly desirable at this time. Information on this topic as it exists now is presented below.

V. KEY COMPONENT TECHNOLOGY

A. IMPROVED PROPELLANT FEEDS

A propellant feed suitable for laboratory testing of a pulsed plasma accelerator should possess the following characteristics:

- a. It should be capable of supplying pulses of propellant of sufficiently short duration to provide maximum availability of propellant in the accelerator at the time of discharge.
- b. The amount of opening should be large enough to inject sufficient quantities of propellant consistent with the desired specific impulse, the power input to the accelerator, and the efficiency.
- c. The leak rate should be a negligible fraction of the total propellant flow rate.
- d. The quantity and distribution of propellant should be reproducible.
- e. The valve should have sufficient life to permit thorough evaluation of accelerator performance without resort to disassembly of the valve.

For projected use in a space system, the propellant feed should have the following additional characteristics:

- f. It should be simple, reliable, and long-lived, implying that the absence of moving parts and heavily bearing surfaces is desirable.
- g. It should utilize a small fraction of the total power input.
- h. It should be operable at the repetition rates associated with engine operation at elevated power levels, e. g. , 10 KW or higher.

The present eddy current valve discussed previously has in general met criteria a-e stated above, but its ability to meet the other criteria is questionable. Its primary drawback is the requirement of excessive energy for actuation and the strongly bearing teflon seat which has a limited life.

A solenoid valve has been built which operates at minimal energy inputs (less than 0.1 joule per shot) but its drawbacks were excessively long pulse widths and the fact that its seating arrangement was similar to that of the eddy current valve. The pulse width can be reduced by the use of

more efficient, lower inductance drive coils and high permeability field concentrators. Its potential for reliable long life operation would still be questionable.

A third category of valve has been built and tested at GE/SSL under company funding. This valve involves the use of a piezoelectric element to produce a seal with a surrounding surface. Several designs have been investigated but the one which has so far operated most favorably into an environmental pressure of 10^{-5} Torr is shown in Figure V-1 and Figure V-2. A voltage is applied across the terminals of a piezoelectric disc. Depending on the polarity, the disc either contracts or expands, making or breaking the seal with a surrounding "O" ring. Both teflon and metal "O" rings have been used in this design, with the metal ring providing the best performance in terms of propellant output for voltage applied. The teflon apparently "follows" the disc, decreasing the effective opening obtained. The piezoelectric valve has been operated with energy input on the order of .01 joules per shot. Although the width of the propellant pulse has not yet been measured, the resonant frequency of the piezoelectric disc is sufficiently high that the pulse width can easily be made low enough for application to the pulsed accelerator. (Such piezoelectric crystals are routinely operated at frequencies to 20 KC or more.)

The only moving element in the piezoelectric system is the piezoelectric material itself. The force on the bearing surface can be adjusted by changing the applied voltage. The need for a bearing surface might be eliminated entirely if the "O" ring is replaced by a cylinder which forms an annular passage with the edge of the piezoelectric disc. The conductance of this passage while the valve is in a closed position could be made sufficiently low to provide a negligible propellant leak rate.

B. THE CAPACITOR BANK

The key factors in the selection of the main discharge capacitors for the repetitively pulsed plasma accelerator are the lifetime (under pulsing conditions), the capacitor "Q", and the operating temperature. The mass of the capacitor bank subsystem, including its cooling provisions, is, of course, critical. Several thousand hours life (billions of high current discharges) will be required for most of the significant space propulsion missions now under study. High efficiency in the engine system demands a "Q" in the 50-100 range. The size of the cooling radiator, which maintains the temperature of the capacitor bank, is a function of the "Q" or capacitor losses, but is much more strongly affected by the operating temperature. Given a reasonable value of "Q" and life, the deciding factor in capacitor selection will be its operating temperature.

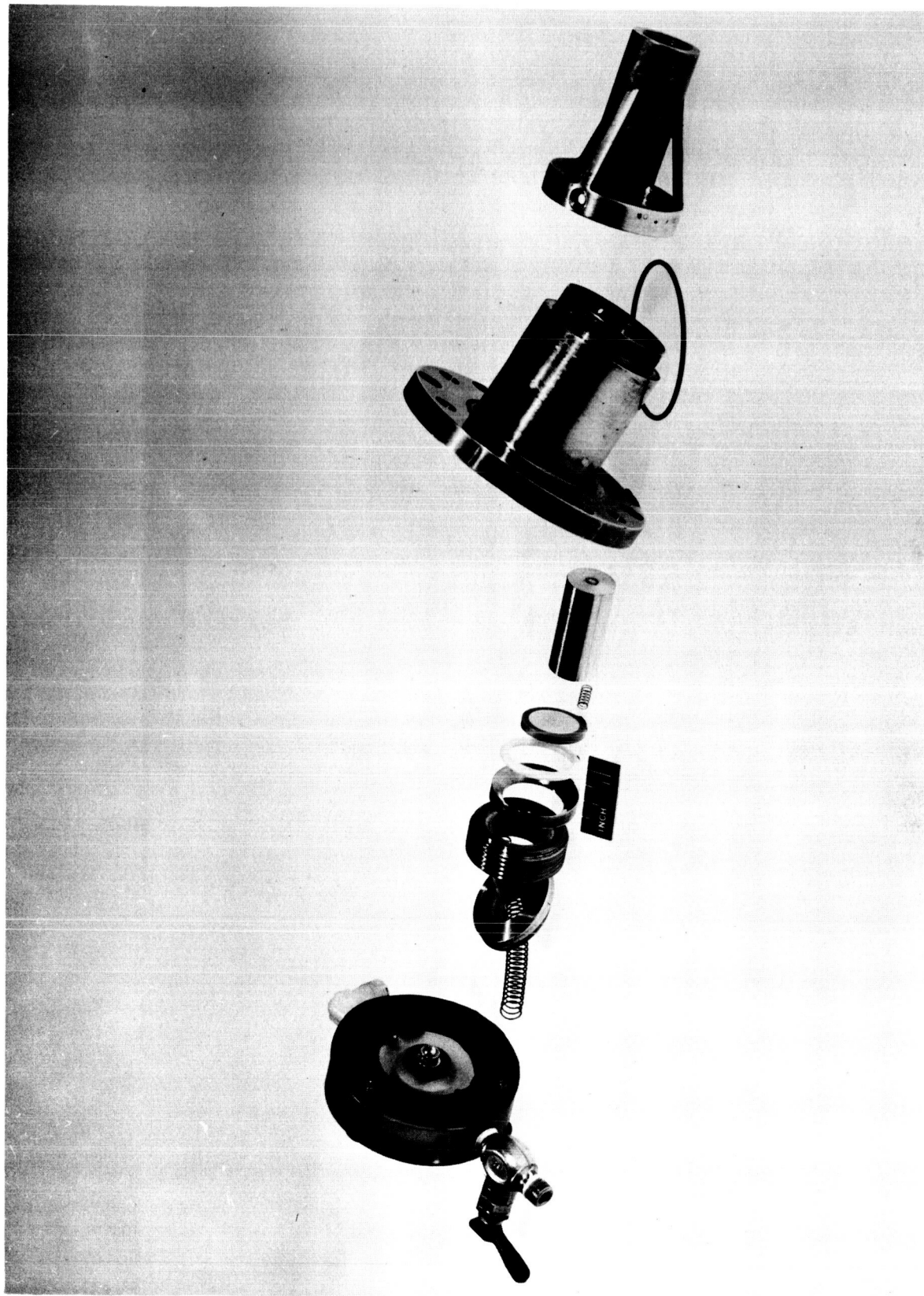
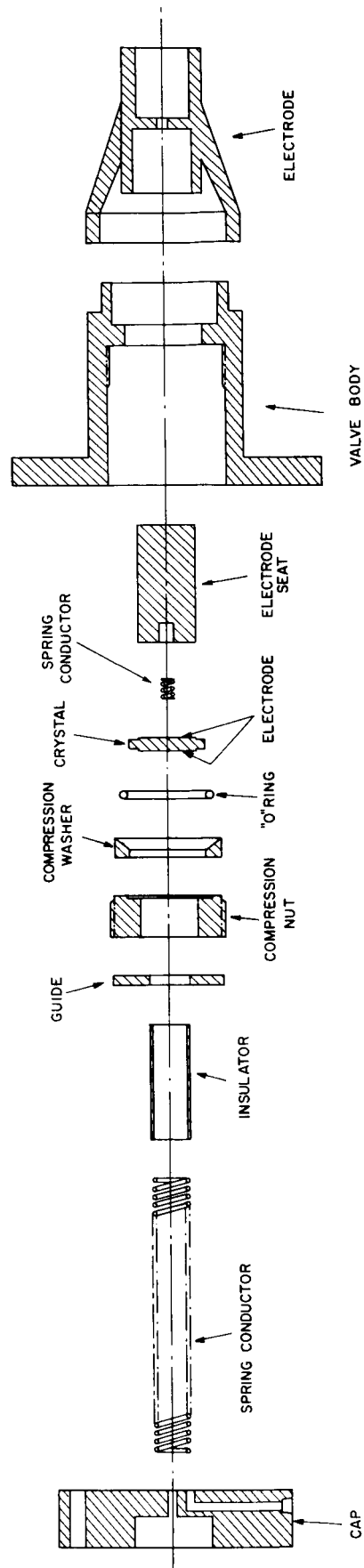


Figure V-1. Piezoelectric Valve and Electrode Components



PIEZOELECTRIC VALVE

0 207-346

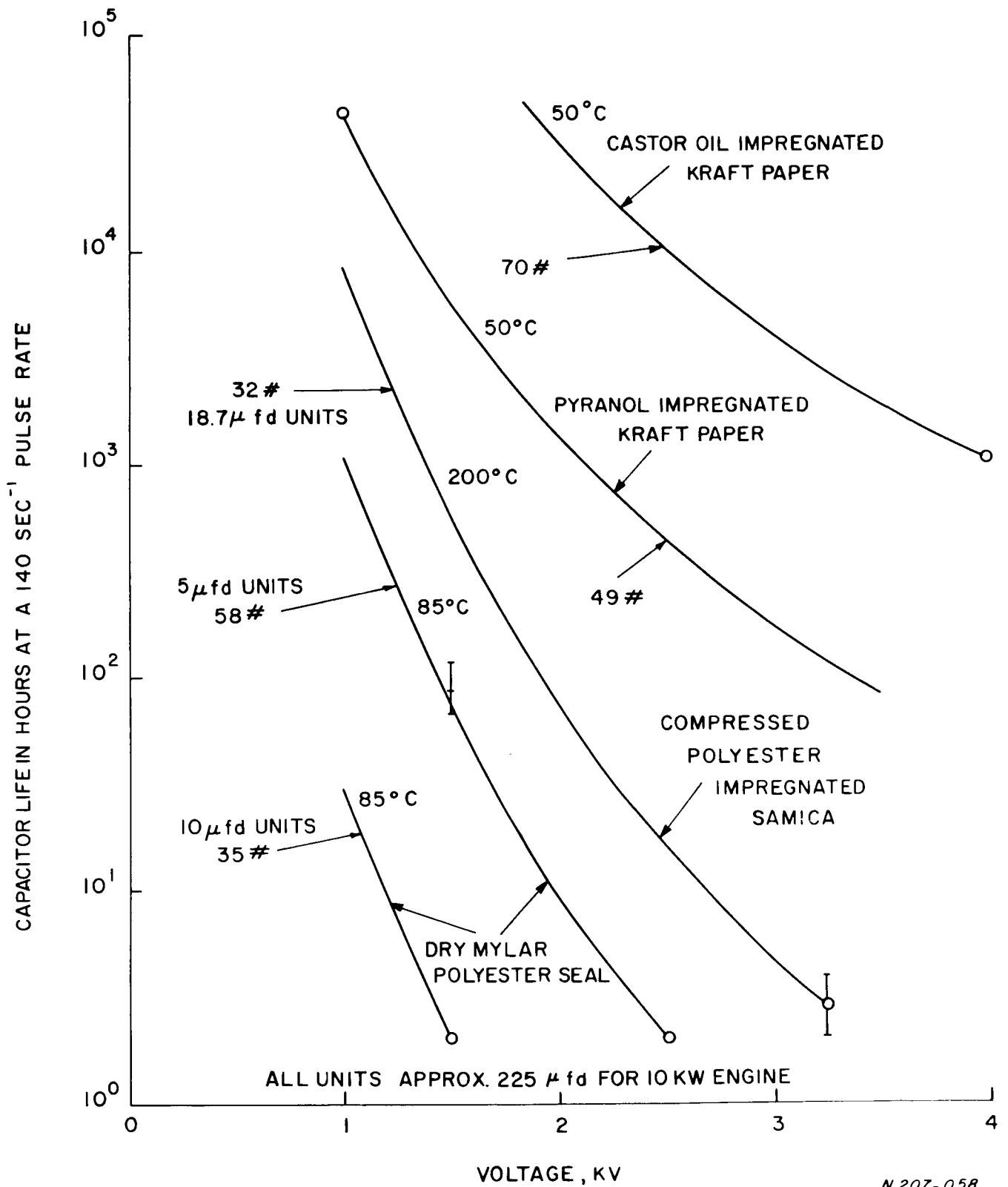
Figure V-2. Piezoelectric Valve and Accelerator Electrode Assembly.

The nominal rating of an optimum capacitor bank for the A-7D, based on extrapolation of present operating test data, is 225 μ fd at 800 volts peak charge. A voltage reversal of 25% is expected, leading to a peak to peak level of 1000 volts. The self-resonance frequency of the bank must be high, compared with the nearly critically damped 40 kc discharge. The values of voltage and capacitance lead to a pulse repetition rate of 140 pps for a power level of 10 KW. The life of the capacitor bank should be of the order of 50 hours (25,000,000 pulses) for laboratory testing of the engine and 5,000 hours (2,500,000,000 pulses) for an operational engine. This is in obvious contrast to the usual ratings of energy discharge capacitors at about 1,000,000 "shots" at high voltage stresses and will require appropriate derating to lower stresses for the extended life.

Three fundamental deterioration mechanisms may work together to lead to the failure of a capacitor. These are: 1) thermal degradation, 2) electrochemical action, and 3) corona damage. The first is basically chemical in nature and follows the Arrhenius Law of about tenfold decrease in life for 30°C higher temperature. The second is a function of the leakage current in the capacitor and is simply proportional to the energized period of the unit. It is important to note that this process is critically dependent on the electric field in the capacitor and life varies as about the inverse fifth power of the applied voltage. The third depends on ionization in gas void pockets in the insulation. These may be simply air bubbles trapped in the windings or cavities formed by degeneration of organic insulating materials. Such voids are of minimal importance at the low voltage level of this accelerator system and are not a source of significant decay in liquid impregnated units. This phenomenon, nevertheless, is the limiting element in solid dielectric systems, in which life varies as the inverse seventh power of the applied voltage.

The voltage surge during the pulse is a key factor in corona damage leading to a life rating in number of pulses, in contrast to the "time-on-voltage" life of corona-free systems. Since we are dealing here with a system involving about 500,000 pulses per hour, both classes of units may be evaluated on a common curve of life vs. applied voltage, as shown in Figure V-3. The curves of life vs. applied voltage are, of course, applicable to the individual units which have been built and rated by the manufacturer at the circled points on the curves and represent about 90% survival probability. The number of capacitors required to approximate the nominal 225 μ fd is shown with each curve as well as the total weight of the capacitor units and the limiting dielectric temperature.

Current developmental research on the coaxial plasma accelerator has made very effective use of dry film Mylar capacitors^{V-1}, which are inexpensive and flexible in their application. It may be seen from Figure V-3



N 207-058

Figure V-3. Capacitor Life vs. Operating Voltage for Various Temperatures, Designs, and Winding Weight.

that they are also heavy (particularly when the necessary coaxial return lead is considered) and of limited life for the eventual engine application. They should continue to be used in parametric research investigations but will be displaced by more suitable insulation systems in the prototype engines.

In contrast to the short lives of the dry film Mylar units is the extreme long life capability of the paper/pyranol and paper/castor oil impregnated capacitors.^{V-2} Both offer excellent prospects for low loss long-lived units with modest weight penalties on the units themselves. Unfortunately, their derating temperature is only 50°C which would pose an extreme problem in radiator design that should be avoided if at all possible. Here, again, in the laboratory such capacitors may provide welcome flexibility in design and will insure trouble-free operation.

Perhaps the best suited of the capacitor systems reviewed, to the specific needs of a prototype pulsed plasma engine, is the compressed polyester impregnated reconstituted mica capacitor^{V-3}. It is the lightest in weight and offers adequate life prospects for real missions. A prototype unit of excellent design has been fabricated and qualified for space flight on a Navy vehicle. The high allowable operating temperature for the dielectric, of 200°C, will be seen to afford important economies in the cooling system design.

A schematic cross-section of the prototype unit is shown in Figure V-4. The unit is fabricated as a single roll with a large circular inner mandrell, and a single layer Samica/aluminum foil winding. The roll is then vacuum impregnated with polyester resin and cured under a static pressure of 4000 psi, which minimizes the void problem. Current carrying tabs are inserted at eight azimuths in each layer of the two foils, proceeding alternately to the inner terminal cylinder, to which the case is also grounded, and to a contact ring which fills most of the end void. This minimizes resistance as does the 8 terminal bushing connection from the ring. The ringing frequency of this 18.7 μ fd unit, when shorted, is in excess of 1 megacycle, implying about 1 nanohenry of intrinsic inductance. With the aid of closely spaced parallel plates feeding the current to the accelerator, the stray inductance of the system may be substantially reduced. High temperature, low loss solid dielectric capacitors of this type are eminently suited to the development of prototype engine systems.

C. ELECTRODE AND INSULATOR MATERIALS

Copper has been used extensively as the electrode material up to this point because of its high electrical and thermal conductivity and relative ease of machining. Under most of the operating conditions thus far encountered,

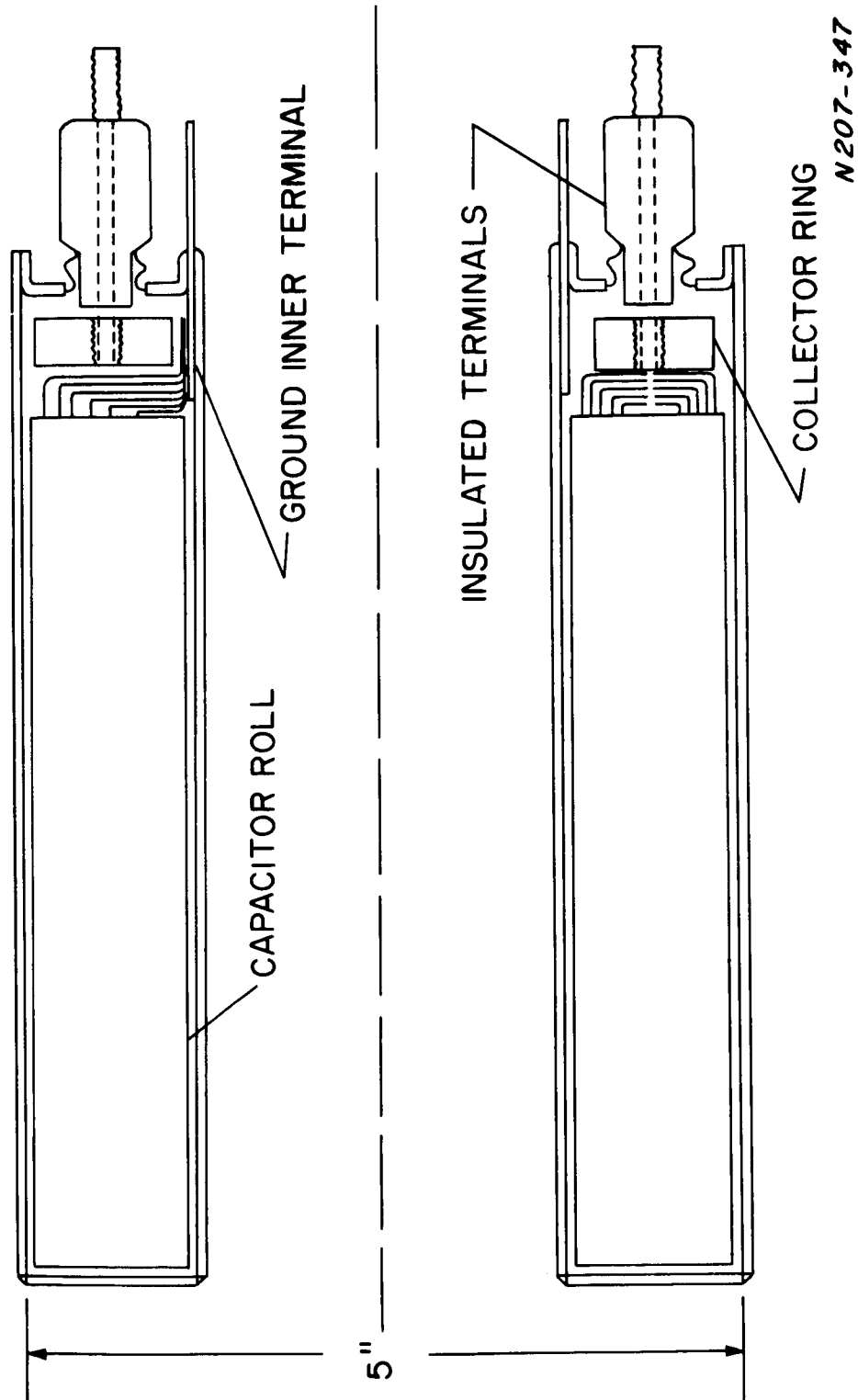


Figure V-4. Schematic Cross-Section of the Pre-Prototype Capacitor

its melting point has been sufficiently high to avoid overheating. There have been a few exceptions to this situation, however, when operating at higher power levels and low propellant mass loading of the accelerator (I_{sp} 's in the higher than 10,000 sec. range).

The sputtering rate of copper when bombarded by species such as xenon, cesium, or mercury ions, is known to be higher than other materials that might be used. Furthermore, it might be quite appropriate to investigate high electron emittance coatings for the cathode of the accelerator. In addition, if the electrodes are to be used as part of the radiator system for handling heating losses, it would be desirable to investigate highly emissive surfaces for this purpose. The use of molybdenum is being considered as a solution to these problems.

Pyrex has been used as the insulator material so far with a high degree of success. The high power limit of such material is not yet known and it may be necessary to go to lucalox or beryllium oxide spacers in higher power designs simply to handle the higher stress and strain to be encountered in high power operation. In addition, erosion rates of various insulating materials will have to be investigated as a function of power level and propellant loading conditions. Specifically, the effects of surface roughness on the breakdown characteristics and the effect of thermal transients and gradients on surface crazing of various insulating materials will have to be considered.

REFERENCES

- V-1. "Hi-Jul Energy Capacitors," Dearborn Electronic Laboratories
Orlando, Florida, Engineering Data 8-TR-61B.
- V-2. "E-200 High Temperature Capacitors," The Bendix Corporation,
Scintilla Division, Sidney, N. Y. #SL-92-2.
- V-3. General Electric Co. Capacitor Specification Sheet #175EC,
G. E. Capacitor Dept. Hudson Falls, New York.

APPENDIX A

OVERALL EFFICIENCY MEASUREMENTS

Overall efficiency, $\eta_o = T^2/2\dot{m}P$, and specific impulse, $I_{sp} = T/\dot{m}g$, are determined from measurements of thrust (T), total mass flow of the propellant (\dot{m}), and input power (P). Details of such measurements are described in this section.

1. Thrust Measurements

a. Thrust Balance

The thrust balance used here is of the loaded column type ^{A-1, A-2, II-1}. It supports all of the major components of the engine, including the valve and main storage bank capacitors, the coaxial plasma accelerator, and certain control circuitry, and was designed to easily accommodate a total loading up to 440 Kg., representing primarily the weight of the engine system, the engine housing, and the necessary counterweights. In spite of this relatively large mass, the thrust balance is capable of providing a measurable reaction to thrusts in the micronewton range. The columns utilized in our assembly consisted of three rectangular flexure plates mounted between a movable engine mounting rack and a stationary lower frame, and loaded to nearly their critical buckling point.

A photograph of the thrust balance assembly engine and capacitor housing mounted on the interchamber plate is shown in Figure A-1. The lower frame and flexure plates are constructed of a 31% Nickel alloy (Super Invar) in order to minimize any drifts which might occur due to thermal expansion transients. The main support frame is made of 304 stainless steel.

Gross correction of thrust balance level is obtained by means of screw jacks between the lower frame and the main support frame. The main support frame, in turn, may be adjusted from outside the vacuum system by a differential screw passing through a vacuum seal in the interchamber plate. This permits fine adjustment of the thrust balance null point without opening the vacuum chamber. Equal loading of the flexure plates is accomplished initially by adding counterweights to a pan affixed to the capacitor frame. Fine balance is subsequently made by sliding additional weights in two orthogonal directions in the horizontal plane.

The movement of the thrust balance under load is detected by a linear variable differential transformer. The transformer core is mounted on the moving portion of the balance and is mechanically independent of a coil

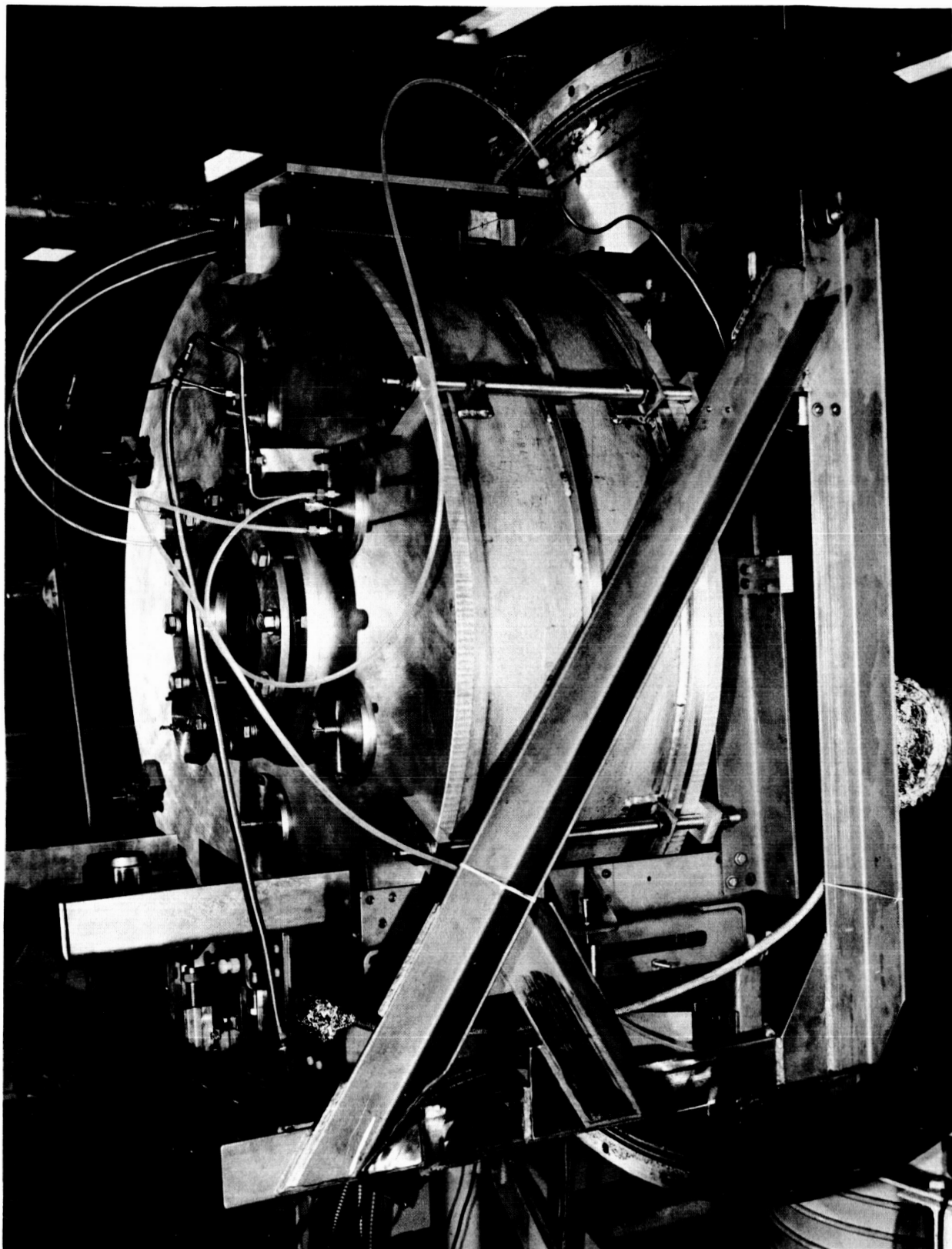


Figure A-1. Thrust Balance with Engine Housing

assembly mounted on the stationary portion. The calibrating element is a thin steel reed with a known force/deflection ratio, cantilevered from the moving portion of the thrust balance. Its free end is statically deflected from outside the vacuum system by a hand-operated screw arrangement passing through a vacuum seal. Calibration of the thrust balance was made before and after thrust runs.

Operation of the thrust balance has generally been in the thrust range below 45 millinewtons. This represents a deflection of the balance of less than 2 mils and is within the linear range of both the balance itself and the differential transformer. Thrust readings, therefore, have been made by recording the deflection directly on a strip chart recorder without use of the null-seeking solenoid.

Figure A-2 shows a chart record for typical thrust runs. The reed calibration prior to the run is shown in Figure A-3. Note that during the run, there was a slight shift in the balance null point, though the initial average deflection and final average deflection were the same. This shift is apparently due to a thermal effect since the balance returns to its original position after a short cooling period. This shift does not affect the accuracy of the readings since continuous monitoring allows the extent of the shift to be observed during the run and the initial and final deflection to be compared. (This will also be true with operation of the nulling solenoid, since final position of the thrust balance can always be compared with initial position and correction made in the solenoid current reading.)

The thrust balance has been operated with capacitor and electrode cooling lines attached. These lines are long flexible metal hose arranged vertically to minimize the coolant flow effect on the thrust stand. Sensitivity is not affected by connection of these cooling lines nor by the flowing coolant inside the lines.

2. Propellant Flow-Rate Measurement

The propellant input mass flow used in the determination of overall efficiency must include the gaseous propellant input and the mass eroded from the accelerator. The methods used for determining these flow rates are discussed below.

a. Gaseous Propellant Flow

The propellant flow into the accelerator during repetitive operation has been measured by two methods. The first, a calibrated tapered-capillary and ball flowmeter manufactured by the Matheson Company (Model 610), was inserted in the propellant feed line up to the valve. At a repetition rate of

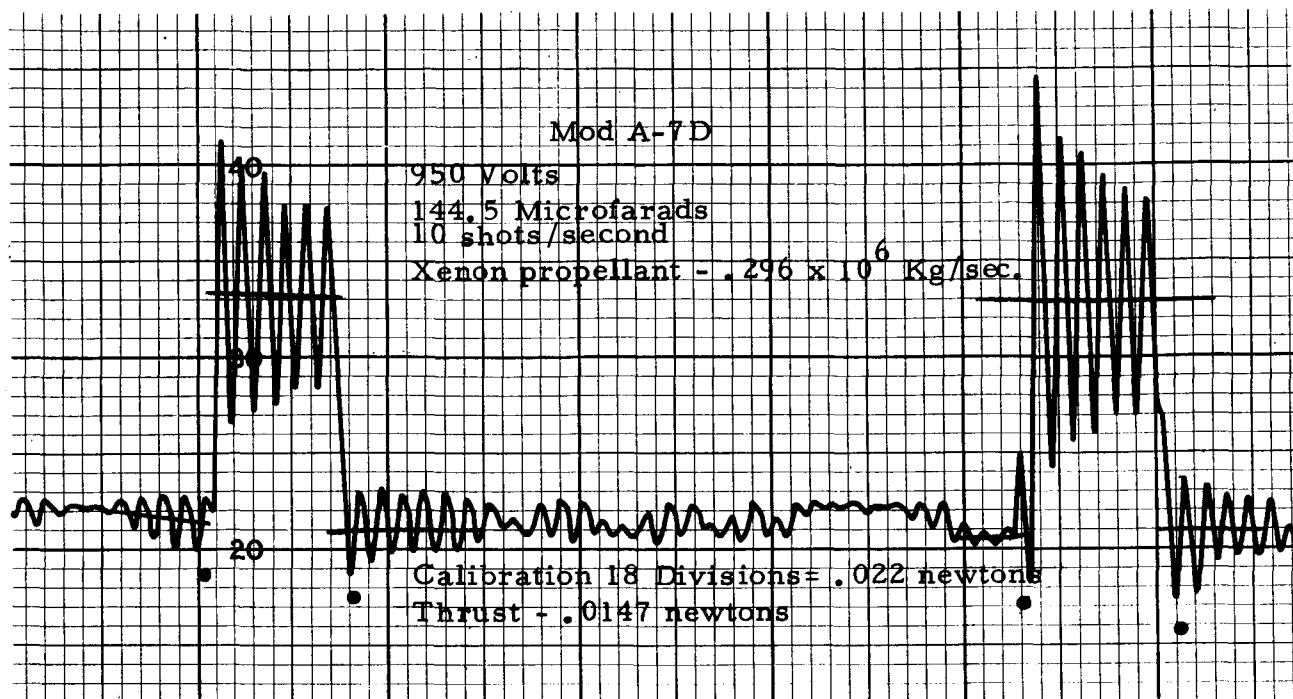


Figure A-2. Thrust Record for A-7D Accelerator

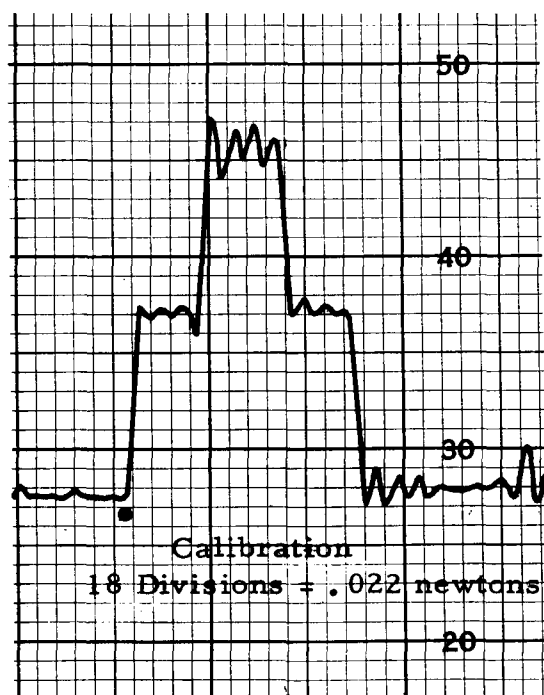


Figure A-3. Thrust Calibration Record

10 cps.; the ball remained essentially in a steady state position to permit accurate readings from the capillary tube. The calibrated accuracy of the flowmeter as specified by the manufacturer is $\pm 1\%$ of full scale reading. With typical measurements made at about $1/5$ of full scale, the accuracy of the measurement was $\pm 5\%$. A check of the calibration supplied by the manufacturer was made for various flow rates using a flowmeter calibrator (Brooks Model 1050) which is claimed by the manufacturer to have an accuracy within 0.2% of indicated volume. The calibrator is a volumetric collecting device. The gas from the flowmeter being calibrated is collected under a mercury-sealed piston in a precision-bore glass tube. Accurate indication of the volume of gas collected in a given time interval is made by timing the movement of the piston adjacent to a scale graduated directly in volumetric units. The mercury "O" ring seal on the piston is essentially frictionless and is leak tight. The soundness of the seal has been tested by filling a given volume and attempting to hold it for periods of up to ten hours. The change in the indicated volume after the latter period of time was found to be negligible. The laboratory calibration of the capillary flowmeter agreed within 5% with the calibration supplied by the manufacturer.

For accuracy greater than can be supplied by the capillary flowmeter, it appears that the flowmeter calibrator described above can itself be used in the propellant inlet line as a reservoir for propellant. The change in volume of the reservoir would thus be measured while the engine is operated.

Another type of flowmeter which has been used is the thermoelectric type (LF series) manufactured by the Haystings-Radist Company. This gauge employs the measurement of the differential cooling of a tube by gas passing through it to generate a D. C. voltage signal which is proportional to the mass flow rate. The signal output is displayed on a meter calibrated in standard c. c. per minute and can also be displayed on a recorder. The quoted accuracy is within 2% over the flowmeter range and is virtually insensitive to pressure and temperature changes. Readings of flow obtained with this meter agreed with those indicated by the capillary flowmeter within $\pm 2\%$.

b. Eroded Mass Flow

The contribution of eroded mass has been determined by periodic weighing of the accelerator components which have by many accumulated hours of running been found to provide the bulk of the eroded mass, i. e., the center electrode section forward of the gas injector ports and the electrodes of the discharge triggering system. Typical periods between weighings were represented by 100,000 shots, with a longer sampling provided by the ten-hour life test of the engine described in Section II.

3. Total Input Power

The measurement of the input power to the capacitor bank involves the determination of the capacitor voltage, the bank capacitance, and the engine firing rate:

$$P = 1/2 C V_o^2 \nu$$

The capacitance of the bank is measured by a calibrated impedance bridge (General Radio 1650-A) at a frequency of 1 KC. The accuracy of the capacitance reading is stated by the manufacturer to be $\pm 1\%$.

The voltage of the bank was measured by a calibrated Tektronix high voltage probe (Model P6015) placed across the capacitor flanges. The 1000:1 attenuated signal is recorded on an oscilloscope. The measurement is made with the engine operating at the desired repetition rate to insure that any possible change in voltage due to changes in the charging resistance will be readily recorded. Accuracy is estimated to be better than $\pm 2\%$.

The engine firing rate is obtained from the oscilloscope traces mentioned above, by using an oscilloscope sweep rate sufficient to record several shots on a single sweep. The time interval between the shots is then measured and compared to the set interval of the control circuit pulse generator. The pulse repetition rates so determined have never been found to differ. Accuracy is estimated to be better than $\pm 2\%$.

When using the Dearborn units, ($Q = 14$), the power consumed in the capacitor due to the finite "Q" was subtracted off when computing the input power:

$$P = \frac{1}{2} C V_o^2 \nu \left(1 - \frac{1}{Q}\right)$$

Q was determined for the entire gun circuit by measuring the width of the resonance peak with a shunt inductor bringing the center frequency to various values between 50 and 100 KC. Such a correction will not be necessary when using higher "Q" capacitors.

References

- A-1. R. F. Conner and J. Hyman, Jr., "Direct Thrust Measurement of Electrical Propulsion Devices," ARS Paper No. 2180-61 at ARS Space Flight Report to the Nation in New York, October 1961.
- A-2. J. R. Anderson, S. L. Eilenberg, J. E. Etter, R. N. Olson, "Evaluation of Ion Engine Performance," ARS Paper No. 2185-61, at ARS Space Flight Report to the Nation in New York, October 1961.

APPENDIX B

GAS DENSITY MEASUREMENTS

The requirement of knowing the distribution and relative quantity of the propellant injected into the pulsed plasma thruster has necessitated the development of a small fast response gauge. Previous experience both by Marshall^{B-1}, investigators in this laboratory, and others^{B-2} have shown that a vacuum tube could be modified to act as such a gauge. However, the tube used in these experiments, the 6AH6, was too large for detailed investigations of a volume as small as the plasma accelerator.

1. Probe Design

To improve spatial resolution, a tube was chosen which is considerably smaller than the 6AH6. This tube, the subminiature CK5702 beam power pentode which can sample a 1/2 cc region, was easily modified so that it would be open for gas molecules. In addition, it has a high second grid power rating. The only modifications required were the removal of the glass envelope and the slitting of the top insulating wafer so that gas molecules impinging from that end could enter the tube. A sample probe is shown in position in front of the muzzle of a pulsed plasma gun in Figure B-1. A self-biasing circuit was chosen for ease of operation and is shown in Figure B-2.

The function of the first grid is to control the emission current. In the region of the second, the electrons have been accelerated to energies where ionization is most probable. The ions created in this region, and the lesser number generated in the vicinity of the third grid and the anode, then move to the least positive electrodes, the anode and third grid. Electrons are collected by the second grid.

The tube was mounted on the end of a 1/2" stainless steel tube by means of a glass leader and nine pin socket. The steel tube entered the vacuum through a sliding seal that allowed axial movement which in turn was mounted on a movable track that permitted radial motion. In addition, the whole assembly could be rotated, with little difficulty, to obtain azimuthal motion. Thus, sufficient flexibility was available for a complete mapping of the gas density in the gun.

2. Probe Operation

At no time during the course of these measurements was an absolute measure of pressure necessary. Relative values and ratios were the form

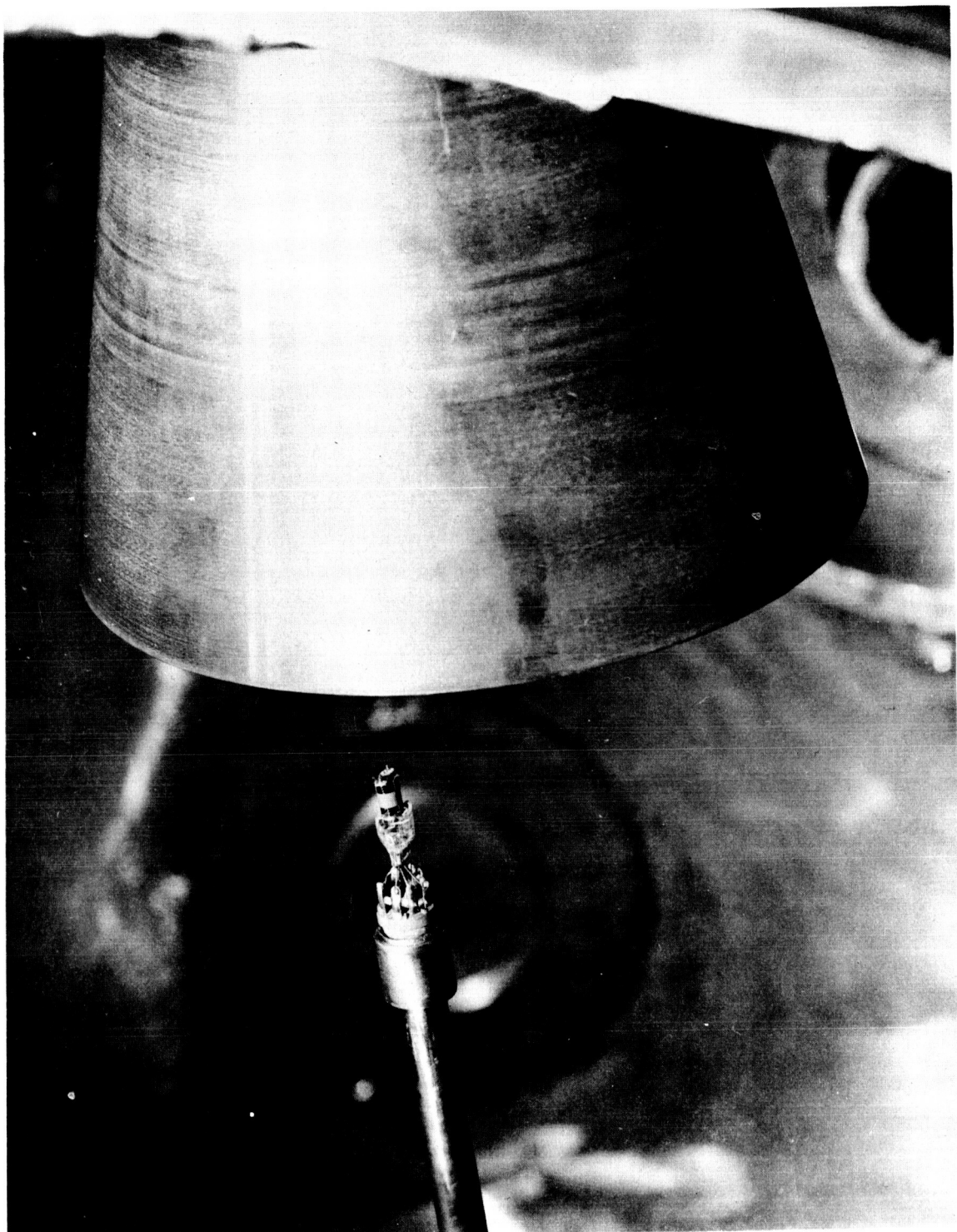
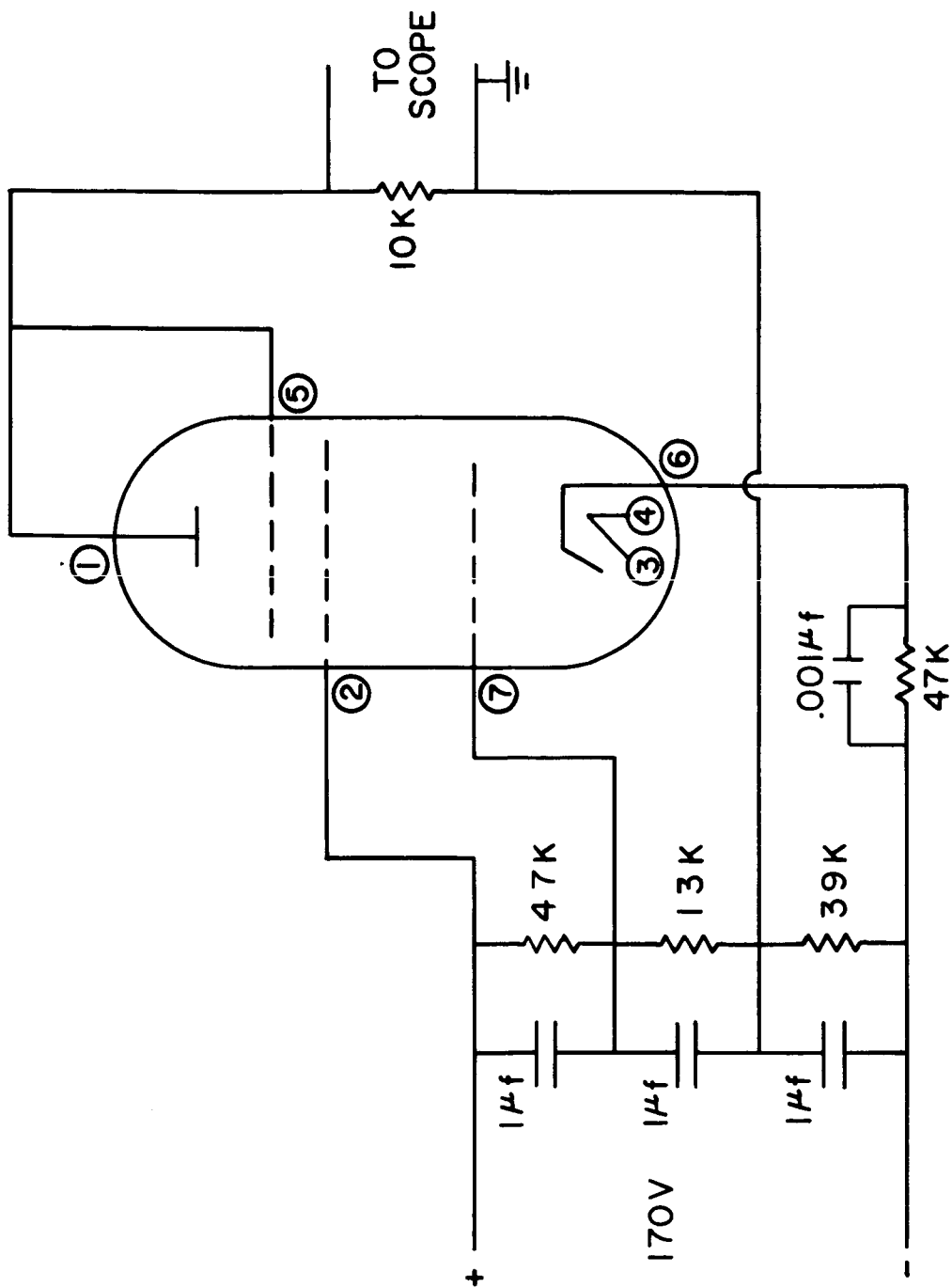


Figure B-1. Gas Density Probe



N 207 - 348

Figure B-2. Electrical Circuit for CK5702 Gas Density Probe.

of all reduced data. Nonetheless, calibrations performed in this laboratory and those independently found by others^{B-3} consistently gave values of about 400 μ Hg/volt. In addition, the response was found to be linear at pressures up to 1 mm Hg, well above the maximum pressures observed at the nozzles.

When measurements were made in the large tank, background pressure was consistently at 10^{-5} mm Hg or below and therefore several orders of magnitude below the lowest observed propellant density.

The probe lifetime under high vacuum conditions was extremely long. However, under continuous testing, degeneration of filament caused the emission to fall after a day or two and the voltage on the filament had to be raised. Ultimately, the filament failed or anomalous voltages were read across the anode resistor. As a check of the tube condition, the anode voltage was monitored and the tube was discarded when it was no longer usable.

The response time as observed in this laboratory was faster than 20 microseconds. However, measurements performed elsewhere^{B-3} indicated a risetime of at least .5 microseconds. Evidently, response is not a serious limitation. A sample trace is shown in Figure B-3. A high degree of repeatability has been observed, even when tests have been separated by several days.

3. Measurements

The data taken during any given run can be divided into two groups, that intended for construction of isobars (constant pressure contour plots) and that intended for the determination of the amount of propellant available to the discharge.

The construction of isobars requires a detailed sampling of the pressure at many positions within the gun. In general, data were taken at about 15-20 axial positions along 6-7 different radial positions in a plane including the gun axis. The pressures at all these positions at a given time are recorded, and constant pressure lines are drawn giving a picture of the propellant distribution.

A series of such pictures at different times displays in detail the progress of the propellant from the feed nozzles.

The determination of the amount of propellant available to the discharge reduces to the problem of determining what fraction of the injected gas has passed the feed nozzles as a function of time and what fraction has

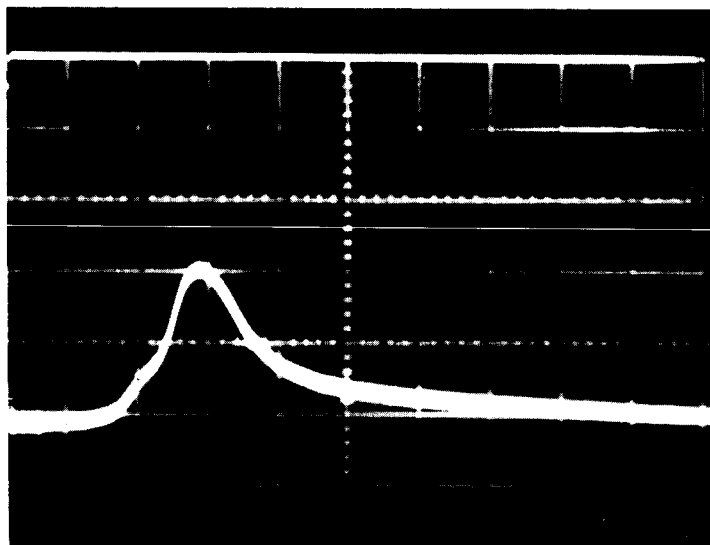


Figure B-3. Sample Gas Density Probe Trace
.5 ms/cm. .01 V/cm.
Xenon Propellant

passed a plane beyond the accelerator muzzle at which the thrust density has become negligible. Current distribution measurements indicate that the current has fallen to 15% of its maximum value 5 cm beyond the gun muzzle, indicating a thrust density of 2.25% of its maximum value. Thus, the propellant that is available to the discharge has been taken to be that which is between the nozzles and a plane 5 cm downstream from the muzzle.

The fraction of the propellant that has left the feed nozzles at a given time T can now be determined if one assumes that the propellant velocity through the nozzle is roughly constant during the passage of the bulk of the gas pulse. Then the ratio of the amount of gas that has flowed through the nozzle up to time T , to the total that will flow for the entire pulse is

$$\frac{K \int_0^T P \delta t}{K \int_0^{\infty} P \delta t},$$

where the constant K contains the propellant velocity, various geometrical factors and conversion factors from density to pressure. The fraction of the propellant that has passed the 5 cm plane can be determined in a similar fashion, only the propellant flux must be integrated over the muzzle area since the flux here is a function of the radial position, while the flux exiting from the feed nozzle is sufficiently localized radially so that this sort of spatial integration is unnecessary. The fraction of the propellant that has flowed through the muzzle at time T is then given by

$$\frac{\int_0^T \int_0^R P r \delta r \delta t}{\int_0^{\infty} \int_0^R P r \delta r \delta t}$$

where R is the radius of the outer electrode and all constants in common in numerator and denominator have been cancelled.

REFERENCES

- B-1. Marshall, J., "Hydromagnetic Plasma Gun," Proceedings of the Fourth Lockheed Symposium on MHD Plasma Acceleration, S. W. Kash, editor, Stanford University Press, 1960.
- B-2. T. J. Gooding et al. Development of a Coaxial Plasma Gas for Space Propulsion NASA CR 54245 .
- B-3. An independent study of the CK5702 Pressure was Performed by E. A. Valsamakis and was Published as Grumman Research Department Memorandum RM-268, Feb. 1965. This report exclusively considers the operation of this probe.

APPENDIX C

MULTIGRIDDED PARTICLE COLLECTOR

The following is a description of the multigridded particle collector used to examine the plasma exhaust from the A-7D plasma accelerator and to provide the data presented in Section II-E.

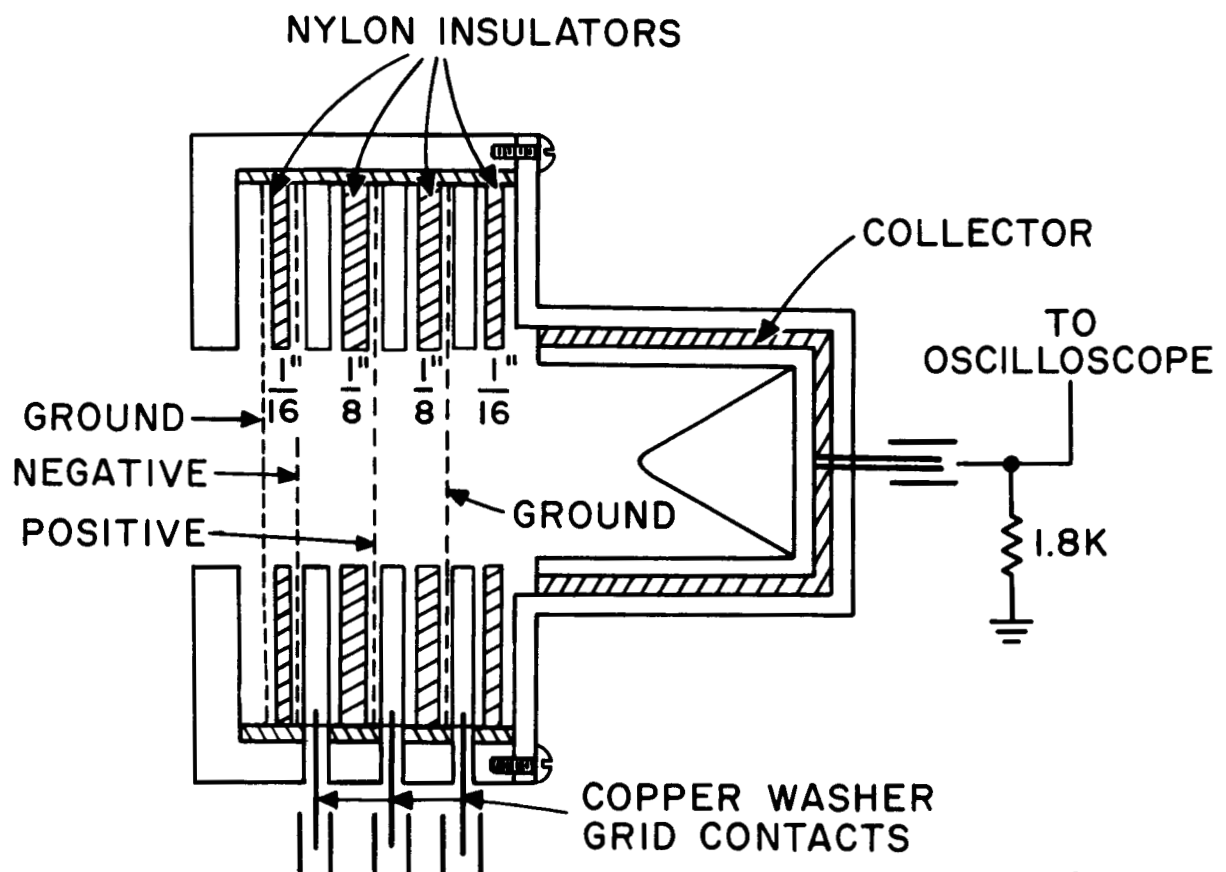
A series of grids sandwiched between insulating washers and contacted by copper washers makes up the controlling structure of the probe. A cup type of collector with a reentrant cone in its center was placed behind the grids (Figure C-1). Voltages were then fed through a multi-pin header soldered at the end of a 1/2" stainless steel tube and the grid and collector assembly was in turn supported by a fitting also attached to the tube (see Figure C-2). The entire assembly was then shielded from plasma not entering the grids themselves by an enclosed can (Figure C-3).

The leads supplying power through the aforementioned header were 50 Ω coax. The circuit supplying them is shown in Figure C-4.

This design was found to be the bare minimum necessary for reliable operation. Grids with 200 wires to the inch were used. This wire spacing and the distance between grids insured there would be no Debye shielding. Actual calibration, by comparing the signals obtained with two grids and four grids in place, shows that the set of four grids had a transmissivity of 1/150. The maximum current allowable through such grids, without altering the maximum potentials applied to the ions, (see Figure C-5) has never been exceeded and has only been approached in the large spacing surrounding the high voltage grid. The front grid (see Figure C-1) was grounded, as was the outer shell. This potential is close to the plasma potential and does not cause extraneous fields to affect the ions before they enter the probe. In addition, this grid acts as a shield for the interior and collects the electrons that are repelled by the following grid. This next grid, 1/16" back, is biased negatively to repel electrons so that only ions enter the following regions. The third grid is separated by 1/8" insulators and has high positive voltages applied to it to control the energy of the ions reaching the collector. The last grid is grounded at the outer shell and acts as an electrostatic shield for the collector.

The collector itself is designed so that the bulk of secondary electrons ejected by ion bombardment go toward other surfaces of the collector. The cone in the collector cup is placed there for this purpose.

The outer shield (all that is visible in Figure C-3) is placed there for the purpose of excluding all plasma from the header and other places where sparking might occur. Otherwise, when high positive potentials were applied to stop heavy ions (i. e., xenon), destructive sparking invariably resulted. (This difficulty was not present for the low voltages required to stop light ions, e. g., nitrogen.)



A205A719

Figure C-1. Gridded Probe for Measurement of Ion Energies

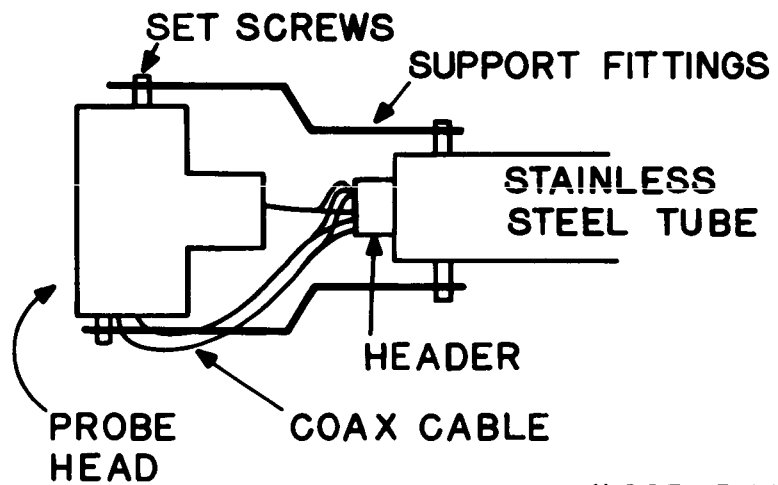


Figure C-2. Probe Head Support

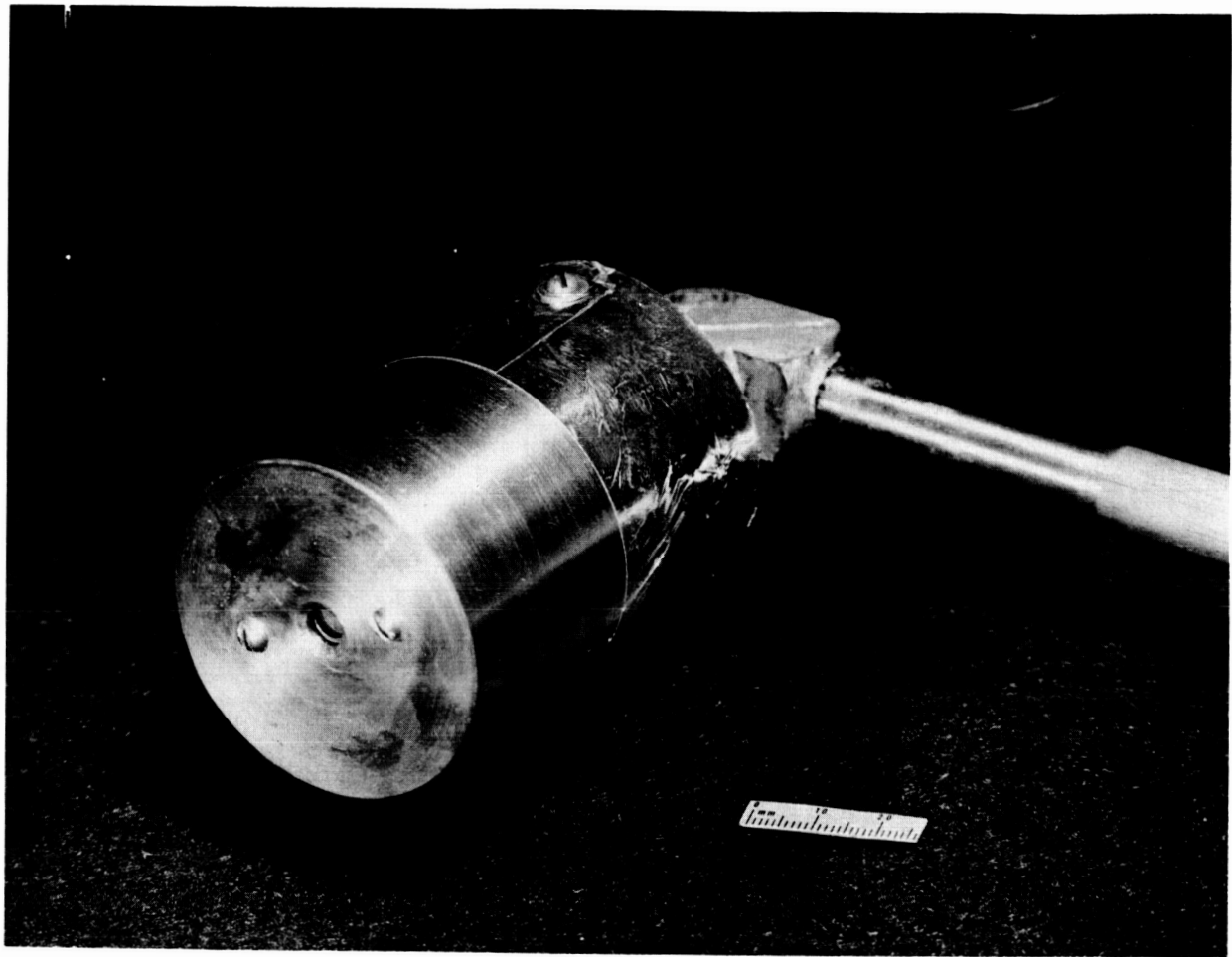


Figure C-3. Gridded Probe in Shield

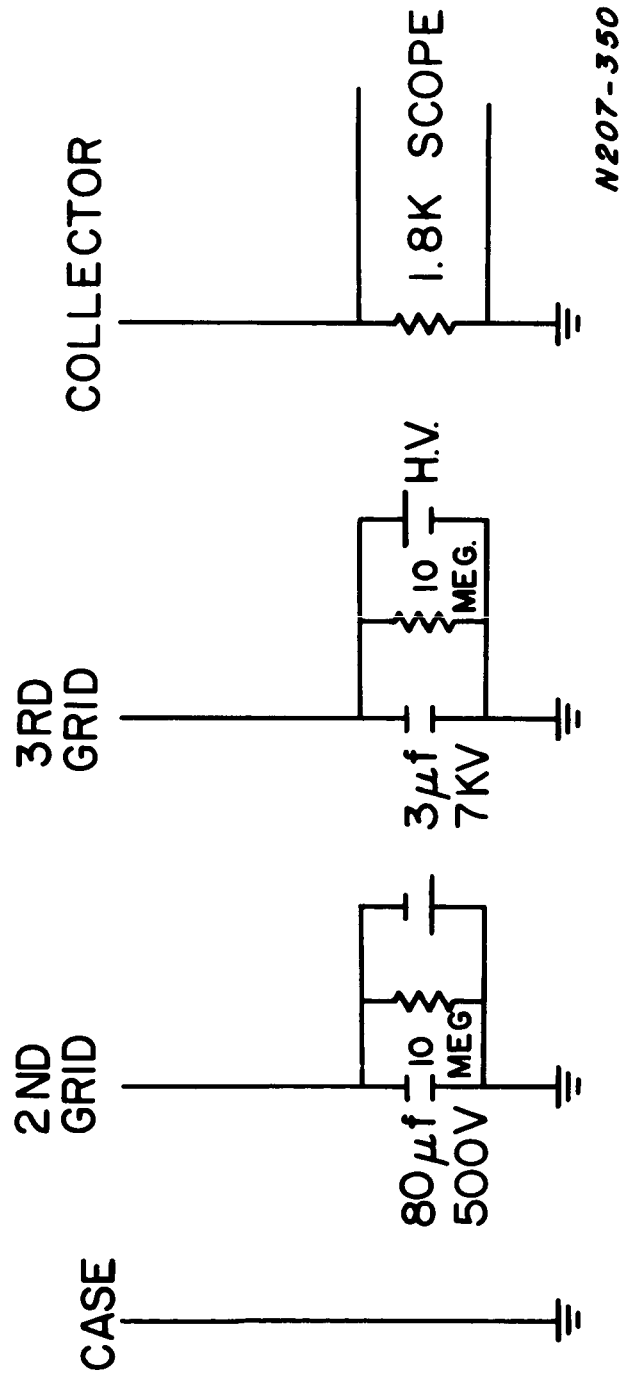
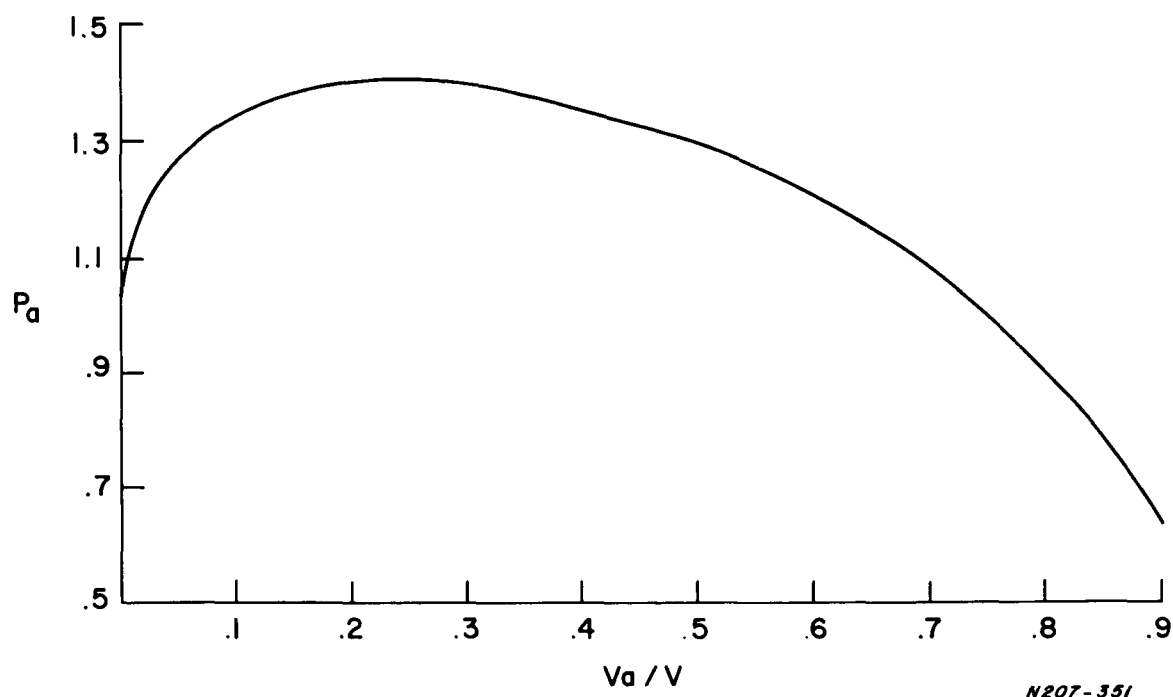


Figure C-4. Electrical Circuit for Gridded Probe



Adapted from Salzburg and Haef, RCA Review, Jan. 1938 (p. 336).

(For currents less than these values virtual cathodes cannot occur, except for $V_c/V_g \gtrsim .32$ where $P_a < 1$ cures this.)

Xenon

$$P_a = 1.44 \times 10^4 \frac{I_o^{1/2} (a/\text{cm}^2) a (\text{cm})}{V^{3/4}}$$

Nitrogen

$$P_a = 8.3 \times 10^3 \frac{I_o^{1/2} a}{V^{3/4}}$$

I_o is incident ion current

V is the energy of ions in volts plus negative potention on 2nd grid

V_a is the positive ion repelling voltage subtracted from the ion energy in volts

P_a is the dimensionless parameter introduced in above reference

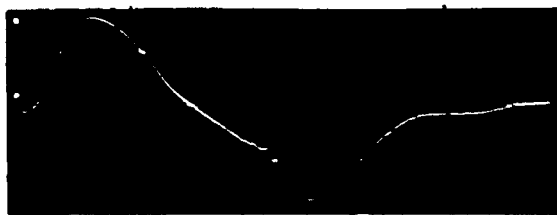
Figure C-5. Variation of Maximum Current Through 2nd and 3rd Grids, Not Allowing a Potential Maximum Above That of 3rd Grid.

APPENDIX D

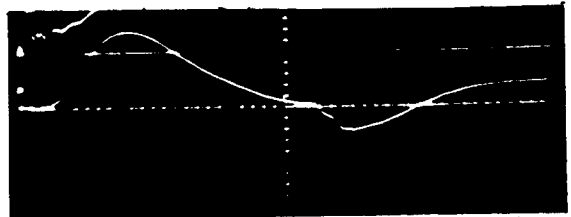
MEASUREMENTS OF MAGNETIC FIELDS IN THE A-7D

ACCELERATOR

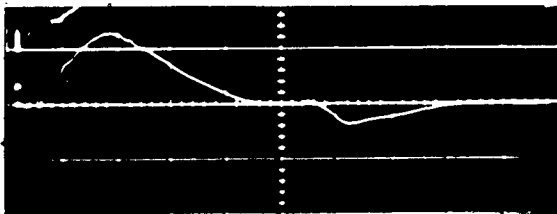
Using a probe mounted on an externally controlled carriage, a series of B_θ field measurements were made at various axial positions in and out of the gun, with 950 volts initially on the 144.5 μ fd energy storage bank. Examples of the signals observed are shown in Figure D-1. The signals are plotted as B_θ vs. position for various times during the discharge in Figure D-2. It is apparent that the current is not sufficiently localized in a thin sheet to support a simple current sheet model for this accelerator.



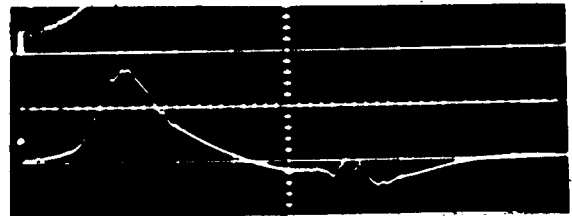
$z = 0 \text{ cm}$.01 volts/cm.



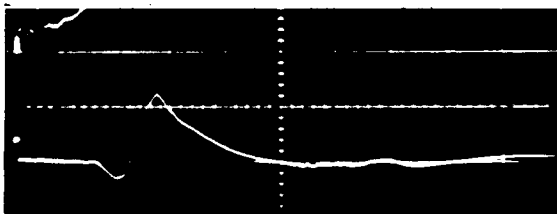
$z = 5.08 \text{ cm}$.02 volts/cm.



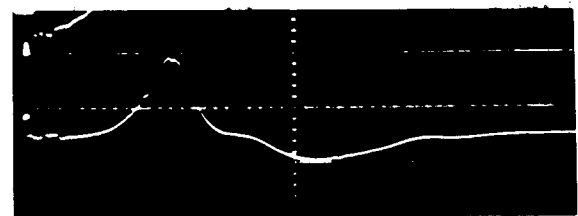
$z = 7.62 \text{ cm}$.02 volts/cm.



$z = 10.16 \text{ cm}$.01 volts/cm.

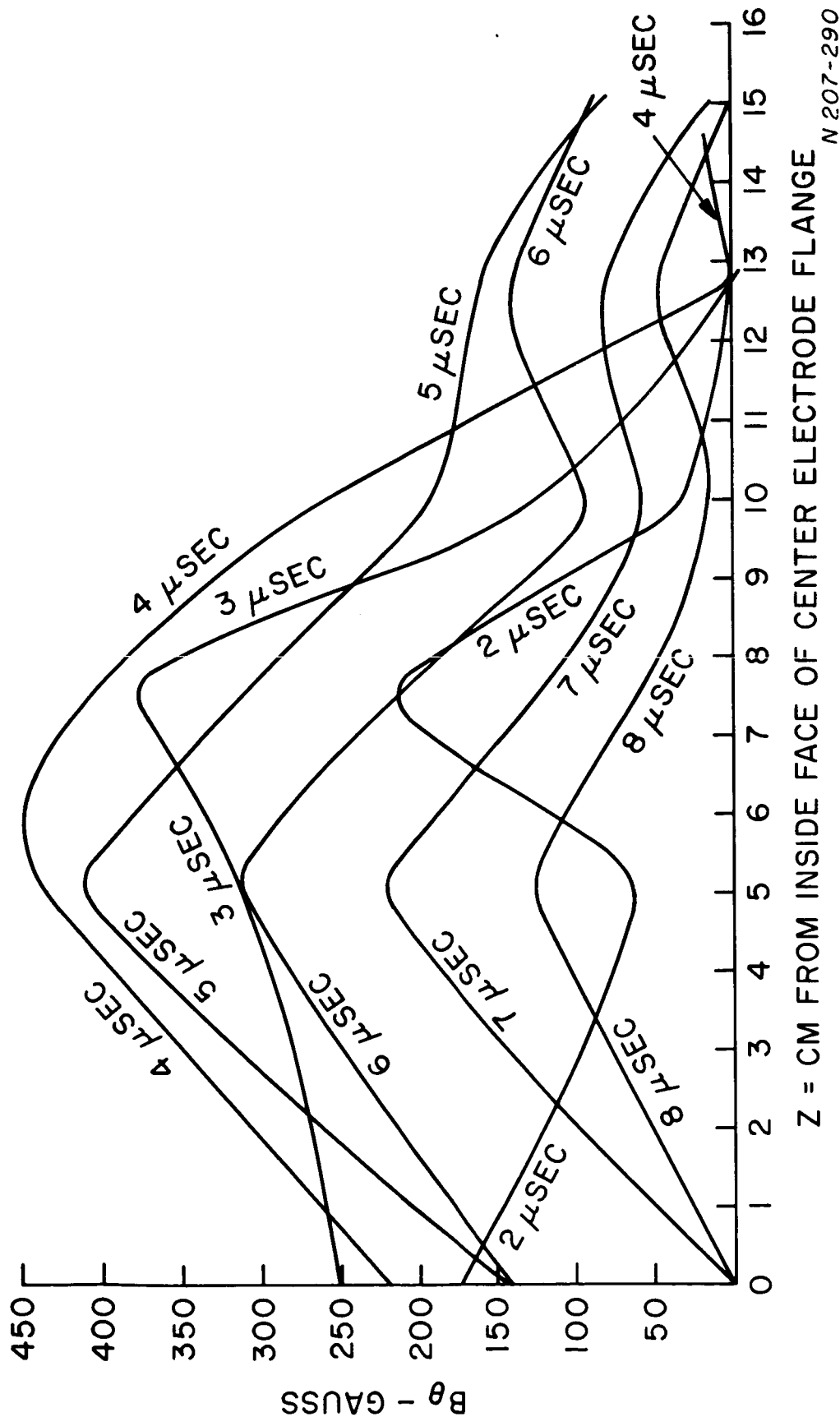


$z = 12.70 \text{ cm}$.01 volts/cm.



$z = 15.24 \text{ cm}$.005 volts/cm.

Figure D-1. B_{θ} Probe Signals for Different Axial Positions Mod A-7D
Accelerator 950 V 144.5 μ fd, Xenon Sweep 2 usec/cm.
Radial position, 4.5 cm from center line of Accelerator.



N 207-290

Figure D-2. B_θ vs. Axial Position for Various Times, A-7D Accelerator, 950 V, 144.5 μ fd, xenon, $\dot{m} = .296$ mg/sec.

APPENDIX E

PLASMA ACCELERATOR THEORY^{E-1}

1. Introduction

Various authors^{E-2, 3, 4, 5, 6} have studied the motion of current sheets in coaxial plasma guns and other accelerators with the intention of verifying one or another of several possible theoretical models describing the energy transfer in a coaxial gun. The general technique has been to present the data as current sheet position vs. time, and compare the resulting curve with predictions from theory. An alternate and convenient technique for checking these models is to find the current sheet velocity as a function of total current flow and mass distribution in the gun. For the two coaxial plasma guns that have been studied^{E-7} in this manner at this laboratory, it was found that the latter method of comparison indicated that none of the various models considered were valid for either gun, for different reasons.

In the case of the Model R gun^{E-7} in which reasonably well-defined current sheets were found to propagate, such a comparison was reasonable, but none of the models (slug, snowplow, Rosenbluth sheath, transparent piston) appeared to fit the experimental data. In all of these models, there is an implicit assumption that the current in the sheet is localized and purely radial. This assumption leads directly to the conclusion that the total instantaneous axial force exerted by the current sheet is

$$F = \frac{1}{2} L' i^2 \quad (1)$$

where L' is the inductance per unit length of the accelerator and i is the instantaneous total current in the gun circuit. An additional assumption is usually made^{E-2, 3, 4, 5, 6} that power is transferred into mechanical motion of the plasma at the rate

$$P_{\text{mech}} = \frac{1}{2} L' i^2 \dot{x} \quad (2)$$

where \dot{x} is the velocity of the current sheet. (An entirely equivalent statement is that the voltage drop across the gun terminals is given by

$$V_{\text{gun}} = i R + \frac{d}{dt} (L i) \quad (3)$$

where

$$L(t) = L_0 + L' x(t) \quad (4)$$

The various models that have been listed, then, specify further different rates at which directed energy is obtained by the plasma and hence an instantaneous energy transfer efficiency. This can be universally expressed as

$$\eta_{E.T.}(x) = \frac{P_{kin}}{P_{mech}} = \frac{\frac{1}{2} A \rho u^2 \dot{x}}{\frac{1}{2} L i^2 \dot{x}} = \frac{u}{2 \dot{x}} = \frac{L}{4 A \rho} \frac{i^2}{\dot{x}^2} \quad (5)$$

where $\rho(x)$ is the particle density ahead of the sheet, $u(x)$ is the velocity given to the particles by the sheet, and the electromagnetic force $(\frac{1}{2} L i^2)$ has been equated to the fluid dynamic pressure $(A \rho u \dot{x})$ across the sheet. Thus, as can be seen from the last equality of Equation (5), the instantaneous efficiency according to these models may be determined by measurement of i , \dot{x} , and $\rho(x)$. When this was done for the data from the R-gun^{E-7}, the $\eta_{E.T.}$ value was much greater than unity for three out of the four conditions examined. It was thus concluded that none of the models listed applied to this particular set of conditions. Recognizing that directed energy can be imparted to a plasma even in the absence of a moving current sheet ($\dot{x} = 0$ for a so-called MPD arc), the assumption embodied in Equations (2) and (3) is open to question. It was concluded that this assumption was the basis for the difficulty in obtaining agreement between the predictions from the various models and the data from our experiments.

In the case of the A-4T gun^{E-7}, the current sheet was too poorly defined to permit sensible comparison with the models listed here. Although fewer data are available for the A-7D, enough are available to state with confidence that the current between the electrodes is not localized sufficiently for comparison with thin-sheet models and in fact is similar in many respects to that in the A-4T. The analysis that follows is specifically directed towards a class of guns similar to the A-7D, but many of the arguments are felt to be universally applicable to all cases of $J \times B$ acceleration, whether there be a well-defined sheet, a more generally distributed volume current varying in time, or a perfectly stationary current distribution.

2. Accelerator Operation Model

The axial injection accelerator operation involves the movement of a discharge from the breech to the muzzle of the gun. As shown in Figure E-1, this concept naturally leads to dividing the acceleration process into the following four distinct stages: 1) current build-up, 2) true cathode acceleration, 3) virtual cathode acceleration, and 4) quasi-stationary discharge acceleration. Each of these stages is described in more detail in the following.

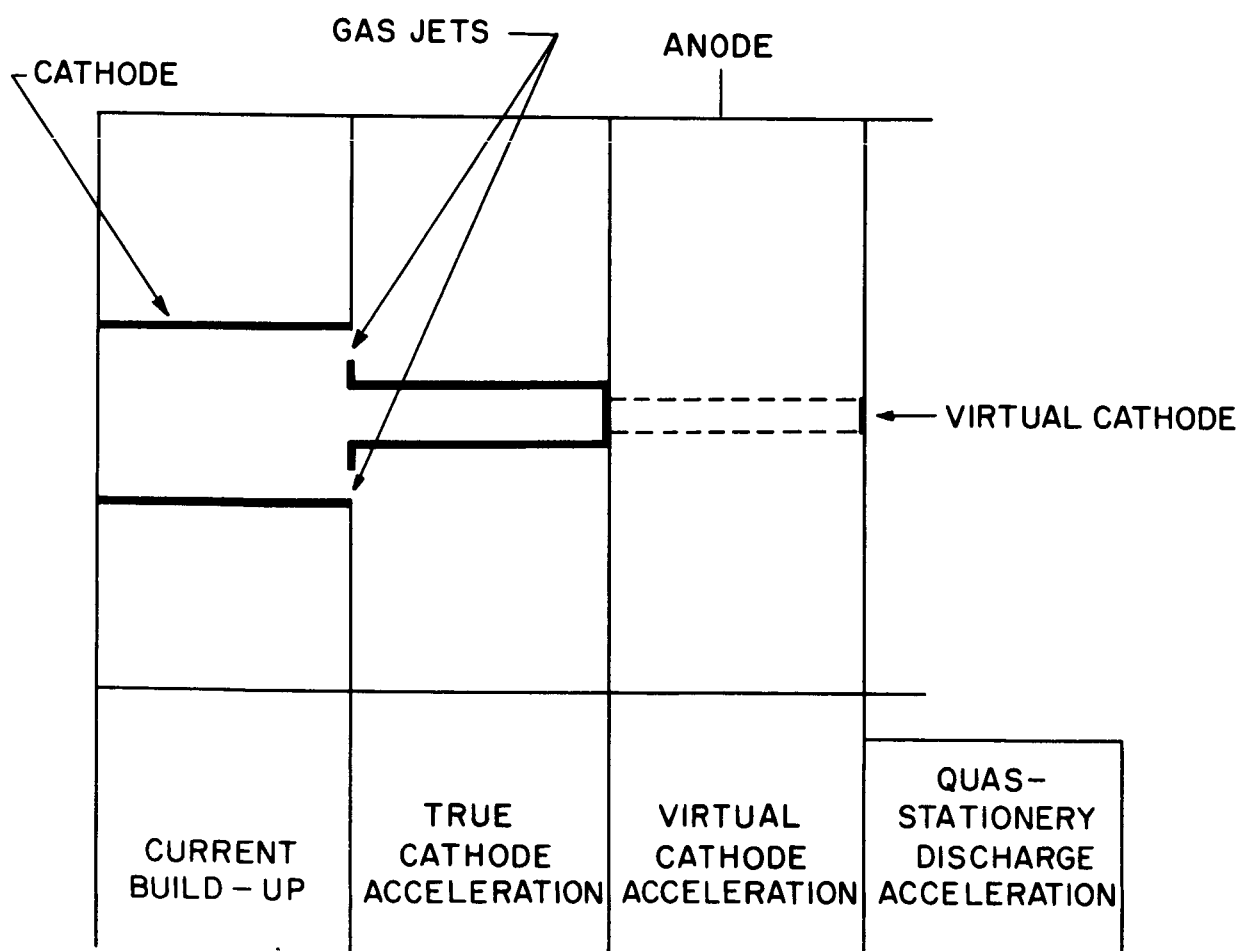


Figure E-1. Four-Stage Acceleration Process in the A-7D Accelerator.

a. Current Build-Up

During this phase, the low-current discharge is moving through a region of low inductance per unit length (since the electrode radius ratio is low) and low gas density (since the gas jets tend to push the propellant ahead of this region). This permits the current to build up rapidly to the high value which is required to give a high force during the second and later stages. At the same time, the low level of applied force ($\frac{1}{2} L i^2$) during this period contributes to a relatively low power consumption.

b. True Cathode Acceleration

The electrode radius ratio in the second stage is high (about 10:1) and by the time the leading edge of discharge arrives here the current has built up to a high level. In addition, the gas density encountered by the current sheet in this stage will be high. Thus, this stage is likely to be the one in which significant propellant acceleration takes place. If considerable energy is left in the capacitors by the time the leading edge of current sheet reaches the end of the true cathode, the third stage and fourth stages may be more important.

c. Virtual Cathode Acceleration

After the leading edge of the current sheet reaches the end of the true cathode, it now appears that it continues to move by means of establishing a virtual cathode. The current in the virtual cathode will tend to be self-pinching so that the effective electrode radius ratio may be considerably greater than the actual electrode ratio of the preceding stage. This will mean that during the virtual cathode acceleration process the inductance per unit length and the force on the plasma may be greater than in the true cathode acceleration stage provided that the current has not yet decayed significantly. The virtual cathode acceleration process ends when a quasi-stationary discharge is established at the muzzle.

d. Quasi-Stationary Discharge Acceleration

Under most operating conditions of the A-7D accelerator, it has been observed that an appreciable amount of energy is left in the capacitor by the time that the discharge has reached a more or less constant position near the muzzle of the accelerator. After this time is reached, currents are observed to flow throughout the inter-electrode volume. In fact, such currents exist also to a substantial degree during the periods of true cathode and virtual cathode acceleration, as described above. Thus, one can envision acceleration of the plasma throughout the inter-electrode volume of the accelerator at these times. The effective electrode radius ratio to be used to calculate the force on the plasma during this stage is presumably some

average of the radius ratios operative at various positions in the accelerator.

e. Corrected Circuit Equations

The experimentally-based difficulties with the conventional moving current sheet model and the conceptual difficulty with the quasi-stationary discharge accelerating a plasma make it clear that one must distinguish between the velocity of the discharge (current sheet) and the velocity of the plasma. This point had been to some extent recognized earlier ^{E-5}. The power involved in accelerating the plasma must then be the force times the velocity of the plasma and not the velocity of the current sheet discharge.

For the case of the quasi-stationary discharge accelerating a plasma, one introduces a circuit equation with an effective plasma velocity, \bar{v} ,

$$\frac{1}{C} q + Ri + L \frac{di}{dt} + L \frac{\bar{v}}{2} i = 0 \quad (6)$$

Equation (6) is solved simultaneously with the equation of momentum conservation

$$F = \frac{1}{2} L i^2 = W (v_d - v_o) \quad (7)$$

and the energy conservation equation which determines \bar{v} .

$$P = \frac{1}{2} L i^2 \bar{v} = W \left(\frac{v_d^2}{2} - \frac{v_o^2}{2} \right) \quad (8)$$

where W is the mass flow rate into the back of the current sheet, and v_d and v_o are, respectively, the velocity of the plasma as it leaves and as it enters the current sheet. This conjecture on how to analyse the case of no collision or radiation losses in the plasma is confirmed by the detailed analysis presented in the following section.

3. Theory of the Quasi-Stationary Discharge Acceleration

In the foregoing, the circuit equations were modified by introducing energy and momentum conservation principles in a consistent way for both the circuit and plasma acceleration equations. In the following, these equations are derived from Faraday's Law to be determined by the bulk motion of the plasma within the discharge volume rather than by the stationary boundaries of the discharge ^{D-8}.

Before developing the circuit equations, it is desirable to consider the detailed structure of the discharge volume (Figure E-2) including the currents, forces, and plasma velocities within it. The discharge is assumed to have a width d and the axial distance from the back end sheet to a point within it is designated by z . The current itself is assumed to be radial with a current distribution at the cathode given by $j(z, t)$ so that the current density at any position within the current sheet is given by

$$j(z, r, t) = \frac{r_1}{r} j(z, t) \quad \begin{cases} r_1 \leq r \leq r_2 \\ 0 \leq z \leq d \end{cases} \quad (1)$$

Thus, the total current that flows between position z in the discharge and the front of the discharge is given by

$$i(z, t) = 2\pi r_1 \int_z^d j(z', t) dz' \quad (2)$$

so that the total current in the entire sheet (from $z = 0$ to $z = d$) and hence in the gun circuit is

$$i(t) = i(0, t) \quad (3)$$

Since the displacement current can be neglected

$$\nabla \times \underline{H} = \underline{J} \quad (4)$$

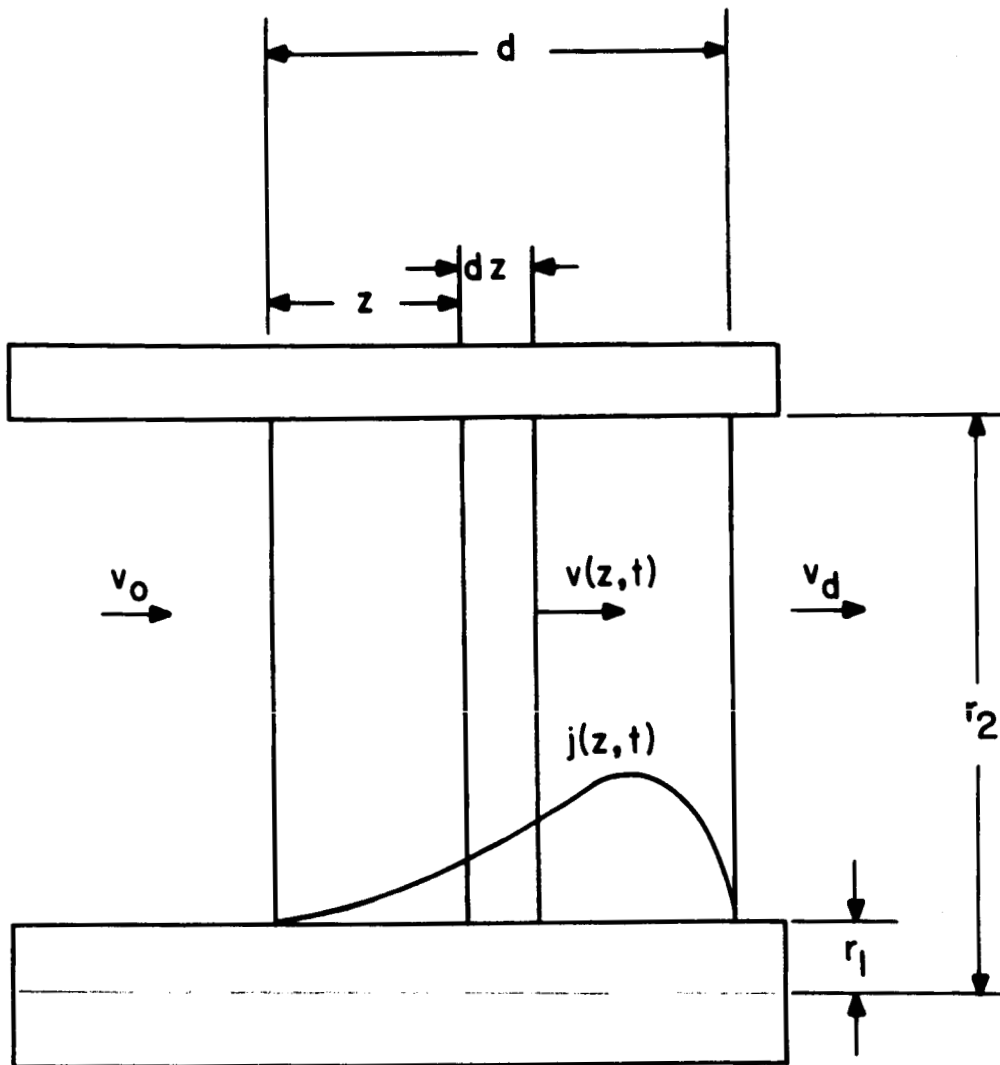


Figure E-2. Schematic of Current Distribution

and the magnetic field at any point within the current sheet can be shown to be

$$B(z, r, t) = \frac{\mu i(z, t)}{2\pi r} = \mu \frac{r_1}{r} \int_z^d j(z', t) dz' \quad (\text{MKS units}) \quad (5)$$

In order to eliminate the necessity of dealing with radial forces and flows, it is assumed that the propellant entering the back of the discharge region has a density distribution given by

$$\rho(z, r, t) = \left(\frac{r_1}{r}\right)^2 \rho(z, t) \quad (6)$$

Finally, it is assumed that the transit time of the plasma through the discharge volume is small compared with the time it takes the circuit parameters of the gun to change so that steady flow can be assumed through the discharge volume. Since a constant area is assumed through the current region, the continuity equation requires that

$$\rho(z, r, t) v(z, t) = \rho(o, r, t) v(o, t) \equiv W \quad (7)$$

As is seen in the following, the density distribution assumed will result in a plasma velocity which is not a function of the radius, thereby maintaining the one-dimensional nature of this analysis.

In the further analysis of the current region, it will be convenient to leave out the explicit dependence on the "circuit time," t , of the parameters involved in defining the current sheet (except for j and i). To avoid confusion, the "current region time" will be denoted by τ , i.e.

$$v = \frac{dz}{d\tau} \quad (8)$$

The total force on the plasma in the discharge volume is seen to be

$$F = \int \left| \underline{j} \times \underline{B} \right| dV = \int_0^d \int_{r_1}^{r_2} j(z, r, t) B(z, r) 2\pi r dr dz \quad (9)$$

or using equation (5)

$$F = L' \left[2\pi r_1 \int_0^d j(z, t) i(z, t) dz \right] \quad (10)$$

where

$$L' = \frac{\mu}{2\pi} \ln \left(\frac{r_2}{r_1} \right) \quad (11)$$

is the inductance per unit length. Noting that

$$\frac{d}{dz} i(z, t) = -2\pi r_1 j(z, t) \quad (12)$$

one obtains the expected result

$$F = L' \int_0^d i(z, t) \frac{d}{dz} i(z, t) dz = \frac{L' i^2}{2} \quad (13)$$

showing that the force exerted by the current is independent of the exact current distribution.

For a given current distribution, the velocity of the plasma at any position in the discharge volume can be calculated as follows

$$v(z) = v_0 + \int_0^{\tau} a d\tau \quad (14)$$

where the acceleration a is given by

$$a = \frac{|\underline{j} \times \underline{B}|}{\rho} \quad (15)$$

Using equation (8), equation (14) becomes

$$v(z) - v_0 = \int_0^z \frac{1}{v} \frac{|\underline{j} \times \underline{B}|}{\rho} dz' \quad (16)$$

or, from equation (7),

$$(v(z) - v_0) \rho_0 v_0 = \int_0^z |\underline{j} \times \underline{B}| dz' \quad (17)$$

Equation (17) gives an explicit way of calculating v at any position within the current sheet. Its relationship to the macroscopic equation for change in momentum for the stationary current distribution can be shown by multiplying equation (17) by $2\pi r$, letting z equal to d , and integrating between the inner and outer electrode to obtain

$$(v_d - v_o) v_o \int_{r_1}^{r_2} 2\pi r \rho_o dr = (v_d - v_o) W = \frac{1}{2} L' i^2 \quad (18)$$

where use has been made of equation (13).

The equation for rate of change of kinetic energy can be similarly derived. In this case, one finds

$$\frac{dv}{d\tau} = v \frac{dv}{dz} = \frac{1}{\rho} \left| \underline{j} \times \underline{B} \right| \quad (19)$$

so that

$$\frac{v^2}{2}(z) - \frac{v_o^2}{2} = \int_0^z \frac{1}{\rho} \left| \underline{j} \times \underline{B} \right| dz' \quad (20)$$

In a manner similar to that used in obtaining equation (18), equation (20) leads to the result

$$(v_d^2 - v_o^2) \frac{W}{2} = \int_{r_1}^{r_2} \int_0^d 2\pi r v(z) \left| \underline{j} \times \underline{B} \right| dz \quad (21)$$

Equation (21) is shown to be equivalent to Equation (8) of the previous section by defining

$$\bar{v} = \frac{\int_{r_1}^{r_2} \int_0^d 2\pi r v(z) \left| \underline{j} \times \underline{B} \right| dz dr}{\frac{1}{2} L' i^2} = \frac{L' \int_0^d v(z) i(z,t) \frac{d}{dz} i(z,t) dz}{\frac{1}{2} L' i^2} \quad (22)$$

Using the foregoing detailed picture of the stationary discharge volume, one can make a more careful study of the accelerator circuit equations. Towards this end one considers the current loop corresponding to the current $2\pi r_1 j(z,t)dz$ which goes through the current sheet at position z (see Figure E-3). The circuit equation for this element of current can be written

$$\frac{q(t)}{C} + R_c i(t) + L_0 \frac{di(t)}{dt} + R' \times i(t) + V_{re}(z,t) + V_{rp}(z,t) = e(z,t) \quad (23)$$

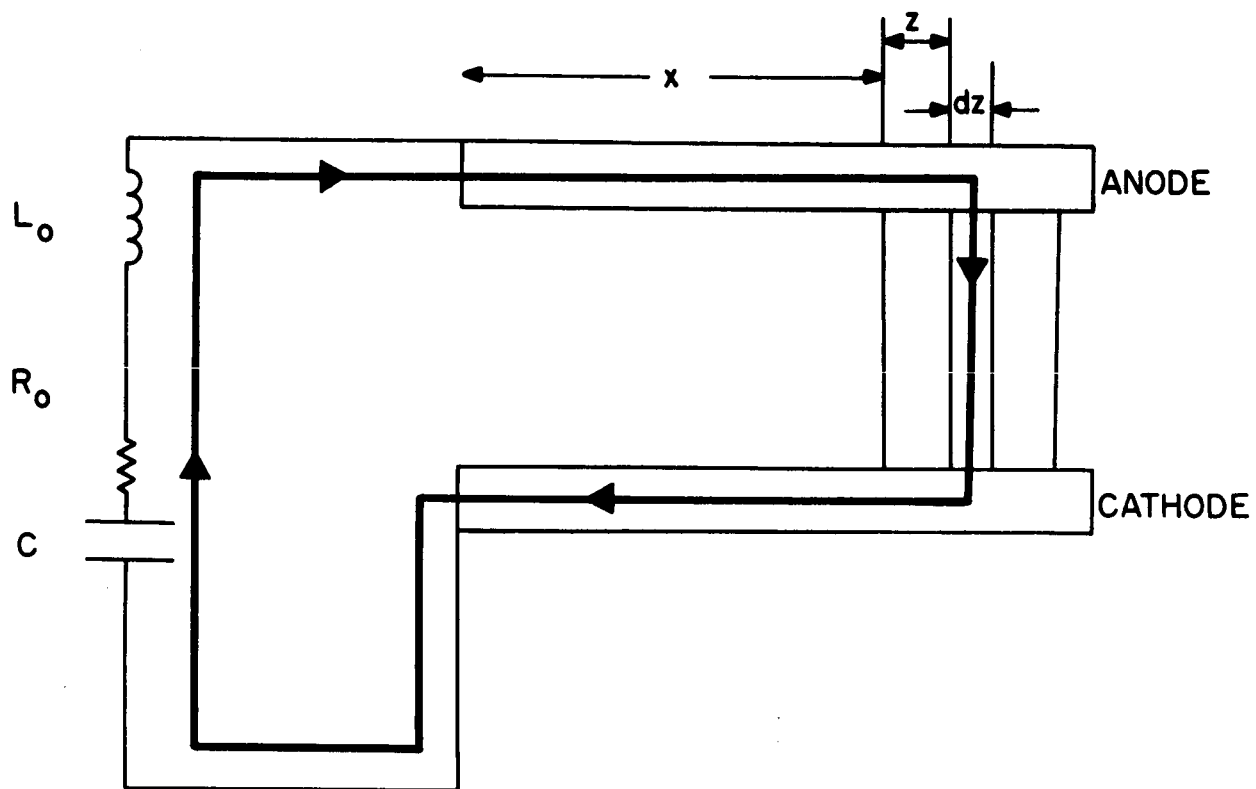


Figure E-3. Differential Current Loop

where

$$R' = \frac{2\pi\delta}{\sigma} (r_2 + r_1) \quad (24)$$

is the resistivity per unit length, δ is the effective skin depth, and σ is the electrode conductivity, V_{re} is the resistive voltage drop from the back end of the current region to the current element, V_{rp} is the resistive voltage drop across the plasma, and \mathcal{E} is the e.m.f. induced by the changing magnetic field for the closed loop which extends from the breech of the gun to the current element at z .

The voltage drop along the electrode next to the current region, V_{re} , can be calculated by noting that the electric field required to drive the current at the inner electrode is given by

$$E_{e1} = i(z, t) \frac{2\pi r_1 \delta}{\sigma} \quad (25)$$

with a similar expression for the outer electrode. Thus,

$$V_{re} = \int_0^z (E_{e1} + E_{e2}) dz = R' \int_0^z i(z', t) dz' \quad (26)$$

The resistive voltage drop across the plasma is given by the expression

$$V_{rp} = \frac{2\pi r_1}{\sigma_p(z)} j(z, t) \quad (27)$$

where σ_p is the plasma conductivity per unit length of the inner electrode.

The electromotive force of the closed loop from the breech of the gun to the element of the current sheet can be calculated from Faraday's law in the general form

$$\begin{aligned} \mathcal{E} &= \oint \underline{E} \cdot d\underline{l} = - \frac{d}{dt} \int \underline{B} \cdot d\underline{S} \\ &= - \int \left[\frac{\partial}{\partial t} \underline{B} + \underline{v} \nabla \cdot \underline{B} - \nabla \times (\underline{v} \times \underline{B}) \right] \cdot d\underline{S} \\ &= - \int \frac{\partial}{\partial t} \underline{B} \cdot d\underline{S} + \oint (\underline{v} \times \underline{B}) \cdot d\underline{l} \end{aligned} \quad (28)$$

where v is the velocity of the integral's moving boundary and use has been made of Stoke's law and the fact that magnetic field is solenoidal. The second term in equation (28) represents the e.m.f. due to the moving element of the plasma at position z . Note that for this element of plasma the only thing that counts is the local velocity of the plasma and the motion of the front and back boundary of the plasma do not enter. The calculation of \mathcal{E} can be carried out explicitly

$$\mathcal{E}(z) = - \int_0^x \int_{r_1}^{r_2} \frac{\partial B}{\partial t} dr dx - \int_0^z \int_{r_1}^{r_2} \frac{\partial}{\partial t} B dr dz' - v \int_{r_1}^{r_2} B dr \quad (29)$$

The value of the first term is relatively straightforward since behind the current region B is a function of r only

$$B = \frac{\mu i(t)}{2\pi r} \quad (30)$$

so that

$$\int_0^x \int_{r_1}^{r_2} \frac{\partial B}{\partial t} dr dx = L' x \frac{di}{dt} \quad (31)$$

For the second term one must take into account the variation of B with z (equation 5)

$$\int_0^z \int_{r_1}^{r_2} \frac{\partial B}{\partial t} dr dz' = \int_{r_1}^{r_2} \frac{\mu dr}{2\pi r} \int_0^z \frac{\partial}{\partial t} i(z', t) dz' = L' \int_0^z \frac{\partial}{\partial t} i(z', t) dz' \quad (32)$$

Finally, one finds that

$$v \int_{r_1}^{r_2} B dr = v \int_{r_1}^{r_2} \frac{\mu i(z, t)}{2\pi r} dr = v L' i(z, t) \quad (33)$$

Thus, one finds that the circuit equation, equation (23), can be written more explicitly as

$$\begin{aligned}
& \frac{q}{C} + (R_0 + R'x) i + (L_0 + L'x) \frac{di}{dt} \\
& + R' \int_0^z i(z', t) dz' + \frac{2\pi r_1}{\sigma_p} j(z, t) + L' \int_0^z \frac{\partial}{\partial t} i(z', t) dz' \\
& + v(z) L' i(z, t) = 0
\end{aligned} \tag{34}$$

To obtain the energy balance equation, equation (34) must be multiplied by $2\pi r_1 j(z, t) dz$ and integrated over the current region. For those terms which do not depend on z (i. e., the first three terms) this is equivalent to multiplying by $i(z)$. The other terms in the resulting power equation can be simplified by noting that

$$\frac{d}{dz} i(z, t) = -2\pi r_1 j(z, t) \tag{35}$$

Thus, one finds

$$\begin{aligned}
& \int_0^d 2\pi r_1 j(z, t) dz \int_0^z i(z', t) dz' = - \int_0^d \frac{d}{dz} i(z, t) dz \int_0^z i(z', t) dz' \\
& = - i(z, t) \int_0^z i(z', t) dz' \Big|_0^d + \int_0^d i^2(z, t) dz \\
& = \int_0^d i^2(z, t) dz
\end{aligned} \tag{36}$$

Similarly one can show

$$\int_0^d 2\pi r_1 j(z, t) dz \int_0^z i(z', t) dz' = \frac{\partial}{\partial t} \int_0^d i^2(z, t) dz \tag{37}$$

Using equations (36) and (37) the resulting power equation can be written

$$\begin{aligned}
& \frac{d}{dt} \left(\frac{q^2}{2C} \right) + Ri^2 + L \frac{d}{dt} \left(\frac{i^2}{2} \right) + R' \int_0^d i^2(z, t) dz \\
& + L' \frac{\partial}{\partial t} \int_0^d \frac{1}{2} i^2(z, t) dz + \int_0^d \frac{1}{\sigma_p} \left[2\pi r_1 j(z, t) \right]^2 dz \\
& + L' \int_0^d 2\pi r_1 v(z) i(z, t) j(z, t) dz = 0
\end{aligned} \tag{38}$$

The first three terms have their usual interpretation. The fourth term corresponds to the resistive losses in the electrode adjacent to the current region. The fifth term corresponds to the magnetic energy stored in the current region and the sixth term corresponds to the Ohmic losses within the current region. The seventh term is the work done on the plasma by the $\underline{j} \times \underline{B}$ forces in the current sheet. Wall losses are not taken into account.^{E-9}

Note that the term in equation (38) for the work done on the plasma can be written as $\frac{\bar{v}}{2} L' i^2$ and is independent of the detailed current distribution (see equation 22). The resistive losses in the current region and the electrode around the current region and the energy stored in the current region are dependent on the detailed current sheet structure. However, if these losses can be ignored or lumped into the overall resistive and inductive energy storage terms by assuming some reasonable current sheet shape, the circuit equation, equation (38), becomes

$$\frac{d}{dt} \left(\frac{q^2}{2C} \right) + R i^2 + L \frac{d}{dt} \left(\frac{i^2}{2} \right) + \frac{\bar{v}}{2} \frac{L' i^2}{2} = 0. \quad (39)$$

Thus, the detailed analysis of the circuit and current sheet results in the same equation which is suggested by energy considerations. Equation (39), must be solved in conjunction with equations (8) and (9) which were suggested by overall energy and momentum considerations and confirmed by the derivation of equations (18) and (21) based on a detailed consideration of acceleration of the plasma through the current sheet.

The detailed current element analysis has been shown to confirm the circuit equations inferred from energy considerations. As expected, this more detailed analysis has the potential of supplying further information. Thus, in equation (23) one sees that the sum of the terms $V_{re}(z, t) + V_{rp}(z, t) - \mathcal{E}(z, t)$ must be independent of z since the balance of the equation does not depend on z . This implies that

$$R' \int_0^z i(z', t) dz' + \frac{2\pi r_1}{\sigma_p} j(z, t) + L' \int_0^z \frac{\partial}{\partial t} i(z', t) dz' + v(z) L' i(z, t) = f(t) \quad (40)$$

where $f(t)$ is the z -independent function given by equation (23). Equation (40) can be seen to be a restriction on allowable current distributions, $j(z, t)$. Indeed, if the plasma conductivity were known as a function of the local current density and B , equation (40) would determine the actual distribution of current, $j(z, t)$, in the sheet when solved in conjunction with equation (17)

$$(v(z) - v_o) W = \int_0^z |j \times B| dz' = \frac{L' i^2(z, t)}{2} \quad (41)$$

Physically the z -independence of equation (40) implies that the current tends to peak towards the front of the current sheet where B is low and that it may have a second peak at the back of the current sheet provided that $v_o \ll v_d$ and that the conductivity is not reduced greatly by the presence of the magnetic field.

If one ignores the electrode ohmic voltage drop and the voltage drop due to the rate of change of magnetic energy stored within the current sheet, equations (40) and (41) can be combined to obtain,

$$-\frac{1}{\sigma_p} \frac{di}{dz} + L' v_o i + \frac{L'}{2W} i^3 = f(t) \quad (42)$$

If σ_p is a function of z but not B and j , equation (50) is an Abel equation of the first kind and can be solved explicitly ^{E-10}. A meaningful calculation would appear to depend on a suitable expression for σ_p even for this simplified case.

REFERENCES

- E-1. The arguments presented here are extracted from the following:
- a). F.W. Mezger, "A constant current sheet velocity model of the coaxial plasma accelerator," GE TIS Report No. R64SD61.
 - b). F.W. Mezger, "A Constant Current Sheet Velocity Model of the Coaxial Accelerator," Paper R2 at the 6th. Annual Meeting of the Plasma Physics Division of the APS (November 4-7, 1964).
 - c). P. Gloersen, B. Gorowitz, A. Ruess and T. Karras, "Dependence of Current Sheet Velocity on the Current in a Coaxial Plasma Gun," Paper R1 at the 6th. Annual Meeting of the Plasma Physics Division of the APS (November 4-7, 1964).
 - d). F. W. Mezger, "Stationary current sheet model for plasma acceleration," GE TIS Report No. R65SD21.
- E-2. M. Rosenbluth, R. Garwin, and A. Rosenbluth, U.S. Atomic Energy Commission, Report LA-1850 (1954).

- E-3. "Hydromagnetic Plasma Gun", J. Marshall in "Plasma Acceleration" by W. Kash - Stanford University Press (1962).
- E-4. P.M. Mostov, J. L. Neuringer, and D.S. Rigney, "Electromagnetic Acceleration of a Plasma Slug," *Phys. Fluids* 4, 1097 (1961).
- E-5. See, for instance, P. J. Hart, "Plasma Acceleration with Coaxial Electrodes," *Phys. Fluids* 5, 38 (1962). This paper also lists several relevant references not listed here.
- E-6. N. A. Black and R. G. Jahn, "Dynamic Efficiency of Pulsed Plasma Accelerator," *AIAA J.* 3, 1209 (1965).
- E-7. B. Gorowitz, P. Gloersen, A. Ruess, and J. Kenney, "Performance study of a repetitively pulsed two-stage plasma propulsion engine," NASA Summary Report No. CR-54064 (August 1964).
- E-8. Integration of volume forces within a discharge has been considered by H. Maecker, *Zeitschrift fur Physik*, 141, 198, 1955, and more recently by J. Yos as an appendix to the paper "Experimental Performance of a High Specific Impulse Arc Jet Engine," R. R. John, S. Bennett, and J. F. Connors, AIAA Paper No. 64-669 at the AIAA Fourth Electric Propulsion Conference, August 31 - September 2, 1964. These discussions are for different current distribution (e. g., a conical distribution is assumed to evaluate the so-called "magnetic blowing" term). Since these papers deal with steady arcs, the question of circuit interaction is not discussed as it does not have the central importance it has for pulsed systems.
- E-9. These have been discussed by K. Thom, J. Norwood, and N. Jalufka In "Velocity Limitation of a Coaxial Plasma Gun," *Physics of Fluids Supplement* 7, No. 11, November 1964, Part 2, Page S67. Since the new efficient guns have a large outer electrode radius, a large electrode radius ratio, and are rather short, wall losses have become less important.
- E-10. Kamke, E., *Differentialgleichungen Lösungsmethoden und Lösungen*, Chelsea Publishing Co., New York, 1959, pages 24-26.

DISTRIBUTION LIST FOR SUMMARY REPORT
CONTRACT NASw-1044

<u>Addressee</u>	<u>Number of Copies</u>
1. NASA-Lewis Research Center 21000 Brookpark Road Cleveland, Ohio Attn: Spacecraft Technology Procurement Section (M.S. 54-2) John H. DeFord	1
Attn: Technology Utilization Office (M.S. 3-19) John Weber	1
Don Vargo	1
Attn: Spacecraft Technology Division (M.S. 54-1) J. H. Childs	2
Dr. H. G. Kosmahl	1
P. Ramins	4
Attn: Library (M.S. 3-7)	2
Attn: Reports Control Office (M.S. 5-5)	1
Attn: Electro-Magnetic Propulsion Division (M.S. 301-1) W. Moeckel	1
E. Callaghan	1
G. Seikel	1
C. J. Michels	1
2. NASA Headquarters FOB-10B 600 Independence Avenue, S. W. Washington, D. C. 20546 Attn: J. Lazar (RNT)	1
J. Mullen	1
3. NASA Scientific and Technical Information Facility P. O. Box 33 College Park, Maryland 20740 Attn: NASA Representative RQT-2448	6
4. NASA-Marshall Space Flight Center Huntsville, Alabama 35812 Attn: Ernest Stuhlinger (M-RP-DIR)	1
5. NASA-Langley Research Center Langley Station Hampton, Virginia 23365 Attn: M. Ellis	1

6. NASA-Ames Research Center
Moffett Field, California 94035
Attn: Dr. Glen Goodwin 1
7. Jet Propulsion Laboratory
Pasadena, California
Attn: J. J. Paulson 1
8. General Dynamics/Convair
P. O. Box 1128
San Diego, California 922112
Attn: A. V. Larson 1
9. Electro-Optical Systems, Inc.
300 North Halstead Street
Pasadena, California 91107
Attn: Dr. T. M. Teem 1
10. The Marquardt Corporation
16555 Saticoy Street
Van Nuys, California 91408
Attn: A. N. Thomas 1
11. Aerospace Corporation
P. O. Box 95085
Los Angeles, California 90045
Attn: Dr. H. Mirels 1
12. Westinghouse Astronuclear Laboratories
Pittsburgh, Pennsylvania 15224
Attn: H. W. Szymanowski, Manager
Electrical Propulsion Laboratory 1
13. AFWL
Kirtland AFB, New Mexico
Attn: Capt. C. F. Ellis/WLPC 1
14. AVCO-Everett Research Laboratory
A Division of AVCO Corporation
2385 Revere Beach Parkway
Everett 49, Massachusetts
Attn: Dr. A. R. Kantrowitz 1
Dr. R. M. Patrick 1
15. Aeronutronics - Ford Motor Company
Newport Beach, California
Attn: Dr. S. R. Bryon 1

16. Space Sciences, Inc.
Natick, Massachusetts
Attn: J. Proud 1
17. Graduate School of Aeronautical Engineering
Cornell University
Ithaca, New York
Attn: Prof. E. L. Resler, Jr. 1
18. Case Institute of Technology
10900 Euclid Avenue
Cleveland, Ohio 44106
Attn: Prof. O. K. Mawardi 1
19. Massachusetts Institute of Technology
Naval Supersonic Laboratory
Cambridge, Massachusetts
Attn: T. K. Kerrebrock and E. E. Covert 1
20. Rensseler Polytechnic Institute
Troy, New York
Attn: Dr. E. H. Holt 1
21. General Technology Corporation
3510 Torrance Boulevard
Torrance, California
Attn: Dr. M. Clauser 1
22. Lockheed Missile Systems Division
Palo Alto, California
Attn: D. Bershader 1
23. United Aircraft Corporation
Research Laboratories
East Hartford 8, Connecticut
Attn: R. G. Meyerand 1
24. Radio Corporation of America
Astro-Electronics Division
Princeton, New Jersey
Attn: T. T. Rebaul 1
25. Litton Systems, Inc.
Beverly Hills, California
Attn: A. S. Penfold 1

26. Allison Division, GMC
Indianapolis, Indiana 46206
Attn: T. L. Rosebrock 1
27. Electro-Optical Systems, Inc.
125 North Vinedo Avenue
Pasadena, California
Attn: Mr. Gordon Cann 1
28. University of California
San Diego, California
Attn: Prof. R. H. Lovberg 1
29. Aeronautical Research Associates of Princeton
Princeton, New Jersey
Attn: R. G. Jahn 1
30. Commander
Aeronautical Systems Division
Wright-Patterson AFB, Ohio 45433
Attn: ASRMPE/R. Rivir 1
31. TRW Systems Group
TRW Inc.
One Space Park
Redondo Beach, California
Attn: Dr. C. L. Dailey 1
32. TRW Inc.
7209 Platt Avenue
Cleveland, Ohio 44107
Attn: R. T. Craig 1
33. Magnetohydrodynamics, Inc.
P. O. Box 1815
Newport Beach, California
Attn: Dr. V. Blackman 1
34. NASA Headquarters
FOB-10B
600 Independence Avenue, S. W.
Washington, D. C.
Attn: RRP/Dr. K. H. Thom 1

35. Aerospace Corporation
P. O. Box 95085
Los Angeles, California 90045
Attn: Library Technical Documents Group 1
Attn: H. Crouch 1
36. Naval Research Laboratory
Washington, D. C. 20025
Attn: A. C. Kolb 1
37. Stevens Institute of Technology
Hoboken, New Jersey
Attn: W. H. Bostick 1
38. AVCO Corporation
Research and Advanced Development Division
201 Lowell Street
Wilmington, Massachusetts
Attn: Dr. R. John 1
39. Giannini Scientific Corporation
3839 South Main Street
Santa Ana, California
Attn: Adriano Ducati 1
40. Los Alamos Scientific Laboratories
P. O. Box 1663
Los Alamos, New Mexico 87544 1
41. Catholic University of America
Dept. of Space Sciences and Applied Physics
Washington, D. C. 20017
Attn: Prof. C. C. Chang 1